UNIVERSITÉ CÔTE D'AZUR

ÉCOLE DOCTORALE
SCIENCES FONDAMENTALES ET APPLIQUÉES

THÈSE DE DOCTORAT

Recherche de signaux d'ondes gravitationnelles transitoires de longue durée avec les détecteurs Advanced Virgo et Advanced LIGO

Adrian Macquet

Laboratoire ARTEMIS, Observatoire de la Côte d'Azur

Présentée en vue de l'obtention du grade de
docteur en Sciences de la Planète et de l'Univers
de l'Université Côte d'Azur

Dirigée par : Marie-Anne Bizouard

Soutenue le : 15 octobre 2021

Devant le jury, composé de :

Nelson Christensen	Directeur de recherche, ARTEMIS	*Président*
Erik Katsavounidis	Professeur, MIT	*Rapporteur*
Tania Regimbau	Directrice de recherche, LAPP	*Rapportrice*
Michael Coughlin	Assistant Professor, University of Minnesota	*Examinateur*
Jérôme Guilet	Ingénieur-Chercheur, CEA	*Examinateur*
Florent Robinet	Chargé de recherche, IJCLab	*Examinateu*

Recherche de signaux d'ondes gravitationnelles transitoires de longue durée avec les détecteurs advanced Virgo et advanced LIGO

Adrian Macquet

Jury :

Président du jury
Nelson Christensen, Directeur de recherche, ARTEMIS, Observatoire de la Côte d'Azur, Université Côte d'Azur, CNRS

Rapporteurs
Erik Katsavounidis, Professor, Massachusetts Institute of Technology
Tania Regimbau, Directrice de recherche, LAPP, Université Savoie Mont-Blanc, CNRS

Examinateurs
Michael Coughlin, Associate Professor, School of Physics and Astronomy, University of Minnesota
Jérôme Guilet, Ingénieur-chercheur, Département d'Astrophysique, CEA
Florent Robinet, Chargé de recherche, IJCLAB, Université Paris-Saclay

Directrice de thèse
Marie-Anne Bizouard, Directrice de recherche, ARTEMIS, Observatoire de la Côte d'Azur, Université Côte d'Azur, CNRS

Résumé

Une nouvelle astronomie avec les ondes gravitationnelles est née en 2015 avec la détection de la première fusion de trous noirs de masse stellaire. Depuis, une cinquantaine de fusions de trous noirs et d'étoiles à neutrons ont été observées par les détecteurs Advanced LIGO et Advanced Virgo. Ces détections permettent d'étudier les populations d'objets compacts, de comprendre la distribution de leur masse, et de contraindre les scenarios de formation de système binaire. Elles permettent également d'étudier la nature de la matière nucléaire dans des environnements extrêmes, ou encore la physique des jets relativistes et des phénomènes d'accrétion, ou bien de tester la validité de la relativité générale. Ces observations, désormais routinières, sont d'une importance majeure et vont continuer à faire progresser notre compréhension de l'univers lors des prochaines campagnes d'observations. Mais découvrir de nouvelles sources astrophysiques ou d'origine cosmologiques d'ondes gravitationnelles fait partie des objectifs majeures de la communauté et nécessite des moyens supplémentaires. C'est sur ce sujet que porte cette thèse.

Plus précisément, les travaux résumés dans cette thèse portent sur la recherche de signaux d'ondes gravitationnelles de longue durée dans les détecteurs Advanced Virgo et Advanced LIGO, c'est-à-dire des signaux transitoires dont la durée se situe entre environ 5 et 1000 secondes.

Les processus astrophysiques pouvant émettre ce type d'ondes gravitationnelles sont variés, mais encore mal modélisés. Ils incluent de potentielles instabilités magnéto-hydrodynamiques dans les étoiles à neutrons nouvellement formées, qui peuvent rendre ces dernières asymétriques et en faire des émettrices d'ondes gravitationnelles, des processus de fragmentation dans les disques d'accrétion autour des trous noirs, ou bien les éruptions géantes qui surviennent dans certains magnétars isolés, associés aux sursauts gamma mous. Ils incluent aussi les signaux de systèmes binaires de trous noirs légers sur des orbites excentriques.

A la différence des fusions d'objets compacts, étoiles à neutrons et trous noirs, la forme d'onde du signal attendu ici n'est pas suffisamment bien modélisée pour permettre l'utilisation de techniques optimales de traitement du signal, comme le filtrage adapté. Les méthodes de détections reposent donc sur des algorithmes qui ne font pas ou peu d'hypothèse sur la nature du signal cherché, et qui sont par conséquent moins sensibles.

Je présente une nouvelle chaîne d'analyse de données que j'ai développée pour rechercher des signaux non modélisés dans les détecteurs de type Advanced Virgo et Advanced LIGO. Ce programme se base sur une méthode déjà éprouvée pour la recherche de signaux en provenance d'un point précis du ciel, et est optimisé pour des recherches sur l'ensemble du ciel sur toute la durée d'une session d'observation. Il implémente une méthode hiérarchique de sélection des données pour réduire le temps de calcul, et se base sur la corrélation des données entre plusieurs détecteurs pour rejeter les artefacts d'origine instrumentale et environnementale.

J'utilise cette chaîne d'analyse pour rechercher des signaux dans les données des campagnes d'observation O2 et O3 d'Advanced Virgo et Advanced LIGO, et j'obtiens des résultats qui ne mettent pas en évidence de nouvelles sources malgré une sensibilité légèrement meilleure pour des types de signaux variés. Je montre aussi que le temps de calcul a été considérablement réduit.

Enfin, je décris la recherche de contreparties en onde gravitationnelles éventuellement émises par trois éruptions géantes de magnétars qui semblent constituer une nouvelle catégorie de sursaut gamma, et démontre que si un évènement de ce type venait à se produire dans la galaxie, il serait possible de d'observer l'émission d'ondes gravitationnelles si celle-ci est au moins 1% aussi énergétique que l'émission électromagnétique avec les détecteurs actuelles à leur sensibilité finale.

Mots-clés : Relativité générale - Ondes gravitationnelles - Objets compacts - Analyse de données

Abstract

A new astronomy with gravitational waves was born in 2015 with the detection of the first stellar mass black hole merger. Since then, about 50 black hole and neutron star mergers have been observed by the Advanced LIGO and Advanced Virgo detectors during three observation periods. These detections allow to study the populations of compact objects, their mass distribution, and the scenarios of binary system formation. They also allow to study the nature of nuclear matter in extreme environments, the physics of relativistic jets and accretion phenomena, to measure the Hubble constant in an independent way, and to test possible deviations from the theory of general relativity. These observations, now routine, are of major importance and will continue to advance our understanding of the universe during the next observing campaigns. But discovering new astrophysical or cosmological sources of gravitational waves is one of the major objectives of the community and requires additional resources. It is on this subject that this thesis focuses.

More precisely, the work summarized in this thesis concerns the search for long duration gravitational wave signals in the Advanced Virgo and Advanced LIGO detectors, i.e. transient signals whose duration is between about 5 and 1000 seconds.

The astrophysical processes that can emit this type of gravitational waves are varied, but still poorly modeled. They include potential magneto-hydrodynamic instabilities in newly formed neutron stars, which can make them asymmetric and thus emit gravitational waves, fragmentation processes in accretion disks around black holes, or giant flares that occur in some isolated magnetars, associated with soft gamma-ray bursts. They also include signals from binary systems of rather light black holes in eccentric orbits.

Unlike mergers of compact objects, neutron stars and black holes, the waveform of the signal expected here is not sufficiently well modeled to allow the use of optimal signal processing techniques, such as matched filtering. Detection methods therefore rely on algorithms that make few or no assumption about the nature of the signal sought, and are therefore less sensitive.

In this thesis, I present a new data analysis pipeline that I have developed to search for unmodeled signals in Advanced Virgo and Advanced LIGO interferometric detectors. This program is based on an already proven method to search signals from a specific point in the sky, and is optimized for searches over the whole sky during an entire observing run. It implements a hierarchical data selection method to reduce the computational time required for analysis, and relies on the correlation of data between multiple detectors to reject artifacts of instrumental and environmental origin.

I use this pipeline to search for signals in data from the Advanced Virgo and Advanced LIGO O2 and O3 observing campaigns, and obtain results that do not highlight new sources despite slightly better sensitivity for various signal types. I also show that the computational time was significantly reduced.

Finally, I describe the search for gravitational wave counterparts possibly emitted by three giant magnetar flares that seem to constitute a new class of gamma-ray bursts, and show that if such an event were to occur in the galaxy, it would be possible to observe gravitational wave emission if it is at least 1% as energetic as the electromagnetic emission with the current detectors at their final sensitivity.

Keywords: General relativity - Compact objects - Gravitational waves - Data analysis

À mes parents

Remerciements

Mes premiers et plus importants remerciements vont à ma directrice de thèse, Marie-Anne Bizouard, qui m'a guidé, encadré, motivé, corrigé et supporté durant toute cette thèse. Je suis encore étonné de la quantité de connaissances que j'ai pu emmagasiner au cours des ces trois années, et j'espère pouvoir toujours continuer d'apprendre et contribuer à l'aventure de l'astronomie gravitationnelle. J'ai eu également la chance d'être aidé et soutenu par de nombreuses personnes, à la fois au sein du laboratoire ARTEMIS et du groupe burst de la collaboration LIGO-Virgo, en particulier Nelson Christensen, ainsi que Michael Coughlin, Claudia Lazzaro, Maxime Fays et Roberto de Pietri du groupe long-duration.

L'Observatoire de la Côte d'Azur, avec sa vue imprenable sur toute la baie de Nice, ses sangliers, chevreuils, arbres fruitiers, est un lieu fantastique et hors du commun des autres laboratoires que j'ai pu connaître. Je mesurerai certainement encore plus la chance que j'ai eu d'y travailler après l'avoir quitté. Mon séjour dans ces lieux a été rendu d'autant plus agréable par la présence de l'excellent restaurant tenu par Dominique, Karima et Nadia, sous la direction de l'innénarable Khaled.

Sur une crête du Mont-Gros, un peu isolée du reste des infrastructures, se dresse la Maison Jumelle, siège du laboratoire ARTEMIS (et de mon bureau, toujours impeccablement rangé). Cette vieille batisse aux parquets qui grincent et aux volets qui se détachent peut sembler au premier abord un drôle d'endroit pour se consacrer au développement et à l'analyse des données des instruments physiques parmi les plus sensibles et les plus modernes du monde actuel; mais on s'y sent pourtant tout de suite remarquablement bien et chez soi, au point que je ne m'imagine pas travailler à nouveau dans un bureau ne disposant pas d'une cheminée en marbre et d'une vue sur la mer. Je tiens à remercier ici Angélique Guitard, mes collègues de bureau et amis Cosmin, Guillaume et Thomas, et toutes les personnes qui m'ont donné envie de venir passer ici mes longues journées de télétravail.

Enfin, je remercie grandement les membres du jury, Nelson Christensen, Michael Coughlin, Jérôme Guilet, Erik Katsavounidis, Tania Regimbau et Florent Robinet, et bien sûr encore une fois Marie-Anne, pour avoir lu, relu, commenté et corrigé cette thèse et pour leurs bienveillants conseils.

Et bien evidemment, tous mes très bons amis de Nice et d'ailleurs, Anthony, Eliott, Guillaume, Paul, Saniya, Vincent, Zac.

Contents

Introduction

In 1905, based on Lorentz's work, Poincaré proposed the concept of *gravific wave* as a consequence of the impossibility of instantaneous action at a distance applied to gravitation [1]. However, it remained not formalized until 1916, after Einstein formulated the general theory of relativity [2]. Using the framework of general relativity, Einstein predicted that small perturbations of the structure of space-time itself could propagate through the Universe at the speed of light, hence named *gravitational waves* [3, 4]. Nevertheless, the nature and even the existence of such waves remained controversial for many more years after that. This, and the fact that their predicted amplitude was extremely small, lead to a loss of interest within the scientific community.

The theoretical obstacles were of two types. First, it was unclear whether gravitational waves had a real effect on matter, or if they were just a coordinate effect without any physical reality. Einstein himself famously changed his mind several times on that question. Secondly, the linear approximation used to describe them was only valid for regions of spacetime where the gravitational field is weak. Yet, the most promising potential sources of gravitational waves were phenomena involving very strong gravitational fields, such as the merger of two compact objects. The equations of general relativity were not solved in the strong field regime, so no one was even sure that the theory allowed generation of gravitational waves in this regime. These obstacles were cleared in the late 1950's notably by Pirani and Bondi [5, 6, 7, 8], who showed that gravitational waves could be associated with the Riemann tensor, an object whose physical reality was indubitable, even in the strong field regime, and that they carry energy. What happened a bit later at the Chapel Hill meeting organized in 1957 in North Carolina [9] is now considered as a crucial moment in the history of gravitational-wave physics. Pirani's presentation at the conference had an especially high impact on those who were thinking about actually constructing a real gravitational wave detector [9, 10]. Also present at the conference, Feynman came with a description of a thought experiment, free of the problems and hinderances of tensor calculus, that shows that gravitational waves contain energy and could be detected. The crux of the *sticky beads argument* is that if one puts two beads on a stick, where the stick is perpendicular to the direction of propagation of the gravitational wave, as the wave propagates by, the stick will be held firm by the atomic and molecular forces while the beads will move with respect to each other. If there is friction between the beads and the stick, then heat will be generated. Clearly the source of this energy is ultimately the gravitational wave [11]. Interestingly, Weber was among the audience and decided soon after to build a detector to detect gravitational waves by measuring vibrations induced in a large mechanical system. His first antenna was a large aluminium cylinder isolated from group vibration by a steel wire and placed inside a vacuum chamber. Piezoelectric sensors were installed to sense the bar's vibration induced by gravitational waves [12]. In 1969, Weber and collaborators claim to have detected gravitational waves [13], but Weber's "signals" have never been confirmed by other bars built by other teams all over the world (USA, Italy, Germany, UK, Brazil, Netherlands, Australia).

In 1974, the discovery of the first binary pulsar, PSR 1913+16 [14], provided the first indirect proof of the existence of gravitational waves. Indeed, the orbital decay of the pulsar is in total agreement with the theoretical value predicted by general relativity, which proves that the system radiates energy in the form of gravitational waves [15]. The interest for detecting gravitational waves was renewed at these singular occasions.

The idea of using laser interferometry to detect gravitational waves emerged in the late 1960's, after the first explicit suggestion by Gertsenshtein and Pustovoid in 1962 [16]. It turns out that the first prototype, a 8.5 m arm long interferometer, has been built by Forward, student of Weber in 1978. In the late 60's Weiss, inspired by Pirani's seminal articles, started to get interested in laser interferometry to detect gravitational waves. Several meter's long projects have then been funded to develop the technology in USA but also in Germany (Billing's team) and in the UK (Drever who would build later the 40 m prototype at Caltech). However, because of the huge technical challenges, and the cost of the large instruments necessary to have a realistic chance of detection, only two major projects in the USA and Europe got funded and the construction of the kilometer-scale laser interferometers LIGO and Virgo only began in the 1990s respectively in the United States and Italy [10]. The UK-German detector GEO has arms of 600 meters and has been very useful for LIGO and Virgo to develop and test new technology. Finally, after more than two decades of development and sensitivity upgrades, the upgraded version of the LIGO detector observed on 14 September 2015 the first confirmed gravitational-wave signal from the merger of two black holes - GW150914 [17]. Since then, several dozens of signals have been detected by the LIGO and Virgo detectors, all from the merger of two compact objects, black holes and neutron stars [18].

The discovery of gravitational waves has definitively closed a hundred years old controversy and constitutes another solid proof of the validity of general relativity. On top of that, it has opened an entirely new field of astronomy. GW150914 was the first direct proof of the existence of black holes. On 17 August 2017, the detection of a gravitational wave signal from the fusion of two neutron stars [19], followed by the detection of a gamma-ray burst from the same part of the sky, opened the era of multi-messenger astronomy. By combining gravitational waves with observations in the electromagnetic spectrum, cosmic rays and neutrinos, we can probe the physics of compact objects and cosmology deeper than ever. Very recently, the mergers of two mixed system – a black hole and a neutron star – have been observed [20]

This thesis presents the work I did between 2018 and 2021 within the LIGO and Virgo collaboration on the detection of long-lived gravitational-wave signals. The first chapter will be dedicated to the theoretical aspects of gravitational waves in the framework of general relativity, and to the principle of interferometric detectors, using the example of Advanced Virgo. Afterwards, I will give an overview of the main astrophysical sources of gravitational waves, with a focus on long-lived transient sources. The core of my work has been the development of a data analysis pipeline to search for unmodeled gravitational waves. This pipeline and the data analysis methods it implements will be presented in the third chapter. Finally, the next two chapters will be devoted to the description of the searches I performed with the pipeline : all-sky searches in the Advanced LIGO – Advanced Virgo 's second and third observing runs in chapter 4, and a study of the potential gravitational wave emission of Magnetar Giant Flares is reported in chapter 5.

Chapter 1

General relativity, gravitational waves and their detection

1.1 Basics of general relativity

It is quite difficult to explain the notion of a gravitational wave (GW) in one or two sentences, since it does not have an intuitive translation in pre-relativistic physics. GW could be thought of as a perturbation of the geometry of spacetime that propagates through the Universe at the speed of light. Yet, to give a meaning to this definition, we need to describe what is meant by the geometry of spacetime. General relativity postulates that space and time do not constitute a fixed, immutable scene in which the physical events take place, but on the contrary, that the geometry of spacetime is not fixed, and is determined by the distribution of its constituent components, matter and energy - which are reciprocally influenced by the geometry.

Since GW are described in the framework of general relativity, the purpose of this first section is to explain the basics concepts of this theory, and to set up the mathematical framework and definitions that will be necessary to describe the physics of GW, mainly following [21], and [22].

1.1.1 Concepts and principles

In the second half of the 19th century, Maxwell formulated the classical theory of electromagnetism in the form of the *Maxwell's equations*, which describe the coupling between electric and magnetic fields, and showed that electromagnetic waves propagate at a constant speed - the *speed of light*, $c = 299{,}792{,}458\,\mathrm{m/s}$ - in the vacuum. In the meantime, the dynamics of macroscopic bodies was still described very accurately by Newton's laws of motion in the framework of classical mechanics.

However, a fundamental contradiction exists between the two theories: classical mechanics obeys the Galilean principle of relativity, which states that the laws of physics should have the same expression in any inertial frame of reference. This is not the case for Maxwell's equations, whose expressions are not invariant under a Galilean transformation. Furthermore, in the 1880's, Michelson and Morley showed experimentally that the speed of light that we measure is the same in all frames, and does not depend on the relative motion of the observers.

This manifest incompatibility led Einstein to develop the special theory of relativity, published in 1905 [23]. The theory reformulates the laws of mechanics in order to make them compatible with the invariance of c and the principle of relativity, which states that the laws of physics should have the same form in any reference frame. As a consequence, the notion of absolute space and time disappears, as well as the concept of simultaneity between two events. If we consider two events E_1 and E_2 described by their respective coordinates in some inertial frame $(c\,t_1, x_1, y_1, z_1)$ and $(c\,t_2, x_2, y_2, z_2)$, the time interval $t_2 - t_1$ between them does not remain the

same when it is expressed in another inertial frame. Instead, it is the *spacetime interval*

$$\Delta s^2 = -c^2 (t_2 - t_1)^2 + (x_2 - x_1)^2 + (y_2 - y_1)^2 + (z_2 - z_1)^2. \tag{1.1}$$

that is invariant under a change of frame. The theory of special relativity successfully unifies classical physics and electromagnetism, but it is not compatible with Newton's law of universal gravitation. Indeed, the latter involves an instantaneous action at a distance between attracting bodies, which is forbidden by the finiteness of c. Therefore, a different theory of gravitation is needed to be compatible with special relativity.

The equivalence principle is one of the main concepts that constitute the roots of general relativity. Newton's second law stipulates that the acceleration $\vec{a}$ of a body is proportional to the force $\vec{F}$ applied,

$$\vec{F} = m_i \vec{a}. \tag{1.2}$$

The proportionality factor between force and acceleration is the *inertial* mass m_i of the body. On the other hand, the force $\vec{P}$ exerted on a body by a gravitational field $\vec{g}$ is proportional to its gravitational mass m_g:

$$\vec{P} = m_g \vec{g}. \tag{1.3}$$

It is clear that inertial mass and gravitational mass are two different quantities in the Newtonian theory. However, all the experiences and observations made to date show that the two masses are equal. As a consequence, the acceleration of a body in a gravitational field does not depend on its mass: $\vec{a} = \vec{g}$. This is called the *weak equivalence principle*.

The equality between inertial and gravitational mass is a coincidence in Newtonian physics, in the sense that it is not fundamental to the theory. Einstein postulates that this principle is true and places it at the center of his theory of gravitation. He proposes the following interpretation, known as the Einstein equivalence principle:

> The outcome of any local non-gravitational experiment in a freely falling laboratory is independent of the velocity of the laboratory and its location in spacetime.

In other words, it is impossible to make a distinction between a particle that accelerates due to the action of a gravitational field and a particle at rest in an accelerating frame. Therefore, it is possible to see gravitation no longer as a force, but as an intrinsic property of spacetime that causes the acceleration of free-falling particles.

1.1.2 Geometrical framework

The idea that gravitation is a geometric property of spacetime is implemented in the framework of Riemannian geometry, which generalizes Euclidean geometry to non-flat spaces. In general relativity, free-falling particles follow geodesics ("straight lines") in a curved spacetime, just like particles in inertial motion follow a straight line in the flat space. In the following paragraphs, I will briefly describe the fundamental concepts of Riemaniann geometry and introduce the mathematical objects that play a significant role in the description of GW.

The geometrical structure of spacetime is a 4-dimensional *manifold*. A manifold of dimension n is a space which resembles locally the flat space $\mathbb{R}^n$, but does not have necessarily the same topological properties. For example, a sphere, such as the surface of the Earth, is a 2-dimensional manifold: at the local level, it "looks" flat and points on the surface can be localized with a set of two coordinates in $\mathbb{R}^2$ (e.g latitude and longitude), but the sphere in its entirety cannot be assimilated to the plane $\mathbb{R}^2$ - its topology is different.

The metric properties of a manifold are entirely described by the *metric tensor*, which allows to compute distances and angles. Considering two infinitely close points p and q and a coordinate

system $\{x^\alpha\}$ such that the coordinates of p and q are respectively (x^α) and $(x^\alpha + dx^\alpha)$, the infinitesimal distance ds between them is given by

$$ds^2 = g_{\mu\nu} dx^\mu dx^\nu, \tag{1.4}$$

where $g_{\mu\nu}$ represent the components of the metric tensor at the point p expressed in this coordinate system. Note that we use the Einstein summation convention that consists in summing over indexes that are repeated in upper and lower position. Greek indexes are summed from 0 to 3, while Latin indexes are summed from 1 to 3 : $v^\mu v_\mu = v^0 v_0 + v^1 v_1 + v^2 v_2 + v^3 v_3$.

For instance, in the Euclidean space $\mathbb{R}^3$ with coordinates (x, y, z), it is clear that $ds^2 = dx^2 + dy^2 + dz^2$, therefore

$$g_{\mu\nu} = \delta_{\mu\nu} \equiv \begin{pmatrix} 1 & 0 & 0 \\ 0 & 1 & 0 \\ 0 & 0 & 1 \end{pmatrix}. \tag{1.5}$$

In special relativity, the invariant spacetime interval is $ds^2 = -c^2 dt^2 + dx^2 + dy^2 + dz^2$, so the metric of spacetime is the *Minkowski metric*

$$g_{\mu\nu} = \eta_{\mu\nu} = \begin{pmatrix} -1 & 0 & 0 & 0 \\ 0 & 1 & 0 & 0 \\ 0 & 0 & 1 & 0 \\ 0 & 0 & 0 & 1 \end{pmatrix}. \tag{1.6}$$

Note that in that case, ds^2 is negative for a particle that moves at a velocity lower than c, and null for a photon. The metric tensor is also symmetric: $g_{\nu\mu} = g_{\mu\nu}$ in any coordinate system. Its inverse has components $g^{\mu\nu}$ such that

$$g^{\mu\sigma} g_{\sigma\nu} = \delta^\mu_\nu. \tag{1.7}$$

In the remainder of this chapter, we will use the metric tensor and its inverse to raise and lower indexes

All the geometrical properties of a manifold are described by the *Riemann tensor*

$$R^\alpha_{\beta\mu\nu} = \partial_\mu \Gamma^\alpha_{\beta\nu} - \partial_\nu \Gamma^\alpha_{\beta\mu} + \Gamma^\alpha_{\rho\mu} \Gamma^\rho_{\beta\nu} - \Gamma^\alpha_{\rho\nu} \Gamma^\rho_{\beta\mu}, \tag{1.8}$$

which is a combination of the first and second derivatives of the metric tensor via the *Christoffel symbols*:

$$\Gamma^\alpha_{\mu\nu} = \frac{1}{2} g^{\alpha\rho} \left(\partial_\mu g_{\rho\nu} + \partial_\nu g_{\mu\rho} - \partial_\rho g_{\mu\nu} \right) \tag{1.9}$$

Two quantities of interest can be constructed from the Riemann tensor: the *Ricci tensor*

$$R_{\mu\nu} = R^\rho_{\mu\rho\nu}, \tag{1.10}$$

and its trace, the *Ricci scalar*

$$R = g^{\mu\nu} R_{\mu\nu}. \tag{1.11}$$

These quantities play an important role in general relativity, as they form a part of the Einstein equation that links the geometry of spacetime to the distribution of mass-energy.

1.1.3 Physics in curved spacetime

The motion of a particle is entirely described by its trajectory in spacetime, called *world line*. In a given coordinate system $\{x^\alpha\}$, a world line can be parametrized by an arbitrary real number λ, such that the coordinates of the particle along its world line are given by the functions $x^\alpha(\lambda)$. Among all possible parametrizations, we define the *proper time* to be the time measured by a clock that follows this world line. It is a physical, measurable quantity that does not depend on

the coordinate system. A fundamental interpretation of the metric tensor $g_{\mu\nu}$ is that the proper time interval $d\tau$ between two infinitesimally close points on a world line is

$$c d\tau = \sqrt{-ds^2}. \tag{1.12}$$

Consequently, the proper time between two points on a world line parametrized by λ_1 and λ_2 is

$$\tau = \int_p^q \sqrt{-ds^2} = \int_{\lambda_1}^{\lambda_2} \sqrt{-g_{\mu\nu} \frac{dx^\mu}{d\lambda} \frac{dx^\nu}{d\lambda}} d\lambda. \tag{1.13}$$

In the absence of any external force, the coordinates $x^\mu(\tau)$ of a particle follow the *geodesics equation*

$$\frac{d^2 x^\mu}{d\tau^2} + \Gamma^\mu_{\alpha\beta} \frac{dx^\alpha}{d\tau} \frac{dx^\beta}{d\tau} = 0. \tag{1.14}$$

Note that this equation depends on the derivatives of the metric tensor via the Christoffel symbols, and therefore on the curvature of spacetime. The geodesics equation generalizes Newton's first law of motion: in a flat spacetime and cartesian coordinate system (t, x, y, z), all Christoffel symbols are zero, so the equation reduces to $\frac{d^2 x^\mu}{dt^2} = 0$, which corresponds to rectilinear uniform motion. The presence of a gravitational field is no longer modelized by an external force, but it is reflected by the fact that the metric diverges from the Minkowski metric. There are three types of geodesics, depending on the sign of the spacetime interval ds^2:

- **Timelike geodesics -** $ds^2 < 0$ correspond to world lines of massive particles. They maximize the proper time between two points.
- **Null geodesics -** $ds^2 = 0$ are the world lines followed by photons. They correspond to particles moving at the speed of light.
- **Spacelike geodesics -** $ds^2 > 0$ minimize the distance between two points. Causality forbids physical particles to follow spacelike geodesics.

As already stated, the core concept of general relativity is the fact that the metric of spacetime is determined by the distribution and the circulation of mass-energy. These properties are encompassed in the *stress-energy tensor* $T_{\mu\nu}$, whose components can be related to the (local) energy density ρ, momentum $\vec{p}$ and the stress tensor $\mathbf{S}$:

$$\begin{aligned} T_{00} &= \rho \\ T_{0i} &= p_i \\ T_{ij} &= S_{ij}. \end{aligned} \tag{1.15}$$

In Newtonian physics, the Poisson equation relates the gravitational potential Φ to the mass distribution ρ:

$$\Delta\phi = 4\pi G\rho. \tag{1.16}$$

In general relativity, the metric of spacetime $g_{\mu\nu}$ is related to the stress-energy tensor via the Einstein field equations

$$\boxed{R_{\mu\nu} - \frac{1}{2} R g_{\mu\nu} + \Lambda g_{\mu\nu} = \frac{8\pi G}{c^4} T_{\mu\nu}.} \tag{1.17}$$

The quantity $R_{\mu\nu} - \frac{1}{2} R g_{\mu\nu}$ is the Einstein tensor. It is the simplest tensor built from the metric and its first and second derivatives are divergence free, hence it ensures the conservation of energy-momentum. Besides, it reduces to the Poisson equation in the weak field limit. The cosmological constant Λ was initially added to the equations by Einstein to ensure that the Universe is static at large scales. Nowadays, after the discovery of the acceleration of the expansion of the Universe in 1998 [24, 25], it is linked to the density of dark energy in the Universe.

1.2 Gravitational waves

1.2.1 Linearized Einstein equations

The Einstein equations are highly nonlinear, which makes the search for exact solutions very difficult in practice. However, it is possible to linearize these equations to get analytic solutions at the first order. The Minkowski metric $\eta_{\mu\nu}$ is a trivial solution of the equations that corresponds to a flat spacetime. Therefore, in the weak field approximation, i.e when the gravitational field is small, the metric of spacetime can be expressed as the sum of the Minkowski metric and a small perturbation $h_{\mu\nu}$:

$$g_{\mu\nu} = \eta_{\mu\nu} + h_{\mu\nu} \tag{1.18}$$

with $|h_{\mu\nu}| << 1$. In practice, this approximation would be valid when the gravitational potential Φ is small compared to c^2. For example, at the surface of the Earth, we have $\Phi \simeq 6.2 \times 10^7\,\mathrm{m^2\,s^{-2}} << \mathrm{c}^2$.

Let us linearize the left hand side of the Einstein equations by expanding the metric $g_{\mu\nu}$ at the first order in $|h_{\mu\nu}|$. First, we need to compute the inverse metric tensor $g^{\mu\nu}$, which can be expressed as

$$g^{\mu\nu} = \eta^{\mu\nu} + k^{\mu\nu} \tag{1.19}$$

with $|k^{\mu\nu}| << 1$. Using the fact that $g^{\mu\sigma}g_{\sigma\nu} = \eta^{\mu\sigma}\eta_{\sigma\nu} = \delta^{\mu}_{\nu}$, and neglecting higher order terms,

$$k^{\mu\nu} = -\eta^{\mu\alpha}\eta^{\nu\beta}h_{\alpha\beta} = -h^{\mu\nu}. \tag{1.20}$$

The Christoffel symbols associated to the linearized metric $g_{\mu\nu} = \eta_{\mu\nu} + h_{\mu\nu}$ are

$$\Gamma^{\alpha}_{\mu\nu} = \frac{1}{2}\eta^{\alpha\sigma}\left(\partial_\mu h_{\sigma\nu} + \partial_\nu h_{\mu\sigma} - \partial_\sigma h_{\mu\nu}\right), \tag{1.21}$$

where we have expanded Eq. (1.9) and neglected terms in second order in $|h_{\mu\nu}|$.

We can now compute the Ricci tensor and Ricci scalar using the linearized expression of the Christoffer symbols. Since we consider only the terms in first order, the quadratic terms disappear and

$$R_{\mu\nu} = \partial_\sigma\Gamma^{\sigma}_{\mu\nu} - \partial_\nu\Gamma^{\sigma}_{\mu\sigma}. \tag{1.22}$$

Therefore,

$$R_{\mu\nu} = \frac{1}{2}\eta^{\alpha\beta}\left(\partial_\mu\partial_\alpha h_{\nu\beta} + \partial_\nu\partial_\alpha h_{\mu\beta} - \partial_\alpha\partial_\beta h_{\mu\nu} - \partial_\alpha\partial_\beta h_{\mu\nu}\right). \tag{1.23}$$

For commodity let us introduce the notations $h \equiv \eta^{\mu\nu}h_{\mu\nu}$ for the trace of $h_{\mu\nu}$ and the *trace-reversed metric perturbation* $\bar{h}_{\mu\nu} \equiv h_{\mu\nu} - \frac{1}{2}h\eta_{\mu\nu}$. Finally, the Einstein tensor can be expressed as a function of $\bar{h}_{\mu\nu}$ and its partial derivatives:

$$R_{\mu\nu} - \frac{1}{2}Rg_{\mu\nu} = \frac{1}{2}\eta^{\alpha\beta}\left(\partial_\nu\partial_\alpha\bar{h}_{\mu\beta} + \partial_\mu\partial_\alpha\bar{h}_{\nu\beta} - \partial_\alpha\partial_\beta\bar{h}_{\mu\nu} - \partial_\beta\partial_\alpha\bar{h}_{\alpha\beta}\eta_{\mu\nu}\right). \tag{1.24}$$

One can recognize in this last expression the d'Alembertian operator $\eta^{\mu\nu}\partial_\mu\partial_\nu$, which is associated to the propagation of a plane wave at the speed of light ($\eta^{\mu\nu}\partial_\mu\partial_\nu = c^2\partial_t^2 - (\partial_x^2 + \partial_y^2 + \partial_z^2)$ in the Minkowskian coordinates system (t, x, y, z)). The linearized Einstein equations resemble a wave equation for $\bar{h}_{\mu\nu}$ with the stress-energy tensor as a source term:

$$\boxed{\eta^{\alpha\beta}\partial_\alpha\partial_\beta\bar{h}_{\mu\nu} - \eta^{\alpha\beta}\left(\partial_\nu\partial_\alpha\bar{h}_{\mu\beta} + \partial_\mu\partial_\alpha\bar{h}_{\nu\beta} - \partial_\beta\partial_\alpha\bar{h}_{\alpha\beta}\eta_{\mu\nu}\right) = -\frac{16\pi G}{c^4}T_{\mu\nu} + \mathcal{O}(|h|^2).} \tag{1.25}$$

In this last equation, we have included the term $\mathcal{O}(|h|^2)$ as a reminder that this approximation is only valid at the first order.

1.2.2 Gauge transformations

The general expression of the linearized Einstein equations is valid in any coordinate system that verifies the condition $|h_{\mu\nu}| << 1$. In general relativity, there is no privileged coordinate system: physical quantities are invariant under a change of coordinates. Therefore, it is reasonable to change coordinates to simplify the equations and get a better understanding of the underlying physics.

If we consider a new system of coordinates $\{x'^{\mu}\} = \{x^{\mu} + \epsilon^{\mu}(x^{\nu})\}$, where the functions ϵ^{μ} satisfy the condition $|\frac{\partial \epsilon_{\mu}}{\partial x^{\nu}}| \sim |h_{\mu\nu}|$ (i.e an infinitesimal change of coordinates), the expression of the metric tensor $g'_{\mu\nu}$ in the new coordinate system is given by

$$g'_{\mu\nu} = \eta_{\mu\nu} + h'_{\mu\nu} \tag{1.26}$$

with

$$h'_{\mu\nu} = h_{\mu\nu} - \partial_{\mu}\epsilon_{\nu} - \partial_{\nu}\epsilon_{\mu} \tag{1.27}$$

and $|h'_{\mu\nu}| \sim |h_{\mu\nu}| << 1$. The components of the Riemann tensor are not affected by such a change of coordinates: $R'^{\alpha}_{\beta\mu\nu} = R^{\alpha}_{\beta\mu\nu}$. Therefore, both system of coordinates depict the same physical system. This property is called *gauge invariance* by analogy with the gauge invariance of the electromagnetic potential, where a transformation of the potential $A_{\mu} \mapsto A_{\mu} + \partial_{\alpha}\psi$ does not change the value of the observable field $F_{\mu\nu} = \partial_{\mu}A_{\nu} - \partial_{\nu}A_{\mu}$.

Lorenz gauge

We can look for infinitesimal changes of coordinates that simplify the expression of the linearized Einstein equations. In particular, we would like to see if it is possible to cancel the terms in $\eta^{\mu\nu}\partial_{\mu}\bar{h}_{\alpha\nu}$ in Eq. (1.25) to obtain a true wave equation of the form

$$\boxed{\eta^{\mu\nu}\partial_{\mu}\partial_{\nu}\bar{h}_{\alpha\beta} = -\frac{16\pi G}{c^4}T_{\alpha\beta}.} \tag{1.28}$$

It happens that this is the case. Since $h'_{\mu\nu} = h_{\mu\nu} - \partial_{\nu}\epsilon_{\mu} - \partial_{\mu}\epsilon_{\nu}$, the components of $\bar{h}_{\mu\nu} = h_{\mu\nu} - \frac{1}{2}h\eta_{\mu\nu}$ in the new coordinates system are $\bar{h}'_{\mu\nu} = \bar{h}_{\mu\nu} - \partial_{\nu}\epsilon_{\mu} - \partial_{\mu}\epsilon_{\nu} + \partial_{\sigma}\epsilon^{\sigma}\eta_{\mu\nu}$, and, after some index manipulation we get

$$\eta^{\mu\nu}\partial_{\mu}\bar{h}'_{\alpha\nu} = \eta^{\mu\nu}\partial_{\mu}\bar{h}_{\alpha\nu} - \eta^{\mu\nu}\partial_{\mu}\partial_{\nu}\epsilon_{\alpha}. \tag{1.29}$$

Therefore, by choosing a linear form ϵ_{α} such that $\eta^{\mu\nu}\partial_{\mu}\partial_{\nu}\epsilon_{\alpha} = \eta^{\mu\nu}\partial_{\mu}\bar{h}$, we can always find a coordinate system in which

$$\partial_{\mu}\left(\eta^{\mu\nu}\bar{h}_{\alpha\nu}\right) = 0. \tag{1.30}$$

Following the analogy with electromagnetism, this condition is called the *Lorenz gauge*, as it imposes the divergence of $\bar{h}_{\alpha\beta}$ to be null (in electromagnetism, the Lorenz gauge consists in choosing the potential A_{μ} such that $\partial_{\mu}(\eta^{\mu\nu}A_{\nu}) = 0$). In the Lorenz gauge, the linearized Einstein equations have the form of Eq. (1.28). Therefore, the transverse-traceless perturbation $\bar{h}_{\alpha\beta}$ of the Minkowski metric $\eta_{\alpha\beta}$ can propagate like a wave through a flat spacetime at the speed of light. This is a *gravitational wave*.

TT gauge

To get a better understanding of the nature of GW and the way they propagate and interact with matter, let us first try to solve the linearized Einstein equations of Eq. (1.28) in the vacuum (i.e where $T_{\mu\nu} = 0$) and in the Lorenz gauge defined by Eq. (1.30). A simple solution of the wave equation in the absence of a source term is the monochromatic plane wave

$$\bar{h}_{\mu\nu}(x^{\alpha}) = A_{\mu\nu}e^{ik_{\sigma}x^{\sigma}}, \tag{1.31}$$

where k^μ is the 4-wavevector that obeys $k^\mu k_\mu = 0$, and $A_{\alpha\beta}$ is a matrix that represents the amplitude of the wave. In addition, the Lorenz gauge imposes an orthogonality condition:

$$k^\mu A_{\mu\nu} = 0. \tag{1.32}$$

There are still an infinite number of coordinates systems that satisfy the Lorenz gauge, so we can impose more gauge conditions in order to simplify the expression of $A_{\mu\nu}$. In particular, it is possible to show that there always exists an infinitesimal change of coordinates such that the field $\bar{h}_{\mu\nu}$ satisfies the Lorenz gauge condition and the two following conditions:

$$\eta^{\mu\nu} A_{\mu\nu} = 0 \tag{1.33}$$

$$A_{0\nu} = 0. \tag{1.34}$$

The first condition cancels the trace of the field. Therefore, in such a coordinate system $\bar{h}_{\mu\nu} = h_{\mu\nu}$. The second one means that the field is orthogonal (transverse) to the 4-velocity of an observer in its own reference frame. Hence, that particular case of the Lorenz gauge is called the *traceless-transverse* (TT) gauge.

If we place ourselves in a coordinates system (t, x, y, z) that satisfies the TT gauge and chosen in such a way that the GW propagates along the z axis, the components of $A_{\mu\nu}$ must obey the following conditions:

- Transverse gauge $\implies A_{0\nu} = 0$.
- Lorenz gauge and transverse gauge $\implies A_{z\nu} = 0$.
- Traceless gauge $\implies \eta^{\mu\nu} A_{\mu\nu} = 0$
- Symmetry of the metric tensor $\implies A_{\mu\nu} = A_{\nu\mu}$.

Therefore, only two degrees of freedom remain, and $A_{\mu\nu}$ has the form

$$A_{\mu\nu} = \begin{pmatrix} 0 & 0 & 0 & 0 \\ 0 & A_{xx} & A_{xy} & 0 \\ 0 & A_{xy} & -A_{xx} & 0 \\ 0 & 0 & 0 & 0 \end{pmatrix}. \tag{1.35}$$

These two degrees of freedom are commonly noted $A_{xx} \equiv a_+$ and $A_{xy} = a_\times$. They correspond to the **two polarization modes** of the GW, which are respectively named *plus* and *cross* polarization.

1.2.3 Emission of gravitational waves

In the absence of source term ($T_{\mu\nu} = 0$), the linearized Einstein equations describe the propagation of GW in the vacuum. To study how GW are generated, we have to solve the equations in the presence of a source, i.e when $T_{\mu\nu} \neq 0$. A major caveat to this approach is that these equations are only valid in the weak field regime, when the gravitational field is small. Yet, because of the factor $16\pi G/c^4 \sim 4 \times 10^{-43}$ in the Einstein equations, a very strong gravitational field is necessary to produce GW at a detectable level. Therefore, a precise modelization of the GW signal emitted by a source requires to solve the full, non-linear Einstein equations, which have in general no analytic solutions. In fact, it was not until 1959 than Pirani and Bondi showed the existence of plane wave solutions to the non linearized Einstein equations [8]. Nevertheless, the results obtained in the weak field approximation are still very useful to understand the physics of GW emission.

We use a Cartesian system of coordinates $\{x^\sigma\} = \{ct, x, y, z\}$ in the Lorenz gauge attached to the source. The general solution to Eq. (1.28) is given by the retarded potential

$$\bar{h}_{\mu\nu}(t, \vec{x}) = \frac{4G}{c^4} \int T_{\mu\nu} \left(t - \frac{|\vec{x} - \vec{x'}|}{c}, \vec{x'} \right) \frac{d^3\vec{x'}}{|\vec{x} - \vec{x'}|}. \tag{1.36}$$

In general, it is very complicated, or even not possible at all, to compute the components of $T_{\mu\nu}$. However, we can as always get an analytic expression after some approximations on the nature and location of the source. Let us suppose that (i) the source is spatially localized in a finite volume of characteristic length L, (ii) far away from the observer ($r = |\vec{x}| >> |\vec{x'}|$), and (iii) that $T_{\mu\nu}$ varies slowly: $\frac{1}{T_{\mu\nu}} \frac{\partial T_{\mu\nu}}{\partial t} << \frac{L}{c}$. Then we can simplify the right hand term of Eq. (1.36)

$$\bar{h}_{\mu\nu}(t, r) \simeq \frac{4G}{rc^4} \int T_{\mu\nu} \left(t - \frac{r}{c}, \vec{x'} \right) d^3\vec{x'}, \tag{1.37}$$

where $r = |\vec{x}|$. Besides, using the conservation law of the stress-energy tensor $\nabla^\mu T_{\mu\nu} = 0$ and the divergence theorem, we can link the temporal and spatial components of this tensor

$$\int x_i x_j \frac{\partial^2 T_{00}}{\partial t^2} d^3\vec{x} = 2c^2 \int T_{ij} d^3\vec{x}. \tag{1.38}$$

For non-relativistic sources, $T_{00} \simeq \rho c^2$ where ρ is the mass-energy density. Therefore, the spatial components of the trace-reversed metric perturbation are given by

$$\bar{h}_{ij}(t, r) \simeq \frac{2G}{rc^4} \ddot{I}_{ij}(t - \frac{r}{c}) \tag{1.39}$$

where $I_{ij}(t) \equiv \int \rho(t, \vec{x}) x^i x^j d^3\vec{x}$ is the quadrupole tensor of the source and the dot indicates the time derivative. Finally we have to express this quantity in the TT gauge. This can be done using the transverse projector

$$P_{ij} = \delta_{ij} - \frac{\hat{x}_i \hat{x}_j}{r^2}. \tag{1.40}$$

The components I_{ij}^{TT} of the quadrupole tensor in the TT gauge are given by

$$I_{ij}^{\mathrm{TT}} = P_{ik} I^{kl} P_{lj} - \frac{1}{2} P_{ij} P_{kl} I^{kl}. \tag{1.41}$$

Therefore,

$$\boxed{h_{ij}^{TT}(t, r) \simeq \frac{2G}{rc^4} \ddot{I}_{ij}^{\mathrm{TT}}(t - \frac{r}{c}).} \tag{1.42}$$

The amplitude of the GW emitted by a system is proportional to the second time derivative of the quadrupole moment.

Example 1: spinning solid

Following [26], we consider the example of triaxial ellipsoid whose quadrupole tensor $\mathbf{I}$ can be expressed in the basis of its principal axes of inertia

$$I_{ij} = \begin{pmatrix} I_x & 0 & 0 \\ 0 & I_y & 0 \\ 0 & 0 & I_z \end{pmatrix}. \tag{1.43}$$

We will suppose that the object spins around its z-axis at pulsation ω. Therefore, the values of $I_{ij}(t)$ at any time t are given by

$$\mathbf{I}(t) = \mathbf{R}(\omega t) \mathbf{I}(0) \mathbf{R}^{-1}(\omega t). \tag{1.44}$$

with

$$R_{ij}(\omega t) = \begin{pmatrix} \cos\omega t & \sin\omega t & 0 \\ -\sin\omega t & \cos\omega t & 0 \\ 0 & 0 & 0 \end{pmatrix}. \tag{1.45}$$

After a straightforward computation we have

$$\ddot{I}_{ij}(t) = 2\epsilon I_z \omega^2 \begin{pmatrix} -\cos 2\omega t & \sin 2\omega t & 0 \\ \sin 2\omega t & \cos 2\omega t & 0 \\ 0 & 0 & 0 \end{pmatrix}. \tag{1.46}$$

For convenience, we have defined the ellipticity $\epsilon \equiv (I_x - I_y)/I_z$. Notice that the expression of $I_{ij}(t)$ is already traceless and transverse. Therefore, using Eq. (1.42), the two polarization modes of the GW seen by an observer located at a distance r on the z-axis are

$$\begin{aligned} h_+(t + r/c) &= -\frac{4G\epsilon I_z \omega^2}{rc^4} \cos 2\omega t \\ h_\times(t + r/c) &= \frac{4G\epsilon I_z \omega^2}{rc^4} \sin 2\omega t. \end{aligned} \tag{1.47}$$

GW are therefore emitted at twice the rotation frequency of the body. Their amplitude $h \equiv \sqrt{\langle h_+^2(t) + h_\times^2(t)\rangle}$ is proportional to $I_z \sim MR^2$, the ellipticity ϵ and the square of the rotation frequency. The order of magnitude of h is

$$h \sim 10^{-22} \left(\frac{I_z}{10^{38}\,\mathrm{kg\,m^2}}\right) \left(\frac{\epsilon}{10^{-6}}\right) \left(\frac{\omega}{1\,\mathrm{kHz}}\right)^2 \left(\frac{1\,\mathrm{kpc}}{r}\right). \tag{1.48}$$

In the case where the observer is located on an axis that makes an angle ι with the z-axis, it can be shown [26] that the polarizations are

$$\begin{aligned} h_+(t + r/c) &= -\frac{4G\epsilon I_z \omega^2}{rc^4} \frac{1 + \cos^2\iota}{2} \cos 2\omega t \\ h_\times(t + r/c) &= \frac{4G\epsilon I_z \omega^2}{rc^4} \cos\iota \sin 2\omega t. \end{aligned} \tag{1.49}$$

Example 2: orbiting bodies

Let us now consider the case of two bodies with masses m_1 and m_2 orbiting each other at a distance a. We will note r_1 and r_2 their respective distances to the center of mass O and $M \equiv m_1 + m_2$ the total mass of the system, such that $r_1 = am_2/M$ and $r_2 = am_1/M$. The bodies orbit with an angular velocity ω. In the reference frame of the center of mass, their coordinate vectors are

$$\vec{x_1}(t) = \begin{pmatrix} r_1 \cos\omega t \\ r_1 \sin\omega t \\ 0 \end{pmatrix}, \vec{x_2}(t) = \begin{pmatrix} r_2 \cos\omega t \\ r_2 \sin\omega t \\ 0 \end{pmatrix}. \tag{1.50}$$

We can compute the GW emission of that system. Considering the bodies as point-like masses, the density distribution is

$$\rho(t, \vec{x}) = m_1\, \delta\left(\vec{x} - \vec{x_1}(t)\right) + m_2\, \delta\left(\vec{x} - \vec{x_2}(t)\right), \tag{1.51}$$

which gives the quadrupole tensor

$$I_{ij} = \begin{pmatrix} \frac{1}{2}\mu a^2 (1 + \cos 2\omega t) & \frac{1}{2}\mu a^2 \sin 2\omega t & 0 \\ \frac{1}{2}\mu a^2 \sin 2\omega t & \frac{1}{2}\mu a^2 (1 - \cos 2\omega t) & 0 \\ 0 & 0 & 0 \end{pmatrix}, \tag{1.52}$$

where $\mu = m_1 m_2/M$ is the reduced mass of the system. The second time derivative of I_{ij} is

$$\ddot{I}_{ij}(t) = -2\mu a^2\omega^2 \begin{pmatrix} \cos 2\omega t & \sin 2\omega t & 0 \\ \sin 2\omega t & -\cos 2\omega t & 0 \\ 0 & 0 & 0 \end{pmatrix}. \tag{1.53}$$

Along with the previous example, we are already in the TT-gauge since $I^i_i = 0$ and $I_{zj} = I_{iz} = 0$, so, using Eq. (1.42), the two polarizations of the GW seen by an observer at distance r on the z-axis are

$$\begin{aligned} h_+(t + r/c) &= -\frac{4G\mu a^2\omega^2}{rc^4}\cos 2\omega t, \\ h_\times(t + r/c) &= -\frac{4G\mu a^2\omega^2}{rc^4}\sin 2\omega t. \end{aligned} \tag{1.54}$$

Like in the example of the triaxial spinning ellipsoid, GW are emitted at twice the orbiting frequency of the system.

Note that these examples describe only the cinematic of the sources. In a realistic case, the amplitude and frequency of the GW would decrease with time, because GW carry energy.

1.2.4 Energy carried and luminosity

It is not obvious to see that GW carry energy. In fact, the question remained controversial for a long time. In 1969, Isaacson showed that GW carry energy by associating an effective stress-energy tensor $t^{\rm GW}_{\alpha\beta}$ to the second order correction of the metric perturbation [27]. The demonstration requires to consider second order terms in the expansion of $g_{\mu\nu}$:

$$g_{\alpha\beta} = \eta_{\alpha\beta} + \epsilon h^{(1)}_{\alpha\beta}(x^\mu) + \epsilon^2 h^{(2)}_{\alpha\beta}(x^\mu) + \mathcal{O}(\epsilon^3). \tag{1.55}$$

At first order in ϵ, solving the Einstein equations in the vacuum give the linearized Einstein equations given in Eq. (1.25), which describe the propagation of GW. However, at the second order they give rise to the effective stress-energy tensor

$$t^{\rm GW}_{\alpha\beta} \equiv \frac{c^4}{32\pi G}\langle \partial_\alpha h^{ij} \partial_\beta h_{ij} \rangle. \tag{1.56}$$

Considering now a GW that propagates along the z direction and using the conservation of the energy-momentum tensor $\partial_m u t^{\mu\nu} = 0$, the flux F of energy, i.e. the energy per unit time and surface area is given [28] by

$$F = \frac{c^3}{16\pi G}\langle \dot{h_+}^2 + h^2_\times \rangle. \tag{1.57}$$

where $< ... >$ is an average over time. Using this last equation and Eq. (1.42), the gravitational-wave luminosity $L_{\rm GW}$ of a source with quadrupole tensor $I^{(TT)}_{ij}$ is

$$L_{\rm GW} = \frac{G}{5c^5}\langle \dddot{I}_{ij} \dddot{I}^{ij} \rangle. \tag{1.58}$$

1.2.5 Effect of gravitational waves on matter

We have seen how the linearized Einstein equations allow GW to propagate through spacetime at the speed of light, and, using an appropriate system of coordinates, got an expression for the components of the perturbation $h_{\mu\nu}$. We now need to see how GW interact with matter if we

want to be able to detect them. Let us consider a monochromatic plane GW. We place ourselves in the TT gauge, such that the metric is $g_{\mu\nu}(x^\alpha) = \eta_{\mu\nu} + h_{\mu\nu}(x^\alpha)$ with

$$h_{\mu\nu}(x^\alpha) = \begin{pmatrix} 0 & 0 & 0 & 0 \\ 0 & h_+ & h_\times & 0 \\ 0 & h_\times & -h_+ & 0 \\ 0 & 0 & 0 & 0 \end{pmatrix} e^{ik_\alpha x^\alpha}, \tag{1.59}$$

and $k_\alpha = (-\omega/c, 0, 0, k_z = \omega/c)$.

Let us consider a free-falling particle. The evolution of its coordinate vector x^μ is driven by the geodesic equation given in Eq. (1.14). In the TT gauge, the third spatial coordinate being aligned in the direction of the wave propagation, we should consider the movement of the free-falling particle in the (x^1, x^2) plane. The Christofell symbols (see Eq. (1.9)) being related to the first derivatives of $h_{\alpha\beta}$, we can see that they are all null to first order in $h_{\alpha\beta}$, leading to

$$\frac{d^2x^i}{d\tau^2} = 0 \tag{1.60}$$

Therefore, in the TT gauge, the coordinates of a free-falling particle are not affected by the GW. However, this rather counter-intuitive result does not mean that GW do not affect the motion of free-falling particles. It is rather a particularity of the TT coordinates, which "follow" the motion of the particle.

Indeed, when one measures in the laboratory the distance between two free-falling particles, materialized for instance by two test-mass mirrors, we use the coordinate system of a local inertial frame (also named Fermi coordinate system) whose origin coincides with the geodesic of one of the mirror. In this coordinate system, the path of a GW generates a displacement of the geodesics. The variation of the distance between the free-falling test-masses is given by the geodesic deviation equation [29] assuming the distance between masses is small compared to the GW wavelength

$$\frac{d^2\xi^\alpha}{d\tau^2} = \frac{d^2\xi^\alpha}{dt^2} = R^\alpha_{\mu\nu\beta}\ U^\mu\ U^\nu\ \xi^\beta \tag{1.61}$$

where ξ^α is the vector connecting two geodesics, U^μ is the four-velocity vector ($U^\mu = dx^\mu/d\tau$) of the free-falling test-masses and $R^\alpha_{\mu\nu\beta}$ is the Riemann tensor which is gauge invariant.

To first order in $h_{\mu\nu}$, assuming coordinate time and proper time are equivalent (test-masses are slowing moving) and considering the two test-masses are separated along the x-axis by L_x, the geodesic deviation equation becomes

$$\frac{d^2\xi^\alpha}{dt^2} = R^\alpha_{00\beta}\ \xi^\beta = R^\alpha_{00x}\ L_x = -R^\alpha_{0x0}\ L_x \tag{1.62}$$

As Eq. (1.62) is gauge invariant, we can use the expressions of the Riemann tensor in the TT gauge (see Eq. (1.8))

$$R^x_{0x0} = R_{x0x0} = -\frac{1}{2}\ddot{H}^{TT}_{xx} \tag{1.63}$$

$$R^y_{0x0} = R_{y0x0} = -\frac{1}{2}\ddot{H}^{TT}_{xy} \tag{1.64}$$

$$R^y_{0y0} = R_{y0y0} = -\frac{1}{2}\ddot{H}^{TT}_{yy} \tag{1.65}$$

where H^{TT}_{ij} is the metric perturbation tensor in a detector frame on Earth which is related to h^{TT}_{ij} by a 3-rotation geometrical transform as we will see in Section 1.3. We thus obtain the

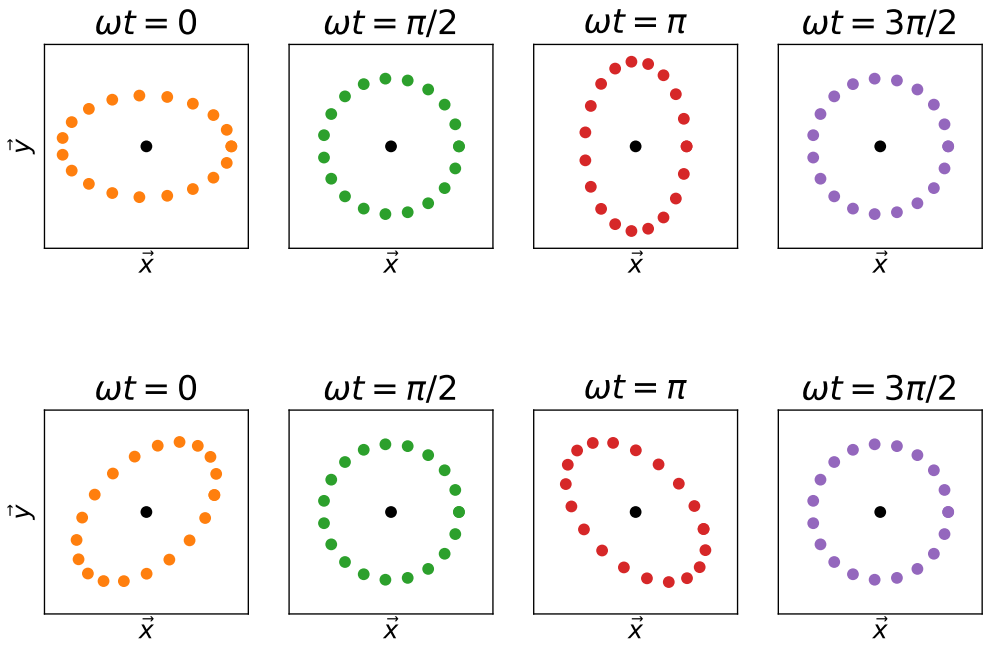

Figure 1.1: Effect of a GW on a circle of free-falling particles. Top figure represents the effect of a + polarized wave as function of time, bottom figure a × polarized wave.

equations that govern the change of the length between two test-masses along the x-axis when a GW is passing by

$$\ddot{\xi}^x = \frac{1}{2}\ddot{H}^{TT}_{xx} L_x \tag{1.66}$$

$$\ddot{\xi}^y = \dot{\xi}^y = 0 \tag{1.67}$$

Similarly, if we consider a third test-mass located at L_y along the y-axis, the displacement along this direction is given by

$$\ddot{\xi}^y = \frac{1}{2}\ddot{H}^{TT}_{yy} L_y \tag{1.68}$$

$$\ddot{\xi}^x = \dot{\xi}^x = 0 \tag{1.69}$$

It is straightforward to integrate Eqs. (1.66) and (1.68). At zero order we have $\xi^i = L_i$. At the first order $\xi^i = L_i + \frac{1}{2}H^{TT}_{ii}\ L_i$. The relative length change in each direction is thus defined at first order in H_{ij} as

$$\frac{\delta L}{L} = \frac{1}{2}H^{TT}_{ii} \tag{1.70}$$

The traceless property of the metric perturbation tensor ($H^{TT}_{yy} = -H^{TT}_{xx}$) is thus implying that at a given instant a GW is inducing a differential effect on length in two perpendicular directions. In Figure 1.1 we generalize this result to a ring of particles in the $(\vec{x}, \vec{y})$ plane (orthogonal to the direction of propagation of the wave) for a GW with only plus ($H^{TT}_{xy} = 0$) and cross ($H^{TT}_{xx} = 0$) polarization respectively.

1.3 Detecting gravitational waves

The factor $G/c^4 \sim 10^{-44}\,\mathrm{m^{-1}kg^{-1}s^2}$ in Eq. (1.42) makes GW much weaker than their electromagnetic counterparts. The commonly used fiducial strain amplitude $h \sim 10^{-21}$ is given

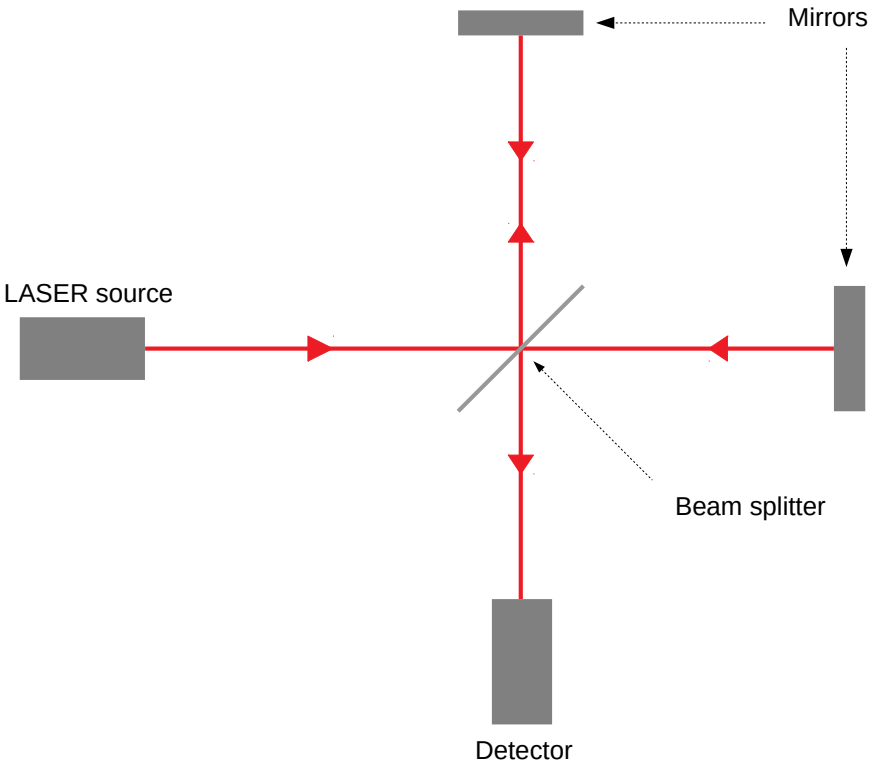

Figure 1.2: Optical scheme of a Michelson interferometer. The initial beam from the laser source is split in two by the beam splitter mirror. Light is reflected by the mirrors at the end of both arms and recombines at the beam splitter. The reflected recombined beam contains constructive or destructive interferences depending on the difference of optical path in the two arms.

by compact binary coalescence sources. Being able to detect such tiny spacetime deformation requires special instrumental techniques. Laser interferometry is known for providing the most precise instrument to measure differential motion. Furthermore, the geometry of a Michelson interferometer with perpendicular arms is perfectly adapted to the differential effect along the two arms of GW on free-falling objects.

1.3.1 Laser interferometry GW detection principle

Figure 1.2 shows the optical layout of a simple Michelson interferometer. We assume the beam splitter and the end mirrors are free to move in the plane of the interferometer. We choose a coordinate system where the beam splitter and the end mirrors are fixed (TT gauge coordinates system). The coordinates origin is at the beam splitter and the arms along the x and y axes have lengths L_1 and L_2 that are roughly equal on a kilometer scale. With a laser of wavelength λ incident on the beam splitter, the electric field seen by the photodetector is

$$\Psi_{det} = \Psi_{in} r_{BS} t_{BS} (r_1 e^{2ikL_1} + r_2 e^{2ikL_2}), \tag{1.71}$$

where r_{BS} and t_{BS} are the reflectivity and the transmittivity of the beam splitter, r_1 and r_2 are the reflectivity of the end mirrors, $k = 2\pi/\lambda$ and Ψ_{in} is the electric field at the beam spliter. The light power exiting the dark port of the interferometer is thus

$$P_{out} = P_{in} r_{BS}^2 t_{BS}^2 (r_1^2 + r_2^2)(1 + C\cos(2k(L_2 - L_1)), \tag{1.72}$$

where P_{in} is the laser power impinging the beam splitter and the contrast C

$$C = \frac{2r_1 r_2}{r_1^2 + r_2^2} \tag{1.73}$$

quantifies the asymetries in reflectivities of the two arms. The amplitude of the light leaving the interferometer depends on the difference in the phase accumulated by the light travelling in the two arms. The interferometer operates with the condition that in the absence of excitation (noise or GW) the light exiting the dark port is null. Let's now see how a GW passing by will modify the laser power at the photodetector. For simplicity, we consider a plus polarized GW incoming from the z direction. In the TT gauge the spacetime interval between two neighboring points connected by a light ray remains null

$$\begin{aligned} 0 = ds^2 = g_{\mu\nu}dx^\mu dx^\nu &= (\eta_{\mu\nu} + h_{\mu\nu})dx^\mu dx^\nu, & (1.74)\\ &= -c^2dt^2 + (1 + h_{xx}(t))dx^2 + (1 + h_{yy}(t))dy^2 & (1.75) \end{aligned}$$

We can calculate the phase shift generated by the passing GW,

$$\Delta\phi = \frac{2\pi}{\lambda}(2L_x - 2L_y), \tag{1.76}$$

where L_x and L_y are the optical paths in the arms along the x and the y direction respectively. Using Eq. (1.74) along the x arm we have

$$L_x = \int cdt = \int_0^L \sqrt{1 + h_{xx}(t - \frac{x}{c})}dx \approx \int_0^L (1 + \frac{1}{2}h_{xx}(t - \frac{x}{c}))dx, \tag{1.77}$$

A photon will travel one arm in $\sim 10\,\mu$s which is much shorter than the typical duration of the signals searched in the $10 - 10^4$ Hz sensitive band. We can thus consider that $h_{xx}(t)$ does not vary during the light travel of a photon. Using $h_{xx}(t) = -h_{yy}(t) = h_+(t) = h_0\cos(\omega_{GW}t)$ where $\omega_{GW} = 2\pi f_{GW}$, Eq. (1.77) becomes

$$\begin{aligned} L_x &= L_1 + \frac{c}{\omega_{GW}}\sin(\omega_{GW}\frac{L_1}{c})\ h_0\ \cos(\omega_{GW}(t - \frac{L_1}{2c})) & (1.78)\\ &= L_1 + \frac{c}{\omega_{GW}}\sin(\omega_{GW}\frac{L_1}{c})\ h_+(t - \frac{L_1}{2c}) & (1.79) \end{aligned}$$

Similarly for the y arm photon trip we have

$$L_y = L_2 - \frac{c}{\omega_{GW}}\sin(\omega_{GW}\frac{L_2}{c})\ h_+(t - \frac{L_2}{2c}) \tag{1.80}$$

Eqs. (1.78) and (1.80) are telling that the distance between two free falling points (distance between the beam splitter and the end mirror) will vary when a GW is passing by and this change is proportional to the amplitude of the GW.

$$\frac{\Delta L}{L} \propto h^+ \tag{1.81}$$

The phase shift induced by the passing GW is thus approximated to

$$\Delta\phi \approx \frac{4\pi}{\lambda}(\delta L + \frac{2c}{\omega_{GW}}\sin(\omega_{GW}\frac{L}{c})\ h_+(t - \frac{L}{c})) \tag{1.82}$$

where $\delta L = L_1 - L_2$ and $L = (L_1 + L_2)/2$. Here we assume the two arms have similar length. In absence of a GW signal, we have the standard Michelson phase shift $\Delta\Phi = 4\pi\delta L/\lambda$.

Eq. (1.82) shows that a measure of the phase shift is a direct measure of the GW strain amplitude. For a signal amplitude of 10^{-21}, the phase shift is of order 10^{-11} rad which is extremely small. From Eq. (1.82) we could conclude that we can increase the phase shift induced by a GW by increasing the arms length. This is not true as the approximation made in Eq. (1.77) assumes that $\omega_{GW} L/c << 1$. In other words the response of a Michelson interferometer as function of the GW frequency is not constant. Besides, one may wonder how long should be the arms to detect a GW of frequency f_{GW}. This is given by maximizing the term $\sin(2\pi f_{GW} L/c)$, i.e. $L = cf_{GW}/4$. For a GW source emitting at ~ 1 Hz, $L \sim 75$ km should be the minimum length of the arms to be able to detect sources emitting at lower frequency. This is of course not feasible, and actually real GW detectors are more complex than a simple Michelson interferometer.

1.3.2 Advanced interferometers

It is common to cite a paper by Gertsenshtein and Pustovoid published in 1962 to date the idea of using a Michelson interferometer to detect GW over a broader range of frequencies than Weber's bar detector [16]. Yet, it took decades of developments to bring on Earth the first and now second generation of interferometric GW detectors that are sensitive enough to detect GW from the merger of two stellar mass black holes for the first time on September 2015 [17].

The current network of ground-based detectors shown in Figure 1.3 is composed of the two Advanced LIGO detectors located at Hanford and Livingston in the USA, the Advanced Virgo detector located at Cascina in Italy, the GEO-600 detector located near Hannover in Germany and the underground KAGRA detector near Kamioka in Japan. A copy of Advanced LIGO detector is currently under construction in India. The arms of Advanced LIGO are 4 km long while Advanced Virgo and KAGRA have arms of 3 km. GEO-600 arms are 600 m long which makes the detector less sensitive than Advanced LIGO and Advanced Virgo and is mainly used so far to test advanced technology. KAGRA is the first detector located underground and whose Fabry-Perot mirrors are cooled down at 20 K to reduce respectively seismic noise and thermal noise.

Figure 1.4 displays the main components added to a simple Michelson interferometer to enlarge its frequency range response and to enhance its sensitivity. A complete description of Advanced LIGO, Advanced Virgo and KAGRA can be found in [30, 31, 32]. There are some differences between detectors (KAGRA is using cryogenic techniques to reduce the thermal noise) but what follows is implemented almost in all four detectors. As already mentioned, an interferometer sensitivity depends on the arm length that cannot be too long because of the cost of the vacuum chamber. Additional partially transmitive test-mass mirrors are added close to the beam-splitter in order to create Fabry-Perot cavities in the two arms. Photons are bounced back and forth many times on average before leaving the cavities, resulting in an increase of the optical path by a factor $2\mathcal{F}/\pi$ where the finesse $\mathcal{F}$ of the cavities is 440 for Advanced Virgo and 500 for Advanced LIGO. The arms of Advanced Virgo are equivalent to the arms of a $\sim 10^3$ km Michelson.

The optical properties of the mirrors of the Fabry-Perot cavities must be exquisite in order to achieve success. The Advanced Virgo mirrors were tested, and the root mean squared surface uniformity is less than 0.5 nm, scattered light is less than 100 parts per million (ppm), and absorption, including coating, is less than 0.4 ppm at 1064 nm[1] for the end mirrors.

The Advanced Virgo input and end mirrors for the Fabry-Perot cavity arms have different radius of curvature (1420 m and 1683 m respectively) and a beam radius as large as 60 mm at the end mirror. The high power circulating in the interferometer, especially within the Fabry-Perot cavities, causes thermal lensing. This is a well known problem and thermal compensation is an integral part of Advanced Virgo and Advanced LIGO design. To maintain the arm-cavity mode structure, it will be necessary to control the radius of curvature of all test masses within

[1] Fused silica mirror blanks are transparent at the frequency of the the Virgo Nd:YV04 laser.

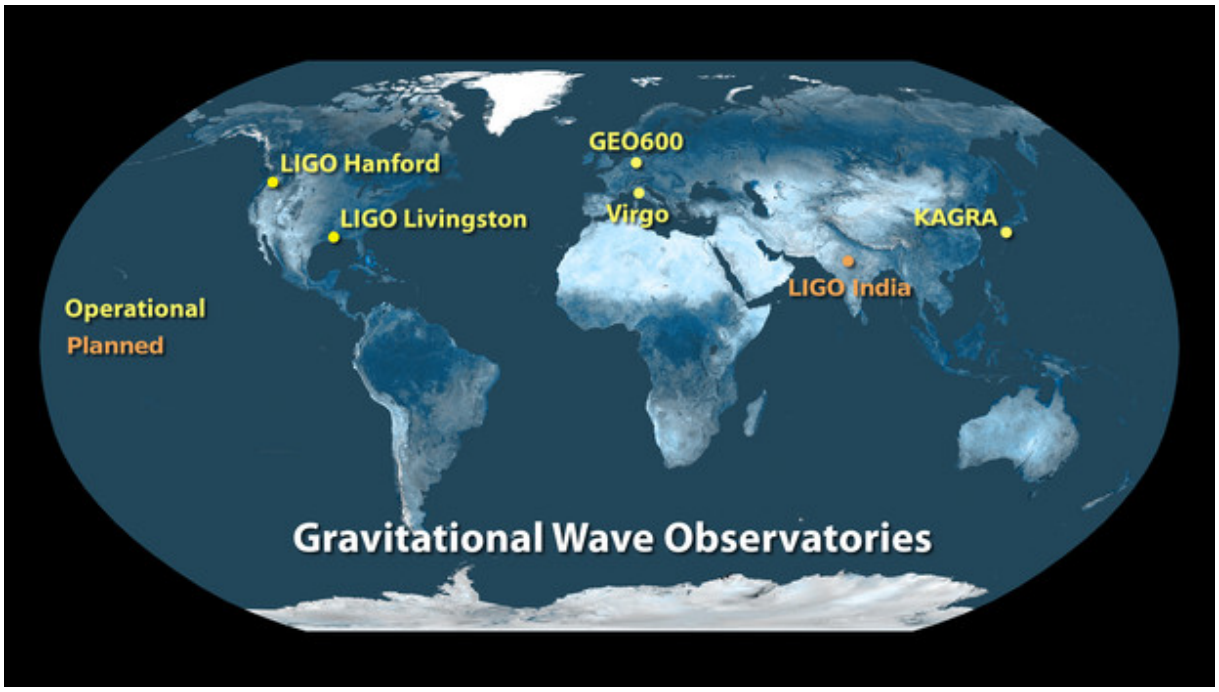

Figure 1.3: Locations on Earth of the different ground-based GW detectors. In yellow are detectors already making observations. LIGO India detector end of construction is planned circa 2025-2027. Credit : LIGO-Virgo-KAGRA collaboration.

$\pm$ 2 m from the initial radius of curvature. A system of ring heaters around optical components and compensation plates illuminated by CO_2 lasers have been installed to control the thermal deformation of the mirrors' surfaces.

The noise sources that inhibit the interferometer performance are discussed below. However, let us consider one's ability to measure the relative phase between the light in the two arms. The Heisenberg uncertainty relation for light with phase ϕ and photon number N is $\Delta\phi\ \Delta N \sim 1$. For a measurement lasting time τ using laser power P, the number of photons of wavelength λ is $N = P\lambda\tau/hc$, and with Poisson statistics describing the light $\Delta N = \sqrt{N} = \sqrt{P\lambda\tau/hc}$. Therefore,

$$\Delta\phi\ \Delta N = \frac{2\pi}{\lambda}(2\delta L)\sqrt{P\lambda\tau/hc} = 1\ , \tag{1.83}$$

where $\delta L = L_1 - L_2$. This implies that

$$\delta L = \frac{1}{4\pi}\sqrt{\frac{hc\lambda}{P\tau}}\ . \tag{1.84}$$

This is the demonstration of the *shot noise* limit of the Michelson interferometer. With more light power the interferometer can measure smaller distance displacements and achieve better sensitivity. The plan for Advanced Virgo is to have 175 W exiting the laser ($\lambda = 1.06\,\mu$m), with 125 W actually making it to the entrance of the interferometer. Currently 40 W is used in Advanced Virgo but the plan is to inject 100 W for the next observing runs.

A nice trick to increase the laser power circulating into the cavities is to add a semi transparent mirror between the laser source and the beam splitter to recycle back into the interferometer the light coming out from the beam splitter. The recycling mirror forms a cavity with the interferometer that increase the laser power by a factor ~ 28 for Advanced Virgo.

Finally, at the output of the interferometer another partially transmissive mirror is added to sends the light back into the system. Thanks to optical fiber, the phase of the light acquired from the GW in one arm while expanding is sent to the other arm when it starts expanding

increasing the phase shift. By repeating over and over this process one can increase sensitivity at a particular frequency determined by the reflectivity of the signal recycling mirror. It is also possible to form another resonant cavity that broadens the bandwidth of the interferometer in the high frequency range of the detector. This system is called signal recycling. LIGO is currently the only dual-recycled interferometer operating with power and signal recycling, but Virgo signal recycling will be ready for the next observing run.

Quantum noise is one of the fundamental limitations to the sensitivity of GW detectors that appear as quantum shot noise, caused by statistical fluctuations in the arrival time of photons at the interferometer output and quantum radiation pressure noise, due to quantum fluctuations in the photon flux impinging on the interferometer mirrors. A key technology to improve the GW detector sensitivity beyond this quantum noise limit is the injection of squeezed vacuum states of light into the dark port of the interferometer. Since up to now the quantum radiation pressure noise is just below the residual technical noise sources at low GW detection frequencies, a broadband sensitivity improvement can be achieved by reducing the shot noise contribution via a moderate injection of frequency-independent squeezed vacuum states, whose fluctuations are reduced in the quadrature of the light aligned with the gravitational-wave signal. In this case, the effect of squeezing injection is equivalent to an increase of the circulating optical power in the detector, without the drawback of an increase of the thermal effects inside the interferometer optics due to their residual absorption and consequent thermal aberrations. In the recent years, Advanced LIGO and Advanced Virgo have operated with injected squeezed light. Advanced Virgo has obtaining up to 3 dB of sensitivity improvement (increasing the binary neutron star sensitivity range by 5-8%) [33] while Advanced LIGO , has achieved 3 dB of sensitivity improvement but operating a dual recycling configuration [34]. Injected squeezed state of light allow to increase the sensitivity without increasing the laser power and thus limiting the thermal effects that are hard to control.

All these enhancements from a simple Michelson interferometer makes Advanced LIGO and Advanced Virgo able to measure phase shift corresponding to mirror displacement much smaller than $\sim 10^{-18}$ m.

1.3.3 Advanced detectors noise sources

GW detectors sensitivity is defined by calculating the amplitude spectral density (ASD) of the detector noise (output of the dark port in absence of a GW signal). The ASD frequency dependence is due to the contributions of different sources of noise. Figure 1.5 shows the noise budget of the Advanced Virgo project as foreseen before construction started. Quantum noise, which includes photon shot noise above 300 Hz and radiation pressure at low frequency. As already seen to decrease the shot noise, one needs to increase the laser power circulating in the cavities. Doing this increases the radiation pressure fluctuation on the mirrors as well as thermal noise within mirrors substrates and coatings. The thermal noise due to the coatings dominates in the mid-frequency range. To decrease the thermal noise or radiation pressure noise two ways are currently pursed: improve the quality of the mirror coatings and increase the size of the mirrors but this later solution requires to adapt the suspension systems. Each detector has developed different design for their isolation system. In Advanced Virgo, mirrors are attached through fused silica fibers to a series of mechanical filters attached to the top of an inverted pendulum. This isolation system is mainly passive and is able to suppress almost all horizontal movements of the mirrors due to the seismic noise above ~ 10 Hz [31]. Finally one should mention the gravity gradient noise that is not yet a problem in ground-based detectors but will become problematic when radiation pressure decreases (for instance when Advanced Virgo is upgraded with larger mirrors). This Newtonian noise is generated by fluctuations of the Newtonian gravitational potential surrounding mirrors. Those fluctuations could come from thermal fluctuations of the atmosphere or ground motions.

So far we have described fundamental noise sources or seismic noises, but many more noise

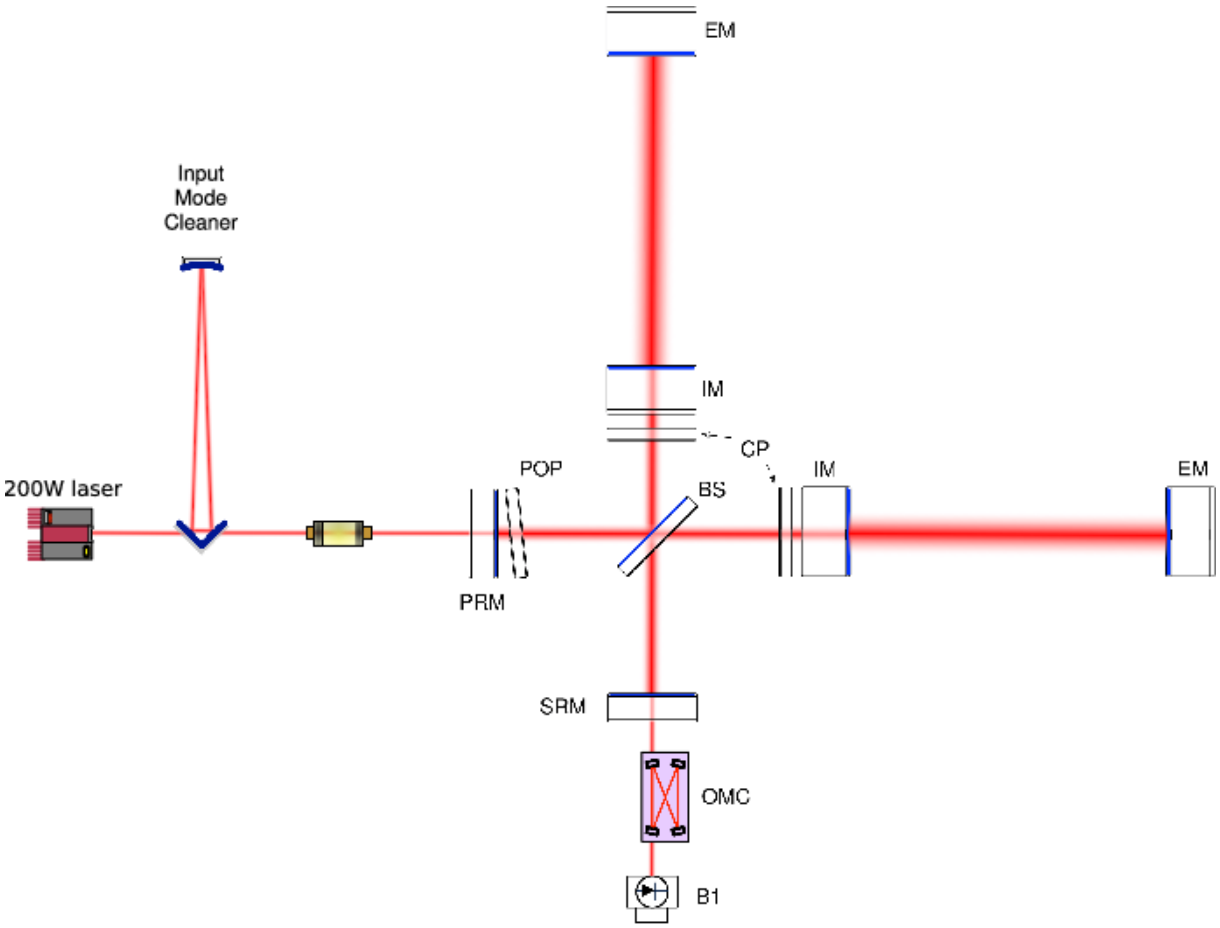

Figure 1.4: Simplified optical layout of Advanced Virgo. Input mirror (IM) and end mirror (EM) are forming the two Fabry-Perot cavities. The recycling cavities at the center of the interferometer are 12 meters long and are formed by the power recycling Mirror (PRM), the signal recycling mirror (SRM) and the two IM mirrors [31]. Compensation plates (CP) and ring heaters around optical components are in charge of controlling the thermal effects that could make cavities unstable to control.

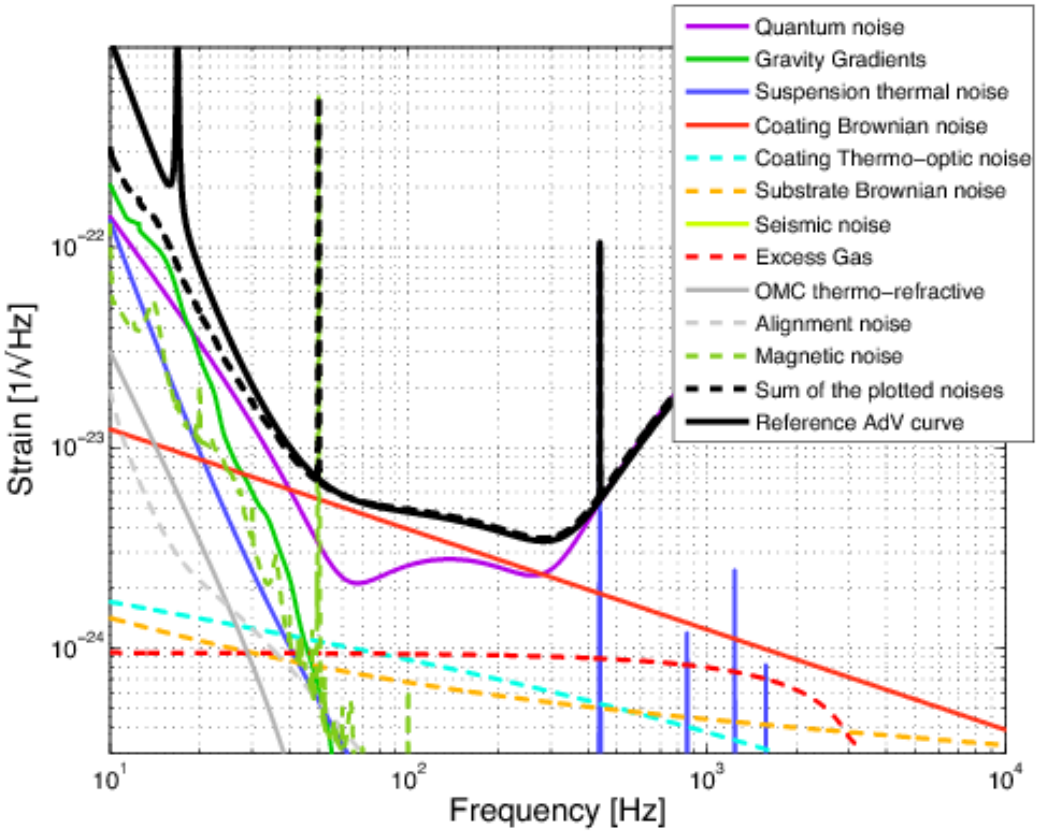

Figure 1.5: Estimated noise budget of the Advanced Virgo detector as anticipated in 2015 [31]. The different curves in color correspond to a specific source of noise, whose addition is used to generate the Advanced Virgo reference sensitivity curve (solid black). Each noise contribution is calculated given parameters and hypotheses described in [31].

sources are contributing to the overall detectors' noise. Among them, we could quote noise from residual gas pressure in the ultra-high vacuum chambers, the laser whose stabilization in frequency, phase, amplitude and pointing is not perfect. There is also noise from the different control systems, including electronics and noise from the environment such as thunder storms or acoustic noise. Another source of noise that is clearly visible on real data ASD shown on Figure 1.6 is due to resonances and mains. Parts of the detectors have mechanical resonances such as many components on the optical benches, or vibration modes such as the violin modes of vibration of the fused silica wires used to suspend the mirrors. Rotors of vacuum pumps or monochromatic forces applied to mirrors to calibrate the detector are also generating narrow high or moderate amplitude spectral lines in almost the whole frequency range of the data.

Despite the huge effort over the years performed by the detectors' teams to mitigate each source of noise, all ground-based GW detectors record data that cannot be fully described assuming the noise is Gaussian and stationary. The data recorded by each GW detector are the subject of data quality studies that are mandatory to GW searches. These studies (see e.g. [35, 36, 37]) determine the period of times where the detectors are functioning in low noise conditions. They also identify and classify the main transient noise sources that may mimic a genuine GW signal or just impact its reconstruction. They also identify and list all narrow spectral lines that are more or less persistent in the data.

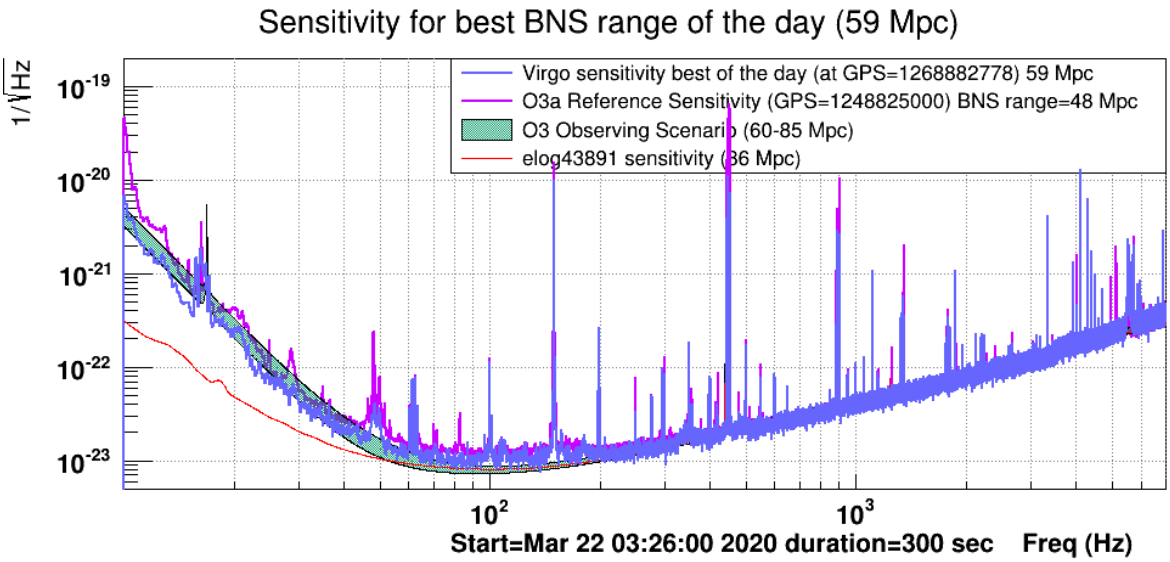

Figure 1.6: Amplitude spectral density of the Advanced Virgo detector on March 23rd 2020 (blue curve) corresponding to one of the last day of the O3 observing run. The magenta curve is a reference ASD estimated during the first part of O3. The green range corresponds to the predicted sensitivity range aimed for the Advanced Virgo detector during O3.

1.3.4 Gravitational wave detectors response

We have seen in Section 1.2.5 that the relative length change of one interferometer's arm is proportional to the metric perturbation tensor. Attaching an inertial reference frame to the interferometer arms, we can use Eq. (1.70) to derive the difference between the relative length changes of the two arms

$$s(t) = \Delta[\frac{\delta L}{L}] = \frac{1}{2}(H_{xx}^{TT} - H_{yy}^{TT}) \tag{1.85}$$

To express the metric perturbation tensor in a frame attached to the detector we first express it in a fixed-Earth reference frame attached to the center of the Earth. We start from Eq. (1.59) that is expressed in the propagation wave frame and apply three Euler's angle rotations that are combined in the orthogonal matrix

$$M = \begin{pmatrix} \cos\Psi\cos\Phi - \cos\Theta\sin\Phi\sin\Psi & \cos\Psi\sin\Phi + \cos\Theta\cos\Phi\sin\Psi & \sin\Theta\sin\Psi \\ -\sin\Psi\cos\Phi - \cos\Theta\sin\Phi\cos\Psi & -\sin\Psi\sin\Phi + \cos\Theta\cos\Phi\cos\Psi & \sin\Theta\cos\Psi \\ \sin\Theta\sin\Phi & -\sin\Theta\cos\Phi & \cos\Theta \end{pmatrix} \tag{1.86}$$

where Θ, Φ and Ψ are the Euler's angles. Note that Ψ corresponds to the polarization angle of the GW. It corresponds to a rotation around the propagation wave axis. Dropping all indices we have

$$H(t) = {}^{t}Mh(t)M \tag{1.87}$$

Eq. (1.85) can be written as

$$s(t) = F^{+}(\Theta,\Phi,\Psi)h_{+}(t) + F^{\times}(\Theta,\Phi,\Psi)h_{\times}(t) \tag{1.88}$$

where F^{+} and $F^{\times}$ are named the antenna pattern functions because they encode the response of the detector to the two GW polarizations. Contrary to telescopes, GW detectors are observing sources from anywhere in the sky at any time except that the response of the detector, the gravitational strain $s(t)$, is not uniform but depends on the relative position of the source with respect to the detector position on Earth at the time of arrival of the GW.

Yet, while Euler's angles are convenient to derive the antenna pattern functions, one usually locate a source in a fixed celestial frame coordinates system using the equatorial coordinates right-ascension $\alpha \in [0, 2\pi]$ and the declination $\delta \in [-\pi/2, \pi/2]$ or the spherical polar angles altitude θ and azimuth ϕ. A third angle, the Greenwich Mean Sideral Time (GMST), which gives the orientation of the Earth at the time of arrival is necessary to change coordinates using the relationship [38, 39]

$$\begin{aligned}
\phi &= \alpha - GMST && (1.89)\\
\theta &= \frac{\pi}{2} - \delta && (1.90)\\
\Theta &= \pi - \theta && (1.91)\\
\Phi &= \phi - \frac{\pi}{2} && (1.92)\\
\Psi &= \psi && (1.93)
\end{aligned}$$

For instance in spherical polar coordinates the antenna pattern functions read

$$\begin{aligned}
F^{+}(\theta, \phi, \psi) &= \frac{1}{2}(1 + \cos^2\theta)\ \cos 2\phi \cos 2\psi - \cos\theta \sin 2\phi \sin 2\psi && (1.94)\\
F^{\times}(\theta, \phi, \psi) &= \frac{1}{2}(1 + \cos^2\theta)\ \cos 2\phi \sin 2\psi + \cos\theta \sin 2\phi \cos 2\psi && (1.95)
\end{aligned}$$

Eq. (1.88) gives the strain amplitude for a detector located at the center the Earth with its arms located along the Earth-fixed frame axes. The last step consist in expressing the strain amplitude in a frame attached to a detector frame defined by the location of the beamsplitter and the two arms orientation vectors. The final expression of F^{+} and $F^{\times}$ is rather complex and the full derivation can be found in [38].

1.3.5 Calibration of the GW detectors

The strain amplitude of the GW detectors is reconstructed from the dark fringe photodiodes measurement and the control signals that are applied to maintain the free-falling masses at their nominal position. The control system of advanced detectors is rather complex with the goal to keep a destructive interference at the interferometer output port. As a consequence, below a few hundred hertz it is necessary to substract the control signals from the dark fringe signal before reconstructing $s(t)$. Above a few hundred hertz, the suspended mirrors behave as free-falling masses. The length variations induced by a passing gravitational wave generate directly variations of the output power of the interferometer.

To reconstruct $s(t)$ it is necessary to calibrate the sensing and control loop elements by measuring their transfer functions. This is usually done by injecting a deterministic excitation signal through the actuators.

Over the years, GW detectors have developed advanced techniques to perform calibration. For instance Advanced LIGO and Advanced Virgo are calibrated using the Photon Calibrator technique that consists in using radiation pressure induced by auxiliary lasers whose power is known absolutely instead of using the main laser wavelength as reference through the free swinging Michelson technique [40]. Actually both techniques are used to cross-validate calibration results whose uncertainty is provided as function of frequency.

Following the same principle, the reconstruction of $s(t)$ is also the opportunity to substract well identified noise source, whose contribution to the dark fringe signal is measured by a witness signal. Not all sources of noise can be substracted but detectors' sensitivity can be improved in some frequency range resulting in an increase of several Megaparsec[2] for the binary neutron star coalescence range [41, 40].

[2]The gain depends on the dataset. In Advanced LIGO during the O2 run, the Hanford detector sensitivity was increased by 20% on average.

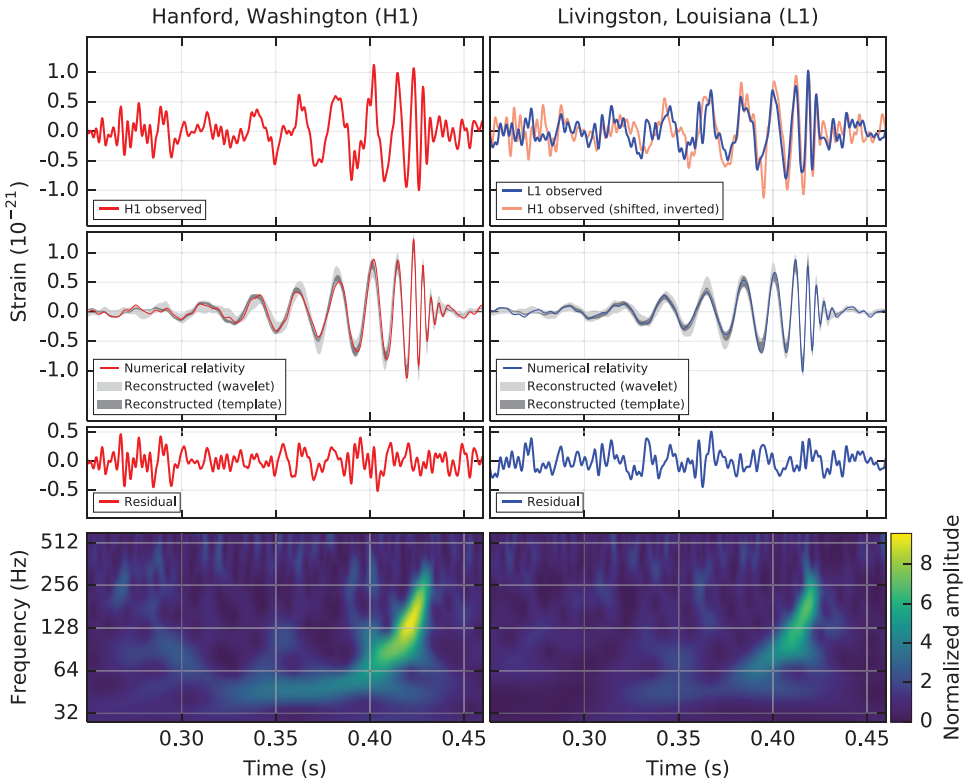

Figure 1.7: GW signal GW150914 in LIGO Hanford (*left*) and Livingstone (*right*). *First row:* strain data (filtered with a bandbass filter between 35−250 Hz). *Second row:* reconstructed signal and waveform template from numerical relativity. *Third row* : residual noise after substrating the template from the signal. *Fourth row:* time-frequency representation of the signal. Figure from [17].

Absolute timing calibration is also critical when performing multi-detector analysis for both detection (cross-correlation assumed the arrival time of the GW to be synchronized) and source sky position determination based also in the arrival time of the signal in each detector. The master timing system is controlled by GPS and provide coherent timing information to all detectors elements.

1.4 Progress of GW astronomy

1.4.1 Observing runs and detections

The life of GW detectors alternates between phases of observation (*observing runs*) and periods of maintenance / commissioning, during which upgrades are carried out to improve the sensitivity of the instruments. Therefore, each observing run provides a better sensitivity than its predecessors. As of 2021, three runs have been performed with Advanced Virgo and Advanced LIGO. Each of them has offered ground-breaking discoveries.

The first observing run (O1) took place between September 2015 and January 2016, with only the two LIGO detectors observing. On September 14th 2015 - a few days before the official start of the run - the first GW signal ever was detected. The signal, represented in Figure 1.7 was seen for 0.2 s between 35 to 250 Hz, and had the characteristic *chirp* morphology expected from the merger of two compact objects. It is consistent with the merger of two black holes of masses $36^{+5}_{-4}\,\mathrm{M}_\odot$ and $29^{+4}_{-4}\,\mathrm{M}_\odot$ observed at a luminosity distance $D_L = 430^{+150}_{-170}\,\mathrm{Mpc}$ [17].

The implications of this discovery were huge. Besides being the first detection of GW, it was

the first direct observation of solar-mass black holes. It was also a fantastic opportunity to test the validity of general relativity in the strong field regime. These tests showed no measurable deviation from the predictions of the theory [42]. Two other binary black hole systems (BBH) were discovered in total during O1, allowing to start to measure the rate of such events [43].

The second run (O2) began on November 30th 2016 for LIGO, and on August 1st 2017 for Advanced Virgo, and ended on August 25th 2017. During the almost 9 months of observation, 7 new BBHs were discovered. The inclusion of Advanced Virgo in the detectors network allowed to constrain more precisely the location of detected events and the polarization of GW [44]. Yet, the major discovery made during O2 was undoubtedly the detection of GW170817, the first GW signal from a binary neutron star (BNS) merger. The signal detected on August 17th 2017 was visible for a duration of $\sim 100\,\mathrm{s}$ in the frequency band of the detectors, and it has been associated to the inspiral and merger of two neutron stars of masses $1.46\,\mathrm{M}_\odot$ and $1.27\,\mathrm{M}_\odot$ at a distance of $\sim 40\,\mathrm{Mpc}$ [19]. A few seconds after the GW signal, the Fermi-GBM telescope recorded a short gamma-ray burst (GRB) [45], which was confirmed later by INTEGRAL [46]. These detections triggered an unprecedented observing campaign across the whole electromagnetic spectrum, and a counterpart was detected 11 hours after the initial GW alert in NGC 4993 [47]. For the first time, the associated kilonova signal was observed very early on confirming the scenario that BNS merger are associated to short GRB and kilonova. The source has been followed in ultraviolet, optical, infrared and radio waves. A search for high-energy neutrinos [48] was also conducted. The simultaneous observation of GW and electromagnetic signal from the same sources marked a milestone in the domain of multi-messenger astronomy. Important constrains on the speed of GWs [49], modified gravity theories and finally the first measurement of the Hubble constant with GWs [50] have been possible with this very first BNS merger.

After more than one and a half year of interruption, the third observing campaign (O3) was launched on April 1st 2019, with a detection range increased by 50% and 100% for Advanced LIGO and Advanced Virgo detectors respectively. Given the rate of events inferred from previous detections, this increase in sensitivity lead the community to expect a rate of ~ 1 detection per week. Indeed, during the first 6 months of O3, from April 1st 2019 to October 31st 2019, 39 GW events have been detected, most of them from BBH mergers [18].

Among the 36 BBH mergers reported so far from O3, GW190521 features the most massive black holes observed so far. The mass of the remnant black hole is estimated to be $142^{+28}_{-16}\,\mathrm{M}_\odot$[51]. This is the first direct evidence of the existence of intermediate mass black holes. Interestingly, it falls within the so-called *mass gap*, a range of masses for which it is supposed that a process called *pulsional pair instability* prevents the formation of black holes from stellar collapse [52]. Therefore, it raises many new questions about the channel of formation of such black holes. The picture of compact binary mergers was completed by the observation of two neutron star - black hole colescences, GW200105 and GW200115 [20].

To this day, Advanced LIGO and Advanced Virgo have detected ~ 50 signals from compact binary mergers [18], most of them being BBH, with two confirmed binary neutron star merger, GW170817 [19] and GW190425 [53], and two neutron star - black hole mergers [20]. These detections allow to estimate the rate of compact binary mergers in the universe, and probe the population of compact objects. With 47 confirmed detection the BBH rate is the most tightly constrained, with $\mathcal{R}_{\mathrm{BBH}} = 23.9^{+14.3}_{-8.6}\,\mathrm{Gpc}^{-3}\,\mathrm{yr}^{-1}$ [54]. Regarding BNS, the rate inferred from the two observed events is $\mathcal{R}_{\mathrm{BNS}} = 320^{+490}_{-240}\,\mathrm{Gpc}^{-3}\,\mathrm{yr}^{-1}$ [54], and the two newly discovered NSBH allow to estimate $\mathcal{R}_{\mathrm{NSBH}} = 130^{+112}_{-69}\,\mathrm{Gpc}^{-3}\,\mathrm{yr}^{-1}$ [20].

1.4.2 Perspectives

The next observing runs of Advanced LIGO and Advanced Virgo are already planned. O4 should start mid 2022 for a duration of 1 year and a sensitivity further improved compared to O3. The designed sensitivity of Advanced LIGO and Advanced Virgo should be reached during O5, by 2025. At the time, Advanced LIGO should reach a detection range for BNS of 330 Mpc, and

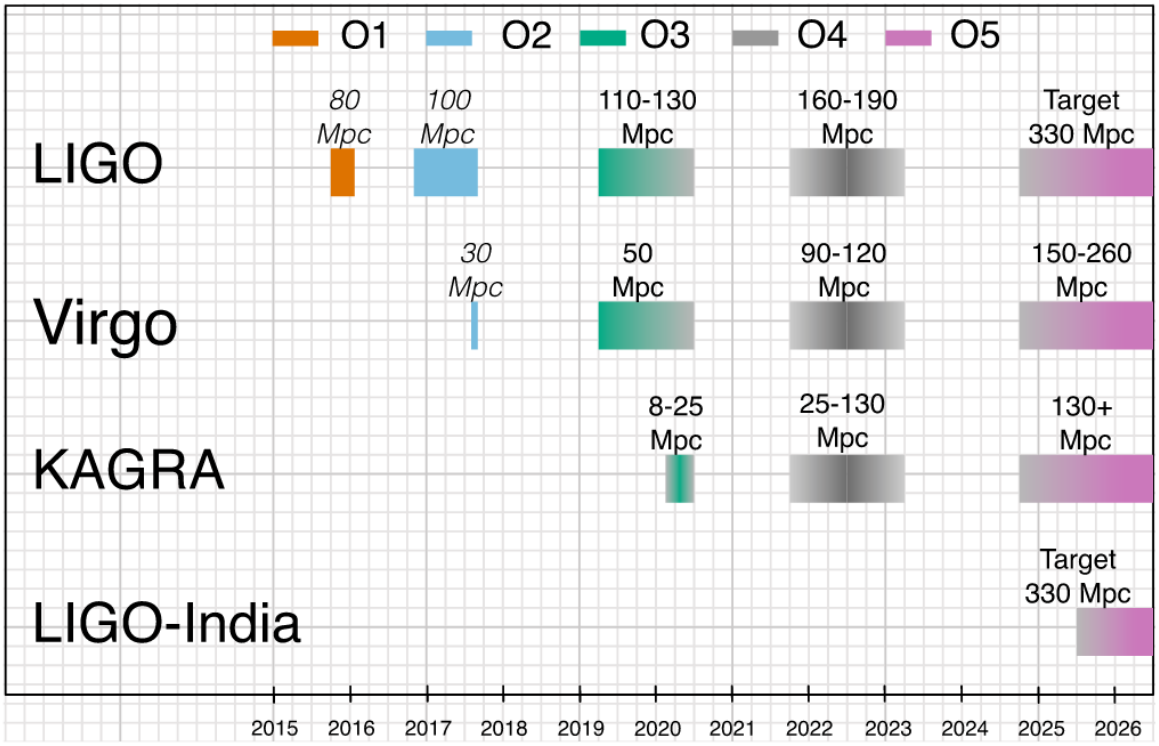

Figure 1.8: Summary of past (O1, O2, O3) and future planned (O4, O5) observing runs of Advanced LIGO, Advanced Virgo, and KAGRA. Achieved and expected sensitivities are given by the BNS detection range in Mpc. For future runs, dates and sensitivities may have large uncertainties. Figure from[55]. The fourth run O4 should start on August 2022.

$150 - 260$ Mpc for Advanced Virgo. New detectors are planned to join the network, KAGRA as soon as O4, and LIGO India in 2025-2027, although there are large uncertainties on the exact dates and sensitivities [55]. A summary of the past and planned observing runs is shown in Figure 1.8.

Increased sensitivity and observing time will surely lead to more and more detections. The sample of compact binary mergers will grow, providing more informations on the populations of black holes and neutron star with especially better measurement of the black hole spins. More detections of BNS mergers will place multi-messenger astronomy in a central place, and may provide new insight on the equation of state and the physics of neutron stars. Finally, we can expect to detect new sources of GW, possibly non related to compact binary mergers, such as magnetars, core-collapse supernovae or the stochastic GW background.

In the more distant future, third-generation detectors like the proposed Einstein Telescope [56] or Cosmic Explorer [57] may reach sensitivities an order of magnitude higher than what is achieved by Advanced LIGO and Advanced Virgo. However, ground-based detectors' sensitivity will always be limited at low frequency (below ~ 1 Hz) because of the Earth' seismic noise. The Laser Interferometer Space Antenna (LISA), whose launch is planned for 2034, will scan the GW universe at frequencies between 10^{-4} and 1 Hz, giving access to new types of potential sources, such as even more massive BBH, white dwarf binaries, and the low frequency components of the stochastic GW background.

Finally, the *international pulsar timing array* [58] is a project that consists in measuring fluctuations of the pulsation of pulsars caused by GW. This allows to probe very low frequencies $< 10^{-8}$ Hz GW emitted by the coalescence of super-massive black holes at the center of galaxies [59].

Chapter 2

Astrophysical sources of gravitational waves

Because of the extreme stiffness of space-time, only a few extreme astrophysical phenomena are able to emit GW at a detectable level. Notably, a good source of GW would be very compact, asymmetric and involve relativistic speeds. Therefore, the most promising candidates are *compact objects*, i.e neutron stars and black holes (and, to a lesser extent, white dwarfs). In fact, the most energetics GW emission mechanisms happen during cataclysmic events that involve one or more compact objects. In this chapter, I give an overview of the main sources of GW related to *transient* GW, and especially long-lived transient, for which the expected signal lasts at least a few seconds.

2.1 Binary systems of compact objects

Binary systems made of two compact objects make excellent sources of GW, since they are highly non-axisymmetric and relativistic. In fact, mergers of two compact objects are the brightest known sources of GW - they can radiate GW with an energy equivalent to several solar masses (a few percent of the total mass of the system), and the only ones detected to this day.

To understand the GW emission of those systems, we can go back to the toy model of Chapter 1: we have seen that two point-like objects of mass m_1 and m_2 that orbit each other at a distance a and orbital pulsation ω radiate a GW strain

$$\begin{aligned} h_+(t) &= \frac{4G\mu a^2\omega^2}{rc^4}\cos(2\omega t) \\ h_\times(t) &= \frac{4G\mu a^2\omega^2}{rc^4}\sin(2\omega t) \end{aligned}$$

where $\mu \equiv m_1 m_2/(m_1+m_2)$ is the reduced mass of the system. At order zero, the dynamics of this system is given by Kepler's third law,

$$a^3\omega^2 = GM, \tag{2.1}$$

with $M = m_1 + m_2$. When the bodies are far away from each other, their GW emission is not detectable by current generation detectors. Indeed, if we consider somewhat realistic values, like $M = 2M_\odot$ and $a = 1\,\mathrm{UA}$, the frequency f of the GW emitted is

$$f = \sqrt{\frac{GM}{\pi^2 a^3}} \sim 10^{-7}\,\mathrm{Hz}, \tag{2.2}$$

far below the detector's sensitive band. Such signals could be seen by pulsar timing array detectors [58].

However, GW carry energy. Because of that, the system will progressively lose energy, and the two objects will get closer and closer, and eventually merge, generating a very bright burst of GW that Advanced LIGO and Advanced Virgo are able to detect. Combining Eq. (1.53) and (1.58), the GW luminosity of the toy model is

$$L_{\rm GW} = \frac{32G}{5c^5}\mu^2 a^4 \omega^6. \tag{2.3}$$

In the meantime, the total energy E of the system is the sum of the kinetic energy and gravitational potential energy

$$\begin{aligned} E &= \frac{1}{2}\mu a^2\omega^2 - \frac{G\mu M}{a} && (2.4)\\ &= -\frac{1}{2}\frac{G\mu M}{a} && (2.5)\end{aligned}$$

We then see that when the system loses energy the separation between the two bodies must decrease as well. The energy-balance equation $L_{\rm GW} = -\frac{dE}{dt}$ that relates the energy loss to luminosity leads to a differential equation for the time evolution of the GW frequency $f_{GW} = \omega/\pi$

$$\frac{df_{GW}}{dt} = \frac{96}{5}\pi^{8/3}\left(\frac{G\mathcal{M}}{c^3}\right)^{5/3} f_{GW}^{11/3}, \tag{2.6}$$

where $\mathcal{M} = \mu^{3/5}M^{2/5}$ is the *chirp mass* of the system.

We can integrate this equation to get some insight about the evolution of the system and the GW emission. The GW frequency is given by

$$f_{GW}(t) = \frac{1}{\pi}\left(\frac{5}{256}\frac{1}{(t_c - t)}\right)^{3/8}\left(\frac{G\mathcal{M}}{c^3}\right)^{-5/8} \tag{2.7}$$

where t_c is the time at the merger. We can re-express the two polarisation modes seen by an observer at distance r on the z-axis

$$\begin{aligned} h_+(t) &= A(t)\cos\phi(t)\\ h_\times(t) &= A(t)\cos\phi(t), \end{aligned} \tag{2.8}$$

with

$$\begin{aligned} A(t) &= \tfrac{G\mathcal{M}}{rc^2}\left(\tfrac{c^3(t_c-t)}{5G\mathcal{M}}\right)^{-1/4} && (2.9)\\ \phi(t) &= 2\left[\phi_c - \left(\tfrac{c^3(t_c-t)}{5G\mathcal{M}}\right)^{5/8}\right] && (2.10)\end{aligned}$$

t_c and ϕ_c represent respectively time and phase at the merger. The amplitude and frequency of the signal depends only on the chirp mass and increases with time, giving it the characteristic *chirp* morphology.

This toy model considers the simple case of non-spinning objects with circular orbits, and uses Newtonian dynamics to derive the expression of the waveforms at the first order. In practice, more precise waveforms are obtained using post-Newtonian expansions of this model by adding corrections at different orders of v^2/c^2 (see e.g [60, 61, 62, 63]). These waveforms takes more parameters than just the masses of the bodies, notably their spin, the tilt angle between the spins and the orbital plane, and the eccentricity of the orbit.

Furthermore, the Newtonian approximation we have used is only valid in a flat space-time. This approximation breaks when the two bodies get close and the gravitational field becomes strong. In Schwarzschild geometry, we can model the coalescence by a succession of quasi-circular

orbits up to the point where the two bodies reach the innermost stable circular orbit (ISCO), whose radius is given by

$$R_{\rm ISCO} = \frac{6GM}{c^2}. \tag{2.11}$$

Therefore, the frequency of the GW at the ISCO is

$$f_{\rm ISCO} = \frac{c^3}{6^{3/2}\pi GM} \tag{2.12}$$

This frequency scales with the inverse of the total mass M of the system. For M=2.8 $M_\odot$, a system formed of two neutron stars, $f_{\rm ISCO} \simeq 1.6\,$kHz and $R_{\rm ISCO}$=25 km which is to be compared to the radius of a neutron star ($\sim$10 km). The dynamics after the ISCO is dominated by strong field effects and leads quickly to the plunge of the two compacts objects. A first solution of the final orbit has been provided by numerical relativity endeavour [64]. Analytical waveforms are now available especially using the *Effective One Body* formalism [65] or phenomenological waveforms [66]. When a black hole is formed a *ringdown* signal is expected from the perturbed newborn Kerr black hole. The exact waveform of the expected signal is obtained from black hole perturbation theory [67]. Also, the GW signal from the merger of two neutron stars is further more complicated to predict because of the tidal effects that might play a significant role when the two bodies get sufficiently close [68].

It is interesting to estimate the duration $\tau = t - t_c$ of the signal in the bandwidth of the detectors. From Eq. (2.7) we obtain

$$\tau \simeq 2.18\,{\rm s} \left(\frac{1.21\,{\rm M}_\odot}{\mathcal{M}}\right)^{5/3} \left(\frac{100\,{\rm Hz}}{f_{GW}}\right)^{8/3} \tag{2.13}$$

For instance, for a two neutron star coalescence, if we can start measuring the signal at 10 Hz, the signal lasts $\sim$ 17 minutes. At 100 Hz, the signal duration is of the order of a few seconds. The other important factor is that the duration scales with $\mathcal{M}^{-5/3}$. The more massive the system, the shorter the signal. In the context of a long-duration GW signal search, we will focus our studies on low mass binary systems (neutron stars or low mass black holes).

Most of the compact binary mergers discovered so far in Advanced LIGO and Advanced Virgo data do not fall under the scope of this thesis, since they produce short duration signals that are well modelled and searched by optimal matched filter algorithms. However, waveforms from the inspiral of highly eccentric systems of low mass system are less well modelled and may be detectable [69]. Hence, these events are potentially a target for long transient searches. Examples of waveforms from eccentric compact binary coalescences are shown in Figure 2.1.

2.2 Binary neutron star post-merger

After the merger of two neutron stars, a post-merger GW signal may be emitted depending on the nature of the remnant object.

There are three main scenarios for the outcome of a binary neutron star merger (BNS) [71]: it can either form directly a black hole, or a supermassive neutron star that will shortly collapse into a black hole, or neutron that will survive for a longer amount of time, or indefinitely. The likelihood of each scenario depends on the mass and spin of the remnant, as well as on the equation of state of neutron stars, which is not precisely known. The theoretical maximal mass for a non-rotating neutron star is the Tolman-Oppenheimer-Volkoff mass $M_{\rm TOV}$ [72, 73], which depends on the equation of state, and is believed to be between $2.2 - 2.7\,M_\odot$.

When the mass M of the remnant is significantly higher than $M_{\rm TOV}$, it collapses immediately into a black hole. In that case the GW emission is expected to be minimal, with only the ringdown signal at $f > 6000[Hz]$ [74, 75].

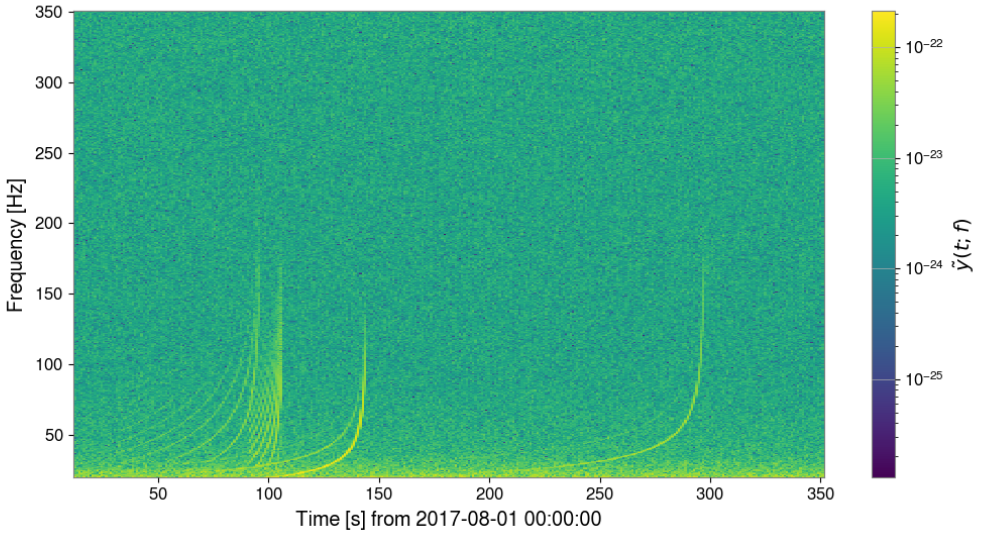

Figure 2.1: Time-frequency representation of a sample of long-duration GW signals from eccentric compact binary coalescences [70].

Scenarios in which the mass of the remnant is lower than $\sim 1.5\,M_{\rm TOV}$ are more promising in term of GW emission because a neutron star is formed. If M is between $1.2 - 1.5\,M_{\rm TOV}$, the newly formed neutron star is said to be *hypermassive* [71]. Only differential rotation is able to prevent the collapse for such masses, but this does not last long. Differential rotation is suppressed on a short time scale ($< 1\,$s) through viscous dissipation and magnetic braking [76], and the nascent neutron star collapses promptly into a black hole. In this scenario, a short GW burst is expected from the excitation of the fundamental oscillation mode (f-mode) of the neutron star, at frequencies between $2 - 4\,$kHz [77, 78]. The short duration and relatively high frequencies do not make this type of signal a promising target for long-duration searches.

When $M \lesssim 1.2\,M_{\rm TOV}$, a *supramassive* or a stable neutron star is formed. When the remnant is supramassive ($M_{\rm TOV} \lesssim M \lesssim 1.2 M_{\rm TOV}$), it is prevented from collapsing by its rotational energy and can survive between a few minutes and a few days before eventually collapse into a black hole [79]. When $M \lesssim M_{\rm TOV}$, it is indefinitely stable. In both cases, long-lived GW may be emitted. Different mechanisms of emission have been proposed, which involve magnetic field and rotation-induced instabilities that grow on timescales $10^2 - 10^4\,$s [71]. Indeed, because of conservation of angular momentum, the neutron star is likely to be rapidly rotating and have a strong magnetic field. These instabilities may deform the star in a non-axisymmetric manner, leading to generation of GW. This scenario, called *millisecond magnetar*, is also a possible outcome of core-collapse supernovae, and we give more details on the various instabilities and characteristics of the signal expected in Section 2.3.3.

In all cases the loss of angular momentum due to GW emission and/or magnetic braking will result in slowing down the rotation of the neutron star, up to the point where it will either collapse into a black hole if $M \gtrsim M_{\rm TOV}$, or become a stable neutron star, and the transient GW emission will be quenched.

Piro et al. [80] estimated the fraction of BNS mergers that give birth to a long-lived neutron star remnant between $23 - 99\%$, depending on the equation of state and mass distribution of neutron stars. Therefore, a significant fraction of the BNS detected could be followed by a long-lived post-merger signal. The volumetric rate of binary neutron star mergers is $\mathcal{R}_{\rm BNS} = 320^{+490}_{-240}\,{\rm Gpc}^3\,{\rm yr}^{-1}$[81], with two confirmed detection, GW170817, at $\sim 40\,$Mpc [19] and GW190425 at $\sim 160\,$Mpc [53]. Searches for a post-merger signal after GW170817 did not

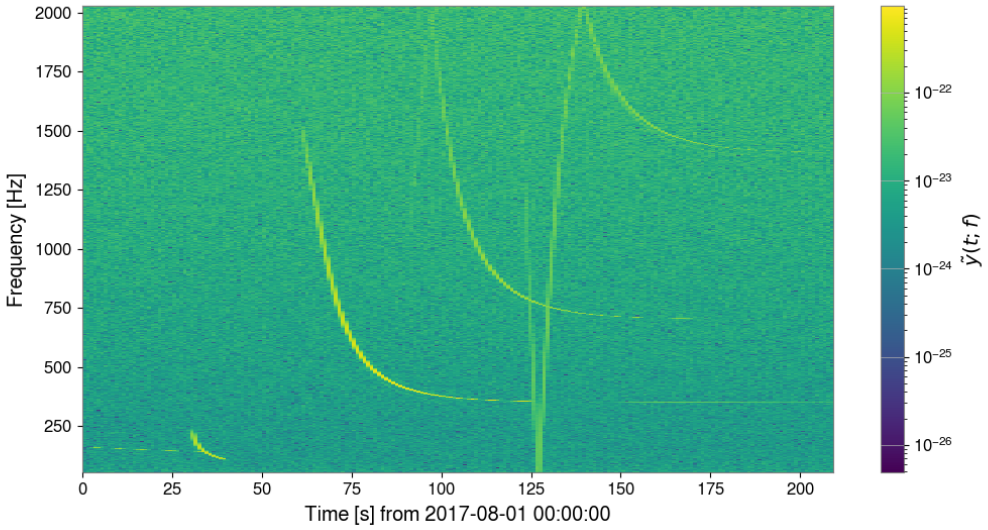

Figure 2.2: Time-frequency representation of a sample of long-duration GW descending chirps expected from accretion disk instabilities around the ISCO [84, 85].

found any signal, neither short or long [82, 83], but they set upper limits on the GW strain amplitude that just one order of magnitude higher than those predicted by models [83]. With the planned increase in detectors' sensitivity, these events are therefore promising candidates for future long-duration searches.

2.3 The death of massive stars

At the end of their life, massive stars (of mass $\gtrsim 10\,M_\odot$) form an extremely dense iron core which is supported by the degeneracy pressure of electrons. The radius R of the core is typically of the order of magnitude of the radius of the Earth ($\sim$ 6000 km). When its mass exceeds the Chandrasekhar limit, pressure is no longer sufficient to counter the core's self-gravity. The latter eventually collapses into a much smaller object, a proto-neutron star of $R \sim 30$ km, in which matter reaches nuclear density. At this point, the nuclear force becomes repulsive and the collapse is stopped. The outer part of the core bounces back, creating a shock wave that propagates outward.

The shock in itself is not sufficient to blow out the stellar envelope, as 99% of the energy is dissipated through neutrino emission [86]. To create a supernova, it must be revived via a mechanism that remains uncertain to this day - but certainly involves neutrinos [87]. If this mechanism is not successful, the stellar envelope is not entirely ejected and matter falls back into the proto-neutron star, which eventually collapse into a black hole [88]. This is the *collapsar* scenario.

On the contrary, if the explosion is successful, the proto-neutron star may survive, at least temporarily. In about 10% of the cases, the remnant neutron star is supposed to be a millisecond magnetar, highly magnetized (with internal magnetic field $B \sim 10^{15}$ G, or even more) [89], and rapidly rotating (rotation period $P \sim 1$ ms) [90].

The two scenarios, collapsar and millisecond magnetar, have been proposed to be the central engine of long GRBs [91, 92]. They are also promising potential sources of GW.

2.3.1 Core bounce

A short-lived GW burst ($< 2\,\mathrm{s}$) may be emitted by the star bounce itself if the core is rapidly rotating and develops a sufficient non-axisymmetric quadrupole moment. However, numerical studies have shown that the expected energy emitted via GW is quite low ($E_{\mathrm{GW}} \sim 10^{-9}\ M_{\odot}c^2$), which restrain the detection horizon to our galaxy [93, 94]. Given that the rate of core-collapse supernovae in the Milky Way is estimated to be $\sim 2-3$ events per century [95], detection of such GW emission is still a long shot.

2.3.2 Accretion disk

In the collapsar scenario, the newly formed black hole is surrounded by an accretion disk or a torus constituted of matter from the collapsing star [96].

Piro and Pfahl [97] showed that a gravitational instability can arise in the outer part of the accretion disk, in the zone where cooling become efficient. Fragments of $\sim 0.1 - 1\mathrm{M}_{\odot}$ with the density of a neutron star may form and migrate inwards. We can roughly model this system as a fragment of mass M_f orbiting the central black hole of mass M_{BH}. The amplitude of the GW strain for a source at a distance r would be

$$h \sim 6 \times 10^{-24} \left(\frac{M_f^{3/5} M_{\mathrm{BH}}^{2/5}}{M_{\odot}} \right)^{5/3} \left(\frac{f}{100\,\mathrm{Hz}} \right)^{2/3} \left(\frac{100\,\mathrm{Mpc}}{r} \right), \tag{2.14}$$

where f is the orbital frequency of the fragment around the black hole. The expected GW signal would be chirp-like (increasing frequency over time), last $\sim 100\,\mathrm{s}$ and have a strain amplitude $\sim 10^{-22}$ at $100\,\mathrm{Hz}$ for a source at $100\,\mathrm{Mpc}$, which is within the detection range of current generation detectors. The GW energy released by a fragment of $M_f = 1\,\mathrm{M}_{\odot}$ falling into a black hole of mass $5\,\mathrm{M}_{\odot}$ would therefore be $\sim 4 \times 10^{-2}\,\mathrm{M}_{\odot}\mathrm{c}^2$ [28].

In addition to fragmentation, different kinds of instabilities may grow in the disk that can lead to GW emission. Van putten proposed a model of rapidly rotating Kerr black hole, surrounded by a rotating, highly magnetized accretion torus located at the level of the innermost stable circular orbit. In this scenario, the torus undergoes turbulence and instabilities that may lead to break the axial symmetry and develop a time varying quadrupole moment, hence GW emission at the orbital frequency of the accretion torus [98]. Those instabilities would be powered by the coupling between the black hole spin and the torus magnetic field, the former transferring angular momentum to the latter. As a consequence of the black hole spin-down, the radius of the ISCO increases, and so does the orbital period of the torus. Therefore, the expected frequency of the GW emitted decreases with time. The GW signal would last ~ 10 s, with a chirp-down morphology and potentially verly large energy released ($E_{GW} \sim 10^{53}\,\mathrm{erg}$) [84, 85], although the latter is based on rather optimistic energy considerations. In figure 2.2, we show a time-frequency representation of a few down-chirping waveforms that are expected from accretion disk instabilities.

2.3.3 Proto-neutron star

Because of their high rotation speed and magnetic field, newly formed magnetars could be a powerful source of GW, provided they develop a significant, time-varying quadrupole moment. We have seen in Section 1.2.3 that a triaxial ellipsoid spinning around its z-axis at pulsation ω generates an average GW strain

$$\langle h \rangle = \frac{4G}{rc^4} \epsilon I_z \omega^2, \tag{2.15}$$

where r is the distance to the source, I_z the inertia moment around the z axis and $\epsilon \equiv (I_x - I_y)/I_z$ the ellipticity parameter. Therefore, to be an efficient generator of GW, a neutron star must develop an asymmetry in the plane orthogonal to its spin axis (here the (x, y) plane).

According to [99], when the toroidal component of the magnetic field is dominant, it can deform the neutron star into a prolate ellipsoid (a rugby ball shape, with $I_z > I_x \simeq I_y$). The ellipticity ϵ_B induced by the volume-averaged toroidal field $\langle B_t \rangle$ can be approximated as

$$\epsilon_B = 10^{-6} \left(\frac{\langle B_t \rangle}{10^{15}\,\mathrm{G}} \right) \tag{2.16}$$

The spinning prolate ellipsoid undergoes precession if the magnetic and spin axes are misaligned. In fact, the situation where both axes are aligned is an unstable equilibrium. The minimal energy level of such a system is when the two axes are orthogonal. This is called the *spin-flip instability*. Therefore, even if the angle between the axes is initially low, this instability drives the magnetic axis orthogonal to the spin axis. The precession energy is dissipated through viscous dissipation. As a result, the system becomes an optimal GW emitter (similar to a spinning bar), and emits GW at frequency $f = \omega/\pi$, and at amplitude $h \propto \epsilon_B\, \omega^2$. Numerical simulations from Dall'Osso et al. [100] showed that such signal could last $\sim 10^3 - 10^5$ s, and that the detection horizon for Advanced LIGO would be around ~ 4 Mpc.

Another potential source of GW emission comes from the high rotation speed. Rotation tends to turn a spherical body into an oblate spheroid (flattened at the poles, like the Earth for example). However, since the symmetry and spin axis are aligned, the corresponding quadrupole moment does not vary with time, hence no GW is emitted in this case. Nevertheless, when the rotation speed is very high - more precisely when the ratio of rotational to gravitational energy is higher than 0.28, another type of instability can be activated, known as rotational instability, or *bar-mode*. This instability would grow in $\sim 10^1 - 10^2$ s and deform the star in the plane orthogonal to the spin axis, giving it a bar shape (or cigar) [101]. It could also explain the presence of a typical X-ray plateau in the light curve of the GRB [102]. In this case, the GW signal emitted could be long-lived ($\sim 10^3$ s) with decreasing frequency and amplitude over time, and amplitude $h \sim 10^{-23}$ at 100 Mpc [103].

R-modes are toroidal oscillation modes that originate from the Coriolis form in rotating bodies. These modes are unstable and are subject to the so-called *Chandrasekhar-Friedman-Schutz instability* [104, 105]. When activated, they can emit GW at 4/3 the spinning frequency of the neutron star [106] that would potentially last for a very long time.

Like the remnant of a BNS merger, the newborn neutron star is expected to rapidly spin down because of GW emission and magnetic dipole radiation. Consequently, the frequency and amplitude of the potential GW emitted will progressively drop, on a time scale of days to weeks. Besides, the relative amplitudes of the magnetic field poloidal and toroidal components, and rotation speed, are critical to understand which GW emission mechanisms are activated and for how long. Conversely, detecting a GW emission from a newborn magnetar would certainly provide a deep insight on the physics of these objects, especially combined with electromagnetic and neutrino observations.

Detection horizons are currently around $3-4$ Mpc for unmodelled searches, and $20-40$ Mpc for optimal matched filter searches [103]. An horizon of 4 Mpc only only places galaxies from the local group within detection range.

The local rate of core-collapse supernovae is estimated to be $\sim 7 \times 10^{-5}\,\mathrm{Mpc}^{-3}\,\mathrm{yr}^{-1}$ [107]. Assuming that 1 event out of 10 results in the formation of a millisecond magnetar, we can expect a rate of ~ 1 millisecond magnetar every 4 years at a distance < 20 Mpc (considering that the local Universe is uniform, which is not the case in reality). Therefore, improving the sensitivity of unmodelled search algorithms could be crucial to detect these sources.

2.4 Isolated neutron stars

Isolated neutron stars may continue to emit GW, even a long time after their birth, through a persistent non-asymmetric deformation or during cataclysmic events whose trigger mechanisms remain mysterious to this day.

2.4.1 Pulsars

Pulsars are rapidly rotating neutron stars that emit beams of electromagnetic radiation (usually radio waves) along their magnetic axis. When the magnetic axis is not aligned with the rotation axis, the radiation observed is periodic, allowing to measure precisely the rotation frequency of the neutron star.

We know from the toy model of a rotating triaxial ellipsoid that the GW emitted is

$$\begin{aligned} h_+(t + r/c) &= -\frac{4G\epsilon I_z \omega^2}{rc^4} \cos 2\omega t \\ h_\times(t + r/c) &= \frac{4G\epsilon I_z \omega^2}{rc^4} \sin 2\omega t. \end{aligned} \tag{2.17}$$

The intrinsic parameters that command the GW emission are the ellipticity ϵ, moment of inertia I_z and rotation period $P = 2\pi/\omega$.

About 300 known pulsars have rotation frequency within LIGO-Virgo sensitive band [108], while the estimated number of isolated neutron stars in the galaxy is $\sim 160,000$ [109]. Despite the expected amplitude of continuous GWs emitted by pulsar is very low, we could detect them by integrating a potential signal over a long period of data.

2.4.2 Magnetars

Magnetars form a class of neutron stars with extremely high magnetic field ($\sim 10^{13} - 10^{16}$ G, $100 - 1000$ times higher than typical neutron stars observed as radio pulsars). Their existence was proposed by Duncan and Thomson in the 1990s [110, 111, 112] to explain the observations of *Soft Gamma Repeaters* (SGRs), sources that emit short bursts (~ 0.1 s) of soft gamma-rays at energies $\sim 10^{38} - 10^{43}$ erg at irregular intervals.

Those bursts are usually divided into 3 categories [113]: *short bursts* that last $\sim 0.1 - 1$ s and release $\sim 10^{41}$ erg, *intermediate bursts*, which have significantly longer duration ($\sim 1 - 40$ s) and higher peak energy ($\sim 10^{41} - 10^{43}$ erg), and *giant flares*, which can release up to 10^{47} erg in gamma rays.

Magnetar giant flares (MGFs) are very rare events. Only three of them have been observed so far from galactic SGRs, from SGR 0526-66 in 1979 [114], SGR 1900+14 in 1998 [115] and SGR 1806-20 in 2004 [116]. In all cases, the initial short peak of gamma-rays was followed by an afterglow X-ray tail at $\sim 10^{44}$ erg.s^{-1}, lasting ~ 100 s, and modulated by quasi-periodic oscillations [117]. These giant flares are the most energetic phenomena known from isolated neutron stars. Scenarios proposed to explain these events involve catastrophic events, such as a sudden reconfiguration of the star's internal structure and / or magnetic field [111, 118], but much remains unclear to this day.

Because of the large energy released, MGFs are promising potential sources of transient GW. GW can be emitted if some oscillations modes of the star are excited. Notably, Ioka [118], and Corsi and Owen [119], showed that a brutal rearrangement of the internal magnetic field could excite the fundamental f-mode at high frequency ($\sim 1 - 2$ kHz), leading to a short (≤ 0.1 s) but powerful burst of GW carrying a maximal energy $E_{GM} \sim 10^{48} - 10^{49}$ erg. However, numerical simulations by Zink 2012 and Ciolfi and Rezzolla 2012 showed that in more realistic conditions, the GW energy expected from excitation of the f-mode would be in the range $10^{34} - 10^{36}$ erg, so virtually undetectable. Nevertheless, MGFs may emit GW at lower frequencies < 600 Hz, via the excitation of other oscillation modes, but the detailed mechanisms remain unknown.

Much remains unclear about the trigger mechanism of MGFs - and less energetic flares - as well as the potential GW associated with these events. However, the fact that the pulsating tails last ~ 100 s makes them a potential source of long-lived transient signals. Besides, in 2021, Burns et al. have shown that extra-galactic MGFs could be associated with a distinct class of short GRBs [120]. Their results imply that the rate of MGFs in the local universe may be several

orders of magnitude higher than the rate of compact binary mergers. In chapter 5, I describe a search for a GW counterpart around 3 extragalactic MGFs, place upper limits on the GW energy emitted, and study the prospects of detection for future observing runs.

2.5 Other sources and summary

Compact binary sytems, core-collapse supernovae and isolated neutron stars constitute the main sources of GW that we expect to see with ground-based interferometers such as LIGO and Virgo. However, other potential sources may exist and could be detected in the future.

A stochastic background of GW could be formed by the sum of all non-resolved sources. Two main components of this background are expected, an astrophysical part composed of unresolved compact binary systems, supernovae and isolated neutron stars, and a cosmological component from inflation, cosmic strings and phase transitions in the early universe [121]. The detection of this stochastic background is a challenge because the expected signal is both random and small. Searches typically use cross-correlation of the data from separated detectors to extract the signal from the uncorrelated noise.

Like stellar mass black holes, the merger of two supermassive black holes is also expected to emit GW. Such events could occur in galaxy mergers. The frequency of the GW emitted is too low to be detected by ground-based interferometric detectors, but the space mission LISA should be able to detect them.

Sources of GW are rather diverse, and so are the types of signals expected. Transient sources are usually classified into two categories, modelled and unmodelled. Modelled signals consist mostly in compact binary mergers for which precise waveforms are known (in practice, this concerns only systems with low eccentricity and mass ratio), and are searched via matched filtering algorithms. To this date, in 2021, ~ 50 black holes binary mergers have been detected by the LIGO and Virgo detectors[18], as well as one binary neutron stars merger and one black hole - neutron star merger. Unmodelled signals are more difficult to detect because of the lack of precise waveform and the large parameter space. This is especially true for long lived signals, for which the energy is spread over a longer duration. Conversely, detecting such signals, or set meaningful upper limits on the GW energy emitted after, say, a core-collapse supernova, would certainly allow to better constrain the models of emission and get better knowledge of this sources.

To summarize, we can classify the potential sources of long-lived transient GW into four main categories.

- **Newly born neutron stars:** either the remnant of a core-collapse supernova or a binary neutron star merger, these objects are expected to be highly perturbated in the first minutes of their existence and may radiate GW via several processes.
  - Spin-flip instability, induced by a strong toroidal magnetic field, can drive the symmetry axis orthogonal to the rotation axis, making the young NS an optimal GW emitter.
  - Rotational instability (bar-mode) may develop in a rapidly spinning neutron star, and induce deformation in the plane orthogonal to the rotation axis, leading to varying quadrupole moment and GW emission.
  - R-modes can grow in a rotating neutron star subject to the Chandrasekhar-Friedman-Schutz instability and long-lasting GW at 4/3 the rotation frequency of the star.
- **Accretion disk instabilities:** newly formed black holes after a core-collapse supernova are surrounded by an accretion disk. Several instabilities may provoke non-axisymmetric deformations of the disk and generate GW.

- **Magnetar Giant Flares:** MGFs are highly energetic burst of soft gamma-rays from isolated magnetars, followed by long-lasting pulsating tails. Several oscillations modes may be excited at the occasion, leading to potential GW emission.
- **Eccentric compact binary coalescences:** merger of compact binaries with low masses and high eccentricities may produce a longer detectable GW signal. Waveforms from eccentric system are less well modelized, making them a pertinent source for long-duration burst searches.

This list is by no means exhaustive, as many processes remain poorly understood or even not known at all. In particular, modelling the GW emission from neutron star oscillations, or accretion disk instabilities, requires complex, multi-dimensional magneto-hydrodynamical simulations that possess a lot of free parameters that need to be constrained. Hence, despite the computed waveforms may depict the global morphology of the signal emitted, they are not precise enough to be used to search for GW in the detectors' data with matched filter algorithms, such as what is done for circular compact binary coalescences. This motivates the need for unmodelled detection algorithms that do not rely on the exact shape of the signal searched.

Chapter 3

PySTAMPAS : a data analysis pipeline to search for long-duration signals

The extremely weak amplitude of GW requires sophisticated data analysis techniques to extract the signal from the detectors' noise, even with the remarkable sensitivity of current generation detectors. The field of GW data analysis is diverse, with a large variety of signals that require different search algorithms. The core of my thesis has been the development of a GW data analysis pipeline targeting unmodelled, long-lived transient signals. In this chapter, I first explain the main concepts and definitions of statistical data analysis applied to GW detection [122], then present the specific goals and challenges of unmodelled transient searches, and finally describe the `PySTAMPAS` pipeline and characterize its performances.

3.1 Gravitational waves data analysis

3.1.1 Basic concepts and definitions

The goal of data analysis is to extract meaningful information - *signal* - from a given data set which may also contain random fluctuations or unwanted information - *noise*. Of course, the definition of signal and noise depends on the problem considered. In the case of GW detection, the signal we want to extract is the detector's response $h(t)$ to a GW given by Eq. (1.88). This signal is buried into the detector's noise $n(t)$, whose various components are described in Chapter 1. We assume that the GW response adds to the detector's noise such that the detector's strain output is

$$s(t) = h(t) + n(t). \tag{3.1}$$

Hypothesis testing

A given data set may or may not contain a signal, so we need a criterion to decide whether or not a signal is present in the data. To use the language of statistics, it means choosing between the *null hypothesis* H_0: data do not contain a GW signal - and the *alternative hypothesis* H_1: data contain a GW signal. When making such a decision, two types of error are possible:

- false positive - claim that H_1 is true whereas it is in fact H_0;
- false negative - claim that H_0 is true whereas it is in fact H_1.

A false positive is called a type I error and a false negative a type II error, and their respective probability are α and β. When we decide on the null hypothesis or the alternative hypothesis, we want to compute these probabilities to estimate the significance of our claim. For GW searches, we usually want to know the probability α of being a false positive, i.e avoid to wrongly claim

a GW detection, and compute the associated probability β to miss a signal. In that context, $(1-\beta)$ is often called the *detection efficiency* of the search.

In order to decide between H_0 and H_1 for a given data set d, we will compute a *detection statistic* $\Lambda[d] \in \mathbb{R}$ which measures the plausibility of H_1 or H_0: $\Lambda[d]$ should increase with the probability of H_1 being true instead of H_0, given the data d observed. By estimating the distribution of Λ under the null hypothesis, i.e when the data contain only noise, we can assess the false-alarm probability α of a candidate event.

3.1.2 Formulation of the problem

Let us consider a GW signal emitted by a point-like source whose direction in the sky is given by the unit vector $\hat{\Omega}$. The signal is described by its two polarization modes $h_+(t)$ and $h_\times(t)$ in the equatorial coordinates[1]. The detector's response $h(t)$ is

$$h(t) = F^+(t,\hat{\Omega})\, h_+(t) + F^\times(t,\hat{\Omega})\, h_\times(t), \tag{3.2}$$

where $F^+(t,\hat{\Omega})$ and $F^\times(t,\hat{\Omega})$ are the antenna factors that weight the polarizations mode according to the direction of the source, as explained in section 1.3.4. Our goal is to build a detection statistic $\Lambda[s(t)]$ that maximizes the efficiency of the search for a given false-alarm probability.

Optimal case: matched filtering

In the optimal case, the signal $h(t)$ is perfectly known, and the noise is a zero-mean Gaussian random process that is fully described by its one-sided power spectral density (PSD) $S(f)$, which is defined as twice expectation value of the squared modulus of the Fourier transform of the noise, i.e

$$S(f) = 2\langle|\tilde{n}(f)|^2\rangle. \tag{3.3}$$

In this case, the Neyman-Pearson lemma states that there exists an optimal detection statistic, the likelihood ratio:

$$\Lambda[s(t)] = \frac{\mathcal{L}\left(H_1|s(t)\right)}{\mathcal{L}\left(H_0|s(t)\right)}. \tag{3.4}$$

The likelihood $\mathcal{L}\left(H|s(t)\right)$ of an hypothesis H given the data $s(t)$ observed is proportional to the conditional probability $P\left(s(t)|H\right)$ of observing $s(t)$ knowing that H is true. Therefore,

$$\Lambda[s(t)] = \frac{P\left(s(t)|H_1\right)}{P\left(s(t)|H_0\right)}. \tag{3.5}$$

Under the null hypothesis, $n(t) = s(t)$, while under the alternative hypothesis, $n(t) = s(t) - h(t)$. Assuming $n(t)$ is a Gaussian random variable,

$$P\left(n(t)|H_1\right) = P\left(n(t)|H_0\right) \propto \exp\left[-\frac{1}{2}\int_{-\infty}^{+\infty} \frac{|\tilde{n}(f)|^2}{S(f)}\right]. \tag{3.6}$$

For convenience and readability we can define the scalar product

$$(a,b) \equiv \int_{-\infty}^{+\infty} \frac{\tilde{a}^\star(f)\tilde{b}(f)}{S(f)}, \tag{3.7}$$

such that finally the likelihood ratio writes

$$\boxed{\Lambda[s(t)] = \frac{e^{-(s-h,s-h)/2}}{e^{-(s,s)/2}}.} \tag{3.8}$$

[1]The effect of the polarization angle ψ is implicitly encoded in the definition of $h_+(t)$ and $h_\times(t)$ so the antenna factors depend only on the sky position.

In practice, the probability distribution $P(s(t)|H_1)$ is not perfectly known. The signal $h(t)$ may depend on several parameters (for example, for a compact binary coalescence, masses, spins, eccentricity, distance, inclination, starting time, etc), so the likelihood ratio is maximized over the whole parameter space. This process can rapidly become computationally expensive, which restricts the applicability of matched filtering to signals which are well modelized by a small number of parameters, such as compact binary coalescence with circular orbits and aligned spins.

Unmodelled searches

For most of the potential long-lived signals presented in Chapter 2, the models are not precise enough to use matched filtering. The lack of knowledge and the diversity of the potential sources require more agnostic detection algorithms that make minimal assumptions on the parameters of the signal searched. To this end, we need to build an *ad hoc* detection statistic. Several detection algorithms have been developed to search for unmodelled GW short-duration signals (often called *bursts*). Most of them rely on an excess power statistic computed over a time-frequency representation of the data, and a network of detectors. In the latter case, an event must be seen in several detectors coincidentally to be considered a candidate signal.

3.2 Description of the search method

In the early 2010's, `STAMP` (*Stochastic Transient Analysis Multi-detector Pipeline*) was developed to search for long-lived, unmodelled GW signals emitted by known GRBs [123]. The search relied on an excess cross-power statistic that is computed by cross-correlating data streams from two different detectors. Later on, a modified version, `STAMP-AS`, was implemented to perform all-sky / all-time searches [124]. This type of search is performed over a whole observing run (months or year-long) and without assumption on the sky location of the source.

Unmodelled all-sky / all-time searches are computationally expensive because of the vast amount of data to analyze and the large parameter space to cover. Consequently, `STAMP-AS` has several limitations that makes it suboptimal. Notably, it has to sacrifice sensitivity in order to keep the computing speed reasonable. When I inherited the pipeline at the beginning of my thesis, I was charged with the development of new features to address these limitations. Because the `STAMP-AS` code had become difficult to maintain and modify over time, I decided to re-write the software from scratch and developed the `PySTAMPAS` pipeline. In this section, I describe the search algorithm that is used in `PySTAMPAS`. It is still based on the `STAMP` formalism - cross-correlation of two detectors data streams, but implements several new features designed to reduce computional cost and increase sensitivity.

3.2.1 Time-frequency analysis

Principle

We are looking for signals of duration $T \sim 10^1 - 10^3\,\mathrm{s}$ whose frequency lies in the sensitive band of the detectors, i.e $20\,\mathrm{Hz} \lesssim f \lesssim 2000\,\mathrm{Hz}$. The unknown duration and frequency evolution leads us to consider *time-frequency* analysis.

A signal $s(t)$ can be represented in the frequency domain by its Fourier transform

$$\tilde{s}(f) = \int_{-\infty}^{+\infty} s(t) e^{-2i\pi f t} dt. \tag{3.9}$$

This representation would be appropriate if we searched for purely monochromatic signals, or signals of very long duration (orders of magnitude longer than the observing time). A time-frequency representation offers a compromise between time and frequency resolution. The principle is to

divide the total observing time $T_{\rm obs}$ into N smaller segments of duration T, and compute a frequency representation of the data for each of the segments. In general, the signal can be decomposed on any set of orthogonal, square-integrable functions. This is the paradigm of *wavelet decomposition*.

The most simple time-frequency representation is given by the short-term Fourier transform. In this case, the signal in each segment is multiplied by a window function that is non zero only in the short segment of time considered, then the Fourier transform is computed. Formally, we can write

$$\tilde{s}_T(t;f) = \int_{-\infty}^{+\infty} w_T(t'-t)\, s(t') e^{-2i\pi f t'} dt'. \tag{3.10}$$

Here, and from now on, we will use the notation $t;$ to denote the time segment start time. A standard choice of window function $w(t)$ is the Hann window:

$$w(t) = \begin{cases} 2\cos^2(\pi t/T + \pi/2) & \text{if } 0 \leq t < T \\ 0 & \text{otherwise} \end{cases} \tag{3.11}$$

(the factor 2 comes from the normalization of the integral). In practice, the output strain of GW detectors is sampled at a frequency f_s. Each segment of length T contains $n_T = T f_s$ data samples $s_k(t;) = s(t + k/f_s)$. We will therefore compute the discrete Fourier transform (DFT)

$$\tilde{s}_T(t;f_j) = \sum_{k=0}^{n_T-1} w(kT/n_T)\, s_k(t;) e^{-2i\pi jk/n_T}. \tag{3.12}$$

The DFT gives access to frequencies between $-f_s/2$ and $f_s/2$ with a frequency resolution $df = f_s/n_T = 1/T$. Since the input signal is real-valued, we can consider only the values of $f_j = j f_s/n_T$ between 0 and $f_s/2$.

Additionally, we consider time segments that overlap by 50% in order not to lose information at the extremities of the Hann window, so the true number of time segments is $N = 2T_{\rm obs}/T$. The output of the process is then a set of $N \times n_T/2$ (complex) values of $\tilde{s}_T(t;f_j)$. It is useful to represent them in a 2-dimensional *time-frequency map* (tf-map) that shows the frequency evolution of the signal as a function of time.

PSD estimation

In our quest to build a detection statistic for unmodelled signals, we need an estimation of the noise PSD $S(f)$. This task is complicated in the case of GW detectors for two main reasons.

1. The actual noise from GW detectors is not purely Gaussian. It contains a lot of non-stationary features such as glitches or wandering spectral lines. These noise artifacts cannot be easily modelized, and may be mistaken for a signal.

2. It is not possible to separate *a priori* a signal from the noise, since we do not know the exact waveform of the signal searched. If the PSD is estimated on a sample of data that contains a signal, the latter may be factored into the PSD and not be accurately reconstructed.

In other words, the risks are to mistake a noise transient for a signal, and conversely, i.e to commit a type I or type II error. Because of those difficulties, there is not an optimal method to estimate the PSD: depending on the morphology of the signal searched and the type of noise artifacts present in the data, different methods may be appropriate.

Recall that the one-sided PSD $S(f)$ is twice the expectation value of the squared modulus of the Fourier transform of the noise:

$$S(f) = 2\left\langle |\tilde{n}(f)|^2 \right\rangle, \text{ for } f > 0. \tag{3.13}$$

For a time-frequency pixel $\tilde{s}(t;f)$, we can write

$$\begin{aligned}\langle|\tilde{s}(t;f)|^2\rangle &= \langle|\tilde{h}(t;f)+\tilde{n}(t;f)|^2\rangle \\ &= \langle|\tilde{h}(t;f)|^2\rangle + \frac{1}{2}S(t;f),\end{aligned} \tag{3.14}$$

assuming that signal and noise are uncorrelated ($\langle\tilde{h}^\star(t;f)\,\tilde{n}(t;f)\rangle = 0$). Therefore, we need a way to estimate

$$\frac{1}{2}S(t;f) = \langle|\tilde{s}(t;f)|^2\rangle - \langle|\tilde{h}(t;f)|^2\rangle. \tag{3.15}$$

It is clear that we have to make (at least implicitly) an assumption on the nature of the signal $\tilde{h}(t;f)$ to estimate $S(f)$. In `PySTAMPAS`, I implemented two PSD estimation methods adapted to different types of signals.

The first one, inherited from `STAMP`, consists of taking the average of $|\tilde{s}(t;f)|^2$ over a given number n_t of neighbouring time segments. Given that time segments have 50% overlap and a Hann window is applied, this method is equivalent to the well-known Welch's method [125]. We will note

$$P^{ta}(t;f) = 2\,\overline{|\tilde{s}(t;f)|^2} \tag{3.16}$$

where the overline denotes the average over the n_t adjacent time segments. The implicit assumptions of this method are

1. the noise is stationary over the period of time considered;
2. no signal is present in the adjacent time segments.

The stationary assumption is valid in most cases for the Gaussian component of the noise. The PSD may vary over time, but usually over time periods much longer than the ones considered in transient searches, except at low frequency ($< 100\,\mathrm{Hz}$), where anthropogenic noise, seismic noise and scattered light can deter the detector's sensitivity. Besides, short glitches that are often present in the data are not taken into account by this method and therefore appear as signal. Regarding the second assumption, it is true for most signals excepted monochromatic or quasi-monochromatic signals. Such signals will be factored in the PSD if their duration is greater than the segment of time over which the PSD is averaged, and therefore not be reconstructed.

With these limitations in mind, I implemented another PSD estimation method whose characteristics are opposite to the ones of the time-average method. The average is replaced by the median, which is more robust against extreme values. Besides, instead of considering neighbouring time segments, we consider neighbouring frequency bins. This provides two advantages. Short glitches, which usually have a large bandwidth, are now factored in the PSD and are not reconstructed as signal. On the contrary, monochromatic signals are much better reconstructed. The main drawback of this method is that spectral lines that are present in the detector's noise are also enhanced. Additionally, signals covering wide-ranging frequency band are poorly reconstructed.

The optimal choice of a PSD estimation method depends on the type of signals targeted. `PySTAMPAS` implements these two complementary methods that may be adapted to a particular search. We show in Figure 3.1 that both methods provide an accurate estimation of the PSD, excepted that spectral lines are less well reconstructed with the frequency-median method. Once the PSD $P(t;f)$ is estimated - using either method - we compute the whitened statistic

$$\boxed{\tilde{y}(t;f) = \frac{\tilde{s}(t;f)}{\sqrt{P(t;f)}}} \tag{3.17}$$

which is the basic pixel statistic for our analysis. Assuming that the noise is Gaussian, the distribution of $|\tilde{y}(t;f)|^2$ should follow a χ^2 law with two degrees of freedom. We verify this result in Figure 3.2.

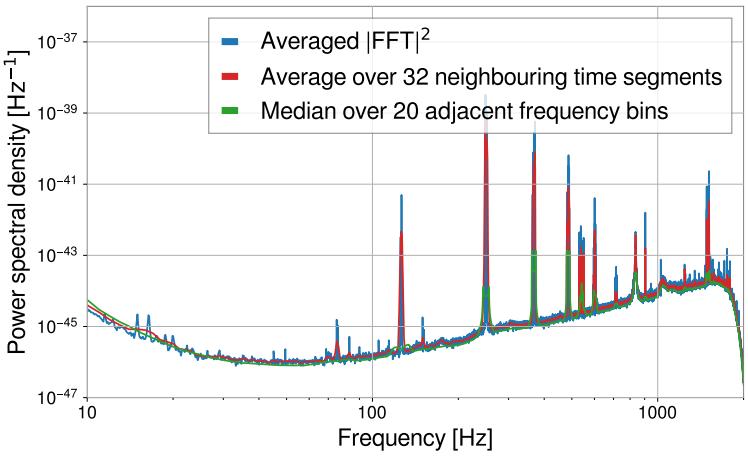

Figure 3.1: Estimation of the PSD for a 100 s long segment of LIGO H1 data from the O2 observing run using the two different methods. The 10 times averaged square modulus of the Fourier transform is shown in blue for reference.

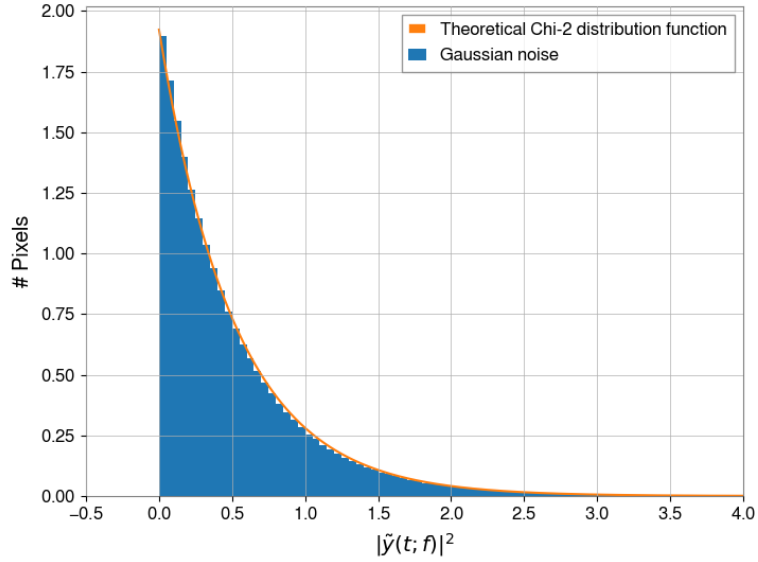

Figure 3.2: Distribution of $|\tilde{y}(t;f)|^2$ for a tf-map built from colored Gaussian noise. The distribution matches closely a χ^2 distribution with two degrees of freedom and a standard deviation $\sigma = 0.5$.

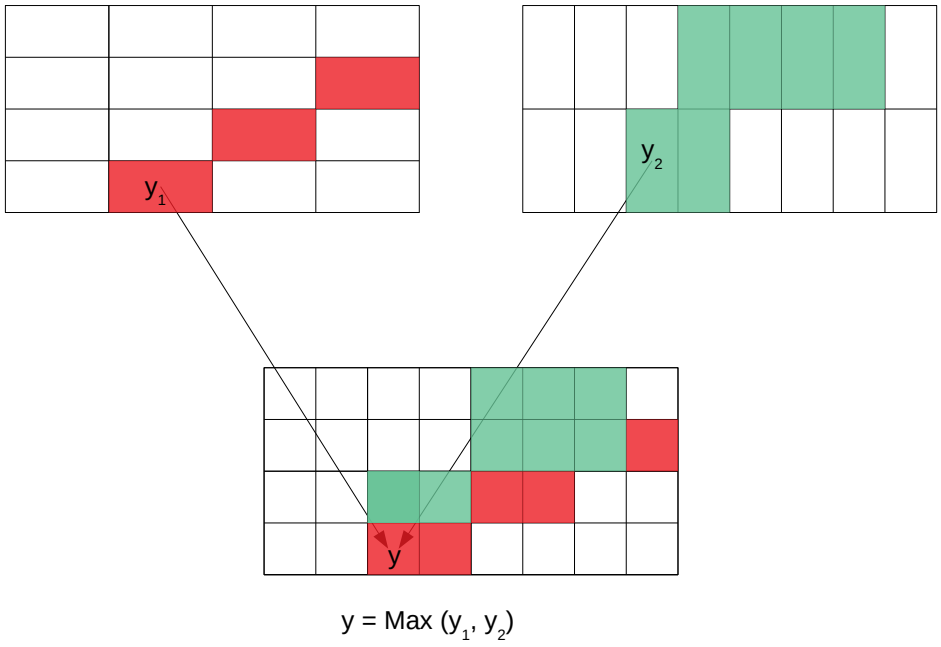

Figure 3.3: Illustration of the method used to combine tf-maps of different resolutions into a single tf-map.

Multi-resolution

We saw that the time and frequency resolutions of tf-maps are linked: $df = 1/T$. High temporal resolution leads to low frequency resolution and conversely. Therefore, the question arises of the choice of the time-frequency resolution. Depending on the duration and spectral evolution of the signal searched, one would like to favor either a good time-resolution (small T, large df) or the contrary. To put it more quantitatively, if a GW signal has a typical frequency evolution rate $\partial f/\partial t$, a good choice of resolution would be one such that $df/T \sim \partial f/\partial t$, so $T \sim (\partial f/\partial t)^{-1/2}$. The `STAMP` pipeline uses a time-frequency resolution of $1\,\mathrm{s} \times 1\,\mathrm{Hz}$ as a compromise. In order to improve signal reconstruction, I implemented a multi-resolution tf-map which combines several time-frequency resolutions.

The algorithm used to build multi-resolution tf-maps is explained in Figure 3.3. To begin with, we choose a set of resolutions $\{T_i \times df_i\}$ and build a tf-map of the data for each resolution. We then define virtual pixels of dimension $\min T_i \times \min df_i$. Each virtual pixel is covered by one pixel of each resolution. We assign to it the value of $\tilde{y}(t;f)$ that corresponds to the largest value of $|\tilde{y}(t;f)|$ among each resolution. An example of a multi-resolution tf-map for a BNS (BNS) merger simulated signal is shown in Figure 3.4. We can see how the first part of the signal is better reconstructed with low time-resolution pixels, while on the contrary the chirping part is reconstructed with high time-resolution pixels. The use of multi-resolution increases the number of pixels in a tf-map, and consequently the computing time needed to build the maps. Yet, this improvement is allowed by the gains in computational cost made by rewriting the pipeline.

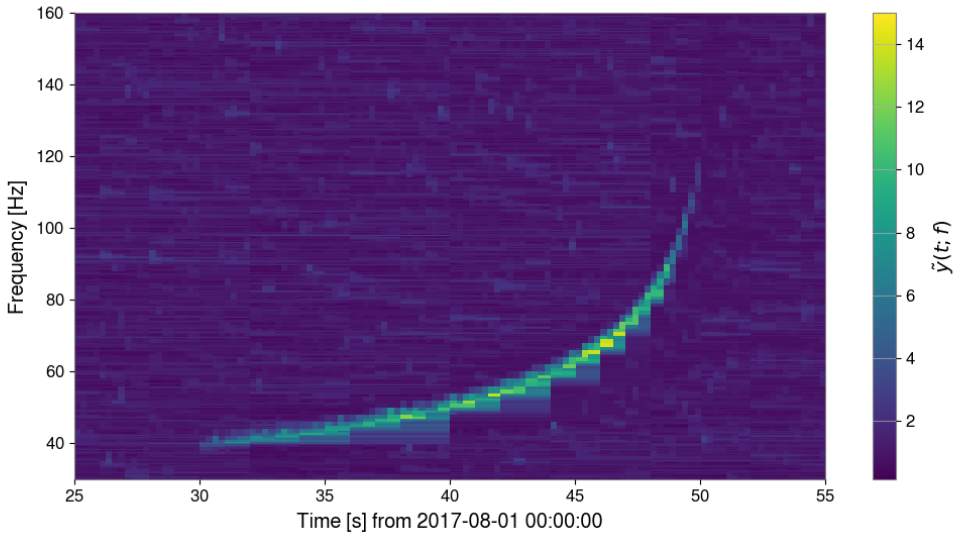

Figure 3.4: An example of a multi-resolution tf-map built from a time series made of colored Gaussian noise and a simulated GW signal from a BNS merger. The map combines 6 time-frequency resolutions ($0.5 - 1 - 2 - 4 - 8 - 16$ s). PSD is estimated using the frequency-median method with a window of 20 Hz.

3.2.2 Clustering algorithm

The typical expected signature of a long-lived GW signal in a tf-map is a cluster of excess power pixels, as can be seen in Figure 3.4. One of the main challenges of the search is to identify and regroup the pixels that contain the signal to reconstruct it accurately. This step is known as *clustering*.

Different strategies of clustering have been developed for long-duration searches, that can be divided into two categories. *Seed-based* clustering algorithms identify excess power pixels in a tf-map and try to group them by proximity. On the contrary, *seedless* algorithms make the assumption that the signal has a certain shape in a tf-map (e.g a family of curves) and try to fit it accordingly. These two strategies are complementary.

Burstegard

The `burstegard` clustering algorithm was initially developed for `STAMP` to extract signals of arbitrary shape in tf-maps [126]. It consists in the following steps.

1. Identify pixels with $|\tilde{y}(t; f)|$ above a given threshold in the map.
2. While pixels not belonging to any cluster remain:
   (a) select one pixel not belonging to any cluster as the cluster's seed. Define a clustering area around that seed.
   (b) Do:
      i. Add pixels that fall within the clustering area to the cluster.
      ii. Select another pixel of the cluster as the active seed, and continue to aggregate pixels.

   until all pixels in the cluster have been the active seed once and the cluster cannot grow anymore.

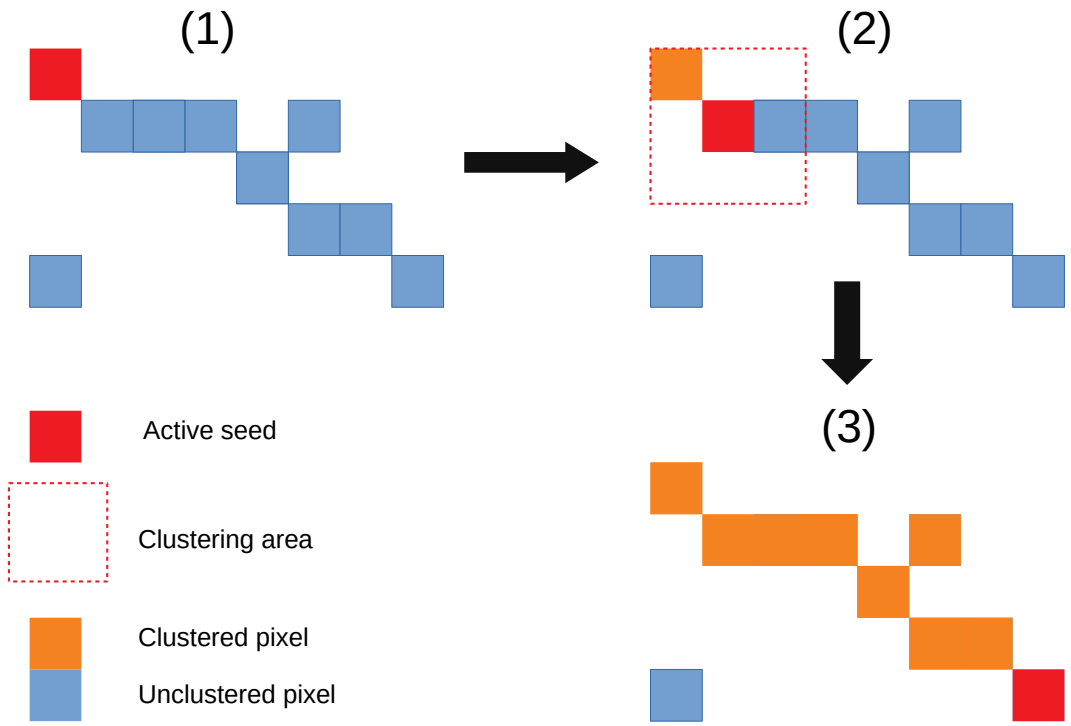

Figure 3.5: Illustration of the `burstegard` algorithm for a single cluster.

(c) If the number of pixels is greater than a given minimal number, save the cluster.

An illustration of the clustering process is shown in Figure 3.5. The algorithm has 4 free parameters:

- the threshold on the value of $|\tilde{y}(t;f)|$;
- the clustering radii in the time and frequency directions;
- the minimal number of pixels per cluster.

These parameters can be tuned in order to be more or less sensitive to signal and noise fluctuations.

Stochtrack

Seedless algorithms have been developed following the idea that most long-lived GW signals have a track-like shape in a tf-map that can be fitted by a family of curves (e.g quadratic Bezier curves) [127]. The principle is to integrate the value of $|\tilde{y}(t;f)|$ along all the curves that can be drawn in the tf-map. The algorithm is the following:

1. try a random curve:
   (a) Select three random points in the tf-map and build the associated Bezier curve.
   (b) Collect all pixels that overlap the curve. They form a cluster Γ.
   (c) Compute the total energy $E = \sum_{t;f\in\Gamma} |\tilde{y}_I(t;f)|^2$ of the cluster.

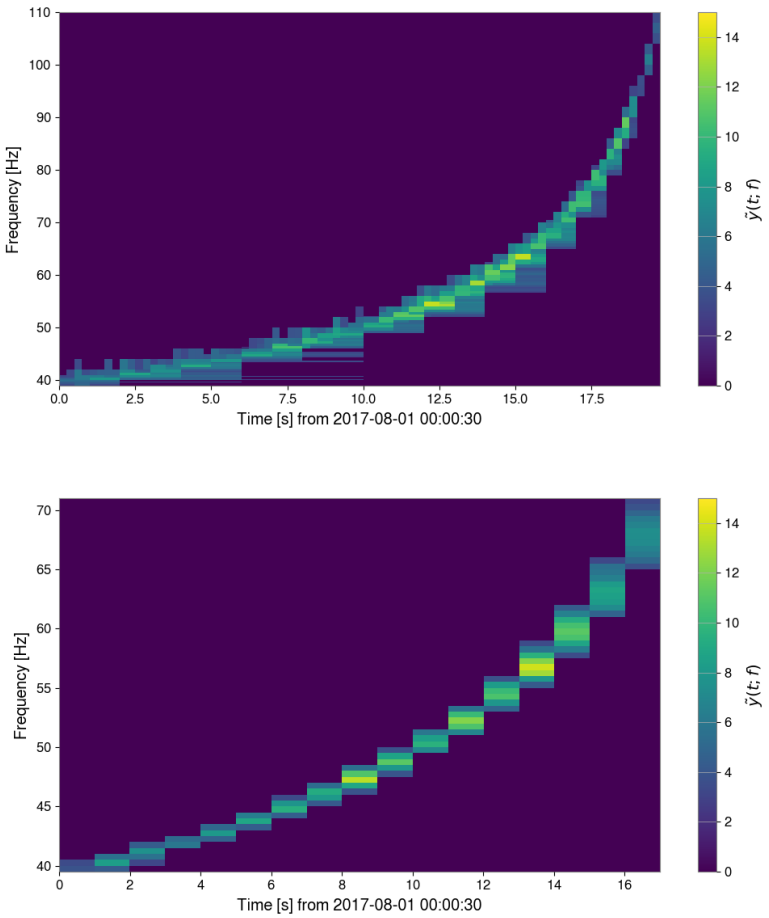

Figure 3.6: BNS merger signal from Figure 3.4 reconstructed with `burstegard` using a multi-resolution tf-map (top panel) and a single resolution tf-map of $1\,\mathrm{s} \times 1\,\mathrm{Hz}$ (bottom panel). The use of multi-resolution allows to better reconstruct the different parts of the signal, with higher frequency resolution at the beginning and higher time-resolution at the end.

2. Repeat the last step N_{tries} times and keep the cluster with the largest energy.

One of the main advantages of seedless algorithms over seed-based one is that they are not sensitive to many noise features. In addition, since no threshold is set on the energy of the pixels, they can be sensitive to long tracks of sub-threshold pixels that would not be seen by `burstegard`. However, by requiring signals to have a specific shape, `stochtrack` makes an assumption on the nature of the signal searched. Consequently, it is sensitive to a narrower range of signals than `burstegard`. More practically, the number of tracks to test in order to successfuly reconstruct a signal is $N_{\mathrm{tries}} \sim 10^7$, which makes this algorithm more expensive. Also, it is possible to parametrize the type of curve tested to be more or less sensitive to different types of signal, as it is done for searches for GW emitted by magnetars [128].

3.2.3 Coherent analysis

So far, our detection method consists in building tf-maps of the whitened statistic $\tilde{y}(t; f)$ from a given detector, then running a clustering algorithm to extract groups of pixels that form candidate GW events. In theory it would be possible to stop here, and build a detection statistic that reflects the significance of each cluster using only single-detector data. However this method would have serious limitations. When the signal searched is not known *a priori*, as it is the case

for un-modeled searches, one can only rely on the clusters' energy to distinguish signal from noise. Yet, real data from GW detectors feature all kinds of noise transients that can generate high energy clusters, making the method inapplicable in practice. Besides, to estimate the distribution of background noise events, one needs to analyze samples of data that do not contain any signal for sure. These constraints lead us to test the coherence of clusters in different detector data streams.

Coherent analysis consist in combining the data streams of several detectors to better discriminate signal from noise. Indeed, a true GW signal would theoretically induce a response in every detector that is observing at the same time (weighted by the detector's antenna factors and intrinsic sensitivity, and modulo the difference in arrival times), while noise from different detectors can safely be considered uncorrelated[2]. These properties allow to construct a much more robust detection statistic and to address the limitations of single-detector searches.

Estimator of the GW strain power

To begin with, let us consider a pair of detectors I and J and a GW signal $(h_+(t), h_\times(t))$ whose source's direction is given by the unit vector $\hat{\Omega}$. The responses induced in the detectors are

$$\begin{aligned}\tilde{h}_I(t;f) &= \sum_A F_I^A(t;\hat{\Omega})\,\tilde{h}_A(t;f) \\ \tilde{h}_J(t;f) &= \sum_A F_I^A(t;\hat{\Omega})\,\tilde{h}_A(t;f)\,e^{2i\pi f\hat{\Omega}\cdot\Delta\vec{x}_{IJ}/c},\end{aligned} \tag{3.18}$$

where the F_I^A are the antenna factors corresponding to each of the two polarization states $A \in \{+,\times\}$. The phase factor $e^{2i\pi f\hat{\Omega}\cdot\Delta\vec{x}_{IJ}/c}$ in detector J takes in consideration the delay of arrival of the signal $\tau = \hat{\Omega}\cdot\Delta\vec{x}_{IJ}/c$ with respect to the other detector, as explained in section 1.3.4. This time delay translates into a phase in the frequency domain[3]. Assuming that noise and signal are uncorrelated, the expectation value of the correlation product between the two detectors' output is

$$\begin{aligned}\langle\tilde{s}_I^\star(t;f)\tilde{s}_J(t;f)\rangle &= \langle\tilde{h}_I^\star(t;f)\tilde{h}_J(t;f)\rangle \\ &= \sum_{A,A'}\langle\tilde{h}_A^\star(t;f)\tilde{h}_{A'}(t;f)\rangle F_I^A(t;\hat{\Omega})F_J^{A'}(t;\hat{\Omega})e^{2i\pi f\tau}.\end{aligned} \tag{3.19}$$

To simplify this expression, we will assume that the GW is *unpolarized*, meaning that

$$\langle\tilde{h}_A^\star(t;f)\tilde{h}_{A'}(t;f)\rangle = \frac{1}{2}\delta_{AA'}\tilde{H}(t;f). \tag{3.20}$$

The quantity $\tilde{H}(t;f)$ is the unpolarized GW strain power spectrum that we want to estimate from the detectors' output. The assumption that the GW is unpolarized is not trivial. For example, the GW emission of a rotating non-axisymmetric ellipsoid or of a binary system are polarized, as we have seen in Chapter 1. Nevertheless, we will show that polarized signals are still well reconstructed under that approximation, because of the large degeneracy between the parameters. Furthermore, it allows to drop the polarization angle ψ and the inclination of the source ι from the computation of the estimator, which reduces considerably the size of the parameter space.

Under this simplification, following [123], we get

$$\langle\tilde{s}_I^\star(t;f)\tilde{s}_J(t;f)\rangle = \epsilon_{IJ}(t;f,\hat{\Omega})\tilde{H}(t;f)e^{2i\pi f\tau}, \tag{3.21}$$

[2]Global electromagnetic fields in the Earth's upper atmosphere could potentially be a source of correlated noise between spatially separated detectors, but they are far too weak to impact the type of search described in this work [129].

[3]Typical values of the time delay range in $\sim 10\,\text{ms}$, which is far shorter than the duration T of the time segments. Therefore the effect is seen only in the frequency domain, and not in the time domain.

with

$$\epsilon_{IJ}(t;\hat{\Omega}) = \frac{1}{2}\left(F_I^+(t;\hat{\Omega})F_J^+(t;\hat{\Omega}) + F_I^\times(t;\hat{\Omega})F_J^\times(t;\hat{\Omega})\right). \tag{3.22}$$

Therefore, the quantity

$$\hat{Y}(t;f,\hat{\Omega}) = \mathrm{Re}\left[\frac{1}{\epsilon_{IJ}(t;\hat{\Omega})} e^{-2\pi i f\tau}\, \tilde{s}_I^\star(t;f)\, \tilde{s}_J(t;f)\right] \tag{3.23}$$

is an estimator for $\tilde{H}(t;f)$:

$$\langle \hat{Y}(t;f,\hat{\Omega})\rangle = \tilde{H}(t;f) \tag{3.24}$$

Coherent SNR of a single pixel

It can be shown (see [123], appendix B) that an estimator for the variance of $\hat{Y}(t;f,\hat{\Omega})$ is

$$\hat{\sigma}_Y^2(t;f,\hat{\Omega}) = \frac{1}{|\epsilon_{IJ}(t;f,\hat{\Omega})|^2} P_I(t;f)P_J(t;f). \tag{3.25}$$

This allows us to define the coherent signal-to-noise ratio (SNR) of a single time-frequency pixel for the detector pair IJ:

$$\mathrm{SNR}^{IJ}(t;f,\hat{\Omega}) = \frac{\hat{Y}(t;f,\hat{\Omega})}{\hat{\sigma}_Y(t;f,\hat{\Omega})} = Re\left[2\,\tilde{y}_I^\star(t;f)\tilde{y}_J(t;f)e^{-2\pi i f\tau}\right]. \tag{3.26}$$

Note that this expression depends only on the whitened single-detector statistics $\tilde{y}_I(t;f)$ and the time delay τ of arrival of the GW between the detectors.

In the general case of a network of N detectors, there are $N(N-1)/2$ pairs over which to perform cross-correlation. We then define the total SNR

$$\mathrm{SNR}(t;f,\hat{\Omega}) = \sum_{I=1}^{N}\sum_{J>I} \mathrm{SNR}^{IJ}(t;f,\hat{\Omega}). \tag{3.27}$$

Coherent SNR of a cluster of pixels

In the previous stage of the analysis, clusters of pixels have been extracted from single-detector tf-maps. A cluster may be the signature of a true GW signal, or just corresponds to noise fluctuations in the detector. The goal is to build a detection statistic for a whole cluster to discriminate both cases, using the coherent SNR of pixels.

The coherent SNR given by Eq. (3.26) depends on the sky location of the source via the delay of arrival between the detectors. Since the primary focus of the pipeline is to perform *all-sky* searches, we need to consider all possible sky positions. Even when performing a targeted search, for example for a GW counterpart around a GRB, the sky location may not be precisely constrained, or it may be given within some error box. It is therefore interesting to work out how the coherent SNR is affected by an error in the sky location. For the sake of simplicity we will restrain ourselves to the case of a 2 detectors network for which there is only one baseline for cross-correlation.

We note $\hat{\Omega}_0$ the true direction to the source, such that

$$\mathrm{SNR}(t;f,\hat{\Omega}_0) = 2\,|\tilde{y}_I^\star(t;f)\tilde{y}_J(t;f)|. \tag{3.28}$$

An error $d\vec{\Omega}$ on the direction induces an error $d\tau = d\vec{\Omega}\cdot\Delta\vec{x}_{IJ}/c$ on the time delay. Therefore,

$$\mathrm{SNR}(t;f,\hat{\Omega}_0 + d\vec{\Omega}) = \cos(2\pi f d\tau)\,\mathrm{SNR}(t;f,\hat{\Omega}_0), \tag{3.29}$$

so the relative loss[4] of SNR is $\epsilon = \cos(2\pi f d\tau)$. We can then determine the maximal error on the delay $d\tau_{\max}$ such that the relative loss is less than ϵ:

$$d\tau_{\max} = \frac{\arccos \epsilon}{2\pi f}. \tag{3.30}$$

The angular maximal resolution $d\Omega_{\max}$ is

$$d\Omega_{\max} = \frac{c d\tau_{\max}}{\Delta x_{IJ}} = \frac{c \arccos \epsilon}{2\pi f \Delta x_{IJ}} \tag{3.31}$$

when $d\vec{\Omega}$ is parallel to $\Delta\vec{x}_{IJ}$. For the two LIGO detectors, $f \sim 100\,\mathrm{Hz}$ and $\epsilon = 0.95$, we get $d\Omega_{\max} \sim 120\,\mathrm{arcminute}$.

In an all-sky search, one needs to consider all sky positions (which reduces to the delay τ for a 2 detectors network) in order to maximize the SNR of the signal. From the previous result, we have to scan all the possible values of τ with a bin size $d\tau_{\max}$ to constrain the SNR loss to less than ϵ. Of course, such maximization does not make sense for a single pixel: we would just find the value of τ that compensates exactly the dephasing between $\tilde{y}_I(t;f)$ and $\tilde{y}_J(t;f)$. It is necessary to consider a cluster of several pixels to break the degeneracy. In practice, for a cluster Γ, we scan the values of τ to maximize the summed SNR

$$\mathrm{SNR}_\Gamma = \sum_{(t,f)\in\Gamma} \mathrm{SNR}(t;f,\tau). \tag{3.32}$$

Note that if the cluster is spread over several frequency bins, the value of $d\tau_{\max}$ is given by the maximal frequency $f_{\max}$ of the cluster's pixels.

From a computational point of view, we are interested in the number N_τ of values of τ to test for a given value of ϵ. For a pair of detectors IJ, possible values of τ range between $-\Delta x_{IJ}/c$ and $\Delta x_{IJ}/c$. Therefore, $N_\tau \simeq 2\Delta x_{IJ}/(c d\tau_{\max})$. However, it is possible to significantly reduce that number. Indeed, we are considering a phase factor, such that $\epsilon = \cos(2\pi f d\tau) = \cos(2\pi f(d\tau + 1/f))$. As a consequence, it is sufficient to test time delays in the interval $[0; 1/f]$ instead of $[-\Delta x_{IJ}/c, \Delta x_{IJ}/c]$ to get the correct phase factor. In the case of a broadband cluster with pixel frequencies between f_{min} and f_{max}, this interval is the largest for $f = f_{min}$, so we need to test time delay values between 0 and $1/f_{min}$ by steps of $d\tau_{\max} \simeq \frac{\arccos\epsilon}{2\pi f_{\max}}$. Finally, N_τ is reduced to

$$N_\tau \simeq \frac{2\pi}{\arccos\epsilon}\frac{f_{max}}{f_{min}}, \tag{3.33}$$

which remains rather small in practice (less than a few hundred). Since the computations are done only over the small subset of pixels that constitute the cluster, it is possible to test hundreds of time delays in a reasonable amount of time and therefore limit the loss of SNR to $\epsilon = 0.95$ for all type of signal.

The process is the same for a network of $N > 2$ detectors, excepted that we cannot rely on the degeneracy between $\hat{\Omega}$ and τ anymore because there are several baselines. We maximize the total summed SNR

$$\mathrm{SNR}_\Gamma = \sum_{I=1}^{N}\sum_{J>I}\sum_{(t,f)\in\Gamma} \mathrm{SNR}^{IJ}(t;f,\hat{\Omega}). \tag{3.34}$$

over N_Ω sky positions uniformly distributed over the sky. We will show in section 3.4 that it is still possible to reconstruct the signal accurately in that case with ~ 100 sky positions tested.

[4]Strictly speaking the SNR loss is $1-\epsilon$, but for convenience we use ϵ to quantify the SNR loss.

Detection statistic

Once we have found the sky position that maximizes SNR_Γ, we can finally build a detection statistic to test the hypothesis of a GW signal versus the null hypothesis. In this respect, SNR_Γ would be a natural candidate, since it is proportional to the signal's strength $\tilde{H}^2(t;f)$. It is in fact the one that is used in `STAMP-AS` and in the targeted version of `STAMP`.

However, the hierarchical method used in `PySTAMPAS` applied on real GW data tend to bias the selection of triggers because of the presence of noise outliers in one detector. When combined with noise fluctuation in the second detector, such triggers may have large SNR_Γ values despite being incoherent. This problem is exacerbated by the fact that we now test many more sky positions than with `STAMP-AS`, which may mechanically lead to larger value of SNR_Γ for noise triggers. This problem is not critical for seedless clustering, since noise features usually do not resemble Bezier curves and are consequently dismissed at the first stage of the analysis, but it is when using `burstegard` which extracts any cluster of excess power pixels no matter its spectral shape.

To counter this effect, we build an *ad hoc* detection statistic that aims to lower the significance of incoherent noise triggers. For each detector, we define the quantity

$$E_I^{res} \equiv \sum_{(t,f)\in\Gamma} |\mathrm{SNR}(t;f) - |\tilde{y}_I(t;f)|^2|. \tag{3.35}$$

It can be seen as the residual energy that is left in the detector's data after subtracting the sum of $|\tilde{y}_I(t;f)|^2$ to the coherent SNR, hence the "incoherent" component of the trigger.

If the trigger corresponds to a coherent GW signal, reconstructed with the right time delay, E_I^{res} is expected to be much smaller than both SNR_Γ and the auto-power energy E_I

$$E_I = \sum_{(t,f)\in\Gamma} |\tilde{y}_I(t;f)|^2. \tag{3.36}$$

In the ideal case of two identical detector with the same alignment and sensitivity, E_I^{res} should even tend to 0 for a true signal. On the contrary, for a noise trigger due to a noise feature in one detector, E_J^{res} in the second detector has no reason to be small. It should be at the order of magnitude of SNR_Γ. We can build the discriminant quantity

$$\Lambda = \frac{\mathrm{SNR}_\Gamma}{\mathrm{SNR}_\Gamma + \sum_I \frac{E_I^{res}}{E_I}}. \tag{3.37}$$

which should tend to 1 for a true GW signal. Since a detection statistic has to be monotone with the significance of the signal, we finally define

$$p_\Lambda = -\log(|1-\Lambda|) \tag{3.38}$$

to be the detection statistic for `PySTAMPAS`.

Summary

`PySTAMPAS` implements an enhanced version of the `STAMP` algorithm [123] which consists in computing a detection statistic based on the cross-correlated data streams between two detectors. The workflow of the analysis is presented in Figure 3.7. New features are implemented to improve signal reconstruction, such as the use of multi-resolution tf-maps and another method to estimate the PSD to better reconstruct quasi-monochromatic signals. In the next section, I describe the practical implementation of the pipeline and explain how it has been optimized for all-sky / all-time searches.

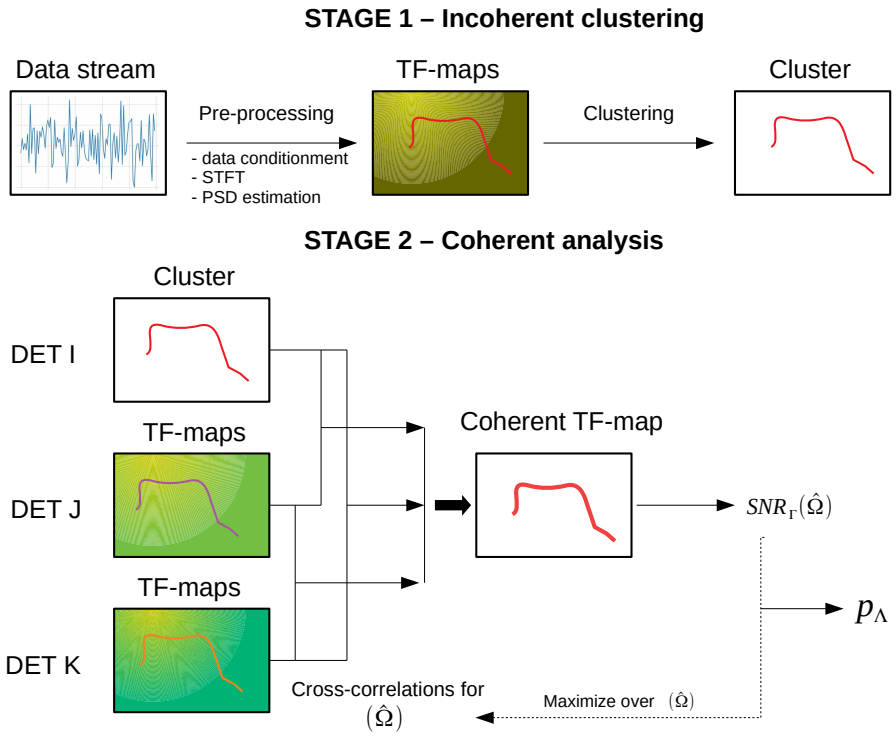

Figure 3.7: Workflow of the hierarchical search algorithm implemented in `PySTAMPAS`. In the first stage, a clustering algorithm is run on time-frequency maps built from single detector data stream. In the second stage, clusters are cross-correlated between detectors to build a coherent detection statistic efficient at detecting coherent excess of energy in a network of GW detectors.

3.3 Implementation of the pipeline

The implementation of the search method into an end to end data analysis software requires to manage several elements: data input/output, pre-processing of the data, allocation of computing resources, background estimation, post-processing of the final outputs, data quality information, user friendly interface, and many more. The bottlenecks of the code in term of computing resources have to be identified and optimized, and each feature must be tested and debugged. Hence the name pipeline for such a piece of software.

3.3.1 Motivation and overview

`STAMP` has been originally designed for targeted searches in which the sky position of the potential source is known. This allows to directly generate coherent tf-maps, and run the clustering algorithm only once on these tf-maps. To generalize the method to the case where the position of the source is unknown, `STAMP-AS` considers different sky positions and runs the whole process for each one. This is particularly costly because the clustering step must be performed again for each position tested, and the correlation product computed for the whole tf-map. In addition, the background distribution is estimated by time-shifting the data from one detector with respect to the other. For each time-slide, the whole process must be repeated. After few analyses of Advanced LIGO and Advanced Virgo data it became rather obvious that the computational cost is a limitation of `STAMP-AS`. It can take several months to search for a GW signal simulating a rather size-limited background dataset ($\sim$ 50 years of background) with only 5 sky positions

tested, leading to a certain loss of sensitivity.

To cope with the computational cost of background estimation, Thrane and Coughlin proposed a hierarchical method [130] that consists in running the clustering algorithm on single-detector tf-maps before computing the coherent statistic. This method was successfully applied to seedless clustering, allowing for rapid background estimation without sacrificing too much sensitivity. It is this method that is implemented in `PySTAMPAS` with seed-based clustering too.

In order to address the `STAMP-AS` issues and implement all the new features I decided to rewrite the pipeline from scratch implementing the method presented in section 3.2. As its name suggests, `PySTAMPAS` is written in Python. This choice of programming language has been driven by its simplicity and readability, and the fact that it is widely used within the LIGO-Virgo community and in general. The main drawback of python is its relative slowness with respect to compiled languages such as C++ and Fortran. However, there are many C-based libraries dedicated to scientific calculation and data analysis that allow to overcome this obstacle.

The core of `PySTAMPAS` is written in Python (3.6+) and makes extensive use of optimized scientific computing packages such as `Numpy` and `Scipy`, as well as the more GW-oriented package `GWpy` [131]. Some bottlenecks of the code are also written in Cython when it is needed to reach the performance of a compiled language.

3.3.2 Data pre-processing

Segments and windows

Data from GW detectors are available under the form of time series of the detector's strain output $s(t)$ sampled at frequency f_s (16384 Hz for Advanced LIGO and 20 kHz for Advanced Virgo). Time series are discontinuous. Some time periods are missing because of bad data quality, or just because the interferometers are not "locked". For each detector we get a list of time segments for which data are available.

Since we perform a coherent search over a network of detectors, we consider only segments of data that are coincident in every detector. Each coincident segment is then divided into windows of duration $T_{\text{win}} \sim 500\,\text{s}$ that overlap by 50%. Overlapping lowers the probability that a signal is split between two windows. Each window is then processed independently, allowing for distributed computing.

Frequency band

The PSD of ground based detectors increases steeply below $\sim 20\,\text{Hz}$ because it is difficult to design efficient seismic attenuators in low frequency regime. This sets a lower limit to the frequency band analyzed. To suppress energy at lower frequencies, we apply a high-pass filter to the data with a frequency cutoff corresponding to the lower bound of the frequency band analyzed (the exact value depends on the characteristics of the data that can vary for each observing run, it is usually between $20 - 30\,\text{Hz}$.)

The upper limit of the frequency band can be chosen more freely, and tuned according to the expected maximal frequency of the type of signals searched. It is generally set around 2000 Hz for long-duration all-sky searches [124, 132, 133]. Since the higher frequency content does not interest us, we resample the time series to $f_s = 4096\,\text{Hz}$.

In a real search, other methods of data conditioning may be applied to deal with non-Gaussian features of the noise. Since these are specific to the characteristics of each observing run, they will be discussed in the next chapters when we will discuss real data searches.

Time-frequency maps

Once the time series for a given window is correctly conditioned, time-frequency maps are built following the procedure described in section 3.2. To avoid any edge effect and ensure phase

continuity between consecutive windows, a buffer of a few seconds of data (typically 4 s) is taken on both sides of each window. The maps are either generated in advanced for the whole run and saved on disk, or built on-the-fly when requested by the analysis.

3.3.3 Coincident analysis

The coincident analysis is the step where true GW signals are searched in the data. The clustering algorithm is run on single detector tf-maps for each window of all detectors, and extracts a set of cluster Γ_I which is the result of cross-correlation computed following Eq. (3.34). Clusters are saved as tf-maps where only the selected pixels have non-zero value.

Note that in practice, the coincident analysis is performed last. In order to remain as ignorant as possible regarding the potential presence of a GW signal in the data, and to avoid biasing the analysis, we first analyze the background distribution and estimate the sensitivity of the search.

3.3.4 Background estimation

The statistical significance of a given trigger of statistic p_Λ is described by its false-alarm probability or p-value, which is the probability of observing at least one noise trigger with statistic equal or higher than p_Λ during the analysis[5].

To estimate this probability, we need to know the *false-alarm rate* (FAR), that is the rate of noise triggers. Assuming noise triggers are mutually independent, they should follow a Poisson distribution, so the false-alarm probability (FAP) associated to a given value of p_Λ is

$$\mathrm{FAP}(p_\Lambda) = 1 - e^{-\mathrm{FAR}(p_\Lambda)T_{\mathrm{obs}}} \tag{3.39}$$

where $\mathrm{FAR}(p_\Lambda)$ is the rate of noise triggers with statistic equal or higher than p_Λ and T_{obs} is the duration of the observation. If the noise was effectively Gaussian and stationary, the simplest way to estimate the distribution of background triggers would be to perform a Monte Carlo study over randomly generated Gaussian noise in each detector. However, for a real GW search, this would not work becuse of the contribution of the numerous noise artifacts in the data. That is why we need to empirically estimate the FAR by analyzing real detectors' data that do not contain GW signal.

It is not possible to remove the GW signal *a priori* from the data, since we do not know its waveform and when it arrives. However, since the analysis relies on the coherence of the data between detectors, it is possible to artificially screen the signal by shifting the data between the detectors by an amount of time greater than the estimated coherence time of a GW (and greater than the light time of flight between the detectors). Hence, even if a GW signal is present in the data, it will always be cross-correlated with noise in the other detectors, so the trigger will not have a high value of p_Λ. Commonly used in GW searches, the *time-slides* method [134] assumes data from at least 2 detectors are searched using coherence or a simple time-coincidence. By performing multiple time-slides with different time-shifts, it is possible to simulate several realisations of the noise and to reach lower values of FAR. This is a good approximation in the limit of low signal event counts.

The workflow of a background analysis for an all-sky search is represented in Figure 3.8. The data set is composed of several coincident segments of data that account for a total duration T_{obs}. It is splitted into N_{win} windows of duration T_{win} that overlap by 50%, such that $T_{obs} = T_{win}(N_{win}+1)/2$. A *lag* consists in shifting the data by a given amount of windows: at the nth lag, window i from detector I is matched with detector J window $i+2n+o_J$, detector K window $i+2(n+1)+o_K$ and so on. The values o_J and o_K are integer numbers that allow to define an offset for each detector, in order to ensure that coincident data are never processed during

[5]The p-value cannot be interpreted as the probability $P(H_0|p_\Lambda)$ of the trigger being a noise trigger. It is rather the likelihood of obtaining p_Λ under the null hypothesis, i.e $P(p_\Lambda|H_0)$.

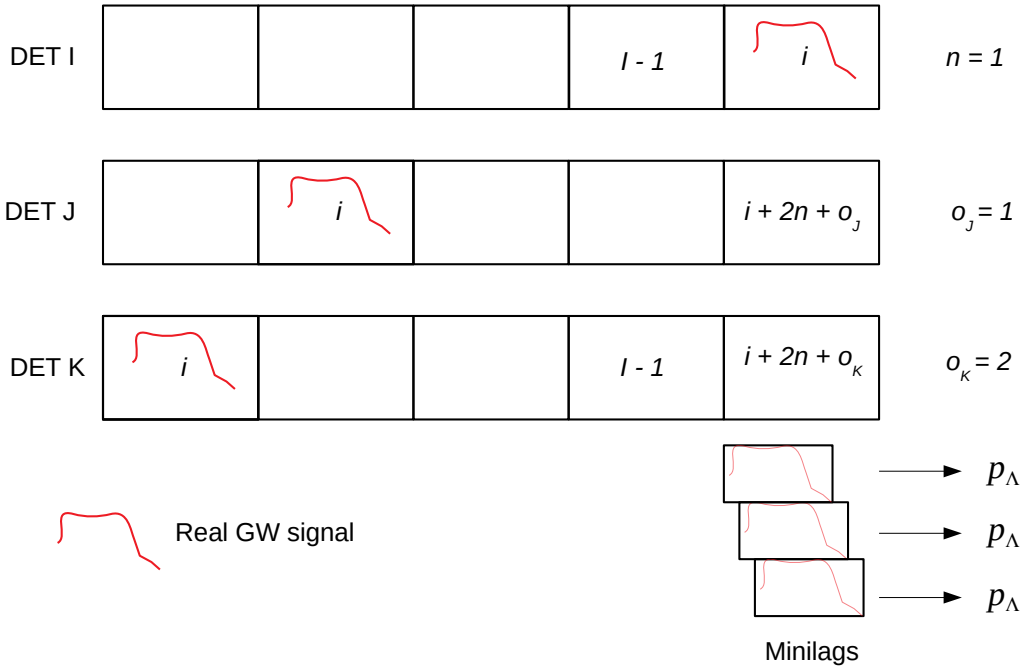

Figure 3.8: Illustration of the way `PySTAMPAS` performs time-slides for the lag $n = 1$, with offsets $o_J = 1$ and $o_K = 2$. In this example, a GW signal is present in window i in all detectors. The cluster extracted from window i in detector I is matched with pixels from window $i+3$ in detector J and $i + 4$ in detector K, ensuring that the signal is not coherent. In addition, 3 minilags are performed for this cluster. For the sake of clarity, overlap between maps is not represented here.

background estimation. Lags are done circularly over the whole run (index of lag windows is computed modulo N_{win}), so the maximal number of lags N_{lags} that can be done is $N_{win}/2$.

In practice, clusters of pixels have already been extracted and saved prior to shifting the data (the interest of that method is precisely to avoid running the clustering step again for each lag). For a given lag, we select the clusters that have been extracted from each detector in the windows selected (i.e window i for detector I, window $i + 2n + o_J$ for detector J and so on), and build a coherent trigger for each of them. To further increase the amount of background simulated, we add the possibility to do *minilags*. When a cluster is processed, a minilag consists in shifting circularly the time axis of the tf-maps in the other detectors by an amount of time greater than the expected coherence time of a signal. For example, doing minilags of 16 s over 512 s tf-maps allows to multiply the amount of background computed by 32.

By performing N_{lags} lags over a full observing run of duration T_{obs}, and n minilags per lag, we simulate an equivalent amount of background

$$T_{bkg} = T_{obs} N_{lags} n. \tag{3.40}$$

The false-alarm rate for a given value $p^\star_\Lambda$ of p_Λ is the number of background triggers that have $p_\Lambda \geq p^\star_\Lambda$, divided by the total background time T_{bkg}:

$$\mathrm{FAR}(p^\star_\Lambda) = \frac{N(p_\Lambda \geq p^\star_\Lambda)}{T_{bkg}}. \tag{3.41}$$

The time-slides method is very useful, since it allows to simulate a vast amount of background data while preserving the non-Gaussian features of the noise. It has however some limitations. In practice, the assumption that noise triggers follow a Poisson distribution may not be true, precisely because of these non-Gaussian features. The rate of noise triggers may vary with time because of instrumental and environmental effects, as we will see in the next chapter when analyzing real data. This may lead to underestimate or overestimate the false-alarm rate if a "calm" period of data in one detector is matched with a noisy period in another one. Besides, in our case, the fact that clusters are selected on single-detector data tends to bias the background analysis towards loud noise transients. Once again, we will see with real data that it is sometimes necessary to develop selection criteria to reject those events in post-processing.

3.3.5 Efficiency estimation

To fully characterize an analysis, we need to estimate the sensitivity of the search, i.e the probability to detect a true GW signal with a false-alarm probability lower than a given threshold. Since we do not know a priori the exact shape of the signals searched, the only way to proceed is to manually inject simulated signals into the data and try to characterize how well they are recovered. Injected signals should be chosen to cover the parameter space of the search in duration, frequency and spectral morphology.

Simulated signals - *waveforms* - consist in two time series describing the two polarization modes $(h_+(t), h_\times(t))$ of the GW, sampled at frequency f_s. In practice, metadata about the signal (duration, frequency range, nominal distance...) are also stored by the pipeline. To simulate a realistic GW signal, several parameters must be defined:

- the direction $\hat{\Omega}$ to the source;
- the time of arrival t_0 of the signal at the center of the Earth (which serves as a reference);
- the inclination and polarization angles ι and ψ that characterize the orientation of the source's reference frame with respect to the Earth equatorial frame;
- a scaling amplitude factor α to set the strength of the signal.

Initial polarization modes are given in the source frame. They must be rotated and expressed in the Earth equatorial frame via the polarization angle ψ and the inclination angle ι:

$$\begin{aligned} h_+^{\mathrm{eq}}(t) &= a_+ \cos 2\psi \, h_+(t) - a_\times \sin 2\psi \, h_\times(t) \\ h_\times^{\mathrm{eq}}(t) &= a_+ \sin 2\psi \, h_+(t) + a_\times \cos 2\psi \, h_\times(t) \end{aligned} \tag{3.42}$$

where $a_+ = \frac{1+\cos\iota^2}{2}$ and $a_\times = \cos\iota$. The delay of arrival between the detector's position $\vec{r}_I$ and the center of the Earth is

$$\tau_I = \frac{\hat{\Omega} \cdot \vec{r}_I}{c}. \tag{3.43}$$

The data are time shifted accordingly to reflect that delay. Antenna pattern factors $F_I^+(t;\hat{\Omega})$ and $F_I^\times(t;\hat{\Omega})$ are first computed in the Earth equatorial frame as a function of $\hat{\Omega}$ and the sidereal time and then adapted to each detector position on Earth.

Finally, the response of the detector is

$$h_I(t) = \alpha \, [F_I^+(t;\hat{\Omega}) \, h_+^{\mathrm{eq}}(t-\tau_I) + F_I^\times(t;\hat{\Omega}) \, h_\times^{\mathrm{eq}}(t-\tau_I)]. \tag{3.44}$$

It is resampled and interpolated to match with the detector's sampling and the first and last seconds are tapered with a Hann window to avoid numerical artifacts.

Signals are injected for different values of α which correspond to different amplitudes (or equivalently distance). For each waveform and each amplitude factor, a number N_{inj} of injections

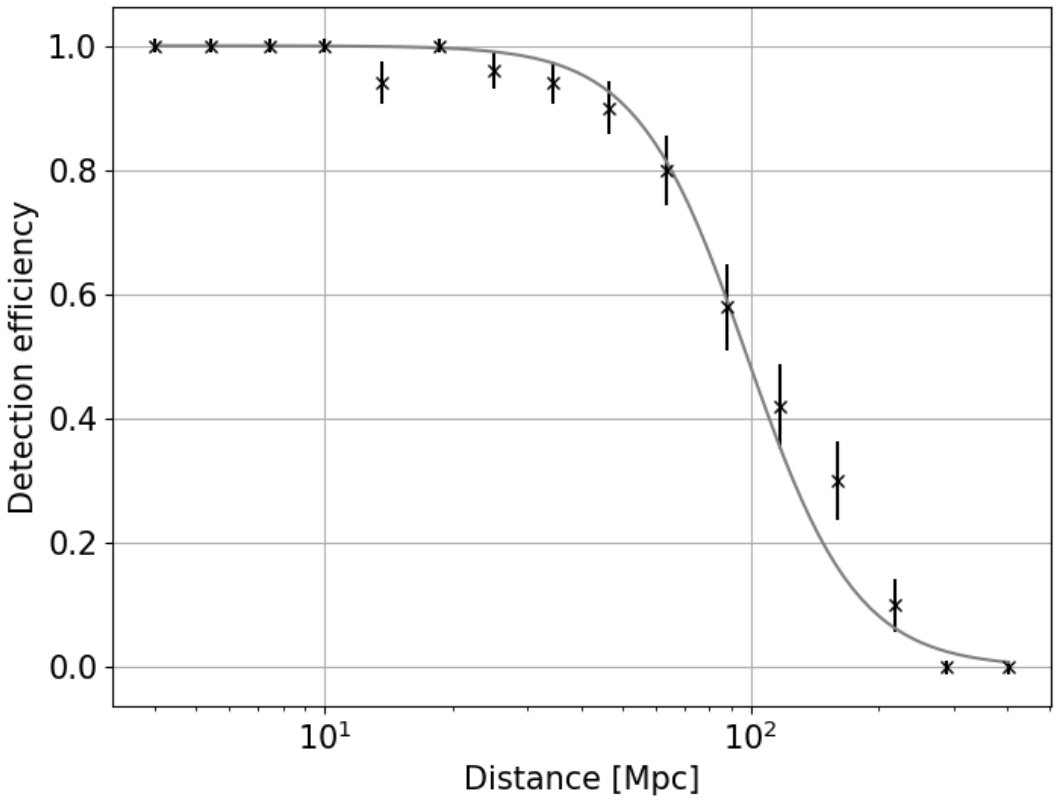

Figure 3.9: Detection efficiency as a function of distance for an accretion disk instability signal (ADI-B, see Table 3.1) added to Gaussian noise colored with LIGO O2 PSD. Error bars at 1σ are computed from Eq. (3.48) for $N_{\rm inj} = 50$.

are performed with random parameters (sky position, arrival time polarization and inclination angles) to get a sufficient statistic. We then compute the ratio of recovered injections $N_{\rm rec}$ over $N_{\rm inj}$ to get an estimation of the detection efficiency:

$$\mathrm{Eff}(\alpha) = \frac{N_{\rm rec}}{N_{\rm inj}}. \tag{3.45}$$

This process is repeated for different amplitude factors to characterize the detection efficiency as a function of the signal's strength.

Several quantities can be used to characterize the strength of a GW signal. One that is commonly used is the *root summed square amplitude* $h_{\rm rss}$ which is defined by

$$h_{\rm rss} = \sqrt{\int \left[h_+^2(t) + h_\times^2(t)\right]\, dt}. \tag{3.46}$$

This quantity is useful because GW detectors are sensitive to the amplitude of the signal: the $h_{\rm rss}$ has the same unit than the detector's amplitude spectral density, allowing for rapid comparison between the two. It is convenient to express the sensitivity of the search to a given signal with a single number. Long duration searches commonly use the value of $h_{\rm rss}$ for which the efficiency is 50%. It is obtained by fitting a sigmoid curve to the data, as can be seen in Figure 3.9.

The error on $\mathrm{Eff}(\alpha)$ are computed assuming that the probability to recover $N_{\rm rec}$ injections while we expect $\hat{\mathrm{Eff}} \times N_{\rm inj}$ injections is given by a binomial probability

Waveform	Parameters	Duration [s]	Frequency [Hz]	Morphology
ECBC-A	$M_1 = 1.4$, $M_2 = 1.4$, $ecc = 0.2$	291	10 - 250	Chirp
ECBC-B	$M_1 = 1.4$, $M_2 = 1.4$, $ecc = 0.4$	178	10 - 275	-
ECBC-C	$M_1 = 1.4$, $M_2 = 1.4$, $ecc = 0.6$	64	10 - 350	-
ECBC-D	$M_1 = 3.0$, $M_2 = 3.0$, $ecc = 0.2$	81	10 - 180	-
ECBC-E	$M_1 = 3.0$, $M_2 = 3.0$, $ecc = 0.4$	49	10 - 200	-
ECBC-F	$M_1 = 3.0$, $M_2 = 3.0$, $ecc = 0.6$	15	10 - 200	-
ISCOchirp-A	$m_{BH} = 5.0$	237	1049-2048	Broadband chirp-down
ISCOchirp-B	$m_{BH} = 10.0$	237	705 - 2048	-
ISCOchirp-C	$m_{BH} = 20.0$	236	196 - 1545	-
ADI-A	$m_{BH} = 5.0$, $a_{BH} = 0.3$	35	135 - 166	Chirp-down
ADI-B	$m_{BH} = 10.0$, $a_{BH} = 0.95$	9	110 - 209	-
SG-C		243	402-408	Mono-chromatic
WNB-A		20	50-400	Band limited white noise

Table 3.1: Name, source parameters, duration, frequency range and spectral morphology of waveforms used to characterize `PySTAMPAS`.M_i is the component compact object mass; *ecc* is the eccentricity of the binary orbit at 10 Hz; M_{BH} and a_{BH} are the mass and normalized spin of the black hole. All masses are expressed in unit of $M_\odot$.

$$p(N_{\rm rec}|\hat{\rm Eff}, N_{\rm inj}) = \frac{N_{\rm inj}!}{N_{\rm rec}!(N_{\rm inj}-N_{\rm rec})!}\hat{\rm Eff}^{N_{\rm rec}}(1-\hat{\rm Eff})^{N_{\rm inj}-N_{\rm rec}} \tag{3.47}$$

The error on the measured $\mathrm{Eff}(\alpha)$ is then given by the Bayes' theorem

$$p({\rm Eff}|N_{\rm rec}, N_{\rm inj}) = \frac{p(N_{\rm rec}|\hat{\rm Eff}, N_{\rm inj})p(\hat{\rm Eff}|N_{\rm inj})}{\mathcal{Z}} \tag{3.48}$$

We will consider that $p(\hat{\rm Eff}|N_{\rm inj})$ is constant as there is no reason to favor any particular $\hat{\rm Eff}$ value over another. The overall constant factor $\mathcal{Z}$ is determined by integrating Eq. (3.48). We finally obtain

$$p({\rm Eff}|N_{\rm rec}, N_{\rm inj}) = \frac{\Gamma(N_{\rm inj}+2)}{\Gamma(N_{\rm rec}+1)\Gamma(N_{\rm inj}-N_{\rm rec}+1)}{\rm Eff}^{N_{\rm rec}}(1-{\rm Eff})^{N_{\rm inj}-N_{\rm rec}} \tag{3.49}$$

where $\Gamma(N)$ is the gamma function defined by $\Gamma(N+1) = N!$. The 1σ confidence interval is computed by numerical integration of $p(\mathrm{Eff}|N_{\rm rec}, N_{\rm inj})$.

3.4 Performances and optimization

We now have a complete pipeline, which is able to search for coherent GW signals in a network of detectors, with background estimation and injection campaign. In this section, I present the work I did to test, optimize and characterize the pipeline to make it ready for real data analyses.

To characterize the pipeline, we use a set of simulated signals whose main properties are described in Table 3.1. They cover a large range of the parameter space in duration, frequency and spectral morphology and come from astrophysical and generic models. Waveforms labeled ECBC represent the inspiral-merger-ringdown GW emission of nonspinning eccentric compact binary coalescences [70]. The ISCOchirp family models broadband chirps from innermost stable circular orbit waves around rotating blackholes [85], and ADI are accretion disk instabilities models from [135]. In addition, we also use a sine Gaussian signal (SG-C) and a band limited white noise burst (WNB-A) to extend the coverage of the parameter space.

3.4.1 Tuning of the parameters

The pipeline has a variety of free parameters that have to be defined by the user before performing a search.

Windows duration

The duration of windows fixes the maximal duration of signal we are able to reconstruct. Following the choice of past Advanced LIGO/Advanced Virgo long duration searches, we fix the duration of windows to 512 s (we choose a power of 2 to be able to easily divide a map when performing minilags). GW transients with duration $>>$ 512 s may exist, but given the current sensitivity of the instruments, it is very unlikely that they could be reconstructed in their entire duration using a method based on excess power in time frequency maps. Besides, continuous wave methods may be more adapted to search for such very long signals. As previously said, consecutive windows overlap by 50% in order not to split a signal between two windows.

Time-frequency resolutions and clustering

When using the hierarchical method, the incoherent part of the analysis is of great importance because it is at this stage that clusters of pixels that constitute the candidate events are extracted. If a GW signal is not or poorly reconstructed, it will be irremediably lost whatever happens in the coherent stage. That is why a particular attention must be given to signal reconstruction in single-detector tf-maps.

In that spirit, we would like to tune the parameters to optimize signal reconstruction at the first stage of the analysis, while keeping computational cost affordable. The main parameters to tune are the time-frequency resolutions of the tf-maps, the clustering threshold and radii and the minimal number of pixels in a cluster. It is however not possible to do a systematic optimization of all the parameters because of the variety of signals targeted. In theory, it would be possible to choose one particular waveform and tune the parameters to maximize detection efficiency for that waveform, but this would introduce a bias in the analysis, effectively favoring one particular class of signal with no guarantee that such an optimization holds for another type of waveform. For this reason, I had to rely on semi-quantitative arguments, and proceeded by trial and error to finally converge towards a reasonable set of parameters.

Since we are targeting long-duration signals, we expect a potential signal to be spread over a large number of pixels, with a small excess power per pixel. Therefore, it is appropriate to choose a relatively low threshold on the individual pixel's energy $|\tilde{y}_I(t;f)|$ for clustering. The drawback is that it increases the number N of pixels to consider while clustering, which can rapidly become computationally expensive given that `burstegard`'s time complexity is $\mathcal{O}(N \log N)$. However, since that step is computed only once per tf-map, it is possible to select a threshold much lower that what would be possible without using the hierarchical approach. I found that a threshold between $1.6 - 2$ over $|\tilde{y}_I(t;f)|$ is generally appropriate. This leads to select $2 - 5\%$ of the loudest pixels of a tf-map (in the Gaussian noise case). For most signals, setting an even lower threshold does not seem to improve signal reconstruction and brings a lot of noise pixels to the reconstructed cluster. The same argument applies for the clustering radius, that fixes the clustering area around a seed pixel. A too large value for this parameter may lead to contaminate a signal with noise pixels that aggregate the main cluster. An illustration of this behaviour is shown in Figure 3.10, with a too low threshold and a too large radius. I found that a clustering area of $1\,\mathrm{s} \times 1\,\mathrm{Hz}$ is appropriate for many GW waveforms tested.

In this configuration, the minimal number of pixels per cluster can be used as a parameter to control the rate of noise clusters that are generated. It depends strongly on the number of time-frequency resolutions used, since the combination can make pixels overlap. The more resolutions, the more pixels in a cluster in average. For a set of 4 different resolutions, values between $30 - 80$ are optimal for this parameter.

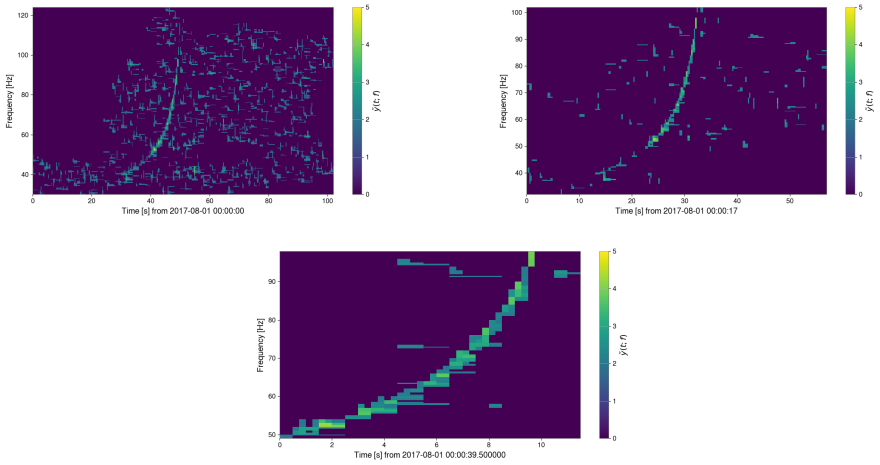

Figure 3.10: Time-frequency maps of a faint BNS merger signal reconstructed with `burstegard` for different sets of clustering parameters. For the top figure, the clustering threshold is set to 1.5 and the clustering radius to $1\,\mathrm{s} \times 1\,\mathrm{Hz}$. The middle figure is made with a threshold of 2 and radius of $3\,\mathrm{s} \times 3\,\mathrm{Hz}$. In both cases, the signal is polluted by noise pixels that have been aggregated to main cluster. The bottom figure shows the cluster obtained with a threshold of 2 and radius of $1\,\mathrm{s} \times 1\,\mathrm{Hz}$. It is an acceptable compromise that allows to reconstruct the signal without adding too much noise pixels to it.

Regarding the time-frequency resolutions, the best choice depends once again on signal morphology. We have seen however that a limited number of resolutions is enough to improve the detection efficiency of non-monochromatic GW signals. Using a set of 4 resolutions ranging from $4\,\mathrm{s} \times 0.25\,\mathrm{Hz}$ to $0.5\,\mathrm{s} \times 2\,\mathrm{Hz}$, we showed that detection efficiency increases by $5 - 40\%$ (at constant FAR), compared to $1\,\mathrm{s} \times 1\,\mathrm{Hz}$ pixels for the waveforms described in Table 3.1. Signals that benefit the most from multi-resolution are those with non-linear frequency evolution, e.g a BNS coalescence signal, which is quasi-monochromatic when its enter the detector's bandwith at the end of the inspiral, before rapidly increasing in frequency before the merger. The effect of multi-resolution on the reconstruction of a BNS signal can be seen in Figure 3.6.

PSD estimation

We have explained the pros and cons of the two PSD estimation methods implemented in `PySTAMPAS` in section 3.2. Both consist in averaging or taking the median over adjacent pixels. The free parameter is the number of adjacent pixels to consider.

For the time-average method, taking a short window may lead to overestimate the contribution of signal in the PSD, hence reducing the sensitivity of the search. On the contrary, taking a very long window may lead to inaccurate estimation of the PSD if it fluctuates on a time scale shorter than the length of the window considered. It should also be noted that since different resolutions are used, the total duration of the n_t adjacent time bins is not the same for each resolution. We finally opt for a rather long window of $n_t = 32$ adjacent time bins which allows to at least partially reconstruct monochromatic signals with duration lower than ~ 50 s.

Now considering the frequency-median method, we will see with real GW data that the main inconvenient is the presence of spectral lines in the data which are enhanced by this method, and can generate loud clusters if they are not correctly masked. The length of the window can also not be too large, since the PSD varies with frequency. A window of 10 Hz on each side of the pixel to be estimated is sufficient to remove most of the short glitches from the data. Consequently, a buffer of 10 Hz must be taken below the low frequency boundary of the search with this method.

3.4.2 Coherent signal reconstruction

Reconstruction of a polarized signal

To derive the expression of the coherent SNR of a pixel given by Eq. (3.26), we assumed that the signal is unpolarized, i.e that there is no correlation between the two polarization modes $\tilde{h}_+(t;f)$ and $\tilde{h}_\times(t;f)$. This allowed us to drop the cross terms $\langle \tilde{h}_+^\star(t;f)\,\tilde{h}_\times(t;f)\rangle$ in the correlation product, simplifying the final expression of the coherent SNR. `STAMP-AS` notably uses this approximation to perform all-sky searches [124]. In practice however, a lot of potential long-lived GW signals are expected to be polarized, such as GW from compact binary mergers or rotating neutron stars. The GW emission is parametrized by two more variables: the polarization angle ψ and the inclination ι, as explained in section 1.3.4. In this case, the authors of [123] showed that polarization induces another phase factor η in the expression of the SNR:

$$\mathrm{SNR}^{IJ}_{\mathrm{pol}}(t;f,\hat{\Omega},\iota,\psi) = Re\left[2\,\tilde{y}_I^\star(t;f)\tilde{y}_J(t;f)e^{-2\pi i f\tau + i\eta}\right] \tag{3.50}$$

with

$$\begin{aligned}
\eta = -\mathrm{phase}[&F_I^+F_J^+(a_+^2\cos 2\psi + a_\times^2\sin 2\psi)\\
&+\ (F_I^+F_J^\times + F_I^\times F_J^+)(a_+^2 - a_\times^2)\cos 2\psi\sin 2\psi\\
&+\ F_I^\times F_J^\times(a_+^2\sin 2\psi + a_\times^2\cos 2\psi)\\
&+\ i a_+ a_\times(F_I^+F_J^\times - F_I^\times F_J^+)],\\
a_+ &= (1+\cos^2\iota)/2,\\
a_\times &= \cos\iota.
\end{aligned} \tag{3.51}$$

In the expression of the coherent SNR of Eq. (3.26), η is not taken into account (it is implicitly set to 0). We will refer to this as an *unpolarized filter*. We investigate the effect of using an unpolarized filter on signal reconstruction for polarized waveforms. We inject polarized signals with different values of ι and ψ at a given sky position $\hat{\Omega}$ and compute the value of

$$\mathrm{SNR}^{\mathrm{pol}}_\Gamma = \sum_{(t;f)\in\Gamma} \mathrm{SNR}^{IJ}_{\mathrm{pol}}(t;f,\hat{\Omega},\iota,\psi)$$

for each injection. Therefore, $\mathrm{SNR}^{\mathrm{pol}}_\Gamma$ is the maximal SNR that is obtained when all parameters - position and polarization - are known. We then maximize the unpolarized SNR_Γ given by Eq. (3.32) over randomly chosen sky positions and compare it to $\mathrm{SNR}^{\mathrm{pol}}_\Gamma$. Figure 3.11 shows the fraction of SNR_Γ / $\mathrm{SNR}^{\mathrm{pol}}_\Gamma$ as a function of the number of sky positions tested for different waveforms injected considering different polarizations: circular polarisation ($\iota = 0$) and linear plus polarisation ($\iota = \pi/2$). We observe that polarized monochromatic waveforms (SG-C and SG-2000Hz) are efficiently reconstructed with an unpolarized filter after a relatively small number of trials, regardless of their frequency (405 Hz and 2000 Hz respectively). However, non-monochromatic signals (ADI-B and ECBC-A) are not accurately reconstructed. The ratio SNR_Γ / $\mathrm{SNR}^{\mathrm{pol}}_\Gamma$ tends to a value that is strictly lower than 1. This demonstrates that using an unpolarized filter to reconstruct polarized signals leads to underestimate the coherent SNR of signals in certain cases.

The phase difference $\Delta\Phi$ of the signal between the two detectors depends on the frequency f, the delay of arrival τ, and the polarization-induced dephasing η :

$$\Delta\Phi(f) = 2\pi f\tau - \eta. \tag{3.52}$$

For a monochromatic signal, f is the same for all pixels, hence there is a degeneracy between τ and η. In this case, maximizing over sky positions (i.e over τ) will lead to reconstruct the SNR of the signal signal correctly because the η term will be factored into the reconstructed τ. However, for a non-monochromatic signal, the degeneracy between τ and η is broken as pixels of different

frequency are present. $\Delta\phi(f)$ is an affine function of f that is described by two parameters. To reconstruct the correct SNR, it is necessary to maximize SNR_Γ over both τ and η. We illustrate this behaviour in Figure 3.12 with an ECBC-A waveform: with the unpolarized filter, the signal dephasing between the two detectors is incorrectly fitted, leading to a relative loss of SNR of $\sim 20\%$.

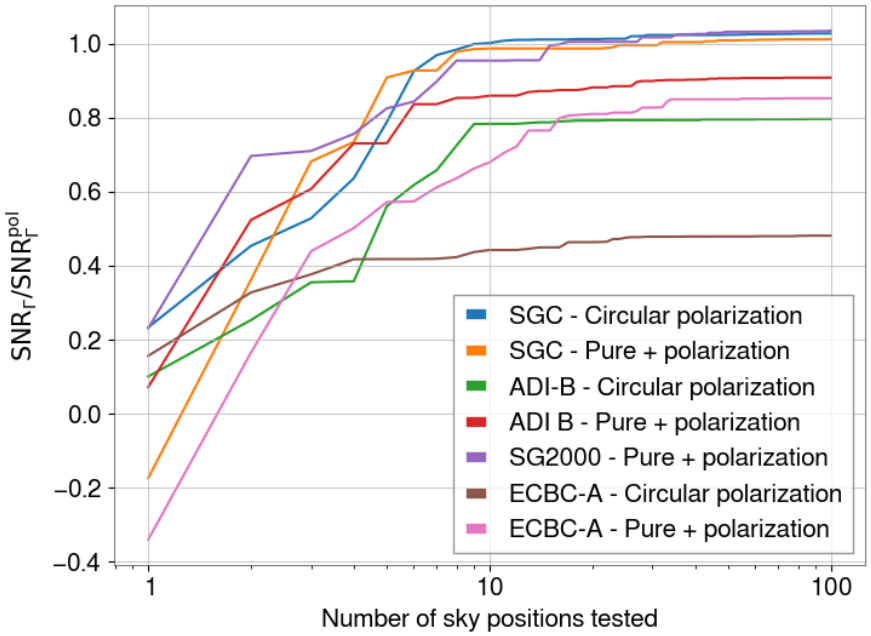

Figure 3.11: Fraction SNR_Γ / $\mathrm{SNR}_\Gamma^{\mathrm{pol}}$ as function of the number of sky positions $N_{\hat{\Omega}}$ tested for different waveforms. $\mathrm{SNR}_\Gamma^{\mathrm{pol}}$ is computed taking into account the actual signal polarization and sky position. The cases of a circularly polarized signal ($\iota = 0$) and of a linearly + polarized signal ($\iota = \pi/2$) are represented. SG-C and SG-2000Hz are monochromatic sine Gaussian waveforms at respective frequency 400 and 2000 Hz.

This study brings to light another sub-optimal characteristic of `STAMP-AS` for polarized signals. Polarized GW signals are not accurately reconstructed because the offset term η is not taken into account when computing the phase term $\Delta\phi$. To reconstruct these signals correctly, it would be necessary to maximize SNR_Γ over both sky positions and polarization angles. As doing this significantly expands the parameter space of the search, and therefore increases computing time, we keep the unpolarized filter for the different analyses that are presented in the remainder of this thesis. Yet, the polarized filter is now implemented into `PySTAMPAS` and ready to be used for known polarized sources.

Number of sky locations to test

We are now interested in the number of sky positions needed to be tested to reconstruct the signal accurately. We have seen in section 3.2 that for a 2 detectors network, this number depends on the ratio $f_{\max}/f_{\min}$ of the frequency boundaries of the signal (see Eq. (3.33)). In Figure 3.13, we verify this result experimentally and investigate also the case of a 3 detectors network, adding Virgo to the two LIGO detectors. Different waveforms are injected, and we compute the ratio ϵ of the reconstructed SNR_Γ to its maximal value as a function of the number of sky positions tested. The two sine Gaussian signals, SG-C and SG-2000Hz, are reconstructed equally rapidly despite having different frequencies (405 Hz and 2000 Hz respectively). In contrast, ISCOchirp-C,

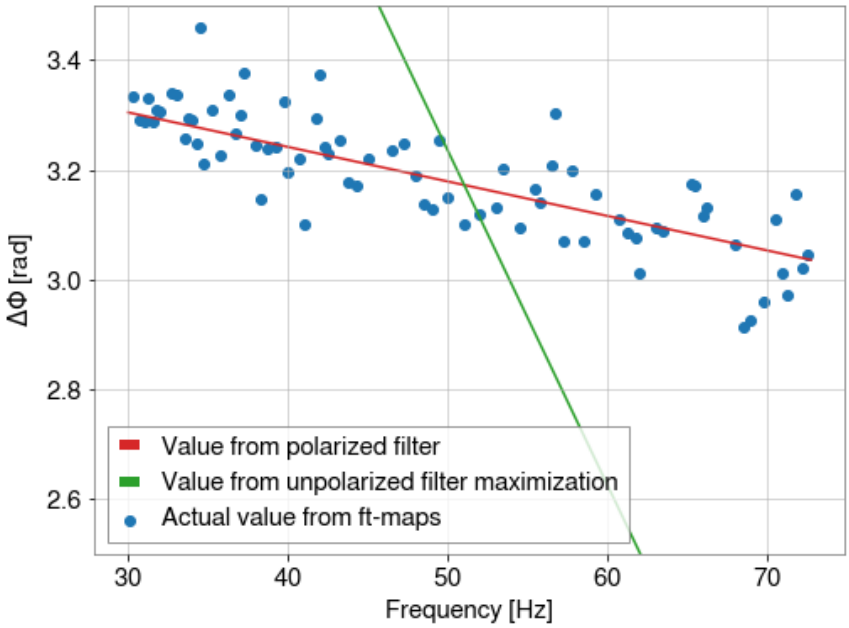

Figure 3.12: Phase difference $\Delta\Phi$ between H1 and L1 for an ECBC-A waveform injected with circular polarization as function of the signal's frequency. The actual values obtained from the tf-maps' pixels are shown in blue. The values predicted by the polarized filter with correct sky position and polarization angles are in red, and the values obtained by maximizing the unpolarized filter over 100 sky positions are in green.

which has the largest value of $f_{\max}/f_{\min}$ among the signals tested, is the one that requires the largest amount of sky positions to be reconstructed at the same value of ϵ. For a 2 detectors network, all the signals are reconstructed with $\epsilon \geq 0.95$ after ~ 100 positions tested.

The same results obtained with a 3 detectors network are shown with dashed lines in Figure 3.13. Monochromatic signals are still reconstructed more rapidly than large-band signals, however the number of sky positions needed is higher than for a two detectors network. This can be explained by the fact that for a 3 detectors network, the degeneracy between $\hat{\Omega}$ and τ is partially broken: for a given value of $\hat{\Omega}$, there are three different values of τ corresponding to the three baselines. This enlarges the parameter space, so more positions need to be tested. In average, a factor 10 more positions are required to reach the same value of ϵ, so a maximum of 1000 sky positions for $\epsilon = 0.95$. This increases the computational cost of the search, but is still feasible with the pipeline.

Effect of a third detector on detection efficiency

Despite the `STAMP` method can be straightforwardly generalized to a network of an arbitrary number of detectors, all-sky searches done with `STAMP-AS` (e.g [132, 133]) have only used the two LIGO detectors at Hanford (H1) and Livingston (L1) so far. Several factors explain this choice. First, the sensitivity of Advanced Virgo was significantly lower than the one of Advanced LIGO during the first three observing runs, by at least a factor 2. Besides, contrary to H1 and L1, whose arms are almost aligned, Virgo (V1) has a different orientation, and is therefore not sensitive to the same parts of the sky than the two LIGO detectors. This feature is useful for parameter estimation, since it breaks the degeneracy between the source's location and polarization, allowing to constrain better the location of the source. However, for an all-sky, unmodelled search, the

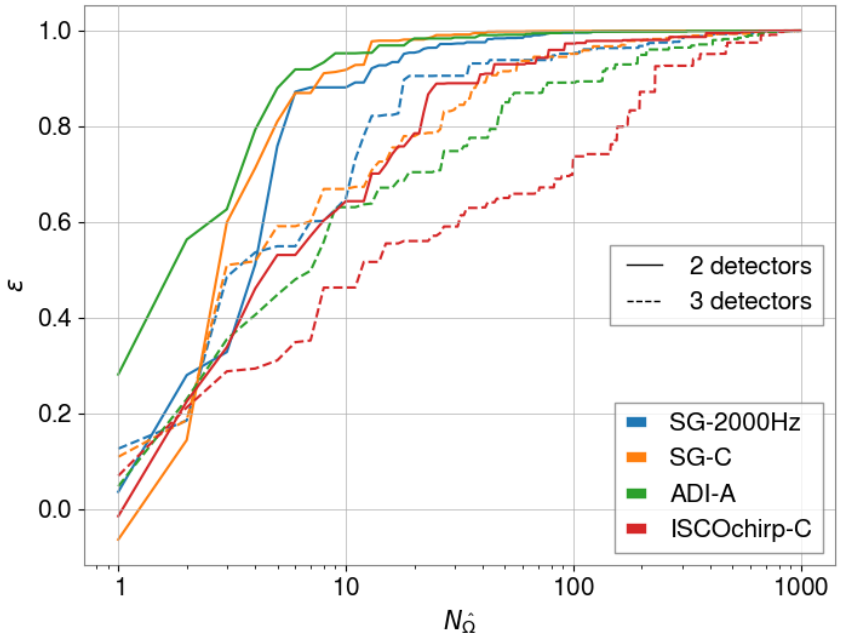

Figure 3.13: Fraction ϵ of SNR_Γ reconstructed as function of the number of $N_{\hat{\Omega}}$ of sky positions tested for different waveforms. Results for 2 and 3 detectors networks are plotted with continuous lines and dashed lines respectively.

benefit is not trivial in terms of detection efficiency. Finally, increasing the size of the detectors network leads to break the total observing time in several network configurations. Because of the 512 s long windows requirement a small fraction of the total observing time is lost. For example, during O3, H1, L1 and V1 were observing coincidentally during only 47% of the run, while the pair H1 - L1 alone was locked for 62% of the run.

To decide whether or not it is relevant to include more detectors in the network for a given search, it is interesting to estimate the gain in detection efficiency it could provide. To do so, we perform Monte Carlo analyses and compute the detection efficiency for an ADI-A waveform with two detectors (H1-L1), and with three detectors (H1-L1-V1). We first perform a background study. Since the definition of p_Λ is normalized to take into account the number of baselines, background distributions are similar for the 2 and 3 detectors network, with just the number of triggers being increased by 1/3 with 3 detectors because of the new clusters provided by Virgo data. In Figure 3.14 we show the detection efficiency as a function of distance for an ADI-A waveform in different configurations. We use the two detectors network H1-L1 as a control study. To simulate realistic conditions, we take the nominal PSD of each detector during O2 to generate Gaussian noise, hence Virgo's sensitivity is about 3 times lower than LIGO's. Finally, we compute the detection efficiency for the same network but setting Virgo's sensitivity to be equal to LIGO's to see if it makes a sensible difference. Results show that detection efficiency is increased by $\sim 25\%$ by adding a third detector with the same sensitivity as the two others in the network. Such non negligible improvement is mainly due to the better coverage of the sky ensured by the presence of a third, non-aligned detector. However, when using a realistic Virgo's PSD, the increase in sensitivity is only of $\sim 10\%$. In a real data analysis, that increase could likely be annulled by an increase of the FAR if the transient noise triggers rate from the third detector is larger than the two LIGO detectors' noise triggers rate. On the other hand, one sees that the efficiency curves for H1-L1-V1 have a slightly different shape than for H1-L1. The consequence is that the maximal distance at which one can detect 90% of the sources in the sky

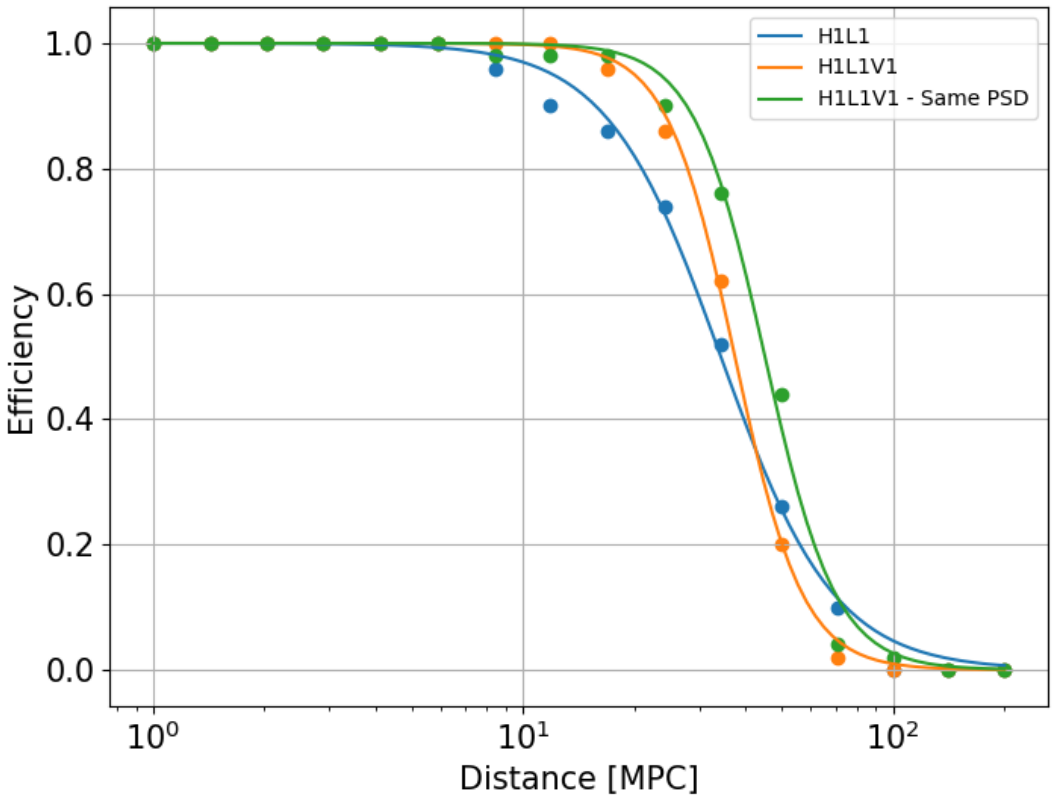

Figure 3.14: Detection efficiency as a function of the distance to the source for an ADI-A signal for different detector networks, considering O2 Advanced LIGO and O2 Advanced Virgo detectors' sensitivity (blue and orange curves) or O2 Advanced LIGO sensitivity for all three detectors (green).

is increased by a factor ~ 1.2 by considering V1 data in the O2 all-sky/all-time search, which is in fact not negligible.

3.4.3 Dependence on the clustering algorithm parameters

To decide what amount of effort it is worth to invest into developing better clustering algorithms, it is interesting to estimate what would be the sensitivity of the search with a "perfect" clustering algorithm, i.e an algorithm that would select all, and only the pixels of the tf-map that contains the signal. To simulate an optimal clustering, we proceed the following way.

1. Choose a waveform with well-defined time-frequency boundaries.
2. Inject that waveform in simulated detector Gaussian noise at a very high amplitude.
3. Run `burstegard` with a selective threshold on $|\tilde{y}(t;f)|$ to extract only the pixels that contain the signal.
4. Save the cluster's pixels to use them as a mask.

We then perform a usual efficiency study by injecting the waveform into the data, excepted that instead of running the clustering algorithm, we select directly the pixels that corresponds to the mask we have defined previously to be the cluster. By doing that, we remove the dependence on

the clustering algorithm and compute the coherent detection statistic on the pixels that contain the injected signal, no matter how faint they are.

In addition, we estimate the detection efficiency using the optimal detection statistic defined in Eq. (3.8). Given the template h injected in Gaussian noise n, we define the complex matched filter SNR for one detector I

$$\rho_I \equiv \frac{(s,h)}{\sqrt{(h,h)}} \tag{3.53}$$

where $s = n + h$ and (a, b) is the scalar product from Eq. (3.7). For noise only, the real and imaginary parts of ρ follow a normal distribution, so the square modulus $|\rho_I|^2$ follows a Chi-square distribution with two degrees of freedom. Then, we define the network SNR for the detector pair IJ (here H1 and L1), $\rho \equiv \sqrt{|\rho_I|^2 + |\rho_J|^2}$. Hence, ρ^2 follows a Chi-square distribution with four degrees of freedom, which we verify empirically. This allows us to assess a p-value and FAR to each injection, which we use to set a threshold on $|\rho|$ that corresponds to a FAR of $1/50\,\mathrm{yr}^{-1}$.

Figure 3.15 shows the detection efficiency as a function of the signal's strength expressed via the distance to the source. Detection efficiencies are computed for a FAR threshold of $1/50\,\mathrm{yr}^{-1}$, corresponding to a threshold on p_Λ of 2.4 or $\rho = 15$. We use three waveforms for this study, in order to investigate a potential dependency on the waveform. Two accretion disk instability signals, ADI-A and ADI-B, and an eccentric compact binary coalescence, ECBC-A (see Table 3.1 for details). To provide a comparison, the results obtained with the same parameters but using `burstegard` are shown, as well as the results obtained with the optimal matched filter[6]. As expected, sensitivity is better with the "optimal" clustering, however not by a huge factor: the relative improvement on the distance at 50% efficiency between the "optimal" clustering and `burstegard` is $\sim 10-20\%$. On the other hand, there is a factor $5-6$ between sensitivity that can be achieved with our method and the sensitivity provided by a perfect matched filter search. This gap seems to be independant of the signal duration and morphology. This result highlights the potential for improvement of clustering algorithms, but also the gap between unmodelled searches based on cross-correlation and searches based on matched filtering techniques. Nevertheless, the latter are not feasible in practice for all-sky searches as discussed earlier. Matched filtering is the optimal filtering technique when the signal is known, but this is not the case of our search.

3.5 Summary and comparison with `STAMP-AS`

To characterize the detection efficiency of the pipeline, We perform a Monte Carlo study over Gaussian noise colored with LIGO's nominal PSD during O2. The set of parameters used for this study is presented in Table 3.2. For the two PSD estimation methods, we first do a background analysis to estimate the value of p_Λ that corresponds to a FAR of $1/50\ yr^{-1}$. Then, we run an injection campaign with the waveforms from Table 3.1 and estimate the h_{rss} at 50% detection efficiency for this FAR threshold. To provide a comparison, we do the same study with `STAMP-AS`. Relative detection efficiencies between `STAMP-AS` and `PySTAMPAS` are shown in Figure 3.16 for each waveform and each PSD method.

For all waveforms but three, the detection efficiency is higher with `PySTAMPAS`. The average relative increase is $\sim 30\%$. The sine Gaussian signal (SG-C) is an extreme case. Reconstruction of monochromatic signals is a weakness of `STAMP-AS` because of the way PSD is estimated. With the frequency-median method, the detection efficiency is increased by a factor 6. Also, using the same time-average method thatn in `STAMP-AS` but with a larger window, it is increased by a factor 4. We notice than the PSD method has a great influence on the sensitivity, which confirms that some waveforms are much better reconstructed with one or the other method. For

[6]The optimal matched filter is computed by matching the data with the exact waveform that is injected, so it is the theoretical maximal sensitivity than can be reached. A realistic search using a matched filter technique would be less sensitive because of the number of templates to test.

Parameters	Value
tf**-maps**	
Window duration	$512s$
Frequency range	$20 - 2000$ Hz
$\Delta t_i \times \Delta f_i$	$[4.0\,\mathrm{s} \times 0.25\,\mathrm{Hz} - 2.0\,\mathrm{s} \times 0.5\,\mathrm{Hz}$ $-1.0\,\mathrm{s} \times 1.0\,\mathrm{Hz} - 0.5\,\mathrm{s} \times 2.0\,\mathrm{Hz}]$
PSD estimation	
Time-average	32 time bins
Frequency-median	20 Hz
Clustering	
Pixel energy threshold	2.0
Clustering radius	$1\,\mathrm{s} \times 1\,\mathrm{Hz}$
Minimum pixels number	30
Coherent stage	
SNR loss $1 - \epsilon$	5%

Table 3.2: Set of parameters used for the Monte Carlo study presented in section 3.5.

instance, the white noise burst (WNB-A) is not reconstructed at all with the frequency-median PSD, because it has a too large bandwidth.

The case of the ISCOchirp family illustrates a limitation of the pipeline. These signals are less well detected than with `STAMP-AS`, with an average 20% loss in sensitivity. The use of a hierarchical method may be the cause of that loss: since clusters are now extracted on single detector data, a signal which generates pixels that are slightly under the clustering threshold in both detectors will not be reconstructed at all, even if it could have been seen in a coherent tf-map. This affects principally the longer signals, for which the energy is spread over a large number of pixels. To better reconstruct these signals, a seedless algorithm may be more suited.

We now summarize the principal improvements of `PySTAMPAS` with respect to `STAMP-AS`.

- Reduced computing time:
  - `Lonetrack` hierarchical method
  - Use of parallel computing for building tf-maps and perform mini-lags.
  - Use of Cython and optimized computing libraries to address bottlenecks of the code.
- Improved detection efficiency:
  - Two PSD estimation methods suited for different signal morphologies.
  - Multi-resolution tf-maps.
  - Limited SNR loss due to sky localization error.
- Generalization to multi-detector network (useful when Advanced Virgo will be included in the analyses).

Current status and potential improvement

At the time of this writing, `PySTAMPAS` is able to perform a full analysis (i.e background estimation, efficiency estimation and coincident analysis), either in an all-sky or a targeted configuration. I have used it to perform full all-sky analyses of the second Advanced LIGO - Advanced Virgo observing run (O2) and the first part of the third run (O3a). The results of those analyses will be presented in the chapter 4. In addition, I also had the occasion to run it in a targeted

search configuration to perform searches for GW counterpart around a sample of GRBs associated with a potential MGF origin. This search, published in [136], is described in chapter 5.

Regarding clustering algorithms, I have focused my optimization efforts on `burstegard`, as the hierarchical method was already implemented in `STAMP` for seedless algorithms. However, a Python implementation of `stochtrack` has been written and plugged into the pipeline. Some work is still needed to test it, but it is planned that `PySTAMPAS` will ultimately be able to carry out analyses with both `burstegard` and seedless algorithms. The study I performed in section 3.4 seems to indicate that there is a maximal value to the detection sensitivity that can be reached with an excess cross-power method. However, as potential long-lived GW signals become better modelled, it may be possible to develop new algorithms that bridge the gap between unmodeled and matched filter searches.

Finally, to be used for data analysis within the LIGO-Virgo collaboration, the pipeline will have to undergo an internal review that is planned for late 2021.

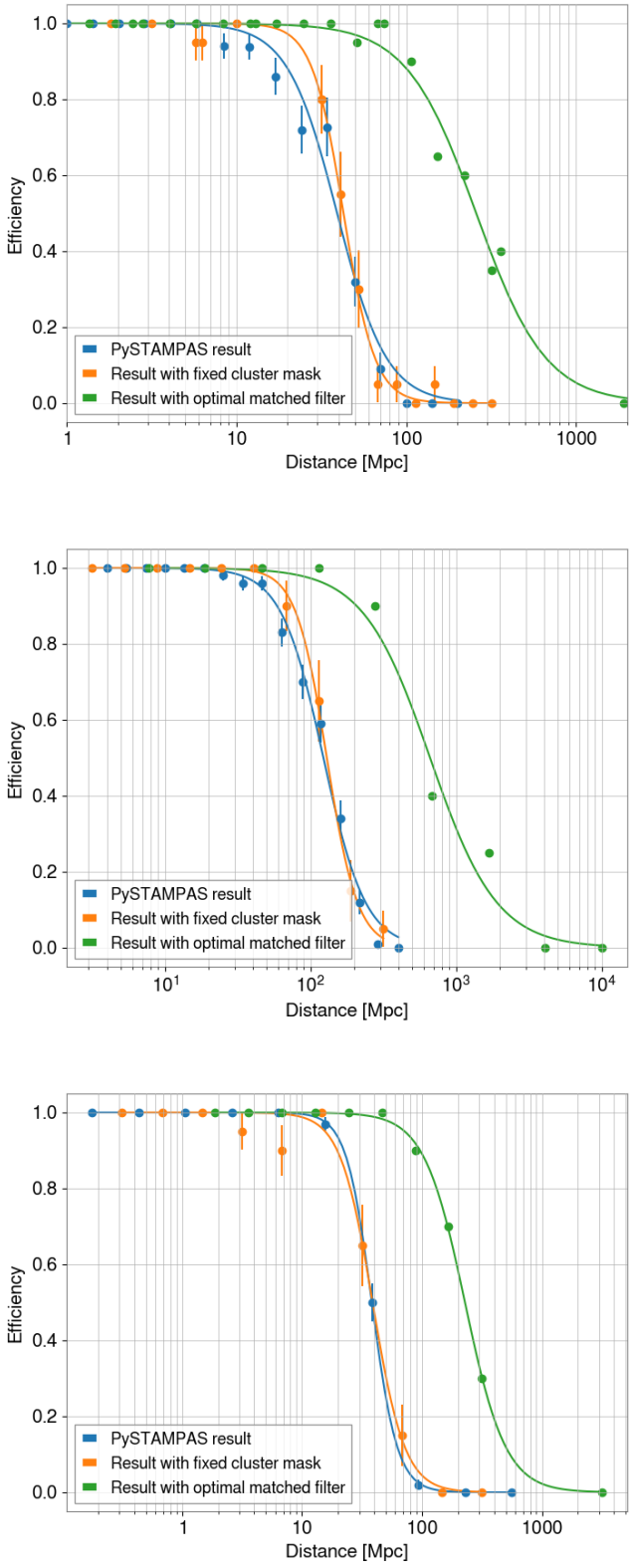

Figure 3.15: Detection efficiency for a FAR of $1/50\,\mathrm{yr}^{-1}$ as a function of the distance to the source for three different waveforms of different duration, ADI-A (40 s, top), ADI-B (8 s, middle) and ECBC-A (296 s, bottom). Results obtained with `PySTAMPAS` using the `burstegard` algorithm are shown in blue. Results for the optimal clustering algorithm are in orange, and results using optimal matched filtering are in green.

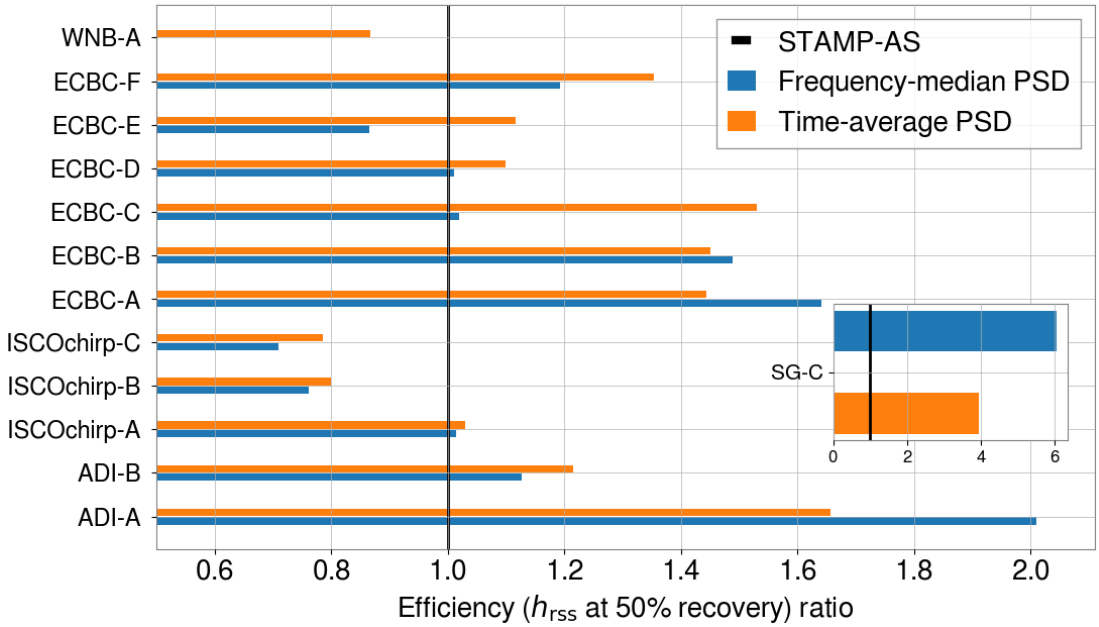

Figure 3.16: Ratio between the h_{rss} at 50% detection efficiency obtained with `PySTAMPAS` and `STAMP-AS` for FAR $= 1/50\,\mathrm{yr}^{-1}$ for both PSD estimation methods over Gaussian noise. The white noise burst waveform WNB-A was not recovered at all using the frequency-median PSD.

Chapter 4

All-sky searches for long-duration transients in the second and third observing runs of Advanced LIGO and Advanced Virgo

In this chapter, I describe several all-sky searches for long duration gravitational wave signals in real data from Advanced LIGO and Advanced Virgo. To begin with, I present the results of the all-sky search for long-duration bursts carried out in the third observing run of Advanced LIGO and Advanced Virgo (O3). I have contributed to the search by running `STAMP-AS`[1] and I derived the upper limits on some of the potential sources that are reported in the LIGO-Virgo-KAGRA collaboration paper recently submitted in Physical Review D journal [137]. In parallel to this work on real GW data, I use `PySTAMPAS` to analyze the second Advanced LIGO - Advanced Virgo observing run (O2) and the first half of the third run (O3a). This is the first full-scale test of the pipeline with real data, and it is also the occasion to compare its performances with the other pipelines used for long-duration transient searches.

4.1 All-sky search for long duration gravitational wave bursts in O3

The third observing run of Advanced LIGO and Advanced Virgo took place between April 1, 2019 and March 27, 2020, with a break between October 1, 2019 and November 1, 2019 for detector commissioning. This was the longest run to date and the first time the three detectors were observing simultaneously for the whole duration of a run. Detectors' sensitivity was increased by 50% and 100% compared to O2 for Advanced LIGO and Advanced Virgo respectively [55].

Among the major discoveries made during this run, we can cite the first detection of intermediate mass black holes [51], and the first two observations of a black hole - neutron star merger [20]. In addition, ~ 50 more GW events from binary black holes mergers were detected [18], allowing to better constrain the BH population and the volumetric rate of compact binary mergers.

Several unmodelled searches have also been performed over this run. I have participated in the all-sky search for long-duration transient signals. Three different pipelines were used to maximize the coverage of the rather large signal's parameter space: `Coherent WaveBurst` [138] and `STAMP-AS`, which come into two declinations, `Zebragard`, that uses seed-based clustering over coherent tf-maps, and `Lonetrack` [139], that performs seedless clustering using Bezier curves

[1] `PySTAMPAS was not yet ready and reviewed for participating to the O3 LIGO-Virgo-KAGRA paper.`

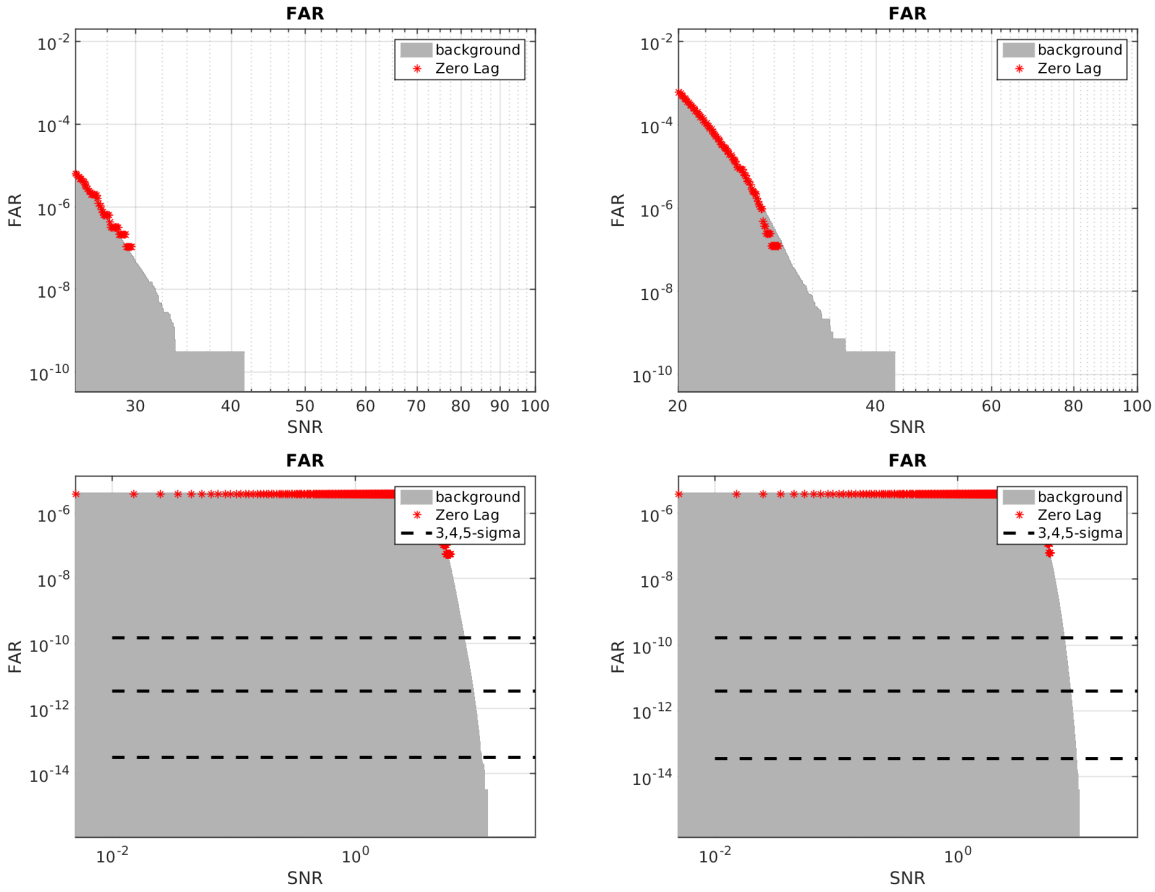

Figure 4.1: Cumulative distributions of background triggers obtained with `STAMP-AS` for O3, on top of which red crosses represent the most significant triggers found in coincidence. Top and bottom panels represent `Zebragard` and `Lonetrack` respectively, while left and right panel represent the two parts of the run, O3a and O3b. All triggers found in coincidence are compatible with background noise.

and uses the hierarchical method that consists in selecting clusters in single detector data before computing cross-correlation.

The data analyzed consist in ~ 204.4 days of coincident data from the two LIGO detectors H1 and L1. Because of the sensitivity gap and its different orientation, Virgo was not included in the analysis as it would not improve detection efficiency.

Results of background and zero-lag analyses are presented in Figure 4.1 for the two parts of the run (O3a and O3b), and for `Zebragard` and `Lonetrack` respectively. To get rid of the most problematic sources of transient noise (glitches) affecting mainly the `Zebragard` analysis, we apply few selection criteria: the first one is based on the balance of incoherent energy (E_I or auto-power as defined in Eq. (3.36) between the two detectors (Rveto). The second one is the fraction of coherent SNR contained in a single time bin (SNRfrac). In addition, depending on the dataset, it is sometimes needed to veto triggers that correspond to periods of bad quality data. Those periods are flagged by different list of veto segments built from the thousands of auxiliary channels that participate to the control or the monitoring of the detectors. Over the years, `STAMP-AS` pipeline has established a procedure to select veto segments that are useful for the `Zebragrad` search. We consider all veto lists (DQ flags and UPV vetoes [37, 140, 141]) and study using a subset of background triggers if they veto significantly families of loud glitches. By significantly, we consider that the coincident rate must be at least 5 times higher than the accidental rate standard deviation. We also exclude a veto list whose efficiency over dead-time is

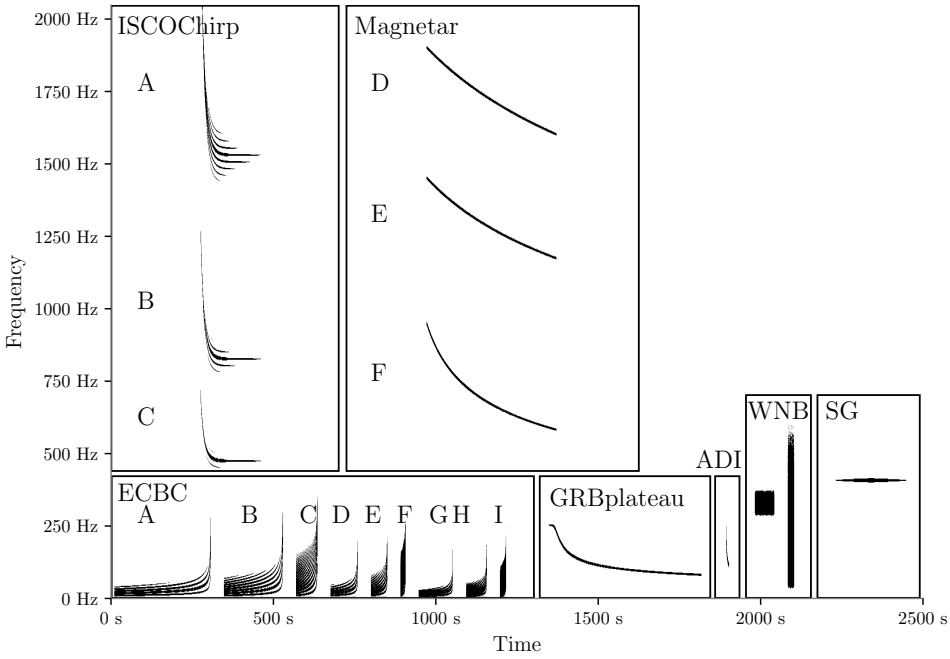

Figure 4.2: Time-frequency representation of the waveforms used in this search. Figure from [137].

smaller than 10 or those which contain too many small segments. It turns out for the O3 analysis, this procedure defined for the O2 long-duration `Zebragard` search led to the selection of none of the veto lists, except one DQ flag list that has been defined by the detector characterization team to flag a known problem with the LIGO Hanford laser power stabilisation system (Flag name: H1:DCH-PSL_FSS_BLRMS_GT0P3).

We note that `Lonetrack` does not need any selection criteria applied on triggers, because seedless clustering is less sensitive to transient noise features than seed-based clustering[2]. In addition, the hierarchical method it implements allows to generate much more background than `Zebragard`, and reach a p-value equivalent to 5σ.

No excess of triggers was found in coincidence compared to the background distribution for either of the three pipelines. The most significant trigger found by `STAMP-AS` has a p-value of 0.14, which is largely compatible with noise. `Coherent WaveBurst` found a trigger with a p-value of 0.088, corresponding to a significance of $\sim 1.7\sigma$, but its morphology is compatible with a fluctuating spectral line. Therefore, we report no statistically significant candidate event for this search.

To characterize the sensitivity of the search to GW signals, we use a set of 20 waveforms that span the time-frequency plane, as can be seen in Figure 4.2. They represent a variety of astrophysical models. In addition to the accretion disk instabilities (ADI), ISCO waves (ISCOChirp) and eccentric compact binary coalescences (ECBC) that are described in Table 3.1, GRBplateau represents a model of GW emission from a newly formed magnetar being the central engine of a GRB [102], and Magnetar waveforms are a model of GW emission from magnetars formed post BNS mergers [142].

All pipelines inject waveforms at random starting times, sky location, polarization angle and cosine of the inclination, and for different values of $h_{\rm rss}$. The lowest value of $h_{\rm rss}$ at 50% detection efficiency and for a FAR of 1 per 50 years obtained among each of the three pipelines is represented in Figure 4.3. On average, detection efficiency increased by a factor 1.8 compared to

[2]This has been confirmed since O1

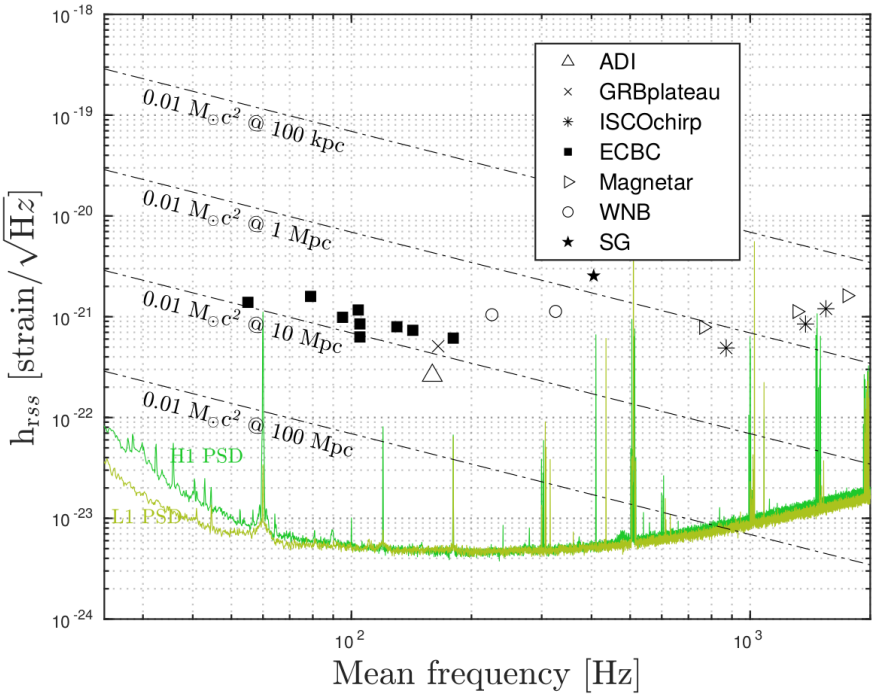

Figure 4.3: Injected $h_{\rm rss}$ versus mean frequency at 50% detection efficiency and a FAR of 1 per 50 years for the different waveforms tested. Only the lower value among all pipelines is shown for each waveform. The averaged amplitude spectral noise densities for H1 and L1 are shown for reference. Dashed-dotted lines represent the GW energy of fractions of $0.01\,{\rm M}_\odot{\rm c}^2$.

the results of the O2 search [133], which is compatible with the increase in detectors' sensitivity between O2 and O3.

Using these results, we place upper limits on the rate of eccentric compact binary coalescences (ECBC), using the "loudest event statistic" [143]. The upper limit at 90% confidence on the volumetric rate of events assuming the distribution of the sources is uniform and isotropic is

$$\mathcal{R}_{90\%} = \frac{2.3}{4\pi T \int_0^\infty dr\, r^2\, {\rm eff}(r)}, \tag{4.1}$$

with T being the total observing time and ${\rm eff}(r)$ the detection efficiency as a function of the distance computed for a FAR of $1/50\,{\rm yr}^{-1}$. We show the upper limits on the ECBC rates per unit volume for different waveforms in Table 4.1, and upper limits on the total event rate as a function of the distance in Figure 4.4.

The search for long-duration, unmodelled transient signals in O3 did not reveal any significant candidate. The evolution of the upper limits on the rate of events and detection efficiency between O2 and O3 are mainly due to the increased detectors's sensitivity and observing time, as there was no significant change made to the pipelines. However, several improvements of the search algorithms are planned for O4. `PySTAMPAS` is planned to replace `STAMP-AS`, and a new pipeline, `CoCoA` [144, 145], may join the analysis. Progress in data analysis, combined with increased detectors' sensitivity, may lead to a first detection, or at least continue to constrain the event rate.

Waveform	$M_1[M_\odot]$	$M_2[M_\odot]$	e	$\mathcal{R}_{90\%}$ [Gpc^{-3}yr^{-1}]
ECBC_A	1.4	1.4	0.2	9.97×10^2
ECBC_B	1.4	1.4	0.4	8.09×10^2
ECBC_C	1.4	1.4	0.6	3.21×10^3
ECBC_D	3.0	3.0	0.2	3.99×10^2
ECBC_E	3.0	3.0	0.4	8.89×10^2
ECBC_F	3.0	3.0	0.6	2.43×10^3
ECBC_G	5.0	5.0	0.2	1.50×10^3
ECBC_H	5.0	5.0	0.4	5.10×10^2
ECBC_I	5.0	5.0	0.6	6.98×10^2

Table 4.1: Rate upper limits per unit volume at 90% confidence level on eccentric compact binary coalescences with various masses and eccentricity e, computed with Eq. (4.1).

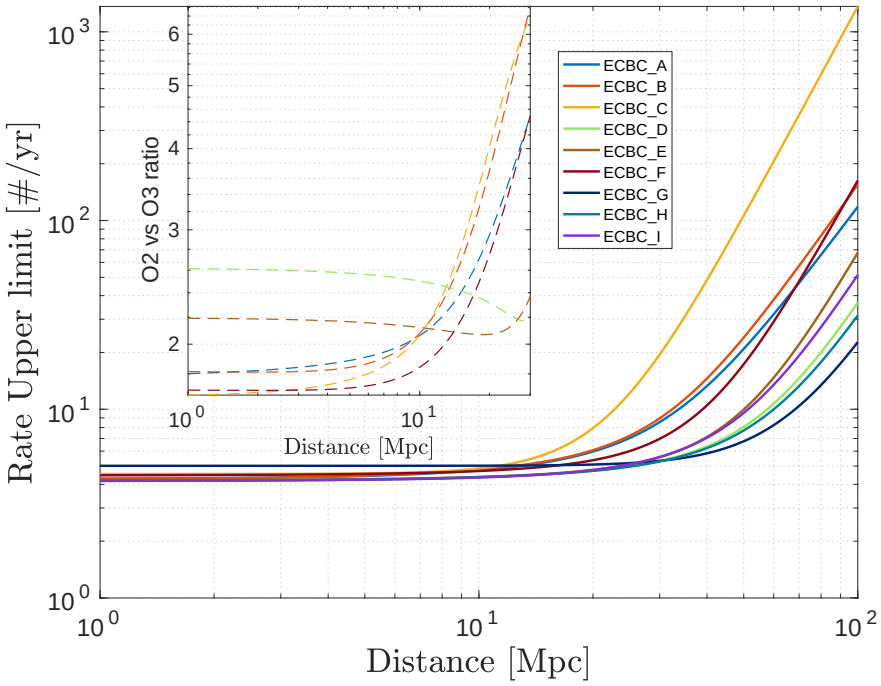

Figure 4.4: Upper limits at 90% confidence level on the rate of eccentric compact binary coalescences as a function of the distance. Only the best result is shown for each waveform. The inset shows the ratio of the rates with respect to O2 results [133] for ECBC_A to ECBC_F.

4.2 Real data analysis with PySTAMPAS

Real data analysis is bringing new challenges compared to Gaussian noise simulations. Non-stationary and non-Gaussian features may degrade the efficiency of the search in various ways. Loud noise transients can generate triggers with a high value of p_Λ, leading to increase the detection threshold and therefore decrease sensitivity. They can also combine with a true GW signal, causing the latter to be poorly reconstructed. Finally, they may bias the PSD estimation, which can also lead to badly reconstructe of signal. The tf-map represented in Figure 4.5 illustrates some of these features. We can notably see the presence of spectral lines, as well as a short noise transient (glitch) at low frequency.

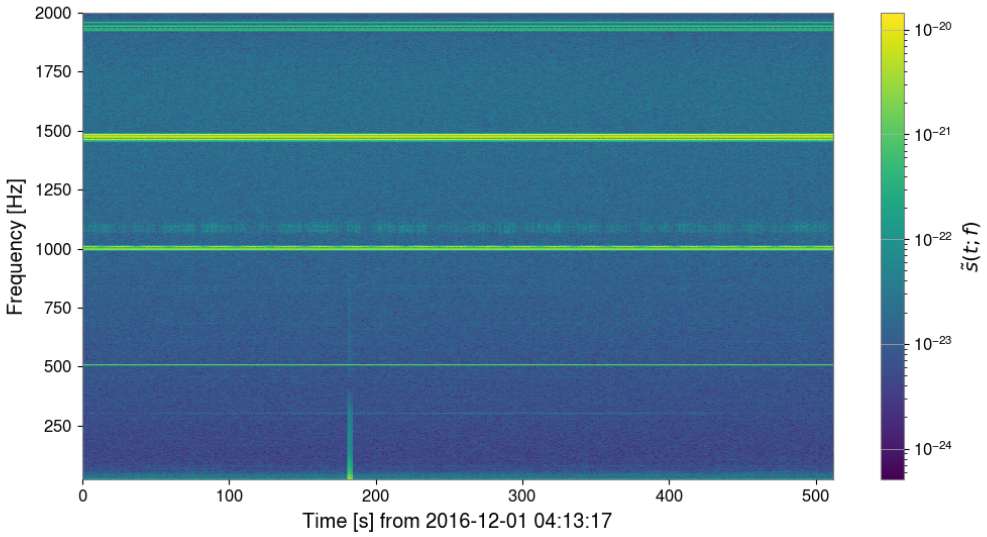

Figure 4.5: Time-frequency map of a 512 s long data segment from LIGO Hanford (LHO) at the beginning of O2. The statistic represented is the modulus of the Fourier transform of the data. This map illustrates the principal non-Gaussian noise features that challenge a search: forest of spectral lines can be seen around 500, 1000, 1480 and 1950 Hz , among others, and a short glitch is present at low frequency, ~ 180 s from the beginning.

4.2.1 Configuration of `PySTAMPAS` for real data analysis

Depending on the method used to estimate the PSD, some noise features may be enhanced when considering the whitened statistic $\tilde{y}(t;f)$. In the top panel of Figure 4.6, we show the tf-map of $\tilde{y}(t;f)$ computed over the same segment of data than in Figure 4.5 using the time-average PSD estimation method. The glitch is particularly visible, forming a column of pixels with high $|\tilde{y}(t;f)|$, 180 s from the beginning of the map. In addition, the PSD is overestimated at low frequency around it, leading to underestimate $|\tilde{y}(t;f)|$. However, most spectral lines do not appear in the map, as they have been factored in the PSD.

Gating

To attenuate the effect of large amplitude glitches, we now use a gating algorithm which consists in identifying peaks directly in the strain time series $s(t)$. The gating algorithm works the following way: First, the time series $s_I(t)$ are searched for peaks. A sample at t_i is identified as a peak if it has a value $|s_I(t_i)|$ at least 10 times larger than the mean value of $|s_I(t)|$ over the neighbouring 2 s of data. In this case, all values of $s_I(t)$ in the segment of data within 2 s of the peak are set to 0. To avoid issue due to sharp edges, the data on the boundaries of the masked segment are tapered. The effect of gating is shown in the bottom panel of Figure 4.6. The glitch has been correctly identified and masked. This gating procedure is implemented in practice using the *gate* method of the `GWpy` package [131]. It is in principle equivalent to the "glitch cut" that was used in `STAMP-AS` [146].

Identification of spectral lines

The frequency-median PSD estimator has opposite characteristics, as can be seen in Figure 4.7. The glitch has been correctly factored into the PSD this time, as it is large band, and does not appear anymore in the tf-map of $|\tilde{y}(t;f)|$. On the contrary, all spectral lines are present and enhanced.

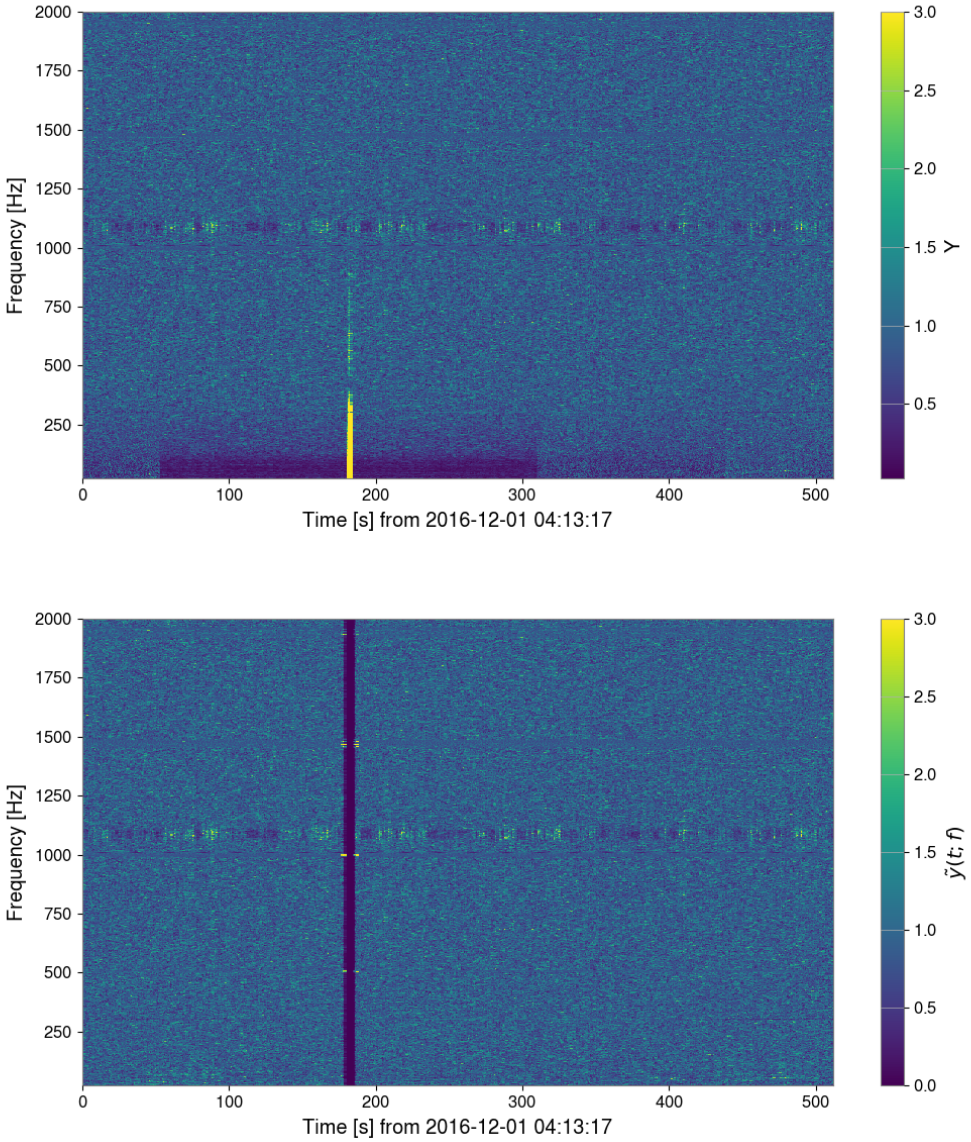

Figure 4.6: *Top*: time frequency map of the same time segment than in Figure 4.5, using the whitened statistic $\tilde{y}(t; f)$ where the PSD has been estimated by averaging over neighbouring time segments. The glitch is clearly visible, and causes to underestimate the SNR at low frequency. Most of the spectral lines have been factored in the PSD, excepted the fluctuating ones around $1000 - 1050\,\mathrm{Hz}$. *Bottom*: same tf-map obtained after the gating procedure. A segment of ~ 5 s of data around the glitch is notched. The PSD around the glitch is not biased.

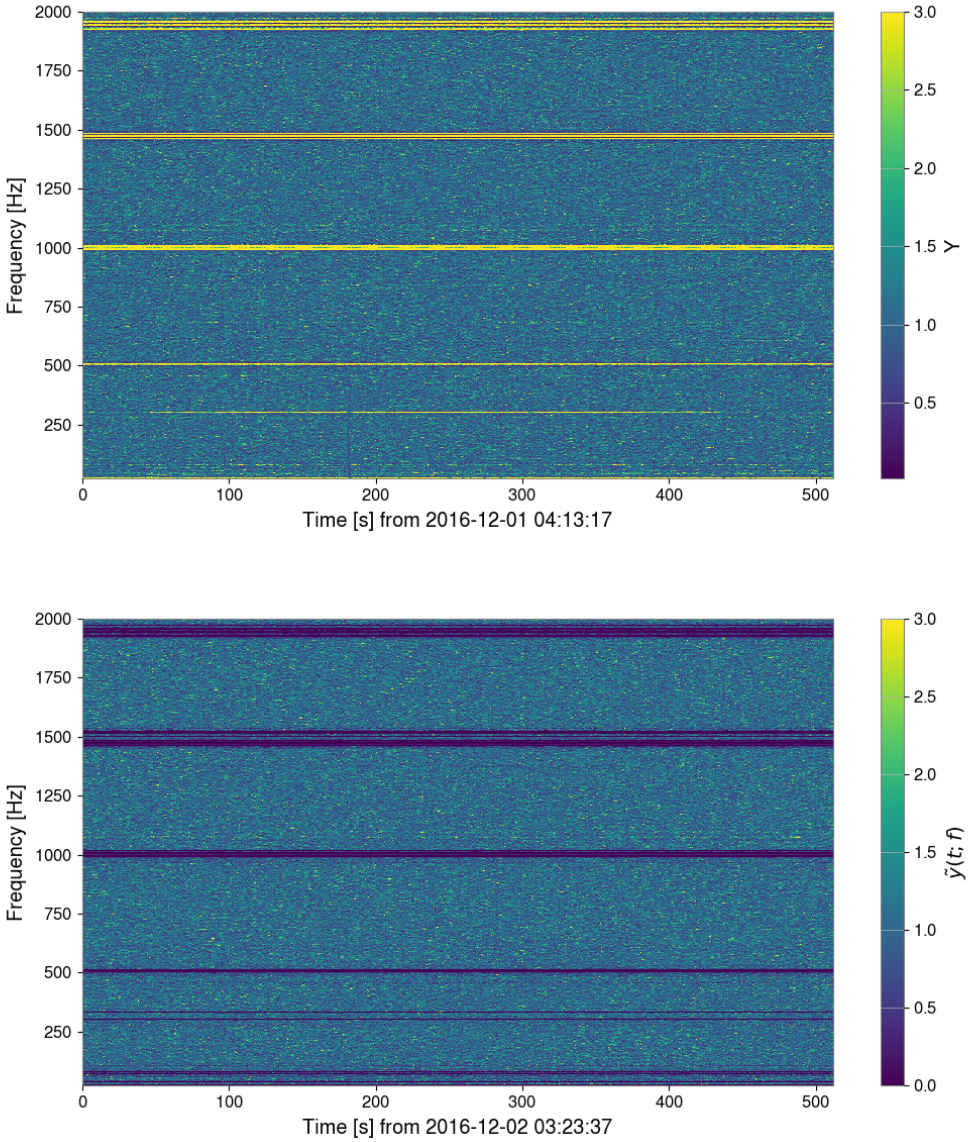

Figure 4.7: *Top :* another time frequency map of the same time segment than in Figure 4.5, where this time the PSD have been estimated by taking the median over neighbouring frequency bins. The glitch has been correctly factored in the PSD, contrary to the lines. *Bottom :* same map after applying frequency masks.

In the STAMP-AS implementation, a mask is applied over frequency bins that correspond to well identified spectral lines. A list of spectral lines to notch is established before the analysis starts. It is sufficient, given that most lines are already factored into the PSD, STAMP-AS using only the averaged neighbouring time segments PSD. This is no longer the case for PySTAMPAS. Therefore, we need a more systematic and automatic method to flag problematic frequency bins.

The goal is to identify frequency bins that are regularly excited throughout the observing run, without discarding any potential GW signal. We proceed in two steps. First, for each tf-map built, we compute the median of $|y(t;f)|$ over all time pixels. If that median is higher than a given threshold, the corresponding frequency bin is flagged as a potential spectral line. Second, we require that frequency bin be flagged in more than a given fraction of the total tf-maps built to be definitely considered a spectral line. By imposing this condition, we reduce the risk of incorrectly flagging a transient monochromatic signal and flag only the frequencies that are excited during a significant part of the run. This analysis is done independently for each time-frequency resolution considered, and each flagged frequency bin is masked. The result of this process is shown in the bottom panel of Figure 4.7, using a threshold of 2 on $|y(t;f)|$ and requiring a frequency bin to be flagged in more than 5% of the total tf-maps built for O2.

Cluster reconstruction

These two methods, gating and frequency mask, allow to get rid of most of the noise features that affect the search. However, they have the drawback of splitting the tf-maps in different parts. If a GW signal crosses a masked frequency bin, or time bins that have been gated, it may be reconstructed in several pieces by burstegard. To address this problem, we add an extra step after the initial clustering. We define the distance between two clusters as the minimal number of pixels between each corner of the clusters. Clusters for which this distance is lower than a certain threshold are then grouped together.

4.3 Analysis of O2 with PySTAMPAS

The second observing run of Advanced LIGO took place between November 30th, 2016 and August 25th, 2017, while Advanced Virgo was active from August 1st to August 25th, 2017. The LIGO-Virgo collaboration has published in [133] the results of an all-sky search for long-duration bursts obtained with 4 different pipelines: two versions of STAMP-AS, Zebragard and Lonetrack implementing a seed-based and a seedless clustering respectively, as well as a long-duration configuration of Coherent WaveBurst and X-Pipeline. In this section, I re-analyse the data with PySTAMPAS to demonstrate and compare its performances to the other pipelines.

4.3.1 Pipeline configuration and data used

The data set we use corresponds to ~ 117 days of coincident data from the LIGO detectors H1 and L1. It is splitted into $36,518$ windows of 512 s duration with a 50% overlap. Strain time series are high-pass filtered with a 22 Hz frequency cutoff, and gated. Time-frequency maps of $|\tilde{y}_I(t;f)|$ are built for each window and each detector. The PSD is estimated with the frequency-median method, using a moving window of 20 Hz around each pixel.

The algorithm to identify spectral lines is run over the maps, and $\sim 5\%$ of the total frequency bins are flagged for each resolution and each detector. A summary of the parameters used for the search is given in Table 4.2. They are almost the same than the ones used for the Monte Carlo study (Table 3.2), except that we increase the minimum number of pixels per cluster to 80 to lower the number of clusters extracted. In the meantime we also increase the clustering radius to $2\,\mathrm{s} \times 2\,\mathrm{Hz}$.

Parameters	Value
tf-maps	
Window duration	$512s$
Frequency range	$22 - 2000$ Hz
Time-freauency resolution	$[4.0\,\mathrm{s} \times 0.25\,\mathrm{Hz} - 2.0\,\mathrm{s} \times 0.5\,\mathrm{Hz}$ $-1.0\,\mathrm{s} \times 1.0\,\mathrm{Hz} - 0.5\,\mathrm{s} \times 2.0\,\mathrm{Hz}]$
PSD estimation	
Time-average	32 time bins
Clustering	
Pixel energy threshold	2.0
Clustering radius	$2\,\mathrm{s} \times 2\,\mathrm{Hz}$
Minimum pixels number	80
Coherent stage	
SNR loss $1 - \epsilon$	5%

Table 4.2: `PySTAMPAS` parameters used in the analysis of the O2 dataset.

4.3.2 Incoherent stage

We first run the incoherent stage of the analysis, which is common for both the background estimation and the zero-lag search.

In total, `burstegard` extracts $12,090$ clusters in H1 and $4,662$ in L1. The rate of clusters is much higher than with Gaussian noise (~ 1 clusters every 20 minutes). Their distribution as function of time and frequency is shown in Figure 4.8 for both detectors. We can see that they are not uniformly distributed, with some periods of time and frequencies containing an excess of clusters. Therefore, despite the gating and frequency masks, a lot of clusters corresponding to noise transients have been extracted.

In Figure 4.9 we show tf-maps of the loudest cluster (ranked by their total auto-power $E_I = \sum_{(t;f)\in\Gamma} |\tilde{y}(t;f)|^2$) from H1 and L1. It is clear that they both correspond to spectral lines. After checking the list of identified lines provided by the detector characterization LSC group, it seems that H1 one corresponds to the excitation of the third harmonic of the mirror's suspensions violin modes, and that L1 one is associated with an harmonic of the 60 Hz electric power line. Despite their high energy, these lines have not been flagged because they are excited too rarely. We proceed to the second stage of the analysis, and compute the coherent statistic over time-shifted data streams before reaching any conclusion.

4.3.3 Background estimation

For each cluster extracted at the first stage, we perform 10 big lags and 32 mini-lags, and compute the coherent detection statistic p_Λ for each time-slide. In total, every cluster extracted in the 117 days of coincident data is time-shifted 320 times, so the equivalent amount of background data simulated is a little more than 100 years.

The full processing (320 lags over $\sim$ 16000 clusters extracted, accounting for $\sim$ 100 years of background noise, and including the first stage) took $\sim$ 50 days of CPU time on the LIGO Caltech clusters. It was performed in about one day of real-life time using distributed computing. To provide a comparison, the non-hierarchical, Matlab implementation of `STAMP-AS` took several weeks of real-life time to simulate 50 years of background, accounting for several years of CPU time. The gain in computing speed is therefore at least a factor 10.

In total, $\sim 16000 \times 320 \simeq 5 \times 10^6$ triggers are generated and ranked along their statistic p_Λ. Since we are mostly interested in large p_Λ triggers, only the ones with p_Λ greater than 2.2 are saved to gain time and memory. The distribution of p_Λ is shown in Figure 4.10, on top of

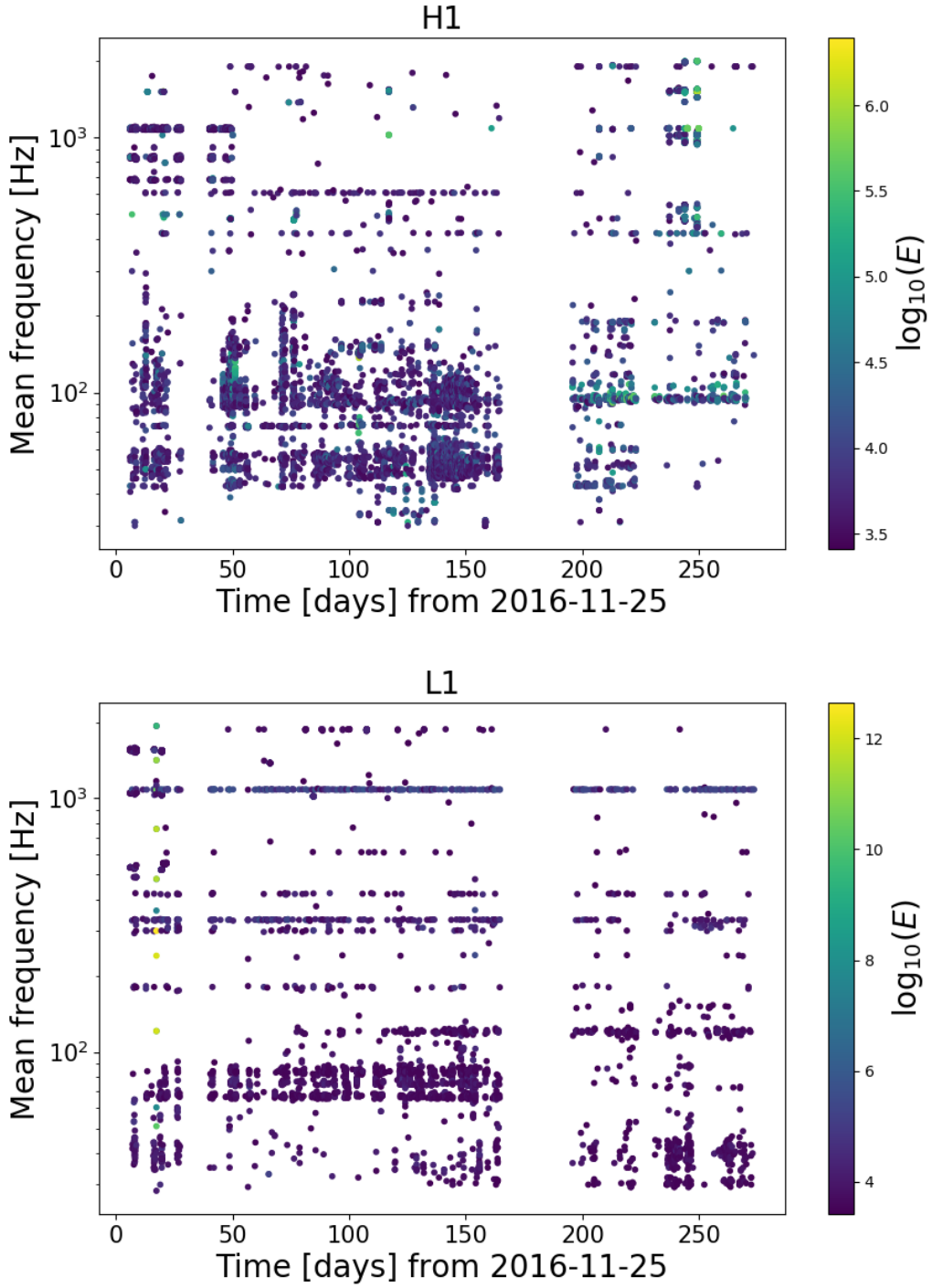

Figure 4.8: Mean frequency and starting time of clusters extracted by `burstegard` from each detector. The colormap represents the total auto-power E of the clusters.

which is plotted the same distribution for an ADI-A signal injected at a distance of 30 Mpc, and for Gaussian noise. We can see that there is a tail in the distribution formed by loud triggers with $p_\Lambda > 3$ that is not present in Gaussian data. Since the tail of the distribution significantly overlaps the distribution of signal, the detection efficiency of the search would be dramatically reduced if we were using only p_Λ. It is therefore necessary to understand the nature of these outlier triggers and develop selection criteria to dismiss them without hurting the efficiency of detecting true GW signals.

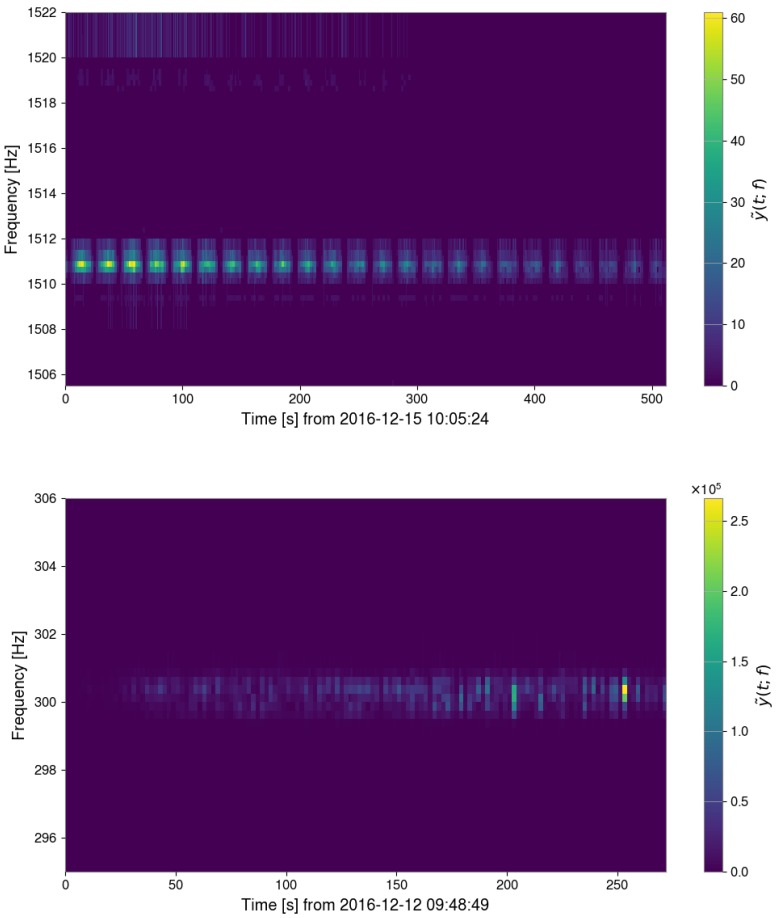

Figure 4.9: Time-frequency maps of the loudest trigger extracted from H1 and L1 during O2 by `PySTAMPAS`. *Top* (H1): it corresponds to a forest of spectral lines associated with the 3rd harmonic of the mirror's violin modes. Frequencies between 1512 and 1518 Hz have been notched by the automatic notch algorithm. *Bottom* (L1): excitation of the 5th harmonic of the 60 Hz power line.

Data quality vetoes

During an observing run, the state of the instruments and the environment are monitored by a multitude of probes and sensors that are primarly used for the control and monitoring of the detectors and then used to evaluate the quality of the data. When they appear to be affected by an instrumental or environmental artifact also visible in an auxiliary channel, a data quality flag (DQ flag) can be created that contains the corresponding times and a description of the issue. Hundreds of DQ flags are defined, by hands or by automatic process, and stored in a database for each detector [147]. They are classified in different categories based on their impact on the quality of the data [37]. Other types of vetoes are also produced from the auxiliary channels: a fast glitch finder algorithm, Omicron [140], produces lists of triggers from all auxiliary channels[3]. Algorithms such that UPV [141], hVeto [148] or iDQ [149][4] analyze the correlation between the glitches found in the GW and the auxiliary channels. In the end, thousands of lists of vetoes are generated. Not every DQ flags nor auxiliary based vetoes are relevant for a given analysis however, and we want to select them carefully in order to minimize the amount of data to be

[3] Auxiliary channels that couple with GW signal are excluded from this list.

[4] iDQ is a supervised learning framework to detect artefacts in GW channel, used online to asses the quality of the LIGO detectors data around GW alerts.

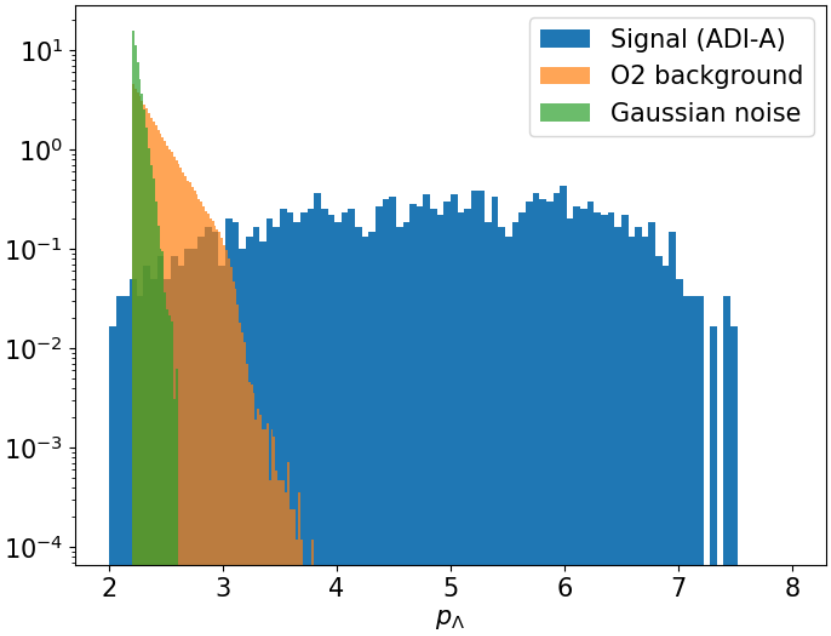

Figure 4.10: Distributions of p_Λ obtained with `PySTAMPAS` for background triggers from O2 before any post-processing selection (in orange); for Gaussian noise (green); and for an ADI-A signal injected at different amplitudes (blue).

Name	Deadtime [s]
L1:DCH-CS_MIC_BLRMS_GT_250	997
L1:DCH-EY_MIC_BLRMS_GT_200	1388
L1 UPV vetoes	7669
H1:DCH-ETMX_L2_UL_DAC_OVERFLOW	176
H1 UPV vetoes	18781
Total	H1: 18957 s / L1: 10054 s

Table 4.3: List of Data Quality flags selected for the analysis of O2 with `STAMP-AS`, and re-used with `pySTAMPAS`.The UPV vetoes are not listed here.

vetoed. Relevant DQ flags for a given type of search are listed in a *veto definer file*. This list is established by the detector characterization group for a few generic transient searches. For instance the short duration burst search. For other searches, the list of useful DQ flags is built by the search team. This is the case for the long duration burst search. The principle is to figure out whether loudest background triggers are correlated in time with DQ flags or glitches in auxiliary channels. This study is done with a subset of background triggers that have a ranking statistic above a given threshold. This work had already been done for `STAMP-AS` for the O2 analysis, and a list of segments that correspond to relevant DQ flags given in Table 4.3 and UPV vetoes was generated. For the O2 `PySTAMPAS` analysis, I use that list to veto the triggers that overlap the DQ flag segments. I describe the method used to select DQ flags for long duration burst search in more detail in section 4.4. The effect of removing those triggers is shown in Figure 4.11. Despite the accumulated dead time of the segments being about 1 day, almost 50% of the loudest triggers ($p_\Lambda > 2.2$) are removed.

The distribution of remaining triggers features one large outlier located $\sim$ 245 days after the beginning of the run. It is caused by a single loud cluster from H1 that generates a trigger

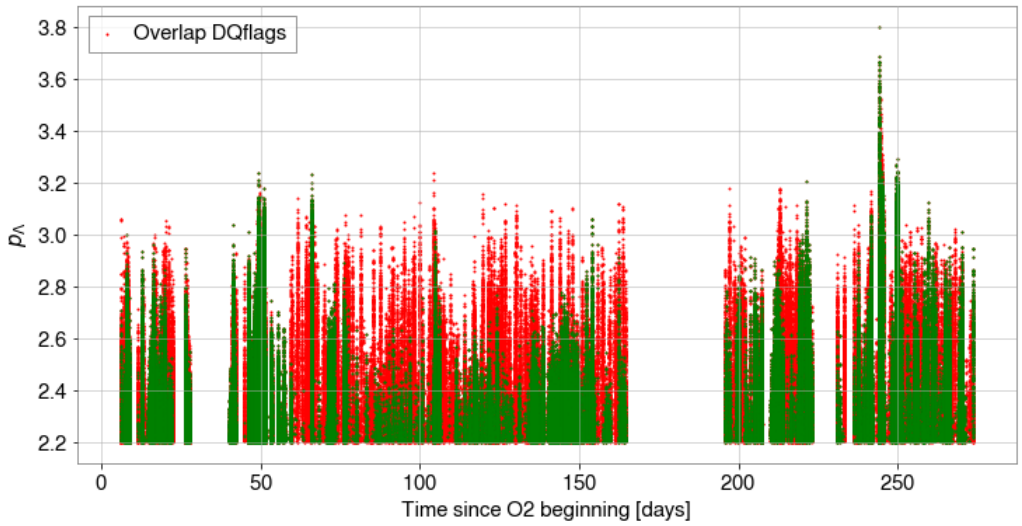

Figure 4.11: Coherent statistic p_λ of background triggers found in O2 by `PySTAMPAS` as a function of their starting time. Red points correspond to triggers that overlap a segment identified in the Data Quality flags list.

with high p_Λ at each time slide. A coherent tf-map of the loudest of these triggers is shown in Figure 4.12. It is a monochromatic line at frequency $\sim 1083\,\mathrm{Hz}$ that is listed as a calibration line. Since this line has been duly identified and categorized, we consider this is safe to veto the corresponding triggers a posteriori. Ideally this frequency bin should have been notched a priori, but as only one map was affected we decided to veto all triggers whose mean frequency is within $[1081 - 1085\,]\mathrm{Hz}$ are vetoed.

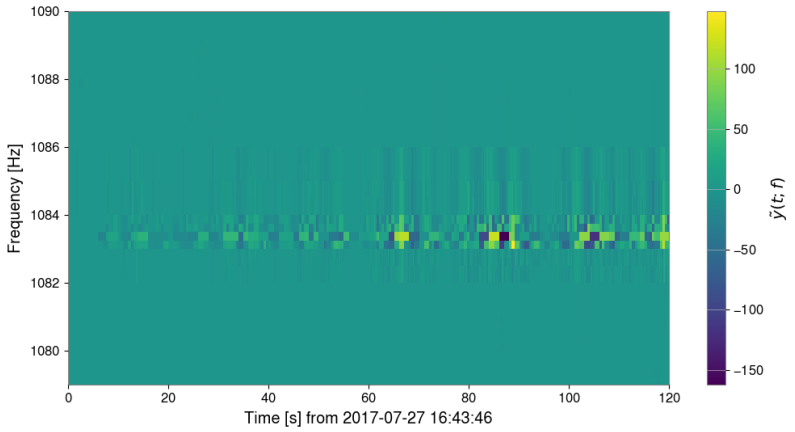

Figure 4.12: Coherent tf-map of the loudest background trigger found in O2 by `PySTAMPAS` after applying DQ flags. It corresponds to a calibration line around 1083 Hz.

The background distribution has been significantly cleaned with the use of DQ flags and the removal of the calibration line, as can be seen with the blue histogram in Figure 4.14. However, there are still a lot of triggers with $p_\Lambda \in 2.6 - 3.2$ that still affects the detection efficiency.

Other post-processing selection

After inspection, the loudest remaining triggers are mostly monochromatic. However, their times and frequencies do not correspond to any identified DQ flags or spectral lines. We need to use additional information to apply a global selection criterion to the triggers that allows to reject noise events while minimally affecting GW signals.

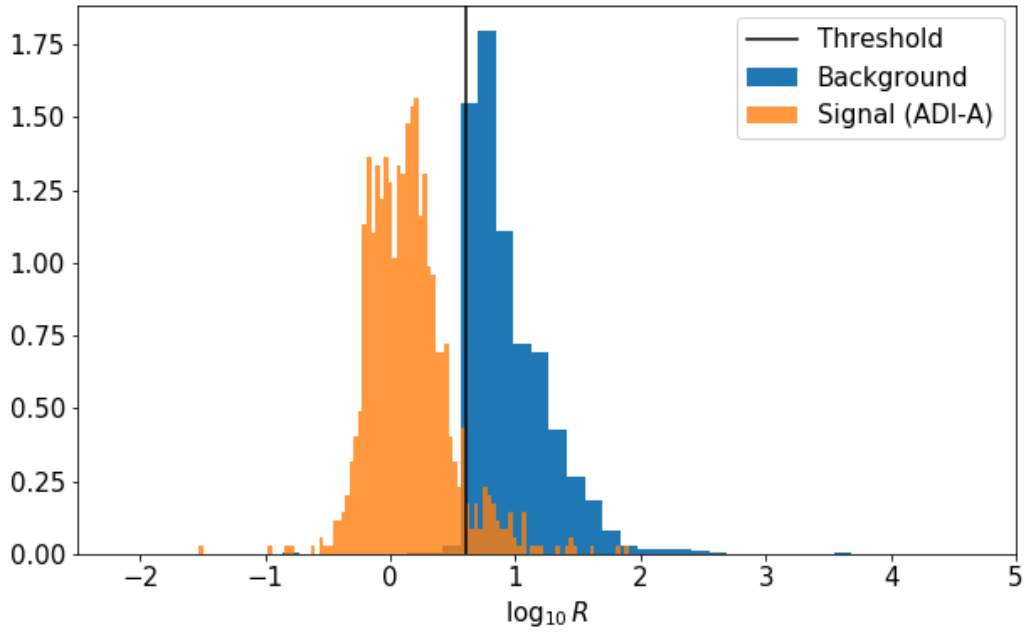

Figure 4.13: Distribution of the discriminant variable R for noise triggers (blue) found in O2 with `PySTAMPAS`, and an ADI-A signal (orange) for a source between 1 and 50 Mpc.

Several criteria of this type have been developed over time for `STAMP` and `STAMP-AS`. One of the simplest, labeled *Rveto*, consists in computing the ratio R of incoherent energies of a trigger in each detector :

$$R = \frac{E_I}{E_J} \tag{4.2}$$

For a true GW signal, $R \sim 1$, provided the detectors have comparable sensitivity and orientation, which is more or less the case here for H1 and L1. Loud noise transients, however, may have a lot of energy in one detector but not in the other. The distribution of $\log_{10}(R)$ for a signal and for background triggers is shown in Figure 4.13. As expected, the distribution is peaked around 0 for the signal, and is shifted to larger values for noise triggers. Based on this result, we can apply a rough selection criteria by requiring R to be lower than 4 for any trigger found. Using this threshold, we can see that the majority of noise triggers will be removed, as well as a small, but non negligible fraction of signal. We apply the *Rveto* selection criteria to the remaining background triggers. The final distribution of the FAR as a function of p_Λ is shown by the green curve in Figure 4.14. This distribution is not far from the Gaussian noise triggers distribution shown on Figure 4.10. We will use a detection threshold of $p\Lambda = 2.6$ that corresponds to a FAR of 1 per 50 years to derive the pipeline efficiency.

It is important to note that in practice, development and tuning of post-processing vetoes should be done over a small sample of background noise that covers the whole run, but not over the full sample, in order not to introduce any bias in the background estimation. Typically, a subsample of $\sim$ 10% of the total time-slides is used to discover the problems and features of

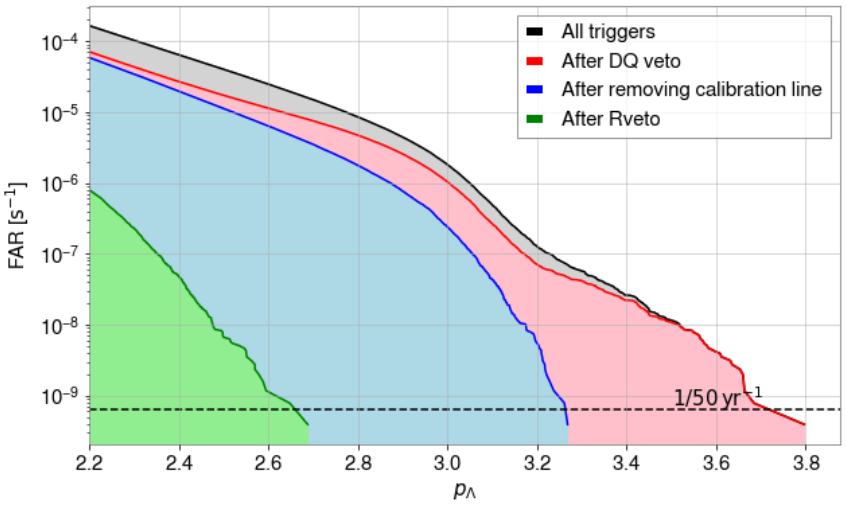

Figure 4.14: False alarm rate (FAR) as a function of p_Λ of the O2 `PySTAMPAS` search obtained after the several post-processing steps applied.

the noise, and the rest is used for the main background estimation. I did not do that for this exploratory work since those data had already been analyzed, and I focused on real data issues, but this is the way we would proceed for a forthcoming search.

4.3.4 Injection campaign

To estimate the sensitivity of the search, we use the waveforms described in Table 3.1. Waveforms are injected in the data at random time, localization and polarization following the procedure described in Section 3.3. Injection times are selected uniformly over the segments of data.

To compute the detection efficiency, we use the threshold of 2.6 on $p\Lambda$ that corresponds to a FAR of 1 per 50 years. The same post-processing selection criteria than in the background study are used: triggers within segments flagged by DQ flags are removed, as well as triggers whose mean frequency is around $1083 \pm 2\,\mathrm{Hz}$ or that have $R > 4$. For each waveform, the h_{rss} at 50% detection efficiency is shown in Figure 4.15 as a function of the WG signal mean frequency. To provide a comparison, results of the `STAMP-AS / Zebragard` O2 analysis are also shown.

For most waveforms, the results of the two pipelines are within the same order of magnitude, and follow the detectors' sensitivity frequency, as expected. However, we note that, excepted for the sine gaussian waveform, the relative detection efficiency gain between `PySTAMPAS` and `STAMP-AS` that we observed with Gaussian noise is not present for this O2 search application. We go from an average improvement of $\sim$ 30% with Gaussian noise to a loss of $\sim$ 20% with real data. Several factors can explain this effect. The detection threshold on p_Λ is higher with real data because of non-Gaussian noise events that contribute to the tail of the distribution, despite the selection criteria we apply. In addition, these selection criteria, especially Rveto, lead to dismiss a fraction of the injections, effectively reducing detection efficiency. Finally, a fraction of the signal is masked by frequency masks, which are more numerous when we use the frequency-median PSD estimation.

This illustrates the difficulties of setting up and configure a new pipeline for real data analysis over a full observing run. Nevertheless, we showed with this analysis that using the frequency median PSD instead of the time-average PSD allows to gain almost a factor 10 on sensitivity for monochromatic signals which represent a large class of potential long duration GW signals. The main drawback of this method is the presence of a multitude of monochromatic noise events that

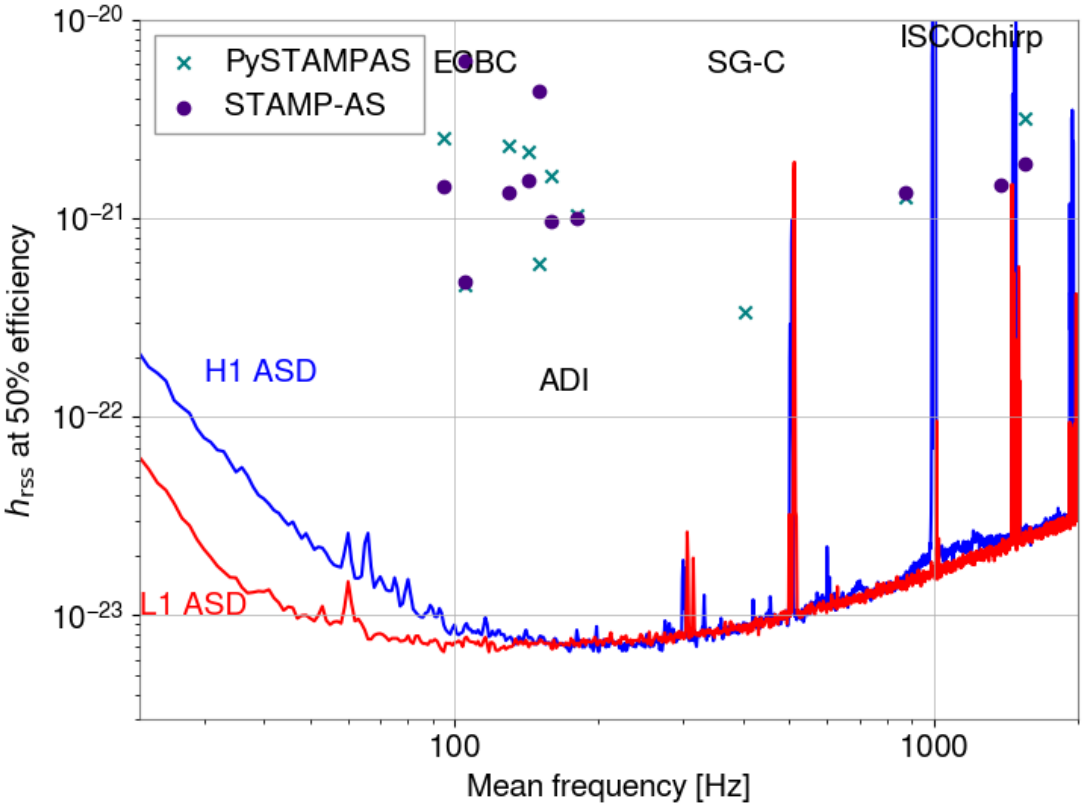

Figure 4.15: Values of h_{rss} at 50% detection efficiency and a FAR of $1/50\,\text{yr}^{-1}$ are represented for each waveform as a function of its mean frequency. Green crosses represent values obtained with `PySTAMPAS`, while purple dots represent the results obtained with `STAMP-AS` for the same waveforms. The detectors' averaged amplitude spectral densities during O2 are shown with the blue and red curves for H1 and L1 respectively.

can not always be flagged or associated to a known spectral line, leading to decrease sensitivity to other types of signal. In Section 4.5, we will go back to these issues and propose methods to increase the sensitivity of `PySTAMPAS` with the frequency-median over real data.

4.3.5 Coincident analysis

The coincident analysis - the actual search for GW signals - is performed the exact same way than the background estimation, except that the data are not time shifted. Using the FAR curve we computed in Figure 4.14, we can associate the values of p_Λ of triggers found in coincidence to a false alarm rate, and estimate their false alarm probability.

Results of the coincident search are shown in Figure 4.16. The FAR of the loudest coincident triggers are represented on top of the FAR curve computed from the background triggers. The same selection criteria than background triggers have been applied to coincident triggers. The most significant trigger has a p_Λ of 2.37, wich corresponds to a false alarm rate of 1 per 163 days. Considering that the observing time is 117 days, and assuming that noise triggers follow a Poisson distribution, the probability to observe at least one noise event with a significance higher than 2.37 (p-value) is $p = 0.51$. Consequently, all triggers found in coincidence are compatible with noise. We can decide for the null hypothesis for this search, i.e no significant GW event was found. To be complete, we show in Figure 4.17 the coherent tf-map of the loudest trigger.

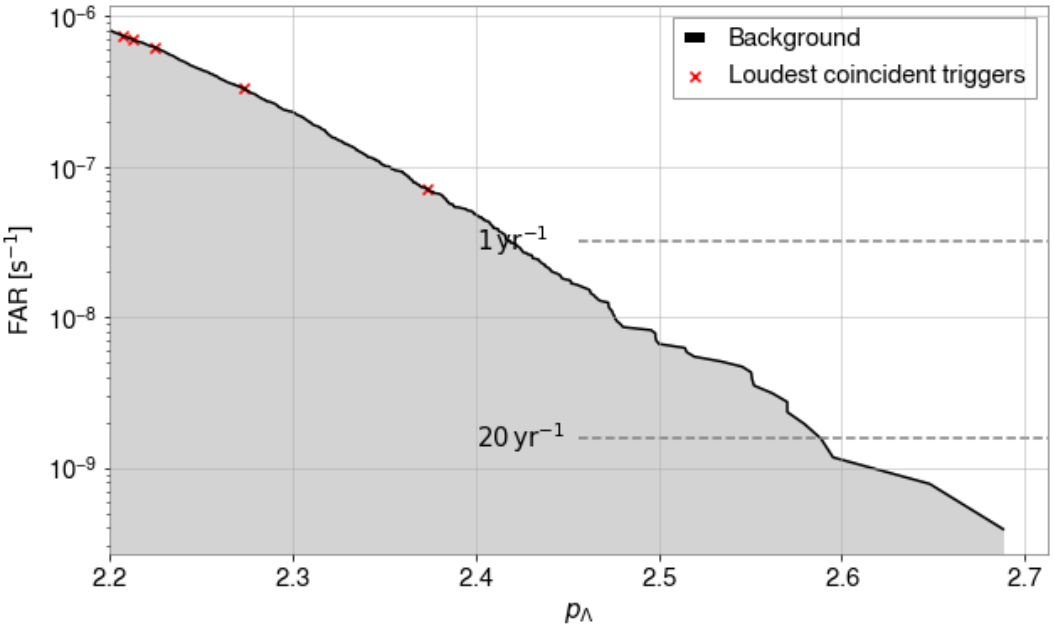

Figure 4.16: False alarm rate of the O2 `PySTAMPAS` search as a function of p_Λ after applying all post-processing selection criteria (DQ flags, Rveto and removal of the calibration line at 1083 Hz). On top of the curve are represented (red crosses) the values for the 5 most significant triggers found in coincidence.

It is a 77 s, narrow-band event with frequencies between $1072 - 1080$ Hz. It is not completely monochromatic[5]. Nevertheless, based on its morphology, and given its low significance, it is compatible with a non-stationary ("wandering") line.

These results are compatible with the ones previously published in [133] obtained with `STAMP-AS`, `Coherent WaveBurst` and the `X-pipeline`, for which the most significant event had a p-value of 0.6.

4.4 Analysis of O3a with `PySTAMPAS`

In parallel to the `STAMP-AS / Zebragard` analysis, I also ran `PySTAMPAS` over the first half of O3 (O3a). The parameters of this search are the same than the ones used for O2 given in Table 4.2, excepted that we use this time the time-average PSD estimator. In order to maximize the sensitivity to long-lived signals, we estimate the PSD by averaging $|\tilde{y}(t;f)|^2$ over 128 neighbouring time segments on each side. The run contains ~ 107 days of coincident data between H1 and L1 that are splitted into $35,578$ windows.

4.4.1 Background estimation

During the first stage of the analysis, 14136 clusters are extracted from L1 and 5204 from H1. The rate of clusters is similar to what has been observed during the analysis of O2. The distribution of clusters as function of time and frequency, shown in Figure 4.18, features an excess of clusters at low frequency (below 100 Hz) in both detectors. As explained before, the PSD tends to vary rapidly at low frequency because of seismic and anthropogenic noise. Since we estimate it by

[5]The closest repertoried spectral line is the calibration line at 1083 Hz, which cannot be associated to this trigger

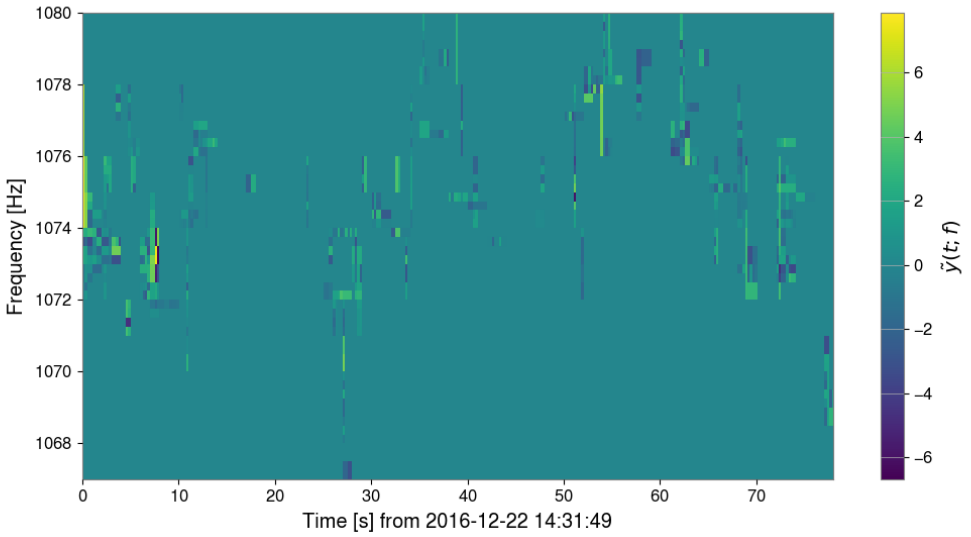

Figure 4.17: Coherent tf-maps of the loudest trigger found in coincidence (zero-lag) between H1 and L1 for the O2 `PySTAMPAS` search.

averaging over a relatively long period of time, these variations are not factored into the PSD and generate pixels with high $|\tilde{y}(t; f)|$. Besides, like in the O2 analysis, some periods of data feature an excess of clusters.

We compute ~ 56 years of background using the time-slides method and set a standard FAR threshold of 1 per 50 years. Background distributions are shown in Figure 4.19 with the FAR as a function of p_Λ for the different selection criteria applied.

Selection of DQ flags

We first check if there are relevant DQ flags for this data set. Among the hundreds of DQ flags that are available, the *burst* and LIGO *detector characterization* working groups pre-select a subsample of them that may be relevant for transient, unmodelled searches. However, not every flag in this list is useful for our specific analysis. To select the ones to use, we apply the following method. First, for each flag, we identify the triggers of large p_Λ value that overlap the segments where this flag is active. If the rate of triggers over these segments is significantly higher than the overall rate of triggers (a typical value would be 10 times the overall rate)[6], the flag is potentially useful and we investigate further. Otherwise, it is dismissed. Then to cross-check the selection, we time shift the data by different amounts of time and compute the rate of triggers that are coincident to the flag's active segments. If this rate is of the same order of magnitude for shifted and non shifted data, it is likely to be a false association and we do not use the DQ flag. Using this method, we finally select 7 DQ flags that account for about 2.5 days of dead time. They are listed in Table 5.3 and correspond to various instrumental and environmental effects (loud glitches, squeezing saturation, thunder, etc).

Post-processing veto *SNRfrac*

After vetoing the triggers overlapping with DQ flags' segments, the tail of the distribution consists in short glitches at low frequency, as illustrated in Figure 4.20. Some glitches may pass the gating step, because they are not loud enough to reach the threshold, or because another louder glitch is present in the data less than 2 s apart. Since those glitches have a very different morphology than

[6]This criteria is equivalent to asking that the ratio veto efficiency over veto deadtime is larger than 10.

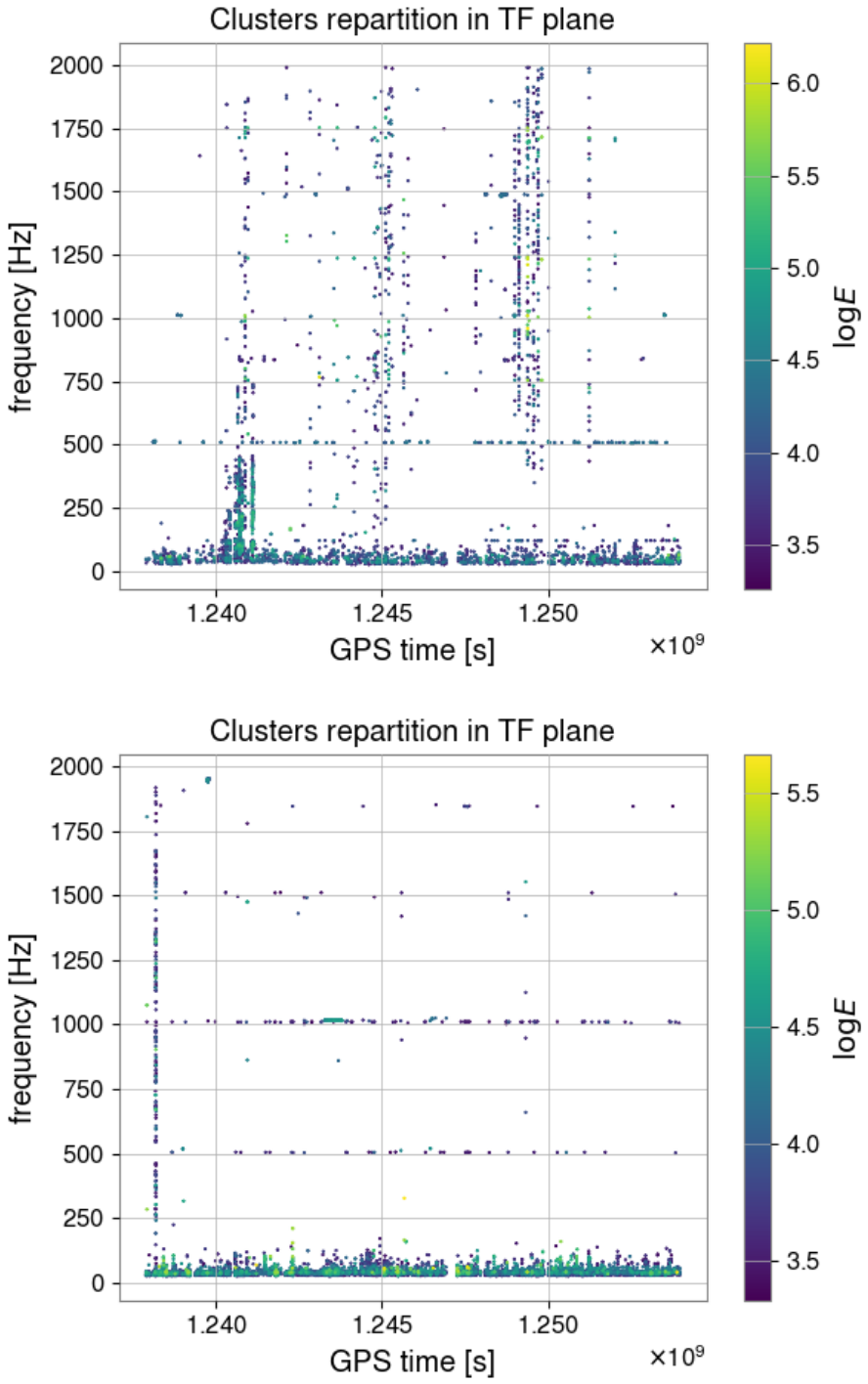

Figure 4.18: Mean frequency and starting time of clusters extracted by `burstegard` from each detector for the O3a `PySTAMPAS` search. The colormap represents the auto-power E of the clusters.

what is expected for a GW signal, it is possible to define a discriminant variable to distinguish them from a signal. The variable *SNRfrac* was implemented in `STAMP-AS`, along with *Rveto*, to deal with short glitches. In this study, we define SNRfrac to be the maximum of the fraction of the summed SNR contained in a single time bin :

$$\mathrm{SNRfrac} = \frac{\max\limits_{t\in\Gamma} \sum\limits_{f} \mathrm{SNR}(t; f, \hat{\Omega})}{\mathrm{SNR}_{\Gamma}}. \tag{4.3}$$

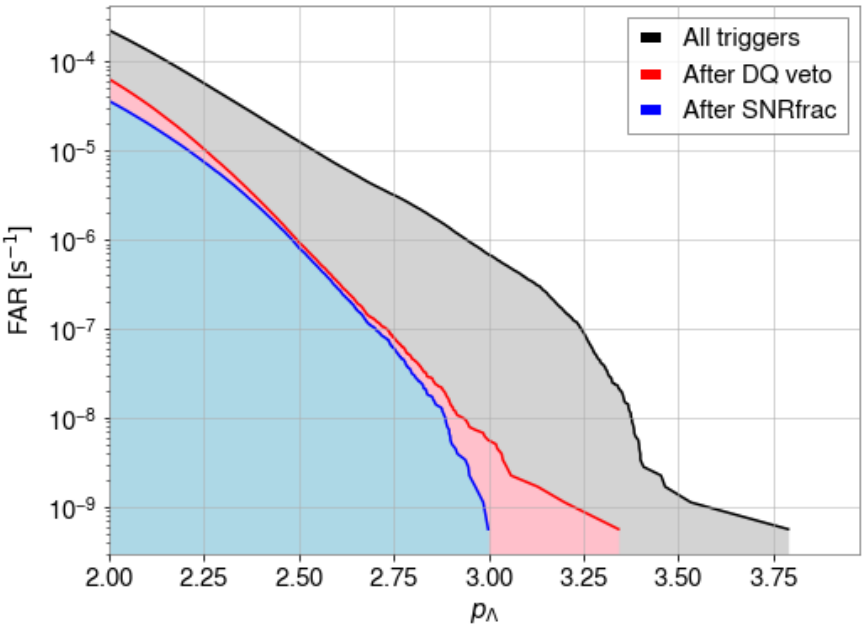

Figure 4.19: False alarm rate as a function of p_Λ of the O3a `PySTAMPAS` search after post-processing selections applied (DQ flags and SNRfrac).

Name	Deadtime [s]
L1:DCH-LSC_PRCL_IN1_GT_P075:1	2661
L1:DCH-POP_LOUD_GLITCHES:2	80181
L1:DCH-SQZ_SATURATIONS:1	2484
L1:DCH-THUNDER_MIC_BP_GT_300:1	2903
H1:DCH-POP_LOUD_GLITCHES:2	51662
H1:DCH-PSL_FSS_BLRMS_GT0P3:1	10203
H1:DCH-WHISTLES:2	41313
Total	191407

Table 4.4: List of DQ flags selected for the analysis of O3a with `PySTAMPAS`.

For a short glitch, the largest part of the energy tends to be located in a single time bin. Therefore, we expect a high value of SNRfrac, as opposed as for a long-lived signal. Similar to what we did with Rveto, we compare the distribution of SNRfrac for signal and noise in Figure 4.21. The distribution for noise triggers is clearly bimodal with a separation at SNRfrac $\simeq 0.4$, while most values are lower than 0.4 for the signal. Therefore, we set a selection criteria of SNRfrac lower than 0.4 for the triggers. The final cumulated distribution of triggers after DQ flags and *SNRfrac veto* is represented by the blue curve in Figure 4.19. The loudest trigger p_Λ value for a a FAR of 1 per 50 years is 3.0.

4.4.2 Efficiency estimation

We use the same set of waveforms as in the O2 analysis to estimate the sensitivity of the search. The method remains identical. The results are presented in Figure 4.22, with also a comparison with `STAMPAS / Zebragard` results [20]. We report an efficiency increased for all waveforms except for the 3 ISCO chirps, a result similar to what has been obtained with Gaussian noise. The average improvement over $h_{\rm rss}$ at 50% detection efficiency compared to `STAMP-AS` is $\sim 25\%$.

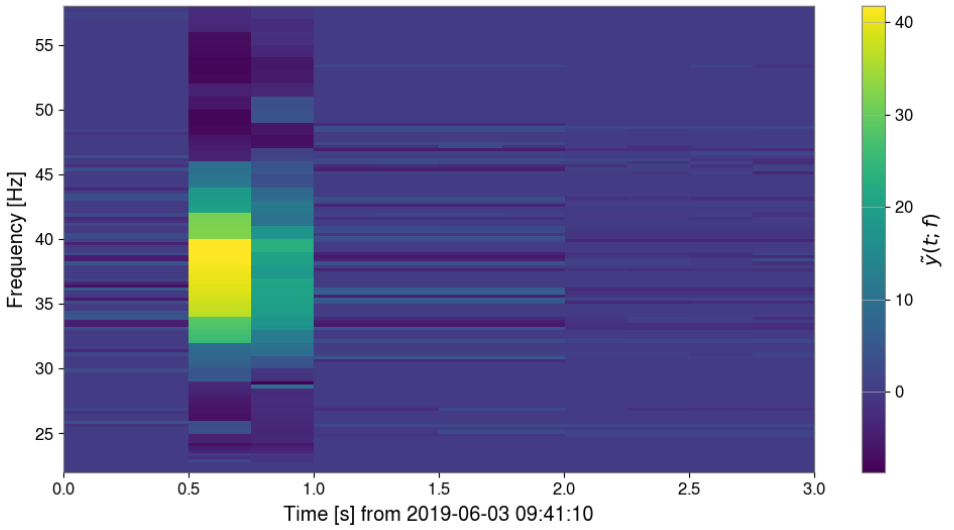

Figure 4.20: Coherent tf-map of the loudest background trigger found in the `PySTAMPAS` O3a analysis before the application of the SNRfrac veto.

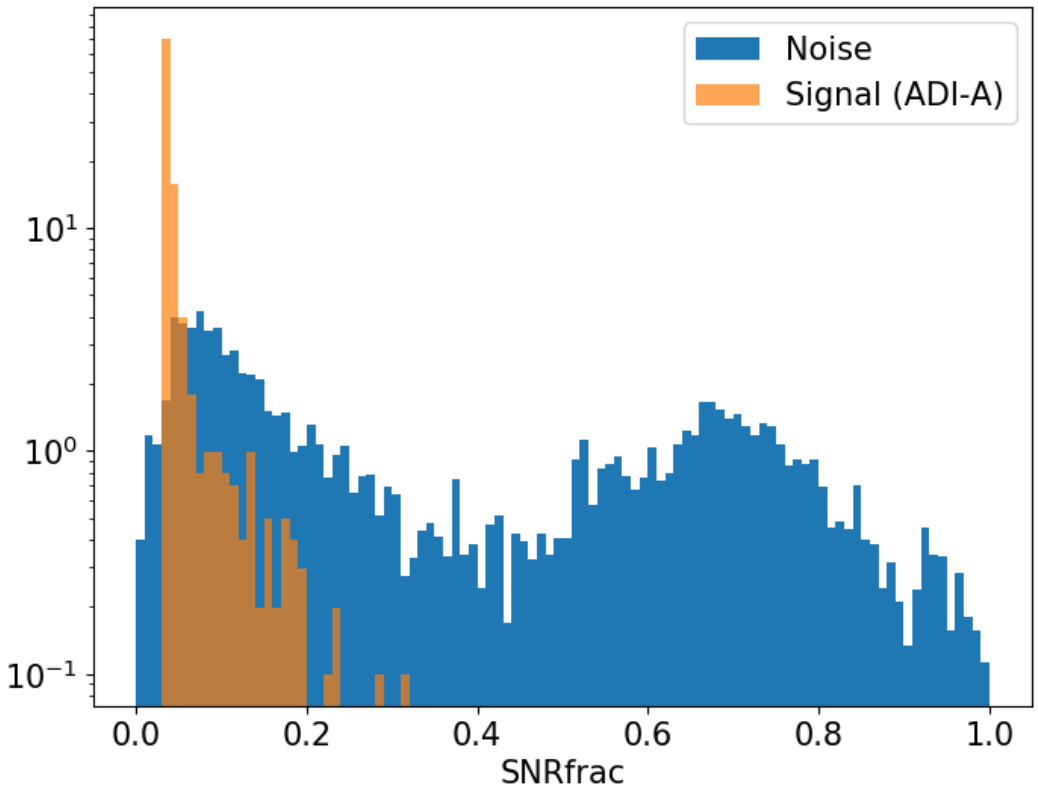

Figure 4.21: Distribution of the discriminant variable SNRfrac for noise triggers found in O3a by `PySTAMPAS` and an ADI-A signal injected at distances between 1 and 50 Mpc.

Notably, sensitivity for the sine Gaussian signal (SG-C) is increased by a factor 2.8. This is

mainly due to the fact that we estimate the PSD over a segment of time that is longer than the duration of this signal.

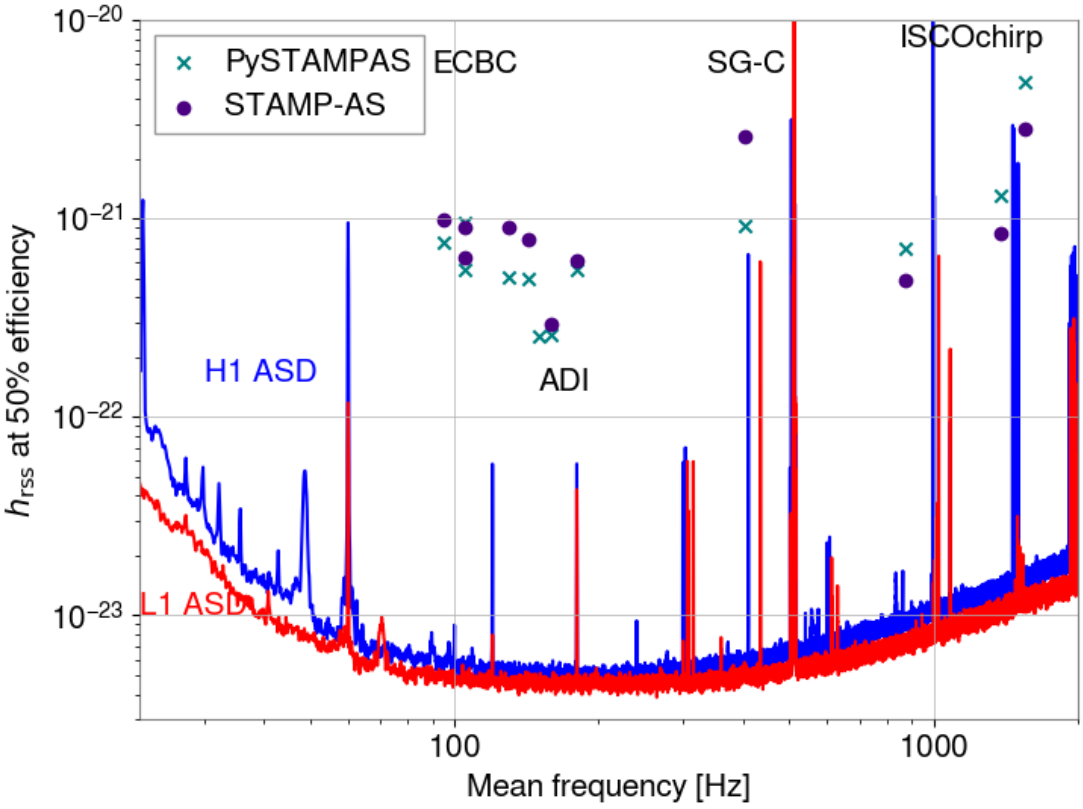

Figure 4.22: Values of h_{rss} at 50% detection efficiency and a FAR of $1/50\,\mathrm{yr}^{-1}$ are represented for each waveform as a function of its mean frequency for the O3a search. Green crosses represent values obtained with `PySTAMPAS`, while purple dots represent the results obtained with `STAMP-AS` for the same waveforms. The detectors' averaged amplitude spectral densities during O3 are shown with the blue and red curves for H1 and L1 respectively.

4.4.3 Coincident analysis

The results of the coincident analysis are shown in Figure 4.23. The loudest trigger has a false alarm rate of 1 per 363 days, corresponding to a p-value of 0.27. Its time-frequency map is represented in Figure 4.24, and is typical of triggers generated by PSD fluctuations at low frequency. Once again, we report no detection of a GW signal.

4.5 Conclusions and potential improvements

We have used `PySTAMPAS` on real data and seen that despite the promising results obtained on Gaussian noise, a substantial amount of work is needed to make the pipeline competitive for real data analysis.

For each run, we used a different PSD estimation method. We saw that the frequency-median PSD offers much better sensitivity to monochromatic signal than `STAMP-AS` or `Coherent WaveBurst`, by at least one order of magnitude (i.e a factor 100 on the GW energy emitted and a factor 1000 in the detection volume being surveyed). However, the numerous spectral lines

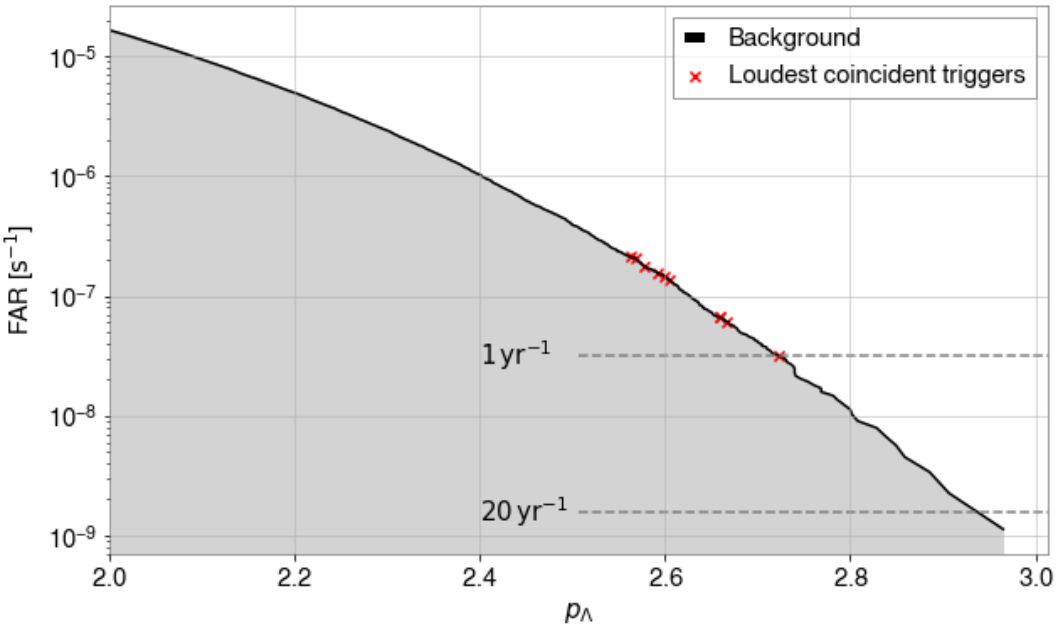

Figure 4.23: False alarm rate of the `PySTAMPAS` O3a search as a function of p_Λ after applying all post-processing selection criteria (DQ flags and SNRfrac). On top of the curve are placed the values for the 10 most significant triggers found in coincidence with red crosses.

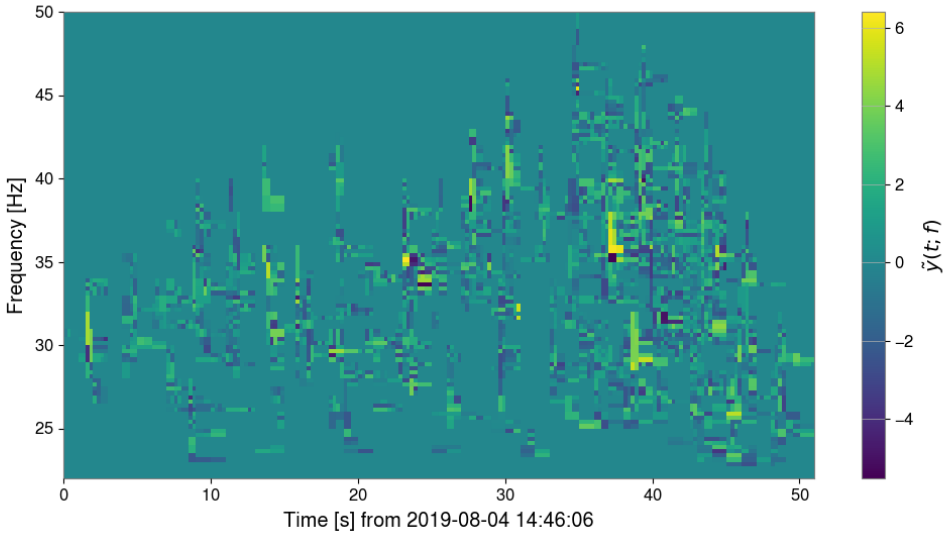

Figure 4.24: Coherent tf-map of the loudest coincident (zero-lag) trigger found by `PySTAMPAS` during O3a.

that are present in the detectors' noise are enhanced with this method and generate a lot of loud background triggers. The use of frequency masks and Rveto allows to clean the background distribution, but it is at the cost of sensitivity to non-monochromatic signals, which are also affected by these cuts. The algorithm we use to flag spectral lines is quite basic, and it may be worthwhile to devote efforts to use or develop more intelligent lines removal techniques in the

future.

The results we have obtained on O3a with the time-average PSD were closer to what we could expect from Gaussian noise analyses, with an overall increase in detection efficiency compared to the previous version of `STAMP-AS`. The discriminant variable SNRfrac is very efficient to remove the short glitches that constitute the loudest background triggers, and it does not affect signal as much as *Rveto* does.

In any case, we showed that it is possible to perform rapid background estimations for all-sky / all-time searches with seed-based clustering. We did not go beyond 100 years of background in these searches because there was no significant event that would have required to estimate background further, but in future runs, with increased detectors' sensitivity, it is plausible that events with FAR lower than 1 per 100 years will be detected. In this case, it would be necessary to generate enough background to correctly estimate the FAR of such events, so rapid background estimation will become crucial. In any case, it is worthwhile to begin with analysing a small amount of background noise to identify the problems, select the appropriate DQ flags and develop post-processing vetoes if necessary, before running a "blind analysis" of several hundred years.

4.5.1 Development of a new detection statistic

We have seen in Section 4.3 that the tail of the background distribution is dominated by non Gaussian noise trigger (mostly transient spectral lines). Applying the *Rveto* selection criteria to clean up this distribution degrades the detection efficiency, as a fraction of the injections is vetoed. Let us investigate this problem further. Recall from Eq. (3.37) that the detection statistic p_Λ involves different quantities: the coherent summed signal to noise ratio SNR_Γ and the normalized residual energies in each detector

$$E_I^{res} = \sum_{(t,f)\in\Gamma} \mathrm{SNR}(t;f) - |\tilde{y}_I(t;f)|^2.$$

To simplify the problem and consider it in way that is symmetric between all detectors, we can define the summed residual energy

$$\Sigma_{\mathrm{res}} = \sum_I \frac{E_I^{res}}{E_I}. \tag{4.4}$$

Therefore, in the limit $\mathrm{SNR}_\Gamma >> \Sigma_{\mathrm{res}}$,

$$p_\Lambda \equiv -\log(|1-\Lambda|) \simeq \log\left(\frac{\mathrm{SNR}_\Gamma}{\Sigma_{\mathrm{res}}}\right). \tag{4.5}$$

The qualitative argument that made us choose this definition for p_Λ is that for a true GW signal, SNR_Γ should be large and Σ_{res} should remain small, while for a noise trigger, even with a high value of SNR_Γ, Σ_{res} has no reason to be small. Without more knowledge on the respective distributions of noise and signal over real data, taking the ratio between these two quantities was a reasonable choice. However, now that we have access to those distributions with real data, we can re-evaluate the relevance of this choice and define a more adapted detection statistic.

In Figure 4.25, we show the distributions SNR_Γ versus Σ_{res} for the noise and signal triggers extracted from the O2 analysis. Noise triggers that overlap DQ flags have been removed, but Rveto has not been applied. Signal triggers correspond to ADI-A and ISCOchirp-B waveforms. The separation between the two populations, noise and signal, is well marked. In particular, when values of SNR_Γ become significant ($\gtrsim 2000$), Σ_{res} is a better discriminant variable between noise and signal. To evaluate the ability of p_Λ to discriminate signal and noise, we draw isovalues of the p_Λ statistic in the figure (black dashed line). We can see the shortcomings of this variable: the tail of the background distribution, at $p_\Lambda \geq 3$, is not separated from the signals despite having

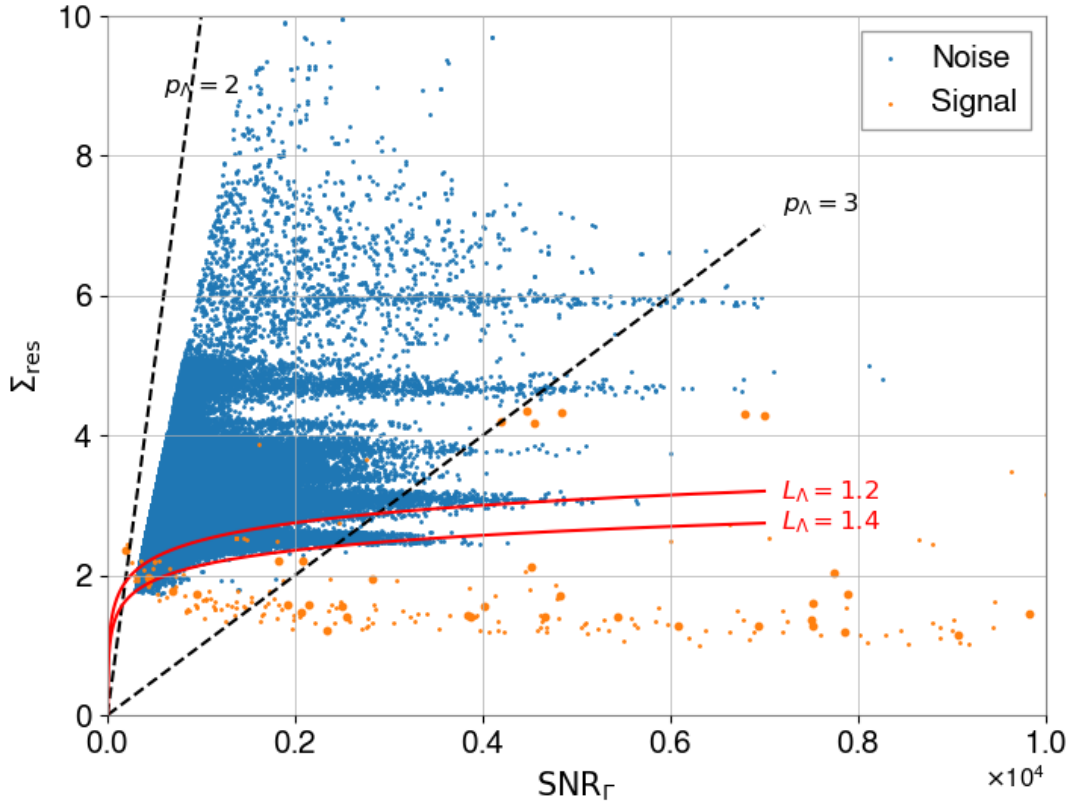

Figure 4.25: Distribution of SNR_Γ versus Σ_{res} for noise triggers extracted in the O2 and O3a analyses (in blue), and for triggers associated with injections (in orange). Two waveforms, ADI-A and ISCOchirp-B, were used and injected at various amplitudes. The black dashed curves represent isovalues of p_Λ, and the red curve are isovalues of the new statistic L_Λ defined in Eq. (4.6).

much larger values of Σ_{res}. This behaviour, which is not present in Gaussian noise simulations, leads to a loss of sensitivity.

By observing the distribution of noise triggers in the $\text{SNR}_\Gamma - \Sigma_{\text{res}}$ plane, it seems that another combination of these two quantities may be more appropriate. If we define

$$L_\Lambda = \frac{\log \text{SNR}_\Gamma}{\Sigma_{\text{res}}}, \tag{4.6}$$

we can see in Figure 4.25 that isovalues of this new statistic (red lines) provide more discrimination between the two populations. To test that hypothesis, we re-compute the FAR distribution as a function of L_Λ instead of p_Λ, then we re-compute the detection efficiencies using a threshold on L_Λ that corresponds to a FAR of 1 per 50 years. The FAR curve obtained is shown in Figure 4.26. Contrary to the curve obtained with p_Λ (Figure 4.14), the tail is absent. Values of h_{rss} at 50% detection efficiency for the different waveforms are shown in Table 4.5 with a detection threshold of 1.5 on L_Λ. We report an increase in sensitivity of 15% in average compared to the results obtained using p_Λ as detection statistic[7].

This work shows that it is possible to significantly improve the detection efficiency by adapting the detection statistic to the characteristics of the noise distribution. The definition of L_Λ we

[7]The extreme value of 4.86 obtained for ECBC-D is removed from the computation of the relative improvement. It grows to 40% when that value is included

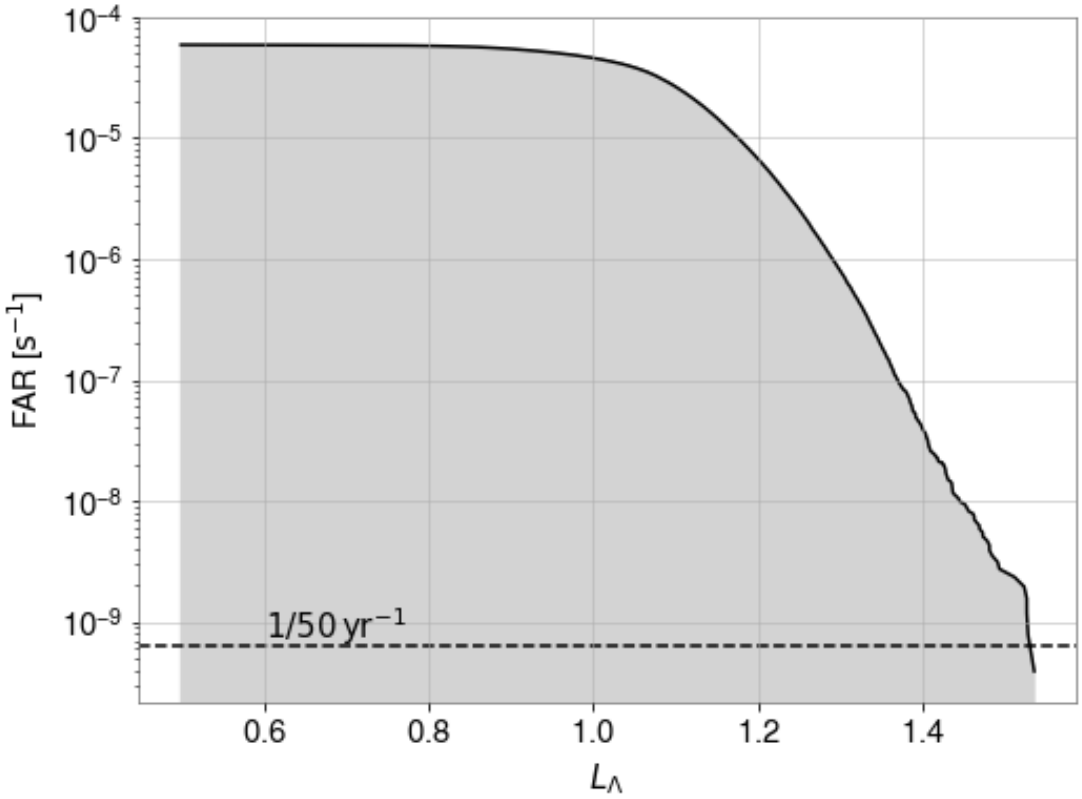

Figure 4.26: False alarm rate as function of the new detection statistic L_Λ for the O2 `PySTAMPAS` search after removing triggers corresponding to DQ flags. Rveto is not applied.

have chosen here gives satisfactory results for the analysis of O2 with the frequency-median PSD, removing the need for post-processing cuts that affect the detection efficiency, and allowing to reach detection efficiency similar or better than `STAMP-AS` for a majority of the waveforms tested.

In this case, the construction of L_Λ is dependant on the data set. We choose its expression by looking at the distribution of two discriminant variables, SNR_Γ and Σ_{res}, over noise and signal. This process could be automated *via* a simple neural network, which would have the advantage of being adaptative to each data set analyzed. However, when training such a neural network, one should be careful to feed it with signals covering a large range of morphologies, in order to avoid overfitting the data and biasing the trigger selection towards a certain type of signal.

4.5.2 Reconstruction of GW170817

The binary neutron star merger signal GW170817 was observed on 17 August 2017 at 12:41:04 UTC by the three detectors H1, L1 and V1. The detection of counterparts along the whole electromagnetic spectrum opened the era of multi-messenger astronomy. The relatively low chirp mass of the system ($M_c \simeq 1.19\,\mathrm{M}_\odot$) means that the signal was present in the sensitive band of the detectors for several dozens of seconds. Hence, it falls within the parameter space covered by long-duration searches. The merger signal was detected with matched filtering techniques with a combined SNR of 32.4 [19]. Despite its very high significance, it was not seen by `STAMP-AS` during the all-sky search on the O2 run [133]. Similarly, I did not found any signal in the re-analysis of this run with `PySTAMPAS` presented in Section 4.3.

Since the GW signal from compact binary mergers is well modelled and depends on a relatively

Waveform	p_Λ	L_Λ	Relative improvement
ADI-A	3.35e-22	3.2e-22	1.05
ADI-B	4.6e-22	4.54e-22	1.01
ISCOchirp-A	1.2e-20	1.32e-20	0.91
ISCOchirp-B	2.53e-21	2.68e-21	0.94
ISCOchirp-C	1.03e-21	1.08e-21	0.95
NCSACAM_A	2.16e-21	1.65e-21	1.31
NCSACAM_B	2.33e-21	1.76e-21	1.323
NCSACAM_C	1.29e-21	1.21e-21	1.07
NCSACAM_D	1.57e-20	3.23e-21	4.86
NCSACAM_E	3.19e-21	1.94e-21	1.64
NCSACAM_F	1.65e-21	1.18e-21	1.40
SG-C	5.97e-22	5.91e-22	1.01

Table 4.5: Values of $h$rss at 50% detection efficiency and a FAR of 1 per 50 year for the different waveforms tested, using the p_Λ (column 2) and L_Λ (column 3) as a detection statistic. The last column displays the relative improvement obtained by using L_Λ instead of p_Λ.

small number of parameters, they are primarily searched with matched filter algorithms, so the fact that GW170817 was not recovered by neither `STAMP-AS` nor `PySTAMPAS` is not critical *per se*. Yet, unmodelled detection algorithms are used to search for a potential post-merger signal for which we have seen in Chapter 2 that there are large theoretical uncertainties or compact binary coalescnece of systems with eccentricity. Un-modelled searches for a post-merger signal to GW170817 have been performed, focusing short-duration (< 1 s), long-duration ($1 - 500$ s) [150] and very-long duration (several days) [82] signals. None of these searches found a candidate GW signal. The search for a long-lived post-merger signal, which was conducted with `STAMP` and `Coherent WaveBurst`, was sensitive on signals up to a distance of ~ 4 Mpc, that is approximately one order of magnitude lower than the distance of GW170817. Yet, as the post-merger signal is expected to be fainter than the merger one, detecting the latter is a good test of the sensitivity of our pipelines. A non-detection of the pre-merger signal is not promising for the prospect of detecting a post-merger signal.

In figure 4.27 we show tf-maps of the data from L1 and H1 around the time of GW170817. A short glitch was present in L1 data at the time of the event [19], thus we use cleaned data from which the glitch has been removed [151]. The signal is clearly visible by eye in L1. Yet, `burstegard` did not extract any cluster in this tf-map. After investigation, it happens that a large number of pixels have a value of $|\tilde{y}(t;f)|$ below the clustering threshold of 2. Therefore, the most energetic pixels are in general separated by a distance larger than the clustering radius of $2\,\mathrm{s} \times 2\,\mathrm{Hz}$, so the clustering fails to reconstruct the signal.

To see if it is possible to reconstruct the signal, we decide to modify the parameters of the clustering algorithm. The two options would be to lower the threshold on $|\tilde{y}(t;f)|$ to add more pixels, and / or to increase the clustering radius. We opt for the latter in order not to add too much noise pixels. In Figure 4.28, we show the cluster extracted by burstegard after setting the clustering radius to $5\,\mathrm{s} \times 5\,\mathrm{Hz}$. Despite a lot of sub-treshold pixels are missing, a part of the signal is reconstructed. To assess its significance, we build the coherent trigger that corresponds to this cluster by matching it with pixels from H1. The coherent tf-map obtained is shown in Figure 4.29. The trigger has a statistic $p_\Lambda = 2.20$, and $L_\Lambda = 1.64$. Since we have changed the clustering parameters, we have to re-estimate the background distribution, as different noise clusters may be extracted too. The FAR of the search with these new parameters is shown in Figure 4.30 as a function of L_Λ, applying the same DQ flags and post-processing vetos than in the O2 analysis of Section 4.3. The trigger corresponding to GW170817 has a FAR of $2.75 \times 10^{-8}\,\mathrm{s}^{-1}$, that is about 1 per 420 days. Hence, it does not pass the detection threshold of 1 per 50 years.

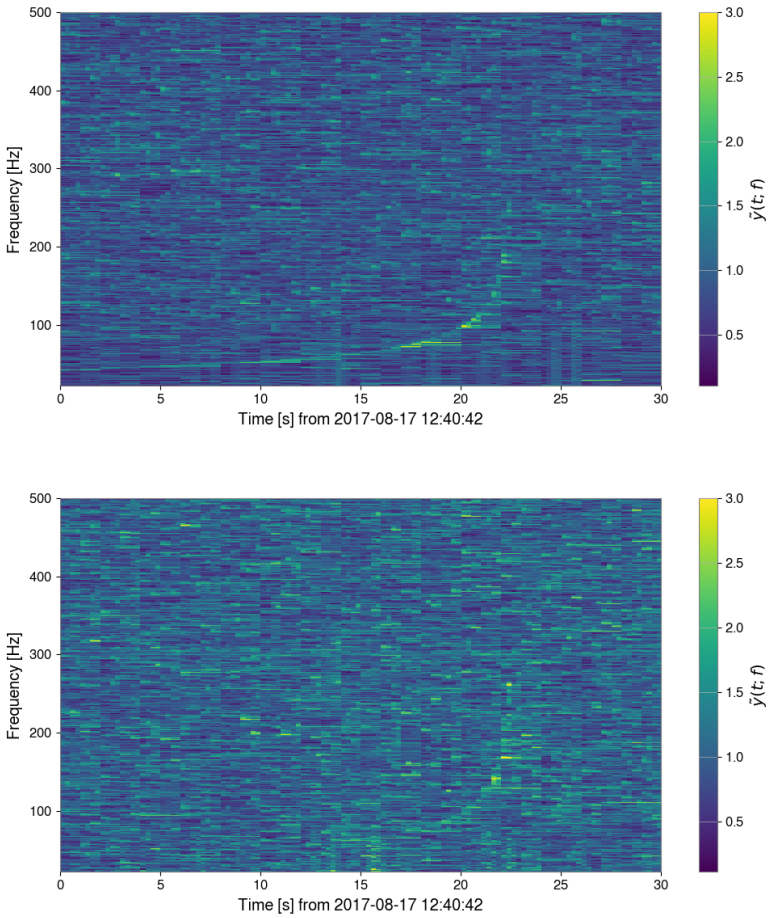

Figure 4.27: Multi-resolution tf-map of the cleaned data from LIGO Livingston (L1, top) and LIGO Hanford (H1, bottom) around the time of GW170817. The maps are made with `PySTAMPAS` using strain data after noise subtraction [151].

Nevertheless, this result highlights a path for future improvement. The distribution of L_Λ shown in Figure 4.30 still has a tail that diminishes the significance of the GW170817 triggers. In purely Gaussian noise, this event would certainly have had a far greater significance, potentially crossing the detection threshold. It is therefore important to find better ways to discriminate non-Gaussian noise triggers for signal. In this respect, discriminant statistics based on spectral shape or coherence between detectors, such as SNRfrac and L_Λ, may be refined and improved.

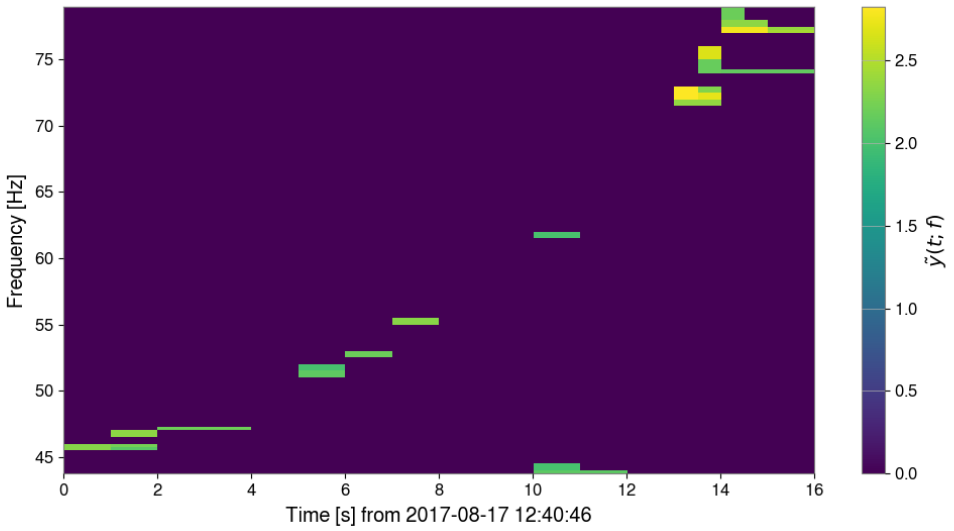

Figure 4.28: Cluster extracted by `burstegard` using a clustering radius of 5 pixels from the tf-map of Figure 4.27.

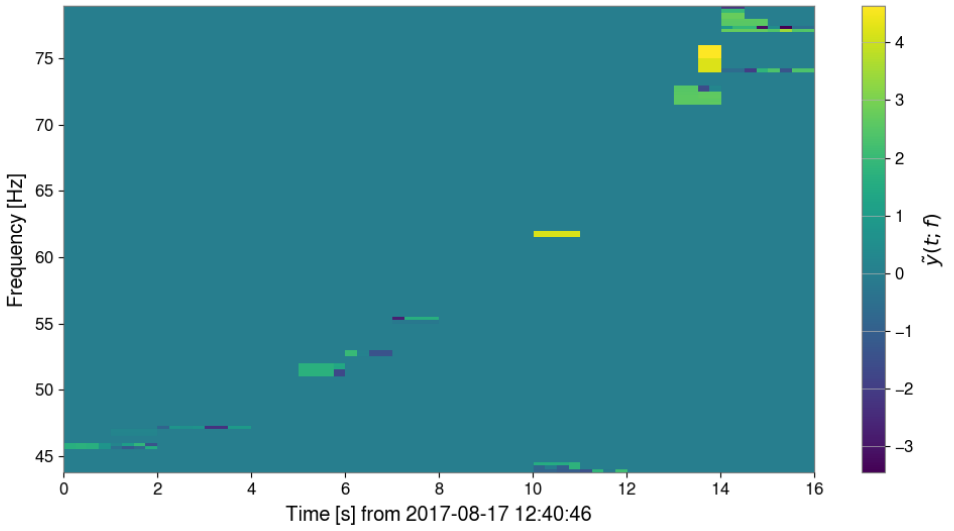

Figure 4.29: Coherent trigger reconstructed by matching the cluster from Figure 4.28 with H1 data.

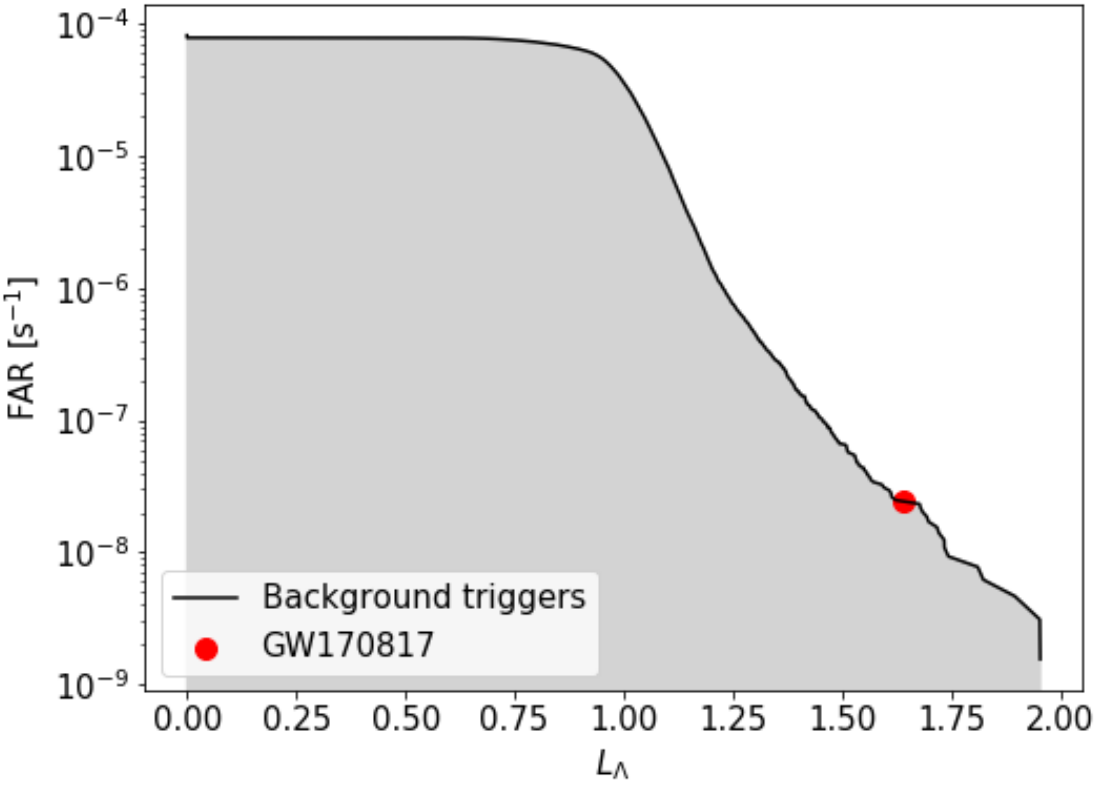

Figure 4.30: Cumulated distribution of background triggers obtained with the configuration of `burstegard` that allows to reconstruct GW170817. We use the statistic L_Λ to better discriminate a signal from loud noise events. The red dot represents the trigger that corresponds to GW170817. It has a FAR of ~ 1 per 420 days.

Chapter 5

Search for long-duration gravitational waves counterpart around Magnetar Giant Flares

In this chapter, I present a targeted search for a gravitational-wave counterpart potentially emitted by 3 short GRBs (GRBs) from nearby galaxies. These results have been published in a paper I wrote with Bizouard, Burns, Christensen, Coughlin, Wadiasingh, and Younes [136].

Unlike all-sky searches, targeted searches look for gravitational wave emission from a particular source. The parameter space is considerably reduced, since the position and time of the targeted source are known with a certain degree of precision. However, the detection method remains the same. It was also an opportunity to use `PySTAMPAS` in a targeted search configuration.

5.1 Magnetar Giant Flares

5.1.1 Context and history

Soft gamma repeaters (SGRs) are astrophysical sources that emit short bursts of soft gamma-rays with peak luminosity in the range $10^{38} - 10^{42}\,\mathrm{erg\,s^{-1}}$ at irregular intervals, separated by months or years of quiescence (see e.g [28, 152, 113]). The first one, SGR 1806-20, was discovered in 1979 in the Large Magellanic Cloud[114], and a handful of SGRs have been observed since then in our galaxy. Among them SGR 1935+2154, first discovered in 2014, has been associated to a fast radio burst, FRB 200428, making the link for the first time between fast radio bursts and magnetar flares [153].

SGRs are now believed to be magnetars, highly magnetized neutron stars with surface magnetic field $B \gtrsim 10^{14}\,\mathrm{G}$, and possibly even larger internal field. In the magnetar model, the huge internal magnetic field constitute the reservoir of energy for the repeated bursts [110, 111, 112].

On rarer occasions, SGRs undergo giant flares, known as *MGF* (MGFs). Those flares typically consist in a short ($\sim 0.1\,\mathrm{s}$) burst of gamma-rays with luminosity around $10^{44} - 10^{47}\,\mathrm{erg\,s^{-1}}$, orders of magnitude higher than "normal" flares. The short burst is followed by a decaying tail in the hard X-rays that can last several hundreds of seconds. Interestingly, this tail features quasi-periodic oscillations (QPOs) at frequencies between $20 - 600\,\mathrm{Hz}$ that could be the signature of non-radial oscillations of the neutron star [117]. Only three MGFs have been observed so far : from SGR 0526-66 in 1979 [114], SGR 1900+14 in 1998 [115] and SGR 1806-20 in 2004 [116, 154], but all three exhibit this typical behaviour, as can be seen in the light curves shown in Figure 5.1.

Beyond the three giant flares observed in the Milky Way, the question arises of potential MGFs from other galaxies. Given the order of magnitude of the energy emitted, $E_{iso} \sim 10^{44} - 10^{47}\,\mathrm{erg}$, only the short gamma-ray flash of an extragalactic MGF could be detected. Because of that,

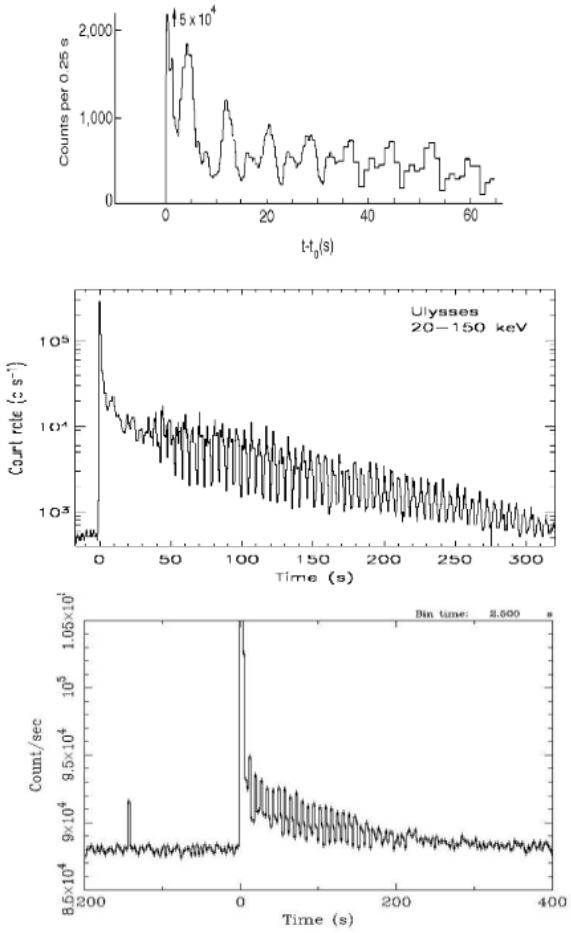

Figure 5.1: Light curves of the three giant flares from galactic SGRs showing the initial burst and pulsating tail. *Top :* SGR 0526-66 (1979), figure from [114]. *Middle :* SGR 1900-14 (1998), figure from [115]. *bottom :* SGR 1806-20 (2004), figure from [116].

such signals would resemble short GRBs emitted by BNS mergers.

Early in 2021, Burns et al. unambiguously identified a sample of 4 short GRBs from nearby galaxies (closer than 5 Mpc) potentially associated to MGF [120]. Indeed, their electromagnetic properties (light curve, spectrum, isotropic energy) differ from the ones of short GRBs, and the no detection of a GW signal from a BNS at such short distances rules out a potential BNS origin. This discovery, added to the three MGFs known from our galaxy, confirms that these sources constitute a significant fraction (more than 1%) of the population of short GRBs [155]. The volumetric rate of MGFs inferred from these events is $R_{\rm MGF} = 3.8^{+4.0}_{-3.1} \times 10^5\,{\rm Gpc}^{-3}\,{\rm yr}^{-1}$ [120], much higher than the rate of compact binary mergers.

Because of the large energy released at a relatively close distance, these sources are potentially observable with gravitational waves [118, 119, 156]. Therefore, the discovery of Burns et al. has motivated us to re-visit these 4 extragalactic GRBs with `PySTAMPAS` to search for a potential gravitational waves counterpart.

For two of these events, GRB 051103 and GRB 070201, unmodelled searches for GW emission had already been performed with `X-PIPELINE` [157], the `FLARE` pipeline [158]. They did not found any GW signal, but set upper limits on the gravitational wave emitted. `X-PIPELINE` set limits at 1.2×10^{52} erg for GRB 051103, while `FLARE` found upper limits at 2.0×10^{51} erg and 7.9×10^{50} erg for GRB 051103 and GRB 070201 respectively [159, 160]. The third event, GRB 070222, was only recently included in the sample of potential MGFs. `X-PIPELINE` set an exclusion distance at 8.9 Mpc for short-duration bursts [161]. Finally, the latest event, GRB 200415a [162], happened after the suspension of O3 in March 2021. Only GEO-HF and KAGRA were observing at the time, but we did not analyze those data. The results of a search for GW counterpart to GRB 200415a in GEO-HF and KAGRA data will be reported in a forthcoming publication of the LIGO-Virgo-KAGRA collaboration. All the upper limits given here are for the $100 - 200$ Hz band, where the detectors are the most sensitive.

5.1.2 Potential gravitational-wave emission processes

Gravitational waves are emitted if the magnetar develops a sufficiently strong time-varying quadrupole moment. Given the large amount of energy released during a giant flare, it is likely that some oscillation modes of the star are excited. However, it is difficult to understand exactly which modes are excited, where and how.

Excitations of the fundamental f-mode were originally thought to be able to generate detectable GW at frequencies $\sim 1 - 2$ kHz [118, 119]. From the reservoir of magnetic energy, Ioka [118] and Corsi and Owen [119] computed the maximal energy released via gravitational waves to be around $\sim 10^{48} - 10^{49}$ erg. However, these optimistic predictions have since been ruled out by numerical simulations, and it is now believed that this mode cannot be excited sufficiently to generate GW at a detectable amplitude unless the magnetic field is orders of magnitude higher that what it is observed [163, 164, 165]. Besides, the high volumetric rate of such events [120] makes it likely that they occur several times during the life of the magnetar, so this disfavours scenarios in which all the reservoir of energy is consumed at once.

Prospects for detecting GW from magnetars still exist however. The QPOs observed in the pulsating tails of several MGFs could be associated with oscillation modes being exited at lower frequencies for a longer amount of time [166]. These could be coupled with GW emission in the $200 - 600$ Hz band [167, 168, 163], for which current detectors are the most sensitive. The QPOs seem to damp on short timescales (~ 1 s), but are continuously re-excited. It is not clear which oscillation modes exactly are associated with the QPOs, and how they couple to GW emission. In particular, we do not know if they involve only the crust or also the core of the magnetar. In the latter case, GW emission could be much stronger than in the former, because the crust represents only a small fraction of the total mass of the star.

Once again the large uncertainties on the models motivate the use of an unmodelled search algorithm, and for this particular case, consider a short-duration and long duration GW emission.

We are particularly interested in constraining the ratio E_{GW}/E_{iso} of gravitational waves energy emitted to the isotropic electromagnetic energy, as it could give an indication on the location of the trigger (internal or magnetospheric).

5.2 Description of the searches

5.2.1 Data sample

Following the discovery of Burns et al. [120], we consider 4 short GRBs which are potentially MGFs. For GRB 051103 [169, 170], GRB 070201 [171, 172] and GRB 070222 [120, 173], we use coincident data from two of the three initial LIGO detectors (H1, H2 and L1) from the 5^{th} science run (S5). GRB 200415a [174, 175] happened after the end of O3 unfortunately. Only KAGRA (K1) and the GEO-HF (G1) were observing at the time, and we did not analyzed those data as they are still covered by the proprietary data period (a collaboration paper is in preparation). However, we considered it for a prospective study to estimate the chance of detecting a GW signal when advanced GW detectors will reach their design sensitivity, expected during O5 [176]. The main properties of each source are summarized in table 5.1

Event	Time (UTC)	Host	Distance (Mpc)	Detectors	Pair efficiency
GRB 051103	09:25:42 UTC 3 November 2005	M81	3.6	H2, L1	0.47
GRB 070201	15:23:10 UTC 1 February 2007	M31	0.77	H1, H2	0.30
GRB 070222	07:31:55 UTC 22 February 2007	M83	4.6	H1, H2	0.32
GRB 200415a	08:48:05 UTC 15 April 2020	NGC 253	3.3	G1, K1	0.47[1]

Table 5.1: Properties of each event and detectors that were observing at the time of each event. Pair efficiency is the quantity ϵ_{IJ} defined in Eq. (3.22). H2 is the 2 km-long arm interferometer that shared the same vacuum chambers than H1 during 2012

5.2.2 Configuration of the pipeline and method

Given that the QPOs damp on short timescales, potential scenarios of GW emission also include short-duration signals. To consider such a possibility, we configure `PySTAMPAS` to search for shorter signals with duration $\sim 1\,$s. To do so, we set up the clustering algorithm to favour short signals composed of a few amount of pixels. Hence, two searches are done for each source : a long-duration one and a short-duration one, which use different configurations of the pipeline.

On-source and off-source windows

Each search around each of the 3 GRBs is performed independently. The methodology is the following. We define two data sets. The search itself is performed on an *on-source* window, that consists in an interval of time that contains the event, and therefore the potential signal we expect to detect. To estimate the background distribution and the sensitivity of the search, we use an *off-source* window. It is a larger data set, which we take as close as possible to the event, but excluding the on-source window. We assume that the characteristics of the noise in the off-source window are representative of the ones in the on-source window.

To choose the duration of the on-source window, we have to take into account the expected duration and the GW signal, and its potential delay with respect to the gamma-ray emission. As we saw, these parameters are poorly constrained [163]. In order not to exclude any possibility, we opt for 512 s on both sides of the GRB trigger time. This allows us to keep the value of T_{win} used in all-sky searches. The on-source window is split into three windows of 512 s that overlap by 50%. Regarding the off-source window, its precise length is not fixed, because of discontinuities in the data available. It consists in about ~ 10 total days of coincident data. It is also split in 512 s, 50% overlapping windows.

Data pre-processing

Following the method described in section 3.2, each window is analyzed independently to search for excess power clusters. The clusters are cross-correlated with the other detector's data and the detection statistic p_Λ is computed.

The data are high pass filtered with 22 Hz frequency cut-off and gated to remove short glitches. Among the two available methods to estimate the PSD, we opt for the frequency-median because it provides increased sensitivity to quasi-monochromatic signals. Like in previous searches, the window for the moving median is set to 20 Hz.

Time-frequency maps of the whitened statistic $\tilde{y}(t, f)$ are built with a time-frequency resolution of $1\,\mathrm{s} \times 1\,\mathrm{Hz}$ and 50% overlap between time segments. We do not use the multi-resolution feature for this study because it is not useful for quasi monochromatic signals. The frequency range of the maps is $30 - 2000\,\mathrm{Hz}$, which is adapted to the PSD of LIGO detectors during the S5 run.

The frequency-median method for PSD estimation makes the analysis very sensitive to spectral lines. We use frequency notches to mask problematic frequency bins. The algorithm used to select the bins to mask is the same than the one used for the all-sky search in O2 data : if a frequency bin has a mean value of $|\tilde{y}(t; f)|$ greater than 2 in more than 5% of the total windows, it is notched. This process is done on the off-source window, and the frequency notches are then applied also to the on-source window.

Clustering

We use `burstegard` as clustering algorithm. Since the parameters of the search are not the same than for an all-sky search, we tune the algorithm differently. Two sets of parameters are defined for long and short-duration searches. In the first configuration, we target long-duration signals. Therefore, we set a rather low threshold on the pixels' energy (corresponding to select $\sim 10\%$ of the total number of pixels of a tf-map), and dismiss clusters that are constituted of less than 20 pixels. The minimal number of pixels is lower than in all-sky searches, but it is compensated by the fact that we use only one resolution, so clusters contain less pixels in average.

Given that there are plausible scenarios for short-duration GW emission, we decided to do a complementary search using a configuration that targets specifically short lived signals (~ 1 s). As the successor of `STAMP`, `PySTAMPAS` was not initially designed to perform such searches. Other data analysis pipelines, such as `Coherent WaveBurst` and the `X-PIPELINE`, are traditionally used for short-duration searches in LIGO-Virgo data. Nevertheless, the detection principle remains the same. To increase sensitivity to short signals, we first decrease the minimal number of pixels per cluster to 5. Indeed, we expect that kind of signals to have all their energy spread over only a few pixels. To compensate for the increased number of noise clusters generated, we increase the threshold on $|\tilde{y}(t; f)|$ to 2.5, leading to consider less than 1% of the total number of pixels in a tf-map.

Coherent analysis

Coherent analysis differs from an all-sky search because the direction to the source $\hat{\Omega}$ is known, and consequently the antenna patterns and time delay between detectors [2].

In practice, the localization of a GRB is given with an error box that can be rather large. Luckily, all 3 events considered here has been associated with a host galaxy whose coordinates are known. Nevertheless, the angular diameter of nearby galaxies on the sky is not negligible. To consider the most extreme case, M31 has an angular diameter of $\sim 3^o$. We can go back to the computations of section 3.2 to estimate the relative loss of SNR $1 - \epsilon$ induced by the uncertainty

[2] The current version of `PySTAMPAS` does not consider a possible error box around an event.

on $\hat{\Omega}$:

$$\epsilon \simeq (\pi f d\tau)^2. \tag{5.1}$$

For GRB 070201 and GRB 070222, the only detectors for which we have data are H1 and H2, which are co-located. There is no delay, therefore $\epsilon = 1$. Only for GRB 051103 we are in the case of spatially separated detectors, H2 and L1, for which the distance is ~ 3000 km. The error box given by the GCN [169] for this event is 120 squared arcminutes. Using this information, we can constrain the maximal loss of SNR (which happens in the case where the error $d\vec{\Omega}$ is parallel to the baseline) to $\sim 8\%$ at 2000 Hz, which is acceptable as a first approximation.

In addition, it should be noted that the antenna factors and time delay are not recomputed for each cluster when performing background and efficiency estimation. Indeed, we want to assess the sensitivity of the search to a precise event that happened at a fixed time and duration. Therefore, we always use the values that correspond to the configuration of the detectors network at the time of the event.

5.2.3 Waveforms tested

Given the theoretical uncertainties on the GW emission processes and the number, it is not really pertinent to use astrophysically motivated waveforms to estimate the sensitivity of the search. Instead, we opt for more generic waveforms, sinusoidal signals damped with an exponentially decaying envelope. These waveforms depend on 3 parameters, the amplitude A_0, central frequency f_0 and decay time T. We create circularly polarized waveforms for which the GW strain is

$$\begin{aligned} h_+(t) &= A_0 \cos(2\pi f_0 t) e^{-t/T} \\ h_\times(t) &= A_0 \sin(2\pi f_0 t) e^{-t/T}. \end{aligned} \tag{5.2}$$

For the long-duration search, we use 6 different signals with $f_0 \in \{100\,\text{Hz}, 250\,\text{Hz}, 500\,\text{Hz}\}$ and $T \in \{2\,\text{s}, 10\,\text{s}\}$. To simulate a short lived signal we use a single sine damped waveform with a decay time $T = 0.2\,\text{s}$ at $f_0 = 100\,\text{Hz}$. Indeed, we saw when doing the long duration search that sensitivity for a monochromatic signal scales with the detector's PSD, so it is not necessary to scan all the frequency range. Nevertheless, this set of waveforms allows to cover the parameter space of low-frequency $20-500\,\text{Hz}$ GW emission scenarios associated with the QPOs. Waveforms are injected with antenna factors and a time delay corresponding to the time and location of the event, but with random values of the polarization angle ψ and cosine of the inclination ι to reflect that we do not know *a priori* the orientation of the source[3]. The lack of precisely modelled signals in this case illustrates the interest of a search algorithm that makes minimal assumptions on the signal's morphology. Indeed, the GW signal emitted during MGFs may be more complex than a simple sine damped. However, we have seen than the pipeline is mainly sensitive to the global characteristics of a signal, namely the mean frequency and duration, so results obtained with sine damped should not be different than ones obtained with more realistic waveforms. A caveat to that claim is the case of repeating signal, for which the search sensitivity could be improved by stacking the signal.

To constrain models, we are particularly interested in the energy E_{GW} emitted in the form of GW, and its ratio with the isotropic electromagnetic energy E_{iso} radiated during the flare. Recalling the quadrupole formula, the GW energy emitted by a source seen at a distance r

$$E_{\text{GW}} = r^2 \frac{c^3}{4G} \int (\dot{h}_+^2(t) + \dot{h}_\times^2(t))\, dt. \tag{5.3}$$

Since r is known from the host galaxy, we can estimate or place limits on the GW energy emitted during the flares.

[3]Targeted searches for GW emitted by GRBs usually consider that the source is seen face-on ($\iota = 0$) because the GRB jet is beamed. We do not make that assumption here, which results in a relative loss of sensitivity for our search by a factor ~ 0.7.

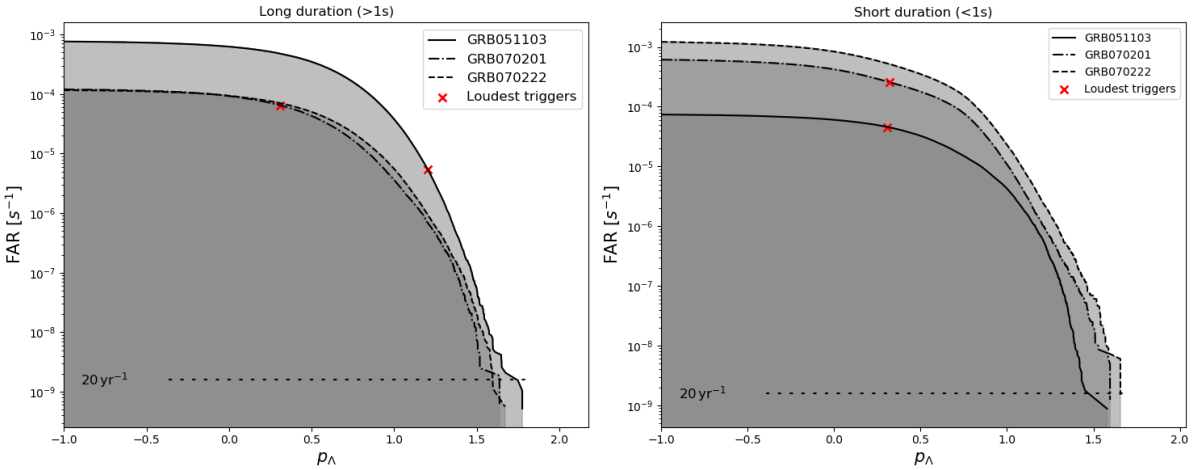

Figure 5.2: Cumulative distribution of background triggers for each GRB. Crosses represent the GW triggers found in the on-source windows of GRB 051103 and GRB 070201. No trigger was found for GRB 070222. The left and right panels show the results of long-duration and short-duration searches, respectively. Figure from [136]

5.3 Results

5.3.1 Background estimation

For each of the 3 searches, the off-source window contains ~ 10 days of data. We perform 1000 time slides, allowing to simulate ~ 27 years of background noise, and fix a detection threshold corresponding to a FAR of 1 per 20 years. Note that to compute the false-alarm probability, the observing time is the duration of the on-source window, which is 1024 s, much shorter than the off-source window. Therefore, a FAR of $1/20\,\mathrm{yr}^{-1}$ corresponds to a FAP of 1.6×10^{-6}, i.e a confidence of more than $4.5\,\sigma$.

For each event, we perform two distinct searches using the long and short duration configurations respectively. To clean the background distributions from loud transient noise, we apply Rveto with a rather high threshold of 10, which has no influence on the sensitivity of the search. The results of background studies are shown in figure 5.2. Distributions of background triggers feature no significant outlier.

5.3.2 Coincident analysis

The FAR of the loudest trigger found in the on-source window is shown on top of the FAR curve in Figure 5.2 for each search. No trigger was found in the on-source window for GRB 070222. Their properties are described in Table 5.2. A coherent tf-map of the most significant trigger found is shown in Figure 5.3. Its frequency around 240 Hz makes it likely to be a fluctuation of an harmonic of the 60 Hz power line. All triggers found in the on-source windows have a FAR and morphology compatible with the null hypothesis, hence we report no significant gravitational wave candidate.

5.3.3 Upper limits on gravitational wave energy radiated

Using the set of sine damped waveforms, we compute the value of GW energy at 50% detection efficiency for each search with a threshold of $1/20\,\mathrm{yr}^{-1}$ on the FAR. The results are reported in Table 5.3.

It is clear from these results that LIGO detectors' sensitivity of the searches during S5 was not sufficient to have a realistic chance to detect a GW emission, since the upper limits on

GRB	Search	$t_{start} - t_0$ (s)	Duration (s)	Frequency range (Hz)	FAP
GRB 051103	Long	286	8	1640-1642	5.5×10^{-3}
	Short	91	2.5	249–251	2.0×10^{-1}
GRB 070201	Long	158	12	237–243	6.4×10^{-2}
	Short	431	1	783–786	4.8×10^{-1}

Table 5.2: Properties of the loudest triggers found in each GRB on-source window for long-duration and short-duration searches. t_{start} refers to the starting time of the GW trigger, while t_0 is the GRB trigger time. The false-alarm probability (FAP) is inferred from the FAR and the duration of the on-source window.

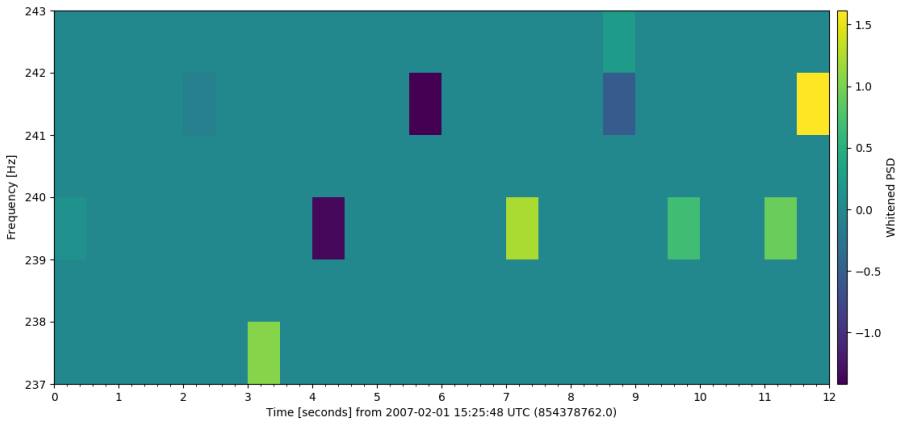

Figure 5.3: Tf-map of the loudest trigger found in the long duration search around GRB070201. It is compatible with an excitation of the 7th harmonic of the 60 Hz power line.

Duration (s)	f_0 (Hz)	GW energy limits (erg)			
		GRB051103	GRB070201	GRB070222	GRB200415a
0.2	100	1.44×10^{52}	3.47×10^{50}	1.69×10^{52}	2.3×10^{49}
2	100	5.95×10^{51}	3.07×10^{50}	9.19×10^{51}	1.43×10^{49}
2	250	2.56×10^{52}	8.83×10^{50}	5.56×10^{52}	1.21×10^{50}
2	500	3.32×10^{53}	1.25×10^{52}	7.13×10^{53}	–
10	100	6.70×10^{51}	2.36×10^{50}	1.24×10^{52}	1.53×10^{49}
10	250	3.22×10^{52}	1.35×10^{51}	6.30×10^{52}	1.14×10^{50}
10	500	4.13×10^{53}	1.69×10^{52}	9.11×10^{53}	–
		Isotropic-equivalent electro-magnetic energy $E_{\rm iso}$ (erg)			
		5.3×10^{46}	1.6×10^{45}	6.2×10^{45}	1.3×10^{46}

Table 5.3: GW energy emitted for a source detected at 50% efficiency for a FAR of 1 per 20 years. Limits for 0.2 s emission have been obtained in the short-duration configuration of the pipeline. Values for GRB 200415a have been obtained using simulated data following the sensitivity of Advanced LIGO at the end of O3. The isotropic electromagnetic energy $E_{\rm iso}$ of each event computed by [120] is given for comparison. Table from [136]

the GW energy emitted we set are $5 - 7$ orders of magnitude higher than the electromagnetic energy detected. However, these limits are improved by about a factor 2 compared to the ones set by previous searches done using the `X-PIPELINE` for GRB 051103 and GRB070201, which demonstrate the capability of `PySTAMPAS` to perform long-duration and short-duration targeted GW searches. They are still higher than the ones reported by `FLARE`, but this pipeline was

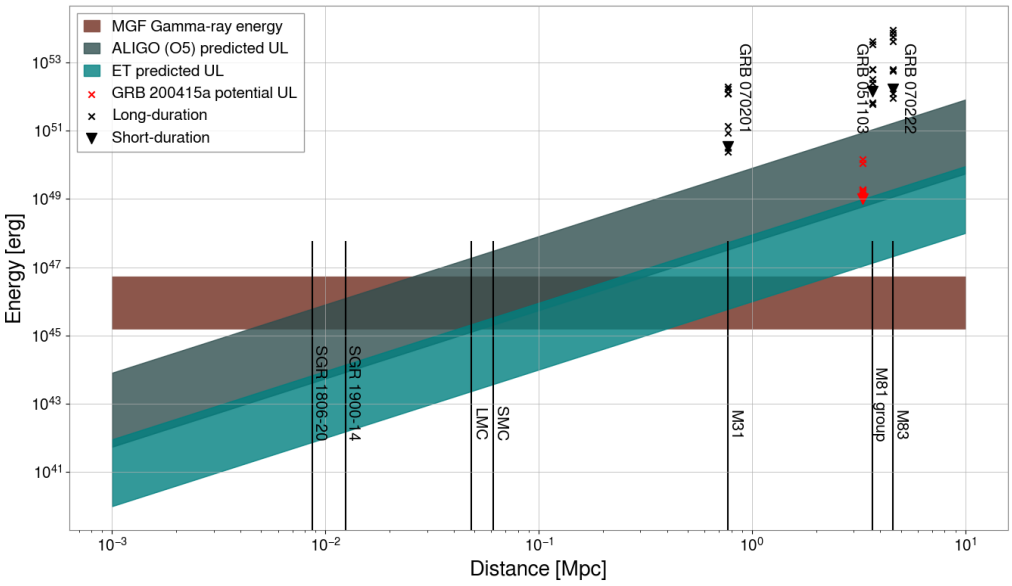

Figure 5.4: Upper limits (UL) on the GW energy emitted by GRB051103 (M81), GRB070222 (M83) and GRB070201 (M31) during are represented with cross markers for long duration emission, and triangular markers for short duration emission. Red markers represent the limits that could have been set up for this GRB 2001415a with LIGO if it was observing at the time. The dark grey band and blue band represent the limit on $E_{\rm GW}$ as function of the distance to the source that will be achievable with Advanced LIGO data at design sensitivity (O5) and Einstein Telescope respectively. The brown band represents the minimal/maximal $E_{\rm iso}$ estimated for the three GRBs analyzed in this study. Distances of nearest galaxies, SGR 1806–20 and SGR1900–14 are also shown.

sensitive to a much more restrained parameter space (only narrow-band signals with duration $\lesssim 0.1\,$s) [158].

For GRB 200415a, the hypothetical limits on the GW energy that could have been observed by Advanced LIGO (O3 sensitivity) if it had been active at the time are $\sim$ 100 times lower than in S5, which is compatible with the gain of a factor 10 in the detectors' strain sensitivity between these runs. However, there is still a gap of more than 3 orders of magnitude between the sensitivity to GW energy and the electromagnetic energy emitted, so potential GW emission processes would have still be difficult to constrain.

5.4 Future prospects and discussion

Despite the large energy released in gamma-rays, we showed that first generation detectors were not sensitive enough to detect a GW emission from an extragalactic MGF, even assuming that the GW energy emitted E_{GW} is much larger than the electromagnetic energy E_{iso}, as could be the case if the trigger of the flare is internal [119]. However, second generation ground-based detectors at designed sensitivity could be sensitive to such values of E_{GW}, and may be able rule out the scenario $E_{GW} >> E_{iso}$ if an event like GRB 070201 happened during a future observing run.

To explore the prospects of a future detection, we perform Monte Carlo studies using Gaussian noise following Advanced LIGO at design sensitivity (expected during O5), and the Einstein Telescope's design sensitivity. We consider the pair H1 L1 of Advanced LIGO, and modelize the

Einstein Telescope with 2 co-located interferometric detectors whose arms form a 60° angle and arbitrarily located in Italy. Using the same set of damped sine waveforms as in the real data search, we compute the detection sensitivity at 50% detection efficiency and FAR of $1/20\mathrm{yr}^{-1}$. Since we are doing a prospective study, signals are injected at random positions on the sky, and the pipeline is then used in the all-sky configuration. Results are summarized in Figure 5.4. We show the upper limit on the GW energy detectable as a function of the distance to the source for different scenarios.

We see that a potential GW emission from an extragalactic MGF will be difficult to detect with second generation detectors if $E_{GW} \sim E_{iso}$. However, third generation detectors such as the Einstein Telescope may be able to approach these values for a relatively close event (e.g in M31).

Prospects of detection are better for galactic events. For SGR 1806-20 and SGR 1900-14, Advanced LIGO at design sensitivity would be able to constrain the GW energy emitted up to 1% of the isotropic electromagnetic energy. Given the fact that 3 galactic MGFs have been observed in the last ~ 40 years, the possibility that such an event happens during a future observing run is not negligible. With a gain of factor ~ 100 in sensitivity to GW energy expected for third generation detectors, the less rare less energetic flares may also come within detection range.

Characterization of gravitational-wave emission from magnetar activity is essential to understand the nature of the unknown trigger(s) of the flares, and how strongly they couple to the interior of the neutron star. This also has implications fore more common short bursts that may share the same physical trigger, since similar QPOs have been reported in those [177, 178]. In addition, given the recent association of a fast radio burst with a short GRB event [153, 179, 180], and proposals that magnetar oscillations may underlie some fast radio bursts, [181, 182, 183, 184], GW studies offer a potentially unique view on the trigger of magnetar bursts. This also motivates the development of new detection algorithms that more specifically targets repeating signals associated with QPOs.

Finally, we note that the volumetric high rate of MGF inferred by [120] potentially allows for a non-negligible contribution to the stochastic GW background [121] by magnetars, which could be pertinent for third generation detectors.

Conclusion

Six years after the first discovery of a gravitational wave signal from the merger of two black holes, gravitational wave astronomy has made tremendous progresses. During the third observing run of Advanced LIGO and Advanced Virgo, which was concomitant with my thesis, compact binary merger detections, that were groundbreaking just a few years ago, became (almost) routine. The frontier is rapidly pushed back, and new sources of gravitational wave may be on the verge of being observed.

Among the potential new sources of gravitational waves not yet observed, this thesis has focused on searches for long-lived (> 1 s) transient signals. Such signals may be emitted in the aftermath of cataclysmic events involving neutron stars or black holes, such as core-collapse supernovae or the remnant of a binary neutron star merger. Models of emission usually involve complex hydrodynamical instabilities, potentially coupled with magnetic field, in a ultra-relativistic framework. Therefore, it is extremely difficult to compute exact waveforms for the gravitational wave signals emitted, so searches have to rely on signal-agnostic methods.

One of these methods, `STAMP`, consists in looking for excess power pixels in a time-frequency representation of the data. To distinguish gravitational-wave signal from the numerous noise transients that are present in the data, it uses the correlation product between data streams from spatially separated detectors. The bulk of my work has consisted in improving and optimizing `STAMP` to perform all-sky searches over a year-long observing run and a network of detectors. It has culminated with the development of a new data analysis pipeline, `PySTAMPAS`, which implements the core of the `STAMP` method along with several new features intended to reduce the computational cost of an analysis and improve detection sensitivity.

I then used this new pipeline to search for long-duration gravitational waves in real detectors' data. I revisited the second observing run of Advanced LIGO/Advanced Virgo, and obtained results comparable with what have been obtained by state of the art pipelines currently used by the LIGO-Virgo-KAGRA collaboration. I also analyzed the first part of the third observing run, in parallel with `STAMP-AS`, and obtained improved upper limits for a wide range of signals tested.

The identification of a sample of short GRBs with a Magnetar Giant Flare origin by Burns et al. in early 2021 [81] has been the occasion to revisit these events with `PySTAMPAS`. Magnetars are promising candidates for detectable gravitational-wave emission, because of their large reservoir of magnetic energy. Knowledge of these objects is still sparse, but it expands rapidly, and characterizing the potential GW emission would be useful to constrain the models, especially for the trigger of the giant flares. I did not detect any signal from the three events that happened in the late 2000's, but I set upper limits on the gravitational-wave energy emitted that are consistent with the literature. I also studied the detection prospects for such events in future observing runs, and showed that Advanced LIGO should be able to detect a GW emission from a galactic magnetar giant flare if the GW energy emitted is more than 1% of the total isotropic electromagnetic energy emitted. Flares from extragalactic magnetars, however, may not be detectable even with third generation detectors, unless the energy emitted via gravitational waves is orders of magnitude higher than the gamma-ray energy.

The first detection of a signal that does not come from a compact binary merger did not happen during O3, but continuous improvement of the sensitivity of detectors, as well as increasing observing time, makes the prospect of a detection more and more likely, and hopefully imminent.

It is therefore important to devote efforts to improve our data analysis techniques in order to maximize the benefit from increased detectors' sensitivity. Detection methods based on an excess cross-power statistic may never reach the sensitivity of optimal matched filter, yet the gap could be partially bridged, for example by developing better clustering algorithms - potentially making more assumptions on the nature of the signal, or by improving the methods to reject transient glitches and spectral lines that increase the false-alarm rate of the search.

The hypothetical detection of an unmodelled gravitational-wave signal in the near future may provide invaluable information on the gravitational-wave emission processes. To be able to constrain the models, our pipeline will have to be extended to be able to reconstruct the waveform of a detected signal, and estimate its parameters.

Bibliography

[1] H. Poincaré. Note de "Sur la dynamique de l'électron". *Comptes Rendus de l'Académie des Sciences Paris*, 150:1504–1508, 1906.

[2] A. Einstein. Die Grundlage der allgemeinen Relativitätstheorie. *Annalen der Physik*, 49:769–822, 1916.

[3] A. Einstein. Nahërungsweise Integration der Feldgleichungen der Gravitation. *Sitzungsber. Preuss. Akad. Wiss. Berlin (Math. Phys.)*, 1:688–696, 1916.

[4] A. Einstein. Über Gravitationswellen. *Sitzungsber. Preuss. Akad. Wiss. Berlin (Math. Phys.)*, 1:154–167, 1918.

[5] F. A. E. Pirani. On the Physical significance of the Riemann tensor. *Acta Phys. Polon.*, 15:389–405, 1956.

[6] F. A. E. Pirani. Invariant formulation of gravitational radiation theory. *Phys. Rev.*, 105:1089–1099, 1957.

[7] H. Bondi. Plane Gravitational Waves in General Relativity. Nature, 179(4569):1072–1073, May 1957.

[8] H. Bondi, F. A. E. Pirani, and I. Robinson. Gravitational Waves in General Relativity. III. Exact Plane Waves. *Proceedings of the Royal Society of London Series A*, 251(1267):519–533, June 1959.

[9] C. M. DeWitt. WADC Technical Report 57-216. In C. M. DeWitt, editor, *Conference on the Role of Gravitation in Physics at the University of North Carolina*. 1957.

[10] P. R. Saulson. Josh Goldberg and the physical reality of gravitational waves. *General Relativity and Gravitation*, **43**:3289–3299, 2011.

[11] J. Preskill and K. S. Thorne. Foreword to feynman lectures on gravitation. In B. Hatfield, editor, *Feynman Lectures On Gravitation*. Addison-Wesley, Reading MA, 1995.

[12] J. Weber. Observation of the thermal fluctuations of a gravitational-wave detector. Phys. Rev. Lett., **17**:1228–1230, Dec 1966.

[13] J. Weber. Evidence for discovery of gravitational radiation. Phys. Rev. Lett., **22**:1320–1324, Jun 1969.

[14] R. A. Hulse and J. H. Taylor. Discovery of a pulsar in a binary system. ApJ, 195:L51–L53, January 1975.

[15] J. H. Taylor, L. A. Fowler, and P. M. McCulloch. Measurements of general relativistic effects in the binary pulsar PSR1913 + 16. Nature, 277(5696):437–440, February 1979.

[16] V. I. Pustovoit and M. E. Gertsenshtein. On The Detection Of Low Frequency Gravitational Waves. *Sov. Phys. JETP-USSR*, **16**:433–435, 1963.

[17] B. P. Abbott et al. Observation of Gravitational Waves from a Binary Black Hole Merger. Phys. Rev. Lett., 116(6):061102, 2016.

[18] R. Abbott et al. GWTC-2: Compact Binary Coalescences Observed by LIGO and Virgo During the First Half of the Third Observing Run. Phys. Rev. X, 11:021053, 2021.

[19] B. P. Abbott et al. GW170817: Observation of Gravitational Waves from a Binary Neutron Star Inspiral. Phys. Rev. Lett., 119(16):161101, 2017.

[20] R. Abbott et al. Observation of Gravitational Waves from Two Neutron Star–Black Hole Coalescences. ApJ, 915(1):L5, 2021.

[21] R. Wald. *General Relativity.* The University of Chicago Press, 1984.

[22] Alexandre Le Tiec. *Gravitation relativiste.* 2016.

[23] A. Einstein. Zur Elektrodynamik bewegter Körper. *Annalen der Physik*, 322(10):891–921, January 1905.

[24] S. Perlmutter, G. Aldering, M. della Valle, S. Deustua, R. S. Ellis, S. Fabbro, A. Fruchter, G. Goldhaber, D. E. Groom, I. M. Hook, A. G. Kim, M. Y. Kim, R. A. Knop, C. Lidman, R. G. McMahon, P. Nugent, R. Pain, N. Panagia, C. R. Pennypacker, P. Ruiz-Lapuente, B. Schaefer, and N. Walton. Discovery of a supernova explosion at half the age of the Universe. Nature, 391(6662):51–54, January 1998.

[25] Adam G. Riess, Alexei V. Filippenko, Peter Challis, Alejandro Clocchiatti, Alan Diercks, Peter M. Garnavich, Ron L. Gilliland, Craig J. Hogan, Saurabh Jha, Robert P. Kirshner, and et al. Observational evidence from supernovae for an accelerating universe and a cosmological constant. *The Astronomical Journal*, 116(3):1009–1038, Sep 1998.

[26] Jolien D.E. Creighton and Warren G. Anderson. *Gravitational-Wave Physics and Astronomy.* WILEY-VCH, 2011.

[27] Richard A. Isaacson. Gravitational radiation in the limit of high frequency. ii. nonlinear terms and the effective stress tensor. *Phys. Rev.*, 166:1272–1280, Feb 1968.

[28] Michele Maggiore. *Gravitational Waves: Volume 2: Astrophysics and Cosmology.* Oxford University Press, 2018.

[29] B. F. Schutz. *The detection of gravitational waves.* Cambridge Univ. Press, 1991.

[30] J Aasi et al. Advanced ligo. *Class. Quantum Grav.*, 32(7):074001, 2015.

[31] F. Acernese et al. Advanced Virgo: a second-generation interferometric gravitational wave detector. *Class. Quantum Grav.*, 32(2):024001, 2015.

[32] Y. Aso, Y. Michimura, K. Somiya, M. Ando, O. Miyakawa, T. Sekiguchi, D. Tatsumi, and H. Yamamoto. Interferometer design of the KAGRA gravitational wave detector. Phys. Rev. D, 88(4):043007, 2013.

[33] F. Acernese et al. Advanced Virgo Status. *J. Phys. Conf. Ser.*, 1342(1):012010, 2020.

[34] M. Tse et al. Quantum-Enhanced Advanced LIGO Detectors in the Era of Gravitational-Wave Astronomy. Phys. Rev. Lett., 123(23):231107, 2019.

[35] J. Aasi et al. The characterization of Virgo data and its impact on gravitational-wave searches. *Class. Quantum Grav.*, 29:155002, 2012.

[36] A. Buikema et al. Sensitivity and performance of the Advanced LIGO detectors in the third observing run. Phys. Rev. D, 102(6):062003, 2020.

[37] Derek Davis et al. LIGO detector characterization in the second and third observing runs. *Class. Quantum Grav.*, 38(13):135014, 2021.

[38] W. Anderson, P. Brady, D. Chin, J. Creighton, K Riles, and J. Whelan. Beam pattern response functions and times of arrival for earthbound interferometer. *LIGO DCC*, T010110-00-A, 2008.

[39] Warren G. Anderson, Patrick R. Brady, Jolien D.E. Creighton, and Eanna E. Flanagan. An Excess power statistic for detection of burst sources of gravitational radiation. Phys. Rev. D, 63:042003, 2001.

[40] F. Acernese et al. Calibration of Advanced Virgo and Reconstruction of the Gravitational Wave Signal $h(t)$ during the Observing Run O2. *Class. Quantum Grav.*, 35(20):205004, 2018.

[41] D. Davis, T. J. Massinger, A. P. Lundgren, J. C. Driggers, A. L. Urban, and L. K. Nuttall. Improving the Sensitivity of Advanced LIGO Using Noise Subtraction. *Class. Quantum Grav.*, 36(5):055011, 2019.

[42] B. P. Abbott et al. Tests of general relativity with gw150914. Phys. Rev. Lett., 116:221101, May 2016.

[43] B.P. Abbott, R. Abbott, T.D. Abbott, M.R. Abernathy, F. Acernese, K. Ackley, C. Adams, T. Adams, P. Addesso, R.X. Adhikari, and et al. Binary black hole mergers in the first advanced ligo observing run. *Physical Review X*, 6(4), Oct 2016.

[44] B. P. Abbott et al. Gw170814: A three-detector observation of gravitational waves from a binary black hole coalescence. Phys. Rev. Lett., 119:141101, Oct 2017.

[45] A. Goldstein et al. An Ordinary Short Gamma-Ray Burst with Extraordinary Implications: Fermi-GBM Detection of GRB 170817A. *Astrophys. J. Lett.*, 848(2):L14, 2017.

[46] B. P. Abbott et al. Gravitational Waves and Gamma-Rays from a Binary Neutron Star Merger: GW170817 and GRB 170817A. ApJ, 848(2):L13, 2017.

[47] B. P. Abbott et al. Multi-messenger observations of a binary neutron star merger. ApJ, 848:L12, 2017.

[48] A. Albert, M. André, M. Anghinolfi, M. Ardid, J.-J. Aubert, J. Aublin, T. Avgitas, B. Baret, J. Barrios-Martí, S. Basa, and et al. Search for high-energy neutrinos from binary neutron star merger gw170817 with antares, icecube, and the pierre auger observatory. ApJ, 850(2):L35, Nov 2017.

[49] B. P. Abbott et al. Gravitational waves and gamma-rays from a binary neutron star merger: Gw170817 and grb170817a. ApJ, 848:L13, 2017.

[50] B. P. Abbott et al. A gravitational-wave standard siren measurement of the Hubble constant. *Nature*, 551(7678):85–88, 2017.

[51] R. Abbott, T.D. Abbott, S. Abraham, F. Acernese, K. Ackley, C. Adams, R.X. Adhikari, V.B. Adya, C. Affeldt, M. Agathos, et al. Gw190521: A binary black hole merger with a total mass of 150 $m_{\odot}$. Phys. Rev. Lett., 125(10), Sep 2020.

[52] R. et al. Abbott. Properties and astrophysical implications of the 150 m binary black hole merger gw190521. ApJ, 900(1):L13, Sep 2020.

[53] B. P. Abbott et al. GW190425: Observation of a Compact Binary Coalescence with Total Mass $\sim 3.4 M_{\odot}$. ApJ, 892(1):L3, 2020.

[54] R. Abbott, T. D. Abbott, S. Abraham, F. Acernese, K. Ackley, A. Adams, C. Adams, R. X. Adhikari, V. B. Adya, C. Affeldt, and et al. Population properties of compact objects from the second ligo–virgo gravitational-wave transient catalog. ApJ, 913(1):L7, May 2021.

[55] B. P. Abbott, R. Abbott, T. D. Abbott, S. Abraham, F. Acernese, K. Ackley, C. Adams, V. B. Adya, C. Affeldt, and et al. Prospects for observing and localizing gravitational-wave transients with advanced ligo, advanced virgo and kagra. *Living Reviews in Relativity*, 23(1), Sep 2020.

[56] M Punturo, M Abernathy, F Acernese, B Allen, Nils Andersson, K Arun, F Barone, B Barr, M Barsuglia, M Beker, et al. The einstein telescope: a third-generation gravitational wave observatory. *Class. Quantum Grav.*, 27(19):194002, 2010.

[57] David Reitze et al. Cosmic Explorer: The U.S. Contribution to Gravitational-Wave Astronomy beyond LIGO. *Bull. Am. Astron. Soc.*, 51(7):035, 2019.

[58] G. Hobbs et al. The international pulsar timing array project: using pulsars as a gravitational wave detector. *Class. Quantum Grav.*, 27:084013, 2010.

[59] Zaven Arzoumanian et al. The NANOGrav 11 yr Data Set: Limits on Supermassive Black Hole Binaries in Galaxies within 500 Mpc. *Astrophys. J.*, 914(2):121, 2021.

[60] Luc Blanchet, Bala R Iyer, Clifford M Will, and Alan G Wiseman. Gravitational waveforms from inspiralling compact binaries to second-post-newtonian order. *Class. Quantum Grav.*, 13(4):575, 1996.

[61] S. Nissanke and L. Blanchet. Gravitational radiation reaction in the equations of motion of compact binaries to 3.5 post-Newtonian order. *Class. Quant. Grav*, 22:1007, 2005.

[62] L. Blanchet, G. Faye, B. R. Iyer, and B. Joguet. Gravitational-wave inspiral of compact binary systems to 7/2 post-Newtonian order. Phys. Rev. D, 65:061501(R), 2002.

[63] Luc Blanchet. Gravitational Radiation from Post-Newtonian Sources and Inspiralling Compact Binaries. *Living Rev. Rel.*, 17:2, 2014.

[64] Frans Pretorius. Evolution of binary black hole spacetimes. Phys. Rev. Lett., 95:121101, 2005.

[65] A. Buonanno and T. Damour. Effective one-body approach to general relativistic two-body dynamics. Phys. Rev. D, 59:084006, 1999.

[66] Parameswaran Ajith et al. Phenomenological template family for black-hole coalescence waveforms. *Class. Quantum Grav.*, 24:S689–S700, 2007.

[67] S. Chandrasekhar and Steven L. Detweiler. The quasi-normal modes of the Schwarzschild black hole. *Proc. Roy. Soc. Lond. A*, 344:441–452, 1975.

[68] Lars Bildsten and Curt Cutler. Tidal Interactions of Inspiraling Compact Binaries. ApJ, 400:175, November 1992.

[69] Michael Coughlin, Patrick Meyers, Eric Thrane, Jialun Luo, and Nelson Christensen. Detectability of eccentric compact binary coalescences with advanced gravitational-wave detectors. Phys. Rev. D, 91(6):063004, 2015.

[70] E. Huerta et al. ENIGMA: Eccentric, Non-spinning, Inspiral Gaussian-process Merger Approximant for the characterization of eccentric binary black hole mergers. Phys. Rev. D, 97(2):024031, 2018.

[71] Nikhil Sarin and Paul D. Lasky. The evolution of binary neutron star post-merger remnants: a review. *arXiv e-prints*, page arXiv:2012.08172, December 2020.

[72] Richard C. Tolman. Static solutions of einstein's field equations for spheres of fluid. *Phys. Rev.*, 55:364–373, Feb 1939.

[73] J. R. Oppenheimer and G. M. Volkoff. On massive neutron cores. *Phys. Rev.*, 55:374–381, Feb 1939.

[74] Masaru Shibata and Keisuke Taniguchi. Merger of binary neutron stars to a black hole: Disk mass, short gamma-ray bursts, and quasinormal mode ringing. Phys. Rev. D, 73:064027, Mar 2006.

[75] Luca Baiotti, Bruno Giacomazzo, and Luciano Rezzolla. Accurate evolutions of inspiralling neutron-star binaries: Prompt and delayed collapse to a black hole. Phys. Rev. D, 78:084033, Oct 2008.

[76] Thomas W. Baumgarte, Stuart L. Shapiro, and Masaru Shibata. On the maximum mass of differentially rotating neutron stars. ApJ, 528(1):L29–L32, jan 2000.

[77] Zhu-Ge Xing, Joan M. Centrella, and Stephen L. W. McMillan. Gravitational radiation from coalescing binary neutron stars. Phys. Rev. D, 50:6247–6261, 1994.

[78] M. Ruffert, H.-T. Janka, and G. Schaefer. Coalescing neutron stars - a step towards physical models. I. Hydrodynamic evolution and gravitational-wave emission. A&A, 311:532–566, July 1996.

[79] V. Ravi and P. Lasky. The birth of black holes: neutron star collapse times, gamma-ray bursts and fast radio bursts. MNRAS, 441:2433–2439, July 2014.

[80] Anthony L. Piro, Bruno Giacomazzo, and Rosalba Perna. The fate of neutron star binary mergers. ApJ, 844(2):L19, jul 2017.

[81] LIGO Scientific Collaboration and Virgo Collaboration. Population Properties of Compact Objects from the Second LIGO-Virgo Gravitational-Wave Transient Catalog. ApJ, 913(1):L7, May 2021.

[82] B. P. Abbott et al. Search for gravitational waves from a long-lived remnant of the binary neutron star merger gw170817. ApJ, 875(2):160, Apr 2019.

[83] B. P. Abbott et al. Search for Post-merger Gravitational Waves from the Remnant of the Binary Neutron Star Merger GW170817. ApJ, 851(1):L16, 2017.

[84] Maurice. H. P. M. van Putten. Gravitational waveforms of kerr black holes interacting with high-density matter. ApJ, 684:L91, 2008.

[85] M. H. P. M. van Putten. Directed searches for broadband extended gravitational wave emission in nearby energetic core-collapse supernovae. ApJ, 819(2):169, 2016.

[86] H. A. Bethe. Supernova mechanisms. *Rev. Mod. Phys.*, 62:801–866, Oct 1990.

[87] Hans-Thomas Janka. Explosion Mechanisms of Core-Collapse Supernovae. *Ann. Rev. Nucl. Part. Sci.*, 62:407–451, 2012.

[88] Evan O'Connor and Christian D. Ott. Black hole formation in failing core-collapse supernovae. ApJ, 730(2):70, Mar 2011.

[89] C. Kouveliotou, S. Dieters, T. Strohmayer, J. van Paradijs, G. J. Fishman, C. A. Meegan, K. Hurley, J. Kommers, I. Smith, D. Frail, and T. Murakami. An X-ray pulsar with a superstrong magnetic field in the soft γ-ray repeater SGR1806 - 20. Nature, 393(6682):235–237, May 1998.

[90] Daniel Kasen and Lars Bildsten. Supernova light curves powered by young magnetars. ApJ, 717(1):245–249, jun 2010.

[91] A. I. MacFadyen, S. E. Woosley, and A. Heger. Supernovae, jets, and collapsars. ApJ, 550(1):410–425, mar 2001.

[92] B. D. Metzger, D. Giannios, T. A. Thompson, N. Bucciantini, and E. Quataert. The protomagnetar model for gamma-ray bursts. MNRAS, 413(3):2031–2056, Mar 2011.

[93] S. E. Gossan, P. Sutton, A. Stuver, M. Zanolin, K. Gill, and C. D. Ott. Observing Gravitational Waves from Core-Collapse Supernovae in the Advanced Detector Era. Phys. Rev. D, 93(4):042002, 2016.

[94] Ernazar Abdikamalov, Giulia Pagliaroli, and David Radice. Gravitational Waves from Core-Collapse Supernovae. 10 2020.

[95] Karolina Rozwadowska, Francesco Vissani, and Enrico Cappellaro. On the rate of core collapse supernovae in the milky way. *New Astron.*, 83:101498, 2021.

[96] S. E. Woosley. Gamma-Ray Bursts from Stellar Mass Accretion Disks around Black Holes. ApJ, 405:273, March 1993.

[97] Anthony L. Piro and Eric Pfahl. Fragmentation of Collapsar Disks and the Production of Gravitational Waves. ApJ, 658:1173, 2007.

[98] M. H. P. M. van Putten. Proposed source of gravitational radiation from a torus around a black hole. Phys. Rev. Lett., 87:091101, 2001.

[99] C. Cutler. Gravitational waves from neutron stars with large toroidal B fields. Phys. Rev. D, 66:084025, 2002.

[100] S. Dall'Osso, L. Stella, and C. Palomba. Neutron star bulk viscosity, 'spin-flip' and GW emission of newly born magnetars. MNRAS, 480(1):1353–1362, October 2018.

[101] D. D. Doneva, K. D. Kokkotas, and P. Pnigouras. Gravitational wave afterglow in binary neutron star mergers. Phys. Rev. D, 92(10):104040, November 2015.

[102] A. Corsi and P Mészáros. Gamma-ray burst afterglow plateaus and gravitational waves: multi-messenger signature of a millisecond magnetar? ApJ, 702:1171, 2009.

[103] Simone Dall'Osso and Luigi Stella. Millisecond Magnetars. *arXiv e-prints*, page arXiv:2103.10878, March 2021.

[104] S. Chandrasekhar. Solutions of Two Problems in the Theory of Gravitational Radiation. Phys. Rev. Lett., 24:611–615, March 1970.

[105] J. L. Friedman and B. F. Schutz. Gravitational radiation instability in rotating stars. ApJ, 199:L157, 1975.

[106] L. Lindblom, B. J. Owen, and S. M. Morsink. Gravitational Radiation Instability in Hot Young Neutron Stars. Phys. Rev. Lett., 80:4843–4846, June 1998.

[107] Weidong Li, Ryan Chornock, Jesse Leaman, Alexei V. Filippenko, Dovi Poznanski, Xiaofeng Wang, Mohan Ganeshalingam, and Filippo Mannucci. Nearby supernova rates from the lick observatory supernova search - iii. the rate-size relation, and the rates as a function of galaxy hubble type and colour. MNRAS, 412(3):1473–1507, Mar 2011.

[108] R. N. Manchester, G. B. Hobbs, A. Teoh, and M. Hobbs. The Australia Telescope National Facility Pulsar Catalogue. AJ, 129(4):1993–2006, April 2005.

[109] Duncan R. Lorimer. Binary and millisecond pulsars. *Living Reviews in Relativity*, 11(1), Nov 2008.

[110] Robert C. Duncan and Christopher Thompson. Formation of Very Strongly Magnetized Neutron Stars: Implications for Gamma-Ray Bursts. ApJ, 392:L9, June 1992.

[111] Christopher Thompson and Robert C. Duncan. The soft gamma repeaters as very strongly magnetized neutron stars - I. Radiative mechanism for outbursts. MNRAS, 275(2):255–300, July 1995.

[112] Christopher Thompson and Robert C. Duncan. The Soft Gamma Repeaters as Very Strongly Magnetized Neutron Stars. II. Quiescent Neutrino, X-Ray, and Alfven Wave Emission. ApJ, 473:322, December 1996.

[113] R Turolla, S Zane, and A L Watts. Magnetars: the physics behind observations. a review. *Reports on Progress in Physics*, 78(11):116901, oct 2015.

[114] E. P. Mazets, S. V. Golentskii, V. N. Ilinskii, R. L. Aptekar, and Iu. A. Guryan. Observations of a flaring X-ray pulsar in Dorado. Nature, 282(5739):587–589, December 1979.

[115] K. Hurley, T. Cline, E. Mazets, S. Barthelmy, P. Butterworth, F. Marshall, D. Palmer, R. Aptekar, S. Golenetskii, V. Il'Inskii, D. Frederiks, J. McTiernan, R. Gold, and J. Trombka. A giant periodic flare from the soft γ-ray repeater SGR1900+14. Nature, 397(6714):41–43, January 1999.

[116] K. Hurley, S. E. Boggs, D. M. Smith, R. C. Duncan, R. Lin, A. Zoglauer, S. Krucker, G. Hurford, H. Hudson, C. Wigger, W. Hajdas, C. Thompson, I. Mitrofanov, A. Sanin, W. Boynton, C. Fellows, A. von Kienlin, G. Lichti, A. Rau, and T. Cline. An exceptionally bright flare from SGR 1806-20 and the origins of short-duration γ-ray bursts. Nature, 434(7037):1098–1103, April 2005.

[117] G. L. Israel, T. Belloni, L. Stella, Y. Rephaeli, D. E. Gruber, P. Casella, S. Dall'Osso, N. Rea, M. Persic, and R. E. Rothschild. The discovery of rapid x-ray oscillations in the tail of the SGR 1806-20 hyperflare. ApJ, 628(1):L53–L56, jun 2005.

[118] K. Ioka. Magnetic deformation of magnetars for the giant flares of the soft gamma-ray repeaters. MNRAS, 327(2):639–662, Oct 2001.

[119] Alessandra Corsi and Benjamin J. Owen. Maximum gravitational-wave energy emissible in magnetar flares. Phys. Rev. D, 83:104014, May 2011.

[120] E. Burns, D. Svinkin, K. Hurley, Z. Wadiasingh, M. Negro, G. Younes, R. Hamburg, A. Ridnaia, D. Cook, S. B. Cenko, R. Aloisi, G. Ashton, M. Baring, M. S. Briggs, N. Christensen, D. Frederiks, A. Goldstein, C. M. Hui, D. L. Kaplan, M. M. Kasliwal, D. Kocevski, O. J. Roberts, V. Savchenko, A. Tohuvavohu, P. Veres, and C. A. Wilson-Hodge. Identification of a local sample of gamma-ray bursts consistent with a magnetar giant flare origin. ApJ, 907(2):L28, jan 2021.

[121] Nelson Christensen. Stochastic gravitational wave backgrounds. *Reports on Progress in Physics*, 82(1):016903, Nov 2018.

[122] Lee S. Finn. Detection, measurement and gravitational radiation. *Phys. Rev. D*, 46:5236–5249, 1992.

[123] Eric Thrane et al. Long gravitational-wave transients and associated detection strategies for a network of terrestrial interferometers. Phys. Rev. D, 83:083004, 2011.

[124] B. P. Abbott et al. All-sky search for long-duration gravitational wave transients with initial LIGO. Phys. Rev. D, 93(4):042005, 2016.

[125] P. D. Welch. The Use of Fast Fourier Transform for the Estimation of Power Spectra: A Method Based on Time Averaging Over Short, Modified Periodograms. *IEEE Transactions on Audio and Electroacoustics*, 15:70, 1967.

[126] Tanner Prestegard. *Unmodeled search for long-lasting gravitational-wave signals with LIGO and studies of underground seismic noise for future gravitational-wave detectors.* PhD thesis, University of Minnesota, 2016.

[127] E. Thrane and M. Coughlin. Searching for gravitational-wave transients with a qualitative signal model: Seedless clustering strategies. Phys. Rev. D, 88(8):083010, October 2013.

[128] B. P Abbott et al. Search for Transient Gravitational-wave Signals Associated with Magnetar Bursts during Advanced LIGO's Second Observing Run. ApJ, 874(2):163, April 2019.

[129] Michael W. Coughlin, Nelson L. Christensen, Rosario De Rosa, Irene Fiori, Mark Gołkowski, Melissa Guidry, Jan Harms, Jerzy Kubisz, Andrzej Kulak, Janusz Mlynarczyk, Federico Paoletti, and Eric Thrane. Subtraction of correlated noise in global networks of gravitational-wave interferometers. *Class. Quantum Grav.*, 33(22):224003, November 2016.

[130] Eric Thrane and Michael Coughlin. Detecting gravitational-wave transients at five sigma: a hierarchical approach. Phys. Rev. Lett., 115, 07 2015.

[131] Duncan Macleod, Alex L. Urban, Scott Coughlin, Thomas Massinger, and Matt Pitkin. gwpy/gwpy: 2.0.3, April 2021.

[132] B. P. Abbott et al. All-sky search for long-duration gravitational wave transients in the first Advanced LIGO observing run. *Class. Quantum Grav.*, 35(6):065009, 2018.

[133] B. P. Abbott et al. All-sky search for long-duration gravitational-wave transients in the second advanced ligo observing run. Phys. Rev. D, 99(10), May 2019.

[134] Michal Was, Marie-Anne Bizouard, Violette Brisson, Fabien Cavalier, Michel Davier, Patrice Hello, Nicolas Leroy, Florent Robinet, and Miltiadis Vavoulidis. On the background estimation by time slides in a network of gravitational wave detectors. *Class. Quantum Grav.*, 27(1):015005, 2010.

[135] M.H.P.M. van Putten. Proposed source of gravitational radiation from a torus around a black hole. Phys. Rev. Lett., 87:091101, 2001.

[136] A. Macquet, M. A. Bizouard, E. Burns, N. Christensen, M. Coughlin, Z. Wadiasingh, and G. Younes. Search for long-duration gravitational-wave signals associated with magnetar giant flares. *The Astrophysical Journal*, 918(2):80, sep 2021.

[137] R. Abbott et al. All-sky search for long-duration gravitational-wave bursts in the third Advanced LIGO and Advanced Virgo run. 7 2021.

[138] S. Klimenko et al. Method for detection and reconstruction of gravitational wave transients with networks of advanced detectors. Phys. Rev. D, 93(4):042004, 2016.

[139] Eric Thrane and Michael Coughlin. Detecting Gravitation-Wave Transients at 5σ: A Hierarchical Approach. Phys. Rev. Lett., 115(18):181102, 2015.

[140] Florent Robinet, Nicolas Arnaud, Nicolas Leroy, Andrew Lundgren, Duncan Macleod, and Jessica McIver. Omicron: a tool to characterize transient noise in gravitational-wave detectors. 7 2020.

[141] Tomoki Isogai. Used percentage veto for LIGO and virgo binary inspiral searches. *J. Phys. Conf. Ser.*, 243:012005, 2010.

[142] Simone Dall'Osso, Bruno Giacomazzo, Rosalba Perna, and Luigi Stella. Gravitational waves from massive magnetars formed in binary neutron star mergers. ApJ, 798(1):25, 2015.

[143] Rahul Biswas, Patrick R Brady, Jolien D E Creighton, and Stephen Fairhurst. The loudest event statistic: general formulation, properties and applications. *Class. Quantum Grav.*, 26(17):175009, 2009.

[144] Robert Coyne, Alessandra Corsi, and Benjamin J. Owen. Cross-correlation method for intermediate-duration gravitational wave searches associated with gamma-ray bursts. Phys. Rev. D, 93:104059, May 2016.

[145] Eric Sowell, Alessandra Corsi, and Robert Coyne. Multiwaveform cross-correlation search method for intermediate-duration gravitational waves from gamma-ray bursts. Phys. Rev. D, 100(12), Dec 2019.

[146] Tanner Prestegard, Eric Thrane, Nelson L. Christensen, Michael W. Coughlin, Ben Hubbert, Shivaraj Kandhasamy, Evan MacAyeal, and Vuk Mandic. Identification of noise artifacts in searches for long-duration gravitational-wave transients. *Class. Quantum Grav.*, 29:095018, 2012.

[147] Ryan P. Fisher, Gary Hemming, Marie-Anne Bizouard, Duncan A. Brown, Peter F. Couvares, Florent Robinet, and Didier Verkindt. DQSEGDB: A time-interval database for storing gravitational wave observatory metadata. 8 2020.

[148] Joshua R. Smith, Thomas Abbott, Eiichi Hirose, Nicolas Leroy, Duncan Macleod, Jessica McIver, Peter Saulson, and Peter Shawhan. A Hierarchical method for vetoing noise transients in gravitational-wave detectors. *Class. Quantum Grav.*, 28:235005, 2011.

[149] Reed Essick, Patrick Godwin, Chad Hanna, Lindy Blackburn, and Erik Katsavounidis. iDQ: Statistical Inference of Non-Gaussian Noise with Auxiliary Degrees of Freedom in Gravitational-Wave Detectors. 5 2020.

[150] Abbott et al. Search for post-merger gravitational waves from the remnant of the binary neutron star merger gw170817. *The Astrophysical Journal Letters*, 851(1):L16, 2017.

[151] J.C. Driggers, S. Vitale, A.P. Lundgren, M. Evans, K. Kawabe, S.E. Dwyer, K. Izumi, R.M.S. Schofield, A. Effler, D. Sigg, and et al. Improving astrophysical parameter estimation via offline noise subtraction for advanced ligo. *Physical Review D*, 99(4), Feb 2019.

[152] Sandro Mereghetti. The strongest cosmic magnets: soft gamma-ray repeaters and anomalous x-ray pulsars. *The Astronomy and Astrophysics Review*, 15(4):225–287, Jul 2008.

[153] C. D. Bochenek, V. Ravi, K. V. Belov, G. Hallinan, J. Kocz, S. R. Kulkarni, and D. L. McKenna. A fast radio burst associated with a Galactic magnetar. Nature, 587(7832):59–62, November 2020.

[154] D. M. Palmer, S. Barthelmy, N. Gehrels, R. M. Kippen, T. Cayton, C. Kouveliotou, D. Eichler, R. A. M. J. Wijers, P. M. Woods, J. Granot, Y. E. Lyubarsky, E. Ramirez-Ruiz, L. Barbier, M. Chester, J. Cummings, E. E. Fenimore, M. H. Finger, B. M. Gaensler, D. Hullinger, H. Krimm, C. B. Markwardt, J. A. Nousek, A. Parsons, S. Patel, T. Sakamoto, G. Sato, M. Suzuki, and J. Tueller. A giant γ-ray flare from the magnetar SGR 1806 - 20. Nature, 434(7037):1107–1109, April 2005.

[155] Eran O. Ofek. Soft Gamma-Ray Repeaters in Nearby Galaxies: Rate, Luminosity Function, and Fraction among Short Gamma-Ray Bursts. ApJ, 659(1):339–346, April 2007.

[156] Ryan Quitzow-James, James Brau, James A Clark, Michael W Coughlin, Scott B Coughlin, Raymond Frey, Paul Schale, Dipongkar Talukder, and Eric Thrane. Exploring a search for long-duration transient gravitational waves associated with magnetar bursts. *Class. Quantum Grav.*, 34(16):164002, jul 2017.

[157] Patrick J. Sutton et al. X-Pipeline: An Analysis package for autonomous gravitational-wave burst searches. *New J. Phys.*, 12:053034, 2010.

[158] P Kalmus, R Khan, L Matone, and S Márka. Search method for unmodeled transient gravitational waves associated with SGR flares. *Class. Quantum Grav.*, 24(19):S659–S669, sep 2007.

[159] J. Abadie, B. P. Abbott, T. D. Abbott, R. Abbott, M. Abernathy, C. Adams, R. Adhikari, C. Affeldt, P. Ajith, B. Allen, and et al. Implications for the origin of grb 051103 from ligo observations. ApJ, 755(1):2, Jul 2012.

[160] B Abbott, Robert Abbott, Rana Adhikari, J Agresti, P Ajith, B Allen, R Amin, SB Anderson, WG Anderson, M Arain, et al. Implications for the origin of grb 070201 from ligo observations. ApJ, 681(2):1419, 2008.

[161] J Aasi, BP Abbott, R Abbott, T Abbott, MR Abernathy, F Acernese, K Ackley, C Adams, Thomas Adams, P Addesso, et al. Search for gravitational waves associated with γ-ray bursts detected by the interplanetary network. Phys. Rev. Lett., 113(1):011102, 2014.

[162] D. Svinkin et al. A bright gamma-ray flare interpreted as a giant magnetar flare in NGC 253. Nature, 589(7841):211–213, 2021.

[163] Burkhard Zink, Paul D. Lasky, and Kostas D. Kokkotas. Are gravitational waves from giant magnetar flares observable? Phys. Rev. D, 85:024030, Jan 2012.

[164] Yuri Levin and Maarten van Hoven. On the excitation of f modes and torsional modes by magnetar giant flares. MNRAS, 418(1):659–663, Sep 2011.

[165] Riccardo Ciolfi and Luciano Rezzolla. Poloidal-field instability in magnetized relativistic stars. ApJ, 760(1):1, Oct 2012.

[166] Kostas Glampedakis and Leonardo Gualtieri. Gravitational waves from single neutron stars: An advanced detector era survey. *Astrophysics and Space Science Library*, page 673–736, 2018.

[167] Kazumi Kashiyama and Kunihito Ioka. Magnetar asteroseismology with long-term gravitational waves. Phys. Rev. D, 83(8), Apr 2011.

[168] Paul D. Lasky, Burkhard Zink, and Kostas D. Kokkotas. Gravitational waves and hydromagnetic instabilities in rotating magnetized neutron stars, 2012.

[169] S. Golenetskii, R. Aptekar, E. Mazets, V. Pal'Shin, D. Frederiks, T. Cline, S. Barthelmy, J. Cummings, N. Gehrels, K. Hurley, T. Cline, I. Mitrofanov, A. Kozyrev, M. Litvak, A. Sanin, V. Tret'yakov, A. Parshukov, W. Boynton, C. Fellows, K. Harshman, C. Shinohara, R. Starr, D. M. Smith, R. P. Lin, J. McTiernan, R. Schwartz, C. Wigger, W. Hajdas, A. Zehnder, J. L. Atteia, C. Graziani, and R. Vanderspek. IPN triangulation and konus spectrum of the bright short/hard GRB051103. *GRB Coordinates Network*, 4197:1, January 2005.

[170] K Hurley, Antonia Rowlinson, E Bellm, D Perley, Igor G Mitrofanov, Dmitry V Golovin, Alexander S Kozyrev, Maxim L Litvak, AB Sanin, W Boynton, et al. A new analysis of the short-duration, hard-spectrum grb 051103, a possible extragalactic soft gamma repeater giant flare. MNRAS, 403(1):342–352, 2010.

[171] S. Golenetskii, R. Aptekar, E. Mazets, V. Pal'Shin, D. Frederiks, T. Cline, A. von Kienlin, G. Lichti, A. Rau, D. Gotz, S. Mereghetti, J. Cummings, S. Barthelmy, N. Gehrels, H. Krimm, K. Hurley, D. M. Smith, R. P. Lin, J. McTiernan, R. Schwartz, C. Wigger, W. Hajdas, A. Zehnder, K. Yamaoka, M. Ohno, Y. Fukazawa, T. Takahashi, M. Tashiro, Y. Terada, T. Murakami, and K. Makishima. IPN localization of very intense short GRB 070201. *GRB Coordinates Network*, 6088:1, January 2007.

[172] K. Hurley, J. Goldsten, S. Golenetskii, R. Aptekar, E. Mazets, V. Pal'Shin, D. Frederiks, T. Cline, A. von Kienlin, G. Lichti, and A. Rau. IPN triangulation of GRB070201 (refined error box using MESSENGER data). *GRB Coordinates Network*, 6103:1, January 2007.

[173] D. S. Svinkin, D. D. Frederiks, R. L. Aptekar, S. V. Golenetskii, V. D. Pal'shin, Ph. P. Oleynik, A. E. Tsvetkova, M. V. Ulanov, T. L. Cline, and K. Hurley. The second Konus-Wind catalog of short gamma-ray bursts. *Astrophys. J. Suppl.*, 224(1):10, 2016.

[174] Fermi GBM Team. GRB 200415A: Fermi GBM Final Real-time Localization. *GRB Coordinates Network*, 27579:1, April 2020.

[175] D. Svinkin, S. Golenetskii, R. Aptekar, D. Frederiks, A. Ridnaia, T. Cline, Konus-Wind Team, K. Hurley, I. G. Mitrofanov, D. Golovin, M. L. Litvak, A. B. Sanin, A. Kozlova, S. Golenetskii, R. Aptekar, D. Frederiks, D. Svinkin, T. Cline, A. Goldstein, M. S. Briggs, C. Wilson-Hodge, A. von Kienlin, X. Zhang, A. Rau, V. Savchenko, E. E. Bozzo, C. Ferrigno, S. Barthelmy, J. Cummings, H. Krimm, D. Palmer, W. Boynton, C. Fellows, K. Harshman, H. Enos, and R. Starr. Improved IPN error box for GRB 200415A (consistent with the Sculptor Galaxy). *GRB Coordinates Network*, 27595:1, April 2020.

[176] B. P. Abbott et al. Prospects for observing and localizing gravitational-wave transients with Advanced LIGO, Advanced Virgo and KAGRA. *Living Rev. Rel.*, 23(1):3, 2020.

[177] D. Huppenkothen, L. M. Heil, A. L. Watts, and E. Göğüş. Quasi-periodic Oscillations in Short Recurring Bursts of Magnetars SGR 1806-20 and SGR 1900+14 Observed with RXTE. ApJ, 795(2):114, November 2014.

[178] D. Huppenkothen, C. D'Angelo, A. L. Watts, L. Heil, M. van der Klis, A. J. van der Horst, C. Kouveliotou, M. G. Baring, E. Göğüş, J. Granot, Y. Kaneko, L. Lin, A. von Kienlin, and G. Younes. Quasi-periodic Oscillations in Short Recurring Bursts of the Soft Gamma Repeater J1550-5418. ApJ, 787:128, June 2014.

[179] S. Mereghetti, V. Savchenko, C. Ferrigno, D. Götz, M. Rigoselli, A. Tiengo, A. Bazzano, E. Bozzo, A. Coleiro, T. J. L. Courvoisier, M. Doyle, A. Goldwurm, L. Hanlon, E. Jourdain, A. von Kienlin, A. Lutovinov, A. Martin-Carrillo, S. Molkov, L. Natalucci, F. Onori, F. Panessa, J. Rodi, J. Rodriguez, C. Sánchez-Fernández, R. Sunyaev, and P. Ubertini. INTEGRAL Discovery of a Burst with Associated Radio Emission from the Magnetar SGR 1935+2154. ApJ, 898(2):L29, August 2020.

[180] C. K. et al. Li. Insight-HXMT Identification of a non-thermal X-ray burst from SGR J1935+2154 and with FRB 200428. *arXiv e-prints*, page arXiv:2005.11071, May 2020.

[181] Zorawar Wadiasingh and Andrey Timokhin. Repeating Fast Radio Bursts from Magnetars with Low Magnetospheric Twist. ApJ, 879(1):4, Jul 2019.

[182] Zorawar Wadiasingh, Paz Beniamini, Andrey Timokhin, Matthew G. Baring, Alexander J. van der Horst, Alice K. Harding, and Demosthenes Kazanas. The Fast Radio Burst Luminosity Function and Death Line in the Low-twist Magnetar Model. ApJ, 891(1):82, March 2020.

[183] A. G. Suvorov and K. D. Kokkotas. Young magnetars with fracturing crusts as fast radio burst repeaters. MNRAS, 488(4):5887–5897, October 2019.

[184] Zorawar Wadiasingh and Cecilia Chirenti. Fast Radio Burst Trains from Magnetar Oscillations. ApJ, 903(2):L38, November 2020.